NORTHWESTERN UNIVERSITY

Intermolecular Charge Transfer: A Design Motif for the Study of Organic Ferroelectricity, Semiconductivity and Exchange in Supramolecular Assemblies

A DISSERTATION

SUBMITTED TO THE GRADUATE SCHOOL
IN PARTIAL FULFILLMENT OF THE REQUIREMENTS

for the degree

DOCTOR OF PHILOSOPHY

Field of Materials Science and Engineering

By

Ashwin Narayanan

EVANSTON, ILLINOIS

September 2018

Abstract

Intermolecular Charge Transfer: A Design Motif for the Study of Organic Ferroelectricity, Semiconductivity and Exchange in Supramolecular Assemblies

Ashwin Narayanan

Intermolecular charge transfer between electron-rich donor and electron-poor acceptor molecules offer great promise in the development of novel, low-cost electronic materials. It is hypothesized that control over the intermolecular interactions and supramolecular self-assembly of these systems could tune electronic properties and discover new functions. To that end, a series of co-crystals were designed, incorporating a naphthalene electron donor and pyromellitic diimide acceptor molecules, following the paradigm of lock-arm supramolecular ordering (LASO). While these co-crystals traditionally grow with 1:1 association between acceptor and donor molecules, the co-crystal of 1-amino-5-naphthol and diethylene glycol-functionalized pyromellitic diimide grew with a 2:1 acceptor to donor ratio, where the molecules orient themselves for charge transfer in nearly orthogonal face-to-face and edge-to-face mixed stacks. The co-crystals, while crystallographically centrosymmetric gave rise to second harmonic generation, which indicates noncentrosymmetric structure. In addition, they displayed room-temperature ferroelectric polarization, a consequence of electron transfer and hydrogen bonding, along two distinct crystallographic axes. Building on the LASO paradigm, a second series of co-crystals were developed, where the diethylene glycol "arms" were functionalized on the donor instead of the acceptor. While changing the donor chemistry did not change the crystallographic refinement of the co-crystals, it did influence the measured nonlinear optical and electronic properties. Specifically, the co-crystal with 1,5-diaminonaphthalene displayed second harmonic activity and room-temperature ferroelectricity. Reducing the nucleophilicity of the electron donor by switching the functional groups on the donor from amines to ester, on the other hand, neither generated

ferroelectric not second harmonic activity. This observation links the strength of the electron donor molecule to the breaking of inversion symmetry and observation of stable ferroelectric polarization. Attempts to make charge transfer complexes more amenable to solution processing saw the development of two series of donor and acceptor molecules, one with complimentary urea and sulfonamide hydrogen bonding groups, and the other with added amino acids. The choice of urea-sulfonamide chemistry promoted heterodimeric charge transfer association between the donor and acceptor molecules upon co-assembly in organic solvents. Casting the co-assemblies onto a film, however, resulted in the phase separation of the two molecules into their respective supramolecular assemblies. Residual charge transfer in the phase separated films, likely due to dopant molecules within bulk supramolecular assemblies, led to an increase in thin-film conductivity by two orders of magnitude when compared against that of separate donor and acceptor films. In addition, the importance of hydrogen bonding in driving long-range supramolecular order and forming conducting pathways between electrodes was established by the lower thin-film conductivities of molecules without urea and sulfonamide functionalities. The second set of solution-based charge transfer complexes, where naphthalene and naphthalene diimide aromatic cores were functionalized with short tetrapeptide sequences, revealed pH-sensitive self-assembly and co-assembly in aqueous media. Having established that fluorescence emission quenching of the self-assembled donor is a consequence of intermolecular charge transfer between the donor and acceptor moieties, quenching was used as a metric for supramolecular exchange between assemblies of donor and acceptor molecules. Despite modulating the molar fraction of donor and acceptor moieties within the supramolecular nanostructures, inter-fiber exchange occurred far faster than that observed between non-interacting supramolecular assemblies. This implies that the driving force for exchange is dominated by charge transfer interactions. In addition, the placement of the aromatic moieties within hydrophobic segments of the amphiphilic molecules implies that charge transfer-mediated exchange requires the dissolution and re-assembly of the supramolecular assemblies to facilitate intermolecular association and inter-fiber exchange.

Acknowledgements

If you know whence you came, there is
really no limit to where you can go
James Baldwin

The people who contributed to the work presented in this thesis have, directly or indirectly, shaped my life over the past 5 years. For that, I am eternally grateful.

Prof. Stupp

I save my first acknowledgement for Professor Stupp, who has been key in guiding the direction of my research, and encouraging me to explore that which is yet understood. I thank Prof. Stupp for welcoming me to the group, and allowing me to choose my research direction despite my initial lack of knowledge in the field. His vision and creativity in pushing the frontiers of science was, and will always be, an inspiration.

Thesis Committee

I would also like to thank my committee members: Prof. J. Fraser Stoddart, Prof. Jiaxing Huang and Prof. Monica Olvera de la Cruz, for the valuable time and advice throughout my graduate career. I would especially like to thank Prof. Stoddart, with whom I was able to work on a number of projects, and whose stories of science and travels and wonder will resonate with me for a long time.

Dr. Liam Palmer

I would be remiss if I did not thank Dr. Liam Palmer. He kept me on track, and picked me up when I fell behind. Even if that meant writing three monthly reports at midnight on a Friday. Thank you for making yourself available to answer any question I had, be it a small research conundrum or

a larger existential crisis. Thank you for bringing unity, community and collaboration to this large group.

Dr. Dennis Cao

None of my research would be possible without the guidance and friendship with Dr. Dennis Cao. Dennis was responsible for all the LASO chemistry and crystal growth, which spurred a number of manuscripts throughout my time at Northwestern. He also taught me all I know about charge-transfer complexes and ferroelectric materials, and masqueraded as my unofficial mentor. From our first lunch at Mandarin House to the day he moved to St. Paul, MN to start his family and career, I have always cherished my time with my colleague and dear friend, Dennis Cao.

Dr. Leonel Barreda

A common thread with my research is my reliance on exceptional chemists. While Dr. Dennis Cao supported me on all the crystal work and some of the peptide synthesis, Dr. Leonel Barreda, was my closest collaborator through the urea-sulfonamide and peptide-CT project. I thoroughly appreciate the mountain of effort he put in to synthesizing the PEG compounds, as well as his patience and creativity in designing the molecules. Words cannot describe how grateful I am. On a lighter note, I still want to know how he came up with my nickname.

Internal Collaborators

My research in the Stupp group would not have been possible without the commitment from my collaborators in the group: Dr. Hiroaki Sai, Dr. Taner Aytun, Dr. Kohei Sato, Dr. Ivan Sasselli, Dr. Mark Hendricks, Dr. Shantanu Sur, James Passarelli and Adam Dannenhoffer. Thank you Dr. Hiroaki Sai, for enduring my badgering about confusing results, for volunteering your time to help run late night experiments, for actually reading and editing my thesis. Dr. Taner Aytun was the first Stupp group member I met at Northwestern, and was instrumental in onboarding me into the group.

He was my coffee buddy, squash partner, late night insomnia cookie companion, and CEO of Taner Express. Dr. Kohei Sato was my expert on cryo-TEM and circular dichroism. I thank him for all the times invalidated my circular dichroism spectra, but made up for it at drinks afterward. Dr. Ivan Sasselli, thank you for all your molecular dynamics simulations and conversations about scotch. Dr. Mark Hendricks, thank you for all the last-minute fluorine NMRs, and for Sherlock. He is an angel. Dr. Shantanu Sur, thank you for teaching me about two-photon confocal microscopy, and inspiring my pursuit of nonlinear optical properties in the LASO co-crystals. James Passarelli, thank you for the DOSY experiments, and flying the flag of the energy materials subgroup. Adam Dannenhoffer, thank you for the variable temperature absorption and flow cell X-ray measurements. Adam does need to work on his fitness though.

External Collaborators

Dr. Anthea Blackburn, Dr. Andrew C.-H. Sue, Dr. Jonathan Barnes and Dr. Laszlo Frazer were my collaborators outside the Stupp group, and I thank them for allowing me to learn from and discover with them. Thank you Anthea for your work on LASO crystallographic assignments. Thank you Andrew for your initial work and knowledge about ferroelectric systems. Jonathan, thank you for teaching me about the ExBox system. And Laszlo, I appreciate your expertise in non-linear optics and your help measuring and interpreting second harmonic data.

Stupp Group Alumni

Two Stupp group alumni were key in my early development as a graduate researcher and scientist. Dr. Amparo Ruiz Carretero was instrumental in my introduction to the Stupp group, as not only was she my first mentor, but she also motivated my research direction in solution-processable charge transfer complexes. Dr. Alok Tayi was my official (remote) mentor, who set the basis for how to measure ferroelectricity in LASO co-crystals. He demonstrated patience in teaching me how to

attach electrodes onto the crystals, and correctly interpret ferroelectric data. I could have, however, done without the drama surrounding that Nature paper.

Stupp Group Members

The soul of a research group is defined by its members. They guide the tone and quality of the work, and ensure a healthy work-life balance. Every single member of the group has, in their own way, helped foster the collaborative, constructive and convivial group ethos, for which I am thankful. If your name does not appear in this next section, I promise it is not for lack of appreciation. To that end, Dr. Oliver Dumele, Dr. D.J. Fairfield, Dr. Christopher Synatschke, Dr. Eduard Sleep, Stacey Chin, Garrett Lau, Nick Sather and many others have played key roles in defining the lab group. Oliver, credited for starting Friday happy hours, thank you for ensuring the lab is never thirsty. D.J., my office mate since the beginning of graduate school, your serene composure throughout your graduate career was an inspiration for all. Your PB&J habit will remain heralded in Stupp group lore. Christopher, Eduard and the stalwart Sunday volleyball crew, thank you for getting me out of the house on a Sunday morning. Stacey, thank you for your musings about food, Nutella cruffins and Joy the Baker. Garrett, thank you for regaling us about your cooking adventures, and for making magnets great again. Nick, thank you for putting up with me through years of living and co-founding, and for using whiskey (in Vale) to make me commit to my entrepreneurial passion.

Undergraduate Students

I have had the pleasure of working with two exceptional undergraduate students: Benjamin Swanson and Emily Moy. Ben, was responsible for a lot of the early explorations into the urea-sulfonamide project. Most of his summer REU was spent debugging a system that invariably did not work, but his efforts motivated the development of the correct molecules for the functional properties we sought. Emily is not a doctor, though the time she spends in lab might persuade a

passerby otherwise. Her effort, patience and dedication to her work has always been exceptional. I am sure her work ethic will carry her far in life.

Archer Group Alumni

My first exposure to academic research came as an undergraduate at Cornell University, under the tutelage of Dr. Rajesh Mallavajula, Dr. Samanvaya Srivastava and Prof. Lynden Archer. I thank them for the opportunity to learn and be part of an academic research environment, and for not re-assigning my (conveniently located) desk to new lab members.

Staff

It takes a lot of work behind the scenes to make a research group function, and a lot more when the research group in question is the Stupp group. I would like to thank Laura Fields, Maura Walsh, Todd Linton and Daniel Cartensen for their undying work to accommodate my last-minute requests, for their patience when plans change, and for ensuring the group operates smoothly.

Without the people who manage core facilities and specific instruments, none of the experiments in my thesis would have occurred. I want to thank Oleksandr Chernyashevsky for maintaining the PPMS system, and for his help in building the ferroelectric probes I used throughout my graduate career. Dr. Dina Arvanitis taught me everything about two-photon confocal microscopy. Dr. Gajendra Shekhawat managed the AFM systems, and helped me whenever I ran out of probes, had a software issue, or wanted to push the instrument to its limit. Dr. Arabela Grigorescu helped with the photophysical measurements on CT complexes. And lastly Dr. Yongbo Zhang, for maintaining the NMR facility at Northwestern, and suggesting the DOSY experiments.

Chicago Friends

Chicago summer and winters would not be the same without the friends I made through my last 5 years in graduate school. Thank you, Dr. Michael Whittaker, Dr. Jade Balla, Dr. Xin Chen,

Dr. Kavita Chandra, Dr. Linda Guiney, Dr. Amy Plunk, Dr. Andrew Mannix, Dr. Ricardo Komai, Michael Knudsen, and the entire Fantasy Football crew for ensuring life is as beautiful as Malört is disgusting. Matthew Peters is credited for introducing me to Bitmoji.

Old Friends

I would also like to thank my friends from Cornell: Nipun Jasuja, Deepak Kaji and Sehj Kashyap, who enabled my nerd and academic tendencies. To my all my friends I grew up with in Singapore, thank you for keeping me weird.

Tier One Family

To my Tier One family, thank you for kicking my butt, and teaching me something in the process. Thank you for not making fun of me when I forget basic choke defenses, or when I mess up a simple combo. Thank you for encouraging me to find and surpass my limits. I appreciate your company, your guidance, your efforts and your care in every class.

PAWS Family

To my PAWS family, thank you for allowing me to re-discover my love of animals, even if my time volunteering is motivated by rather selfish means (dogs $\geq$ humans). Thank you for welcoming me into the wonderful organization, for correcting me when I mess up a showing, and for not chastising me when I arrive underdressed for Fur Ball. And thank you for introducing me to my girlfriend, even though it took you all forever to find out.

Shamoyita DasGupta

To the woman who keeps me sane and silly, buoyant and bullish, daffy and defiant, thank you. Thank you for all your patience and kindness, even when I am late to the Christkindlmarket, or when I abruptly modify date night. Thank you for constantly pushing me, and challenging me to

go further, faster. I cherish all the PAWS shifts we spend together, even if it involves picking up mountains of dog poop and complaining about obstinate adopters. The pages that dictate my life would be very different without you in them. I thank you my Jupiter, my love.

My Family

To my cousins, aunts and uncles, thank you for supporting me throughout my time in the United States, for providing a reason to celebrate and a shoulder to cry on. Your presence has truly made me find peace and a home away from home.

And finally, I would like to thank the people who have always loved for, cared for, and provided for me: my father V. Narayanan and mother Shubha Iyer Narayanan. They motivated me to find my passion and purpose, be it through athletics or academics. They never tempered my intellectual curiosity and thirst for discovery, be it during my first lesson in optics involving ants and a magnifying glass (I was three), or my first failed chemistry experiment studying the thermal stability of fatty acid salts (I aged a mixture of soaps in the summer sun. I was six). They constantly challenged me, pushing me to go outside my comfort level.

They were always there for me, through triumph and struggle, through failed experiments, late nights and early mornings, through an ACL tear and broken finger, through the Polar Vortex and the Summer of Fun. They forced me to communicate my research to an audience far removed from the scientific community, and made me learn to appreciate the impact of my work. My biggest fans and worst critics, their daily sacrifice is the compass that steered me here today, and the wind that powers where I go tomorrow.

I thank you, and love you, dear mum and dad.

LIST OF ABBREVIATIONS

A Acceptor

A^- Ionized Acceptor

AFM Atomic Force Microscopy

ATR-FTIR Attenuated Total Reflectance Fourier Transform Infrared Spectroscopy

C_{ox} Oxide Capacitance

CD Circular Dichroism

CD_3CN Deuterated Acetonitrile

CD_3SOCD_3 Deuterated Dimethyl Sulfoxide

$CDCl_3$ Deuterated Chloroform

CF_3CO_2H Trifluoroacetic acid

CG-MD Course Grained Molecular Dynamic Simulations

CH_2Cl_2 Dichloromethane

Chloranil Tetrachloro-1,4-Benzoquinone

cryo-TEM Cryogenic Transmission Electron Microscopy

CT Charge Transfer

D Donor

D^+ Ionized Donor

dabcoHClO$_4$ diazabicyclo[2.2.2]octane

DC Direct Current

DCM Dichloromethane

DEG Diethylene Glycol

DFT Density Functional Theory

DIEA N-N-diisopropylethylamine

DMAP 4-dimethylaminopyridine

DMF Dimethylformamide

DMSO-d$_6$ Deuterated Dimethyl Sulfoxide

DMTTF 4,4-dimethyltetrathaifulvalene

DOSY Diffusion Ordered Nuclear Magnetic Resonance Spectroscopy

E_{CT} Charge Transfer Energy

E_{in} Incident Photon Energy

E_C Coercive Field

EPR Electron Paramagnetic Resonace

Et$_3$N Triethylamine

EtOAc Ethyl Acetate

EtOH Ethanol

Fmoc Fluorenylmethyloxycarbonyl chloride

FRET Förster Resonance Energy Transfer

FTIR Fourier Transform Infrared Spectroscopy

GIXS Grazing Incidence X-ray Scattering

H_2br Bromalillic Acid

H_2ca Chloranillic Acid

HFIP 1,1,1,3,3,3-hexafluoro-2-propanol

HOMO Highest-Occupied Molecular Orbital

HPLC High-Peformance Liquid Chromatography

HR MS (ESI) High-Resolution Electrospray Ionization Mass Spectrometry

I-V Current-Voltage Curve

I_{DS} Source-Drain Output Current

iPrOH Isopropyl Alcohol

ITC Isothermal Titration Calorimetry

KDP Potassium Dihydrogen Phosphate

LASO Lock-Arm Supramolecular Ordering

LED Light Emitting Diode

LUMO Lowest Unoccupied Molecular Orbital

Me_2CO Acetone

MeCN Acetonitrile

MeOH Methanol

MW Molecular Weight

NDI Naphthalene Diimide

NIT Neutral-to-Ionic Transition

NLO Non-Linear Optical

NMePh N-methylphenazinium

NMP N-methyl-2-pyrrolidone

NMR Nuclear Magnetic Resonance

NP Naphthalene

OFET Organic Field Effect Transistor

OPA Optical Parametric Amplifier

OPV Organic Photovoltaics

P Polarization

P-E Polarization-Electric Field Graph

$\mathbf{P}_{max}$ Maximum Polarization

$\mathbf{P}_R$ Remant Polarization

PA Peptide Amphiphile

PAH Polycyclic Aromatic Hydrocarbon

PhMe Toluene

Phz Phenazine

PMDI Pyromellitic Diimide

PPMS Physical Property Measurement System

PTFE Polytetrafluoroethylene

PUND Positive-Up-Negative-Down Ferroelectric Polarization

PVDF Polyvinylidene Fluoride

Py Pyrene

PyBOP Benzotriazole-1-yl-oxy-tris-pyrrolidino-phosphonium hexafluorophosphate

QBr_2I_2 Dibromodiiodo-1,4-benzoquinone

QBr_4 Tetrabromo-1,4-benzoquinone

$QBrCl_3$ 2-Bromo-3,5,6-trichloro-1,4-benzoquinone

QCl_4 Tetrachloro-1,4-benzoquinone

RP-HPLC Reverse-Phase High-Performance Liquid Chromatography

RT Room Temperature

SAXS Small Angle X-ray Scattering

SEC Spectroelectrochemical

SHG Second Harmonic Generation

SOMO Singly Occupied Molecular Orbital

STORM Stochastic Optical Reconstruction Microscopy

SWCNT Single-Walled Carbon Nanotube

T_c Curie-Weiss Transition Temperature

TBAI Tetrabutylammonium Iodide

$TBAPF_6$ Tetrabutylammonium Hexafluorophosphate

TCNQ 7,7,8,8-tetraquinodimethane

TEM Transmission Electron Microscopy

TFA Trifluoroacetic acid

TFT Thin-Film Transistor

TGS Triglycine Sulfate

THF Tetrahydrofuran

TIPS Triisiopropylsilane

TLC Thin-layer Chromatography

TOF LC-MS Time-of-Flight Liquid Chromatography-Mass Spectrometry

TPPZ 2,3,5,6-tetra(2-pyridinyl)pyrazine

Tris 2-amino-2-(hydroxymethyl)propane-1,3-diol

TTF Tetrathiafulvalene

UPS Ultraviolet Photoelectron Spectroscopy

V_G Gate Voltage

V_T Carrier Threshold Voltage

Here's to the crazy ones

The misfits

The rebels

The troublemakers

The round pegs in the square holes

The ones who see things differently

They're not fond of rules. And they have no respect for the status quo

You can quote them, disagree with them, glorify or villify them

About the only thing you can't do is ignore them

Because they change things; they push the human race forward

And while some may see them as the crazy ones, we see genius

Because the people who are crazy enough to think they can change the world, are the ones who do.

- **Apple Inc.** (1997)

(attribted to Rob Siltanen)

To my parents who taught me, and my teachers who raised me.

CONTENTS

LIST OF TABLES

LIST OF FIGURES

1 Introduction

1.1 Supramolecular chemistry and peptide amphiphiles

Where molecular chemistry studies the covalent bond and its rules to govern the structure and properties of a system, supramolecular chemistry is the chemistry of the intermolecular bond, covering the association between two or more molecular species.[1–4] Supramolecular chemistry can be viewed as organization of small or molecular entities into structures of higher complexity, from which unrealized functional architectures and properties stem. What makes supramolecular chemistry, as a form of information-directed self-assembly, fascinating and challenging is the ability to tune or program the system to form complex higher order structures with little intervention during the actual process of assembly itself. To put in in lay terms, it is like asking a set of Lego bricks to build a structure on their own.

To understand supramolecular chemistry is to understand the interplay between covalent interactions, as well as noncovalent interactions between atoms and molecules. Tuning the strengths of these intermolecular forces, be they hydrogen bonding, solvophobic interactions, electrostatics, π-π stacking, metal-ligand interactions and electron transfer,[5,6] can help realize complexities such as motion,[7–9] capture,[10,11] as well as biological[12] and electronic[13] function. The dynamic nature of these weak intermolecular forces also introduces the element of kinetics and thermodynamics of stability and exchange[1] between supramolecular assemblies, making the field rich with the potential for sweeping innovation.

Arguably the best examples of function driven by supramolecular assembly can be found in nature itself. Critical biological systems, such as proteins,[14] DNA,[15,16] and receptors[17] routinely exploit noncovalent interactions to impart or disrupt order and function. Among these examples, proteins are likely the most commonly studied, due to their innate ability to assemble in a hierarchical manner (namely primary, secondary, tertiary and quaternary structures).[18] At its core, the

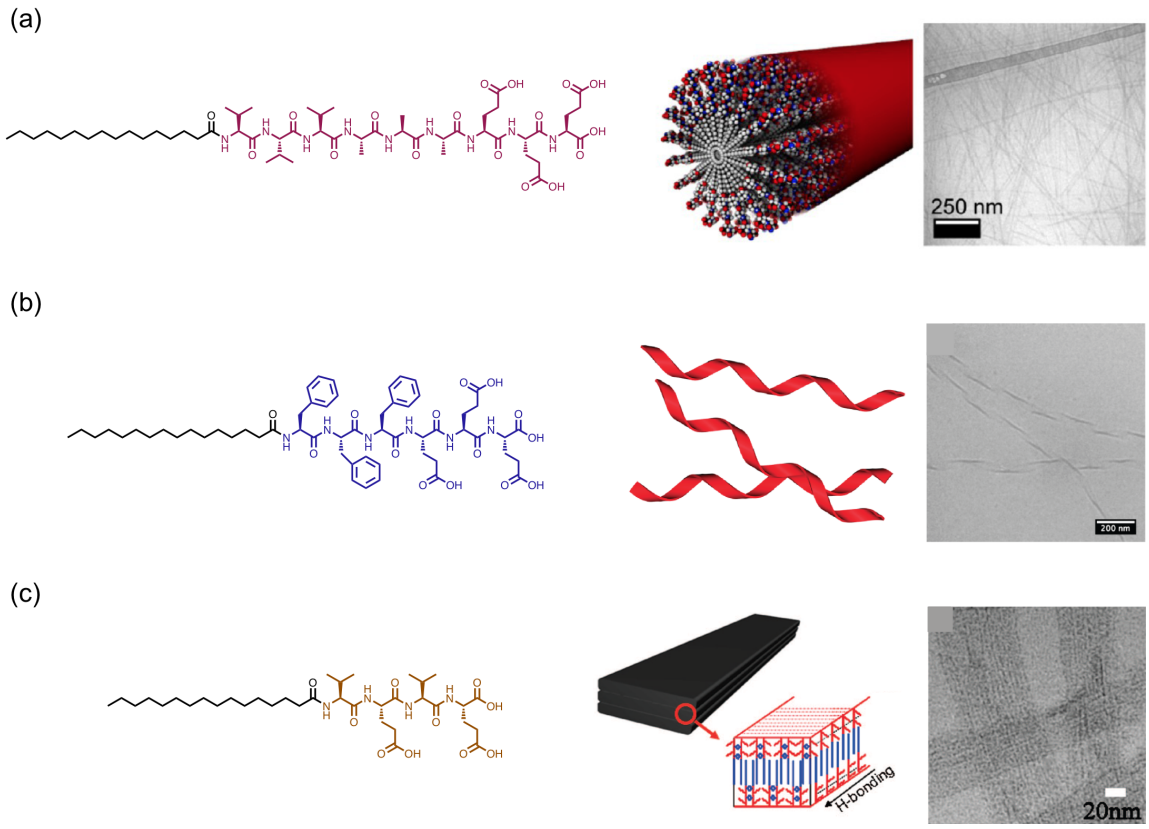

Figure 1.1: Chemical strucuture, morophological schematic and cryogenic transmission electron micrograph of peptide amphiphiles (a) $V_3A_3E_3$, which forms cylindrical nanostructures,[20] (b) F_3E_3, which forms twisted ribbon nanostructures,[21] and (c) VEVE, which forms wide ribbon nanostructures.[22]

building block of proteins are amino acids, which can polymerize *covalently* to form polypeptides, as well as *noncovalently* to form higher order structures. These noncovalent amino acid interactions, primarily hydrogen bonding and solvophobic interactions, typically occur on the angstrom scale, and drive the assembly of peptides into either (i) random coil arrangements, where internal order is negligible, (ii) α helices, defined by a right handed screw conformation, or β sheets, characterized by the lateral arrangement (parallel or antiparallel) of amino acids.[19] Integrating these biological structure-driving motifs into a molecular system introduces unparalleled control over the morphology and function of the supramolecular assembly.

Early efforts to incorporate amino acids into supramolecular architectures involved covalently attaching aliphatic or lipid sequences to peptides.[23–25] Since the covalent attachments were largely hydrophobic, the resulting molecular system was amphiphilic, and followed Israelachvili's rules of amphiphilic self-assembly[26] in aqueous solutions. This later led to the first use of this novel "peptide amphiphile" (PA) motif to induce the self-assembly of supramolecular nanostructures in aqueous solutions.[27] These peptide amphiphiles consisted of three distinct components: (i) an aliphatic tail (typically a linear alkyl chain) to enable hydrophobic collapse, (ii) a β-sheet forming amino acid sequence, to drive long-range order and assembly through intermolecular hydrogen bonding interactions, and (iii) a charged headgroup (typically charged amino acids) to introduce a hydrophilic moiety and complete the molecule's amphiphilicity.[19,20,28,29] In keeping with these design criteria, the peptide amphiphiles have been shown to assemble into long nanostructures in aqueous solutions, capable of mimicking extracellular matrices.[12] To amplify the biological functionality of these materials, additional biological epitopes and binding sequences may be added to the end of the charged headgroup, sequences that target a particular biological function.[12] In this way, peptide amphiphiles have become a platform technology for a wide variety of biological and medical applications, be it in the space of vascular,[30,31] orthopedic,[32,33] neurology[34–36] as well as imaging and diagnosis.[37,38]

Unique among peptide amphiphiles is the modularity and diversity in structure, obtainable by small changes in the chemistry and order of amino acids within the molecular structure. The canonical peptide amphiphile[27] incorporates a palmitic acid aliphatic tail to three valine (V), three alanine (A) and three glutamic acid (E) amino acids (commonly known as $C_{16}V_3A_3E_3$), which assembles (Figure 1.1a) into cylindrical nanofibers with a known diameter. This nanostructure morphology is preserved even after removing the valine amino acids.[21] However, switching the alanines for phenylalanines (F) resulted in the formation (Figure 1.1b) of twisted ribbons in water, likely due to aromatic stacking between phenylalanine residues. This ribbon-like morphology can also be preserved (Figure 1.1c) using an alternating valine-glutamic acid peptide sequence,[22] where the combination of hydrophobic collapse and dimerization between glutamate groups on adjacent am-

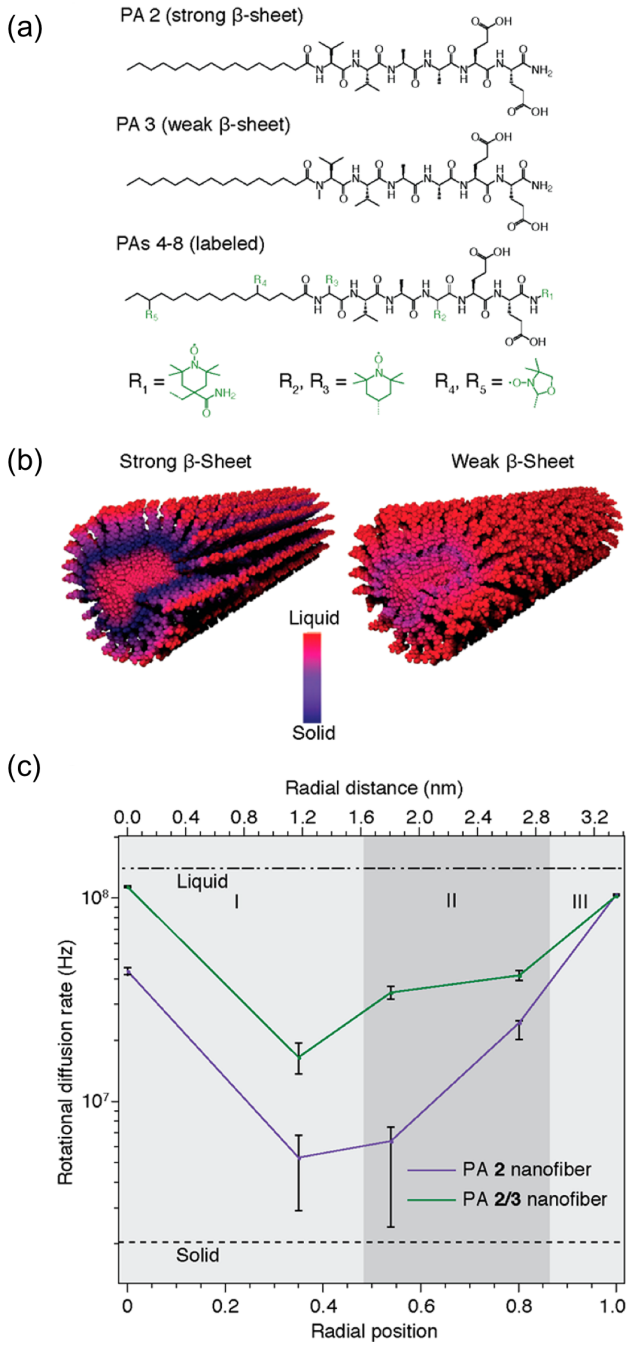

Figure 1.2: (a) Chemical structures of peptide amphiphiles used in internal dynamics studies. Note the presence and position of the nitroxyl electron spin radical group on the amphiphile. (b) Heat map of the liquid and solid-like rotational dynamics of the spin radical group located at various positions within the nanostructure. (c) Rotational diffusion rates plotted against the radical position within the nanofiber.[29,39]

phiphilic molecules promotes lateral aggregation and the formation of wide ribbons. Changing the number of -VE repeat units,[40] as well as the order of V and E amino acids,[41] have also been shown to influence not only the width of the wide nanostructures, but also the helicity and morphology of the assembled structures. These are but a few examples of the breadth of functional architectures possible using the PA molecular assembly motif.

While the morphology of PA nanostructures illustrate the modularity in static assembly, the dynamics of PA nanostructures is also a topic of great interest, especially given the dominance of noncovalent interactions in the overall assembly architecture. A quantitative study[39] of the internal dynamics of PA nanostructures used electron paramagnetic resonance spectroscopy (EPR) to elucidate rotational diffusion rates on nitroxyl radical electron-spin labelled PAs (Figure 1.2a). Through the cross section of the PA (Figure 1.2b) the rotational diffusion rate was highest in the core and exterior of the nanostructure, with the lowest diffusion rate in the interior of the nanostructure with the highest density of hydrogen bonding β-sheet architectures (Figure 1.2c). The rotational diffusion rates can be altered by altering the β-sheet strength of the PAs, with a strong β-sheet PA having slower, or more solid-like dynamics than a weak β-sheet PA.

In addition to the internal dynamics of PA nanostructures, dynamics of exchange between non-interacting PA nanostructures also provide insights as to exchange dynamics between supramolecular biological lipids.[42] This led to the use of stochastic optical reconstruction microscopy (STORM), which can resolve up to 10 nm segments within a single nanostructure, as a tool to understand inter-fiber exchange. To do so, water-soluble sulfonated dyes were conjugated to PAs (Figure 1.3a), each dye capable of fluorescing at distinct but different wavelengths. The dyed PAs were then mixed (Figure 1.3b), correlative image analysis was used to quantify the spatial distribution of the non-interacting, but separately dyed PAs. A comparison of the spatial distribution after 1 minute and 48 hours (Figure 1.3c), revealed an exchange of clustered molecules, as opposed to typical homogeneous monomeric exchange. This is likely due to the strong and yet discontinuous hydrogen-bonding interactions within the β-sheet of individual nanofibers, highlighting the propensity of

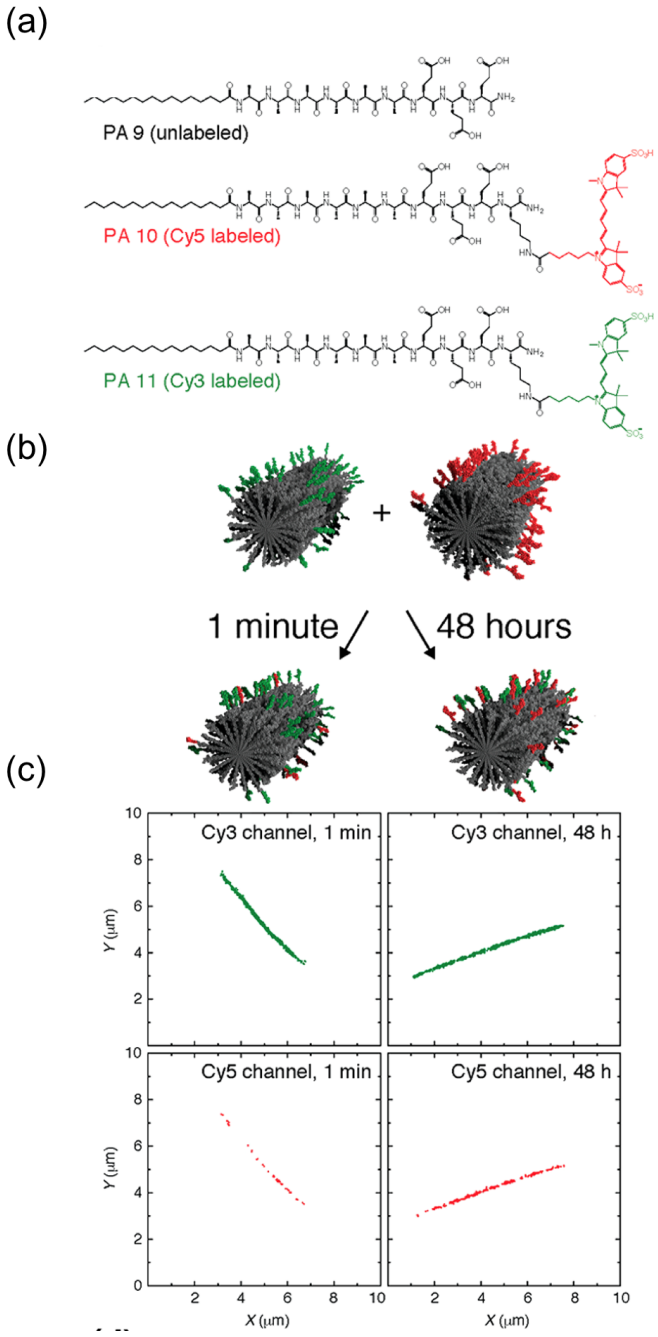

Figure 1.3: Chemical structures of peptide amphiphiles used in nanofiber exchange dynamics studies. Note the presence of sulfonated dyes used in STORM measruements. (b) Schematic of inter-fiber exchange oer time. (c) Localization maps of PA nanofibers after a period of 1 minute and 48 hours.[29,42]

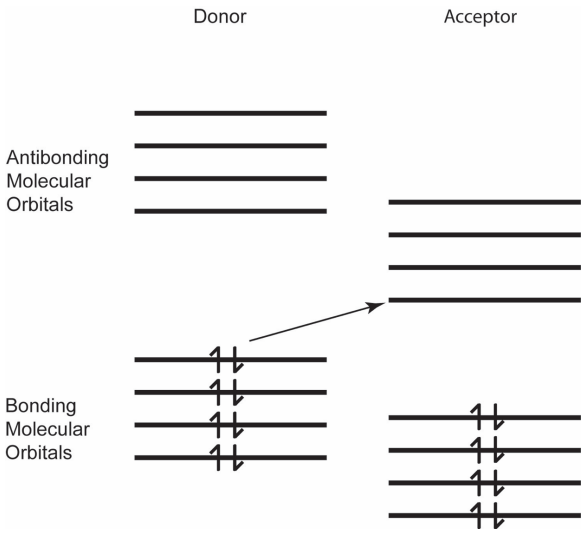

Figure 1.4: Lowest energy transition in charge transfer (CT) interactions represented by the transfer of an electron from the highest-occupied molecular orbital (HOMO) of the electron donor to the lowest unoccupied molecular orbital (LUMO) of the electron acceptor.[43]

using intermolecular, intra-fiber hydrogen bonding to influence the dynamics of supramolecular architectures.

1.2 CHARGE TRANSFER INTERACTIONS

Charge transfer (CT) is the shift of electrons from an electron-rich (donor) moiety to an electron-poor (acceptor) moiety.[43] Specifically, charge transfer refers to the electronic transition wherein an electron is transferred from the highest occupied molecular orbital (HOMO) of the donor (D) to the lowest unoccupied molecular orbital (LUMO) of the acceptor (A) (Figure 1.4).[44] This transition forms a dipole moment between donor and acceptor molecules, and the excited electron is partly delocalized between the donor and acceptor in weak electron resonance. The transition varies from that of ionic salts (such as NaCl), wherein the electron is tightly bound to the anion.[45]

One of the earliest studies of charge transfer complexes was that on the complex between iodine and benzene and alkylbenzenes. Benesi and Hildebrand[46] observed a strong ultraviolet absorption near 300 nm when iodine vapor was bubbled into aromatic solvents such as benzene, an energetic

transition that was neither present in iodine dissolved in inert solvents, nor in the aromatic solvents themselves. Initial hypotheses suggest that the observed absorption band corresponds to a benzene electronic transition traditionally forbidden by electronic selection rules, one that is now allowed in the presence of iodine molecules. Robert Mulliken took this study further, and observed[47,48] that the spacing between iodine and benzene molecules in crystalline complexes could not be achieved by Van der Waals forces alone, and that additional weak resonant electrostatic interactions between partially ionized benzene and iodine molecules could provide a reasonable explanation for the observed crystallographic spacing. He then asserted, in a celebrated "note added in proof"[47] that the additional electronic absorption bands observed be due to charge-transfer interactions between benzene and iodine.

Charge transfer between an electron donor and acceptor can be described and evaluated from a quantum-mechanical perspective (see Appendix I for full derivation) to derive the energy of charge-transfer interactions (E_{CT}) (Figure 1.5) between ground (W_N) and excited (W_E) states of the CT complex, as a function of ionization potential of the donor (I^D), the electron affinity of the acceptor (E^A), the non-bonding interactions (G_0) between the donor (D) and acceptor (A), the coulombic attraction (G_1) between ionized (D^+) and (A^-) and the resonance stabilization energies of the CT complex in the ground (X_0) and excited (X_1) states:

$$\begin{aligned} E_{CT} &= h\nu_{CT} \\ &= I^D - E^A + (G_0 - G_1) + (X_0 + X_1) \end{aligned} \tag{1}$$

As alluded to previously, the strength of CT interactions is largely governed by the ionization potential of the donor molecule, and the electron affinity of the acceptor molecule. Good electron donors have low ionization potentials, while good electron acceptors have high electron affinities. In addition, the propensity of donor and acceptor moieties to engage in charge transfer can also be governed by structural and thermodynamic elements, such as sterics, π-π overlap and entropy.[49] The electronic transition as a result of charge transfer typically manifests itself in a distinct absorp-

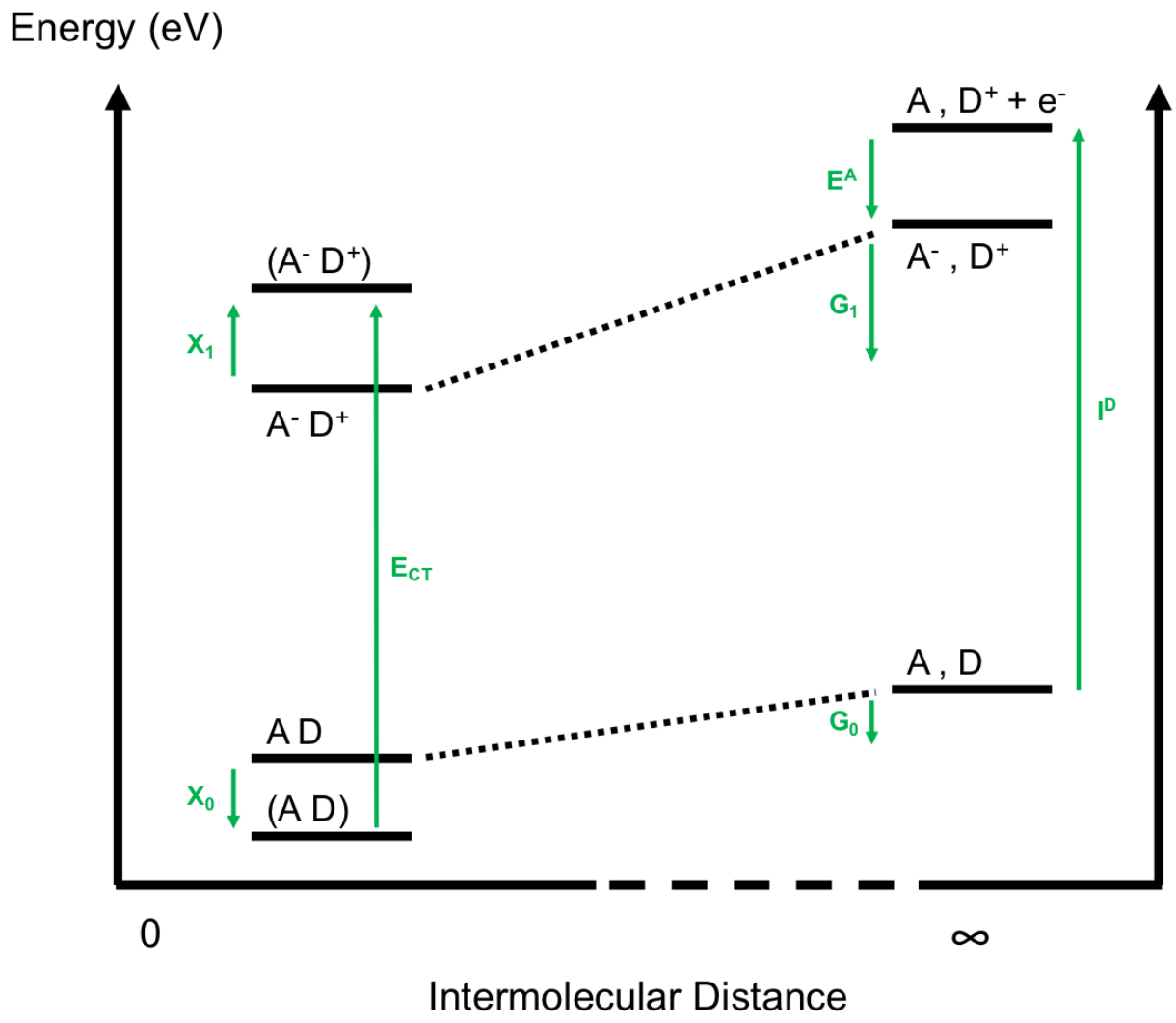

Figure 1.5: Simplified energy level diagram for electron transfer between an electron donor (D) and an electron acceptor (A). The energy of charge transfer (E_{CT}) can be described as a function of (1) the ionization potential (I^D) of the donor, (2) the electron affinity (E^A) of the acceptor, (3) the non-bonding interactions (G_0) between the neutral donor (D) and acceptor (A) molecules, (4) the coulombic attraction (G_1) between the ionized donor (D^+) and acceptor (A^-) molecules, the (5) ground state resonance stablization ($AD \rightarrow (AD)$) energies (X^0) and the (6) excited state resonance stabilization ($A^-D^+ \rightarrow (A^-D^+)$) energies ($X_1$) of the CT complex.[43]

tion band that corresponds to the energy of the intermolecular CT interaction. This band is separate from the absorption of the individual component molecules, and usually appears at considerably longer wavelengths.[44] In solution-based CT complexes, it is common to observe both the absorption of the CT complex as well as that of the component molecules due to the partial dissociation of the complex into its respective component species.

Numerous moieties have been examined for their propensity to form CT complexes, be they atoms, functional groups, or aromatic units.[49–51] This thesis will focus on CT complexes based on core aromatic units, with electron donating or withdrawing substituents. The extent and magnitude of CT can be modulated based on the geometry of the donor and acceptor molecules, and dictated by their electrostatic complementarity. In addition, electron donating moieties such as methyl (CH_3), amine (NH_2) or hydroxyl (OH) functionalities can be used as substituents to increase the relative electron density in an aromatic core, lowering the ionization potential of the molecule. The inverse is true with withdrawing groups such as cyano (C≡N) and carbonyl (C=O) functionalities, which increase the ionization potential and electron affinity of the aromatic core.

1.2.1 *Intramolecular Charge Transfer*

Within the field of organic electronic and self-assembling materials, there are two types of CT interactions: intramolecular and intermolecular. Intramolecular CT refers to CT interactions that happen between a donor and an acceptor, connected by a π-conjugated bridge.[52,53] This class of interactions can either occur on a small molecule level,[54–56] or that along the backbone of a conjugated polymer.[57–59] The conjugated system of π electrons renders it possible to have efficient CT interactions and charge separation, leading to small bandgaps and broad absorption spectra. The ability to control the degree of CT by either changing the chemistry of the donor and acceptor moietiesref or that of the conjugated linker[60,61] allows for the realization of both novel electronic states and supramolecular assemblies, a key factor for ensuring practical photovoltaic,[62–65] light-emitting diode (LED)[54,66] or nonlinear optical[60,61,67] applications.

1.2.2 *Intermolecular Charge Transfer*

In contrast, intermolecular charge transfer interactions involve the transfer of electrons between distinct donor and acceptor molecules though space..[43,51,68–70] As a result, the underlying physics behind intermolecular CT is slightly different compared to its counterpart, one that is more nuanced in its propensity to unveil new electronic properties of materials.

One of the hallmarks of intermolecular CT complexes is the conformational freedom provided to each constituent donor and acceptor moiety. While intramolecular complexes are largely constrained by the conjugated linker connecting the donor and acceptor cores, intermolecular complexes are free to rotate and translate to minimize free energy. In fact, it is this capability that lead Mulliken[47] to discover this complementary interaction and coin the term 'charge transfer complex'.

Early studies[48–50,71,72] on intermolecular CT complexes argued that the relative orientation of the two moieties is largely to maximize overlap between the HOMO of the donor and the LUMO of the acceptor. In crystalline complexes, this overlap and orientation is largely temperature dependent, as exemplified by Herbstein and Snyman,[73] where they discovered a crystallographic phase transition in pyrene-pyromellitic dianhydride co-crystals at approximately 200K. Below the phase transition, the pyrene molecules alternate between two different orientations (12° apart) with respect to the pyromellitic anhydride molecules. Above the phase transition, the ordered structure changes to a more disordered conformation, where the component molecules appear in mean positions, indicative of dynamic motion of the pyrene molecules within the co-crystal.[74]

The same way in which temperature influences molecular orientation and packing in CT co-crystals, solvents influence CT interactions in solutions. Specifically, solvent polarity has been shown[75–77] to drive CT complexation in aromatic donor and acceptor molecules, through complementary electron transfer and solvophobic interactions. Such is the importance of solvent, that the association constant between donor and acceptor molecules can vary by two orders of magnitude depending on the polarity of the solvent, or mixtures of solvents used.

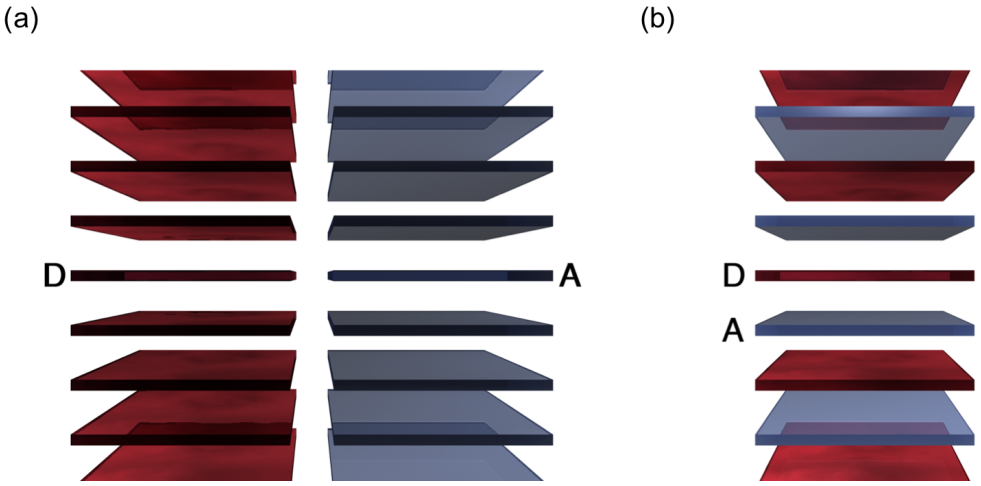

Figure 1.6: Two primary modes of supramolecular assembly in CT complexes include (a) segregated stacks, where donor and acceptor moieties assemble into discrete arrays, and (b) mixed stacks, with an alternating assembly of donor and acceptor moieties along the direction of charge transfer

While the association and dimerization of charge transfer complexes is of interest to those seeking a fundamental understanding of the molecules interact, the practical applications for these materials open up when considering how these complexes assembly in a supramolecular architecture. The mode of assembly dictates the physics and materials properties that these complexes exhibit, from insulating and ferroelectric[78–83] to conducting and metal-like.[84–89] It is this wide range of properties, spanning nearly the entire breadth of electronic properties, that makes charge transfer complexes so unique and fascinating. There are currently two primary modes of supramolecular assembly (Figure 1.6) for these complexes: segregated stack and mixed stack. Each, through minute changes in packing architecture, provides a handle on tuning the electronic properties of the resulting materials, and is therefore worthy of further study.

Segregated Stack Complexes

The assembly of segregated stacks in intermolecular CT complexes is characterized by separate arrays of donor and acceptor molecules.[90] This stacking motif does not occur in lieu

of charge transfer between the donor and acceptor molecules, and instead is complementary to the CT process. Among the earliest[70,89,90] discoveries of segregated CT stacks were ionic salts of 7,7,8,8-tetraquinodimethane (TCNQ). In these systems, TCNQ would play the role of the electron acceptor, and would be ionized in the presence of a cation molecules that range from alkali metals such as cesium (Cs)[91] to organic aromatic molecules such as N-methylphenazinium (NMePh) or tetrathiafulvalene (TTF).[92] Solid state crystals of these complexes would form (Figure 1.7) illustrate alternating periodicity of D and A molecules within the plane of the aromatic molecules, with face-to-face aromatic interplanar stacking of equivalent D or A molecules. If complete one-electron charge transfer (i.e. every donor contributes one electron to the acceptor) is assumed, then these segregated stacks represent arrays of positive and negatively charged ions. This implies an attractive electrostatic binding interaction within the plane of donor and acceptor molecules (Figure 1.8a). However, the interplanar binding interaction is strongly repulsive, due to strong repulsive interactions between ions of the same charge. This warrants a relaxation of the aforementioned assumption, such that either (i) there is incomplete charge transfer from donor to acceptor, warranting the presence of mixed valence states and reducing the repulsive interactions between neighboring stacks, and (ii) a deviation from 1:1 stoichiometry (Figure 1.8b).[90]

A unique property of segregated stack complexes is their conductivity as a CT salt. Early examples of conducting CT salts include that of TTF-bromine (Br), which displays conductivities up to 400 $(\Omega cm)^{-1}$ at 300 K,[88] and TTF-TCNQ , with conductivities up to 652 $(\Omega cm)^{-1}$ at 300 K.[87] It is interesting to note that in the case of TTF-TCNQ, the conductivity is significantly reduced at temperatures below 66 K, attributed to a Jahn-Teller-type (Peierls) distortion at the transition temperature. The abnormality in these reported conductivity values lies in the fact that if the acceptor is assumed to be completely ionized, the Coulomb interaction should be large and the unpaired electrons should localize on the acceptor. As a result the activation energy for electrical conduction should be high, and the crystal insulating. LeBlanc,[86] however, proposed that the presence of the polarizable cations screens the repulsive interactions between neighboring acceptor molecules, therein

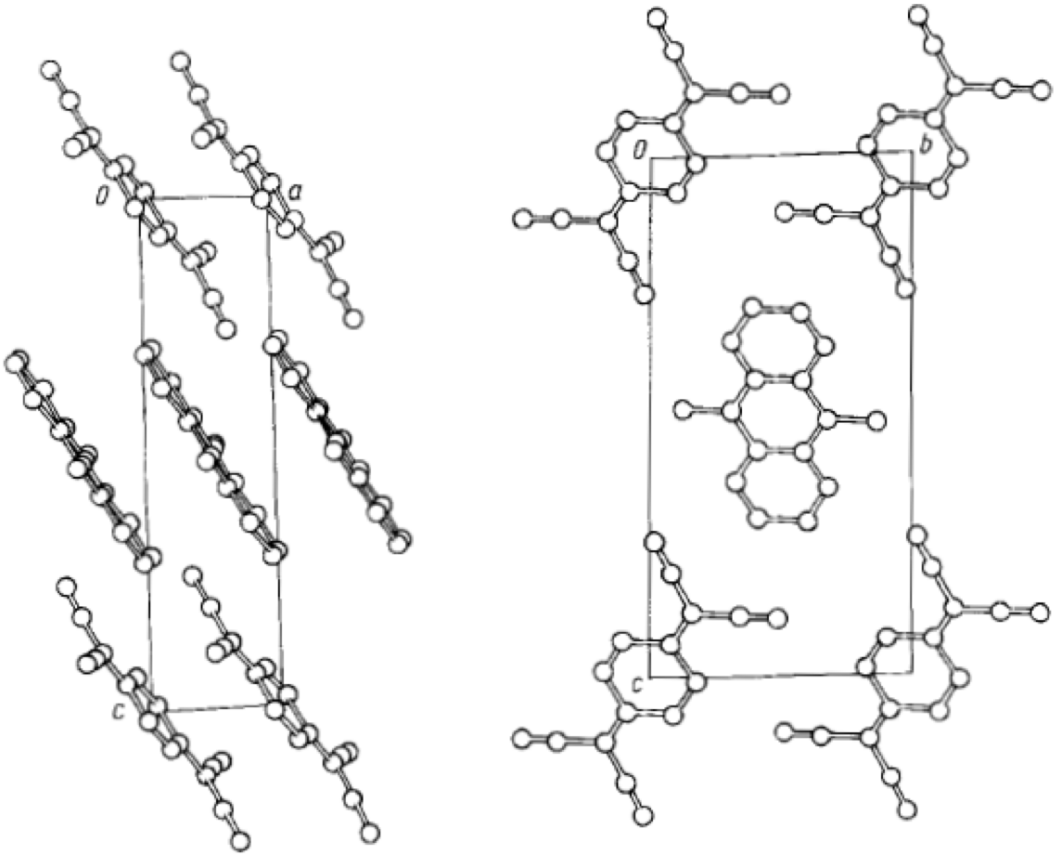

Figure 1.7: Solid-state crystal structures of the co-assembled N-methylphenazinium (NMePh) and tetrathiafulvalene (TTF). The molecules assemble in an alternate stacking arrangement in the plane of aromatic molecules, and segregated stacking arrangement between planes.[92]

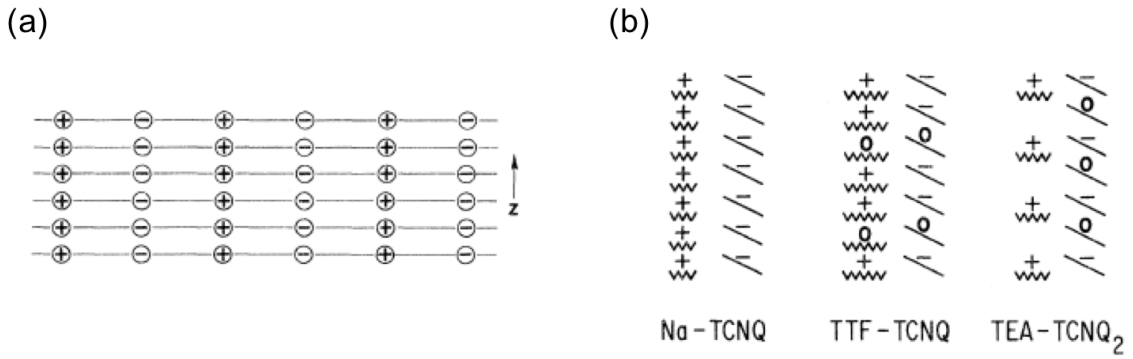

Figure 1.8: (a) Schematic of segregated stack assembly, highlighting alternating intraplanar arrangement or donor/acceptor moieties, and segregated interplanar arrangement. (b) Schematic of three different modes of charge transfer: complete ionicity, incompletely or mixed-valence ionicity and stiometric deviations.[90]

reducing the repulsive interactions and activation barrier for conduction (akin to a Mott-Hubbard model). Torrance[45] revised and added to that hypothesis, and asserted that the acceptor molecules are only partially reduced, and the CT complex is of mixed valence. As a result, on a short time scale, the stack of acceptors can be viewed as containing both neutral and ionic acceptor molecules. Exciting an electron from a neighboring ionic to a neutral acceptor is now possible, therein lowering the barrier of electrical conductivity for these segregated CT stacks.

More recent developments in segregated stacks of CT complexes have involved conductivity at the interface of bulk donor and acceptor crystals,[85] photoconductivity in coaxial nanotubes of electron donor and acceptor layers,[63,93] as well as the influence of chemistry and hydrogen bonding on supramolecular interactions between segregated donor and acceptor molecules.[94,95] The breadth and scale of development within the field of segregated CT complexes is clearly evident, highlighting its place in the discovery of novel electronic and responsive systems.

Mixed Stack Complexes

Mixed stack charge transfer complexes are characterized by an alternating periodic arrangement of donor and acceptor molecules along the axis of charge transfer.[43] In other words, mixed stack CT

complexes occur when every other molecule that is electrostatically coupled through charge transfer interactions is a donor or acceptor, therein creating a linear array of alternating D and A molecules. While the molecular stacking orientation and angle may differ from complex to complex (due to orbital overlaps, sterics, etc.) the general observed alternating structure among planar aromatic donor and acceptor molecules is consistent. Among the first complexes to be characterized in a mixed stack manner was in fact the complex between iodine and benzenes discovered by Benesi and Hildebrand,[46] that which started the entire debate and discovery of intermolecular charge transfer!

A key characteristic among mixed stack CT complexes is their ability to form dimerized lattice structures of alternating donor/acceptor molecules. That the strength of intermolecular CT complexes are so heavily dependent on the overlap integral between complementary donor and acceptor molecules indicates that small changes to the molecular orientation or spacing between the molecules could significantly alter the overlap integral, and thereby the strength of charge transfer, also referred (ρ) to as the ionicity of the complex. Torrance et al. were the first to discover this modularity in the ionicity of CT complexes, when they discovered a transition from a 'neutral' state ($\rho < 0.5$) to an 'ionic' state ($\rho > 0.5$) in the complex TTF-chloranil (QCl_4) upon the application of pressure[96] or the reduction in temperature.[97] Coined a Neutral-to-Ionic Transition (NIT), this change in the charge transfer state was elucidated using spectroscopic (Figure 1.9a), where a red-shifted absorption band pointed to an increase in the acceptor's electron affinity, as well as X-ray crystallography (Figure 1.9b), where the lattice constant decreased due to the increased ionicity. Further studies shed light on the possibility that this NIT transition was a first-order transition, characterized by an abrupt change in ionicity at the transition temperature/pressure.

An unexpected result of the NIT in TTF-QCl_4 and its related complex TTF-$QBrCl_3$ is that the change in ionicity corresponds to a change in centrosymmetry of the overall crystal. While alternating stacks of donor and acceptor molecules are assumed to equally distributed to minimize the lattice energy, rendering a centrosymmetric lattice. However, crystallographic refinements of both TTF-QCl_4[98] and TTF-$QBrCl_3$[80,99] illustrated the loss of inversion symmetry at the NIT transition.

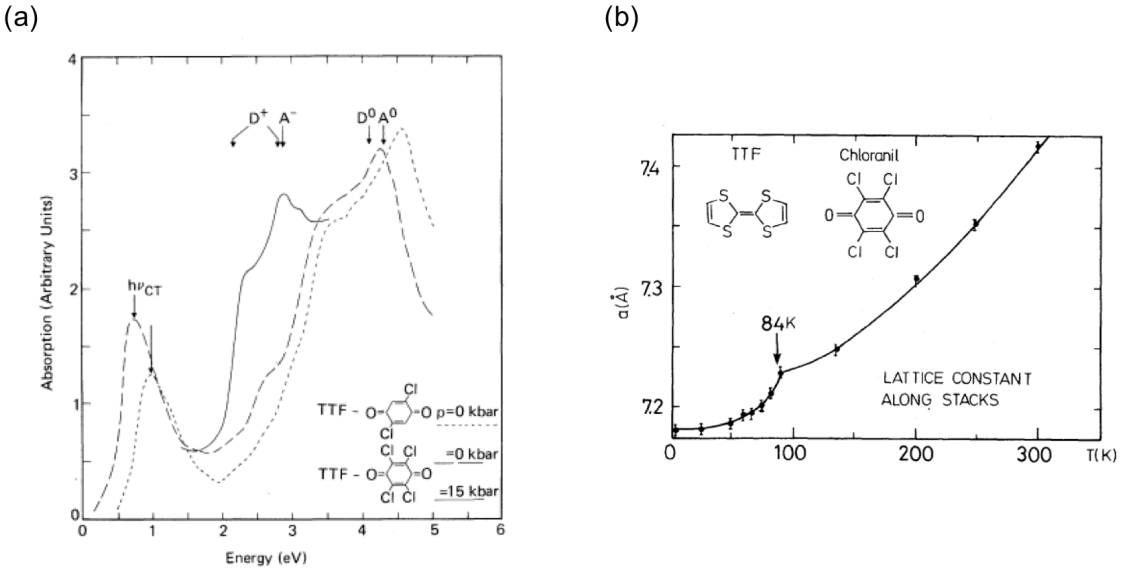

Figure 1.9: (a) Spectroscopic determination of neutral-ionic transition (NIT) for a TTF-TCNQ complex upon the application of pressure to the crystal.[96] (b) Crystallographic determination of NIT as a function of temperature.[90]

This suggests that the traditionally perfectly alternating donor and acceptor molecules lose their periodicity and prefer to dimerize with one of the complementary molecules on either side, effectively doubling the size of the unit cell. This abrupt asymmetry and lattice instability can be attributed to a Peierls instability, where lattice distortion and electronic coupling results in band splitting into two equivalent but distinct energetic states.

The transition from 'neutral' to 'ionic' charge transfer state in mixed stack CT crystals not only has implications for the centrosymmetry of the overall lattice, but also on the electronic properties of the structure. Centrosymmetric 'neutral' CT states have an equal periodic distribution of partially ionized donor and acceptor molecules, rendering a zero overall dipole moment (Figure 1.10a). Upon dimerization, however, the asymmetry in distribution of donor and acceptor molecules means that the individual dipoles that arise from $D^{\rho+}A^{\rho-}$ do not cancel each other out, rending a net dipole moment, or polarization along the direction of electron transfer (Figure 1.10b). The direction of this polarization is, of course, entirely arbitrary, as a net polarization in the oppo-

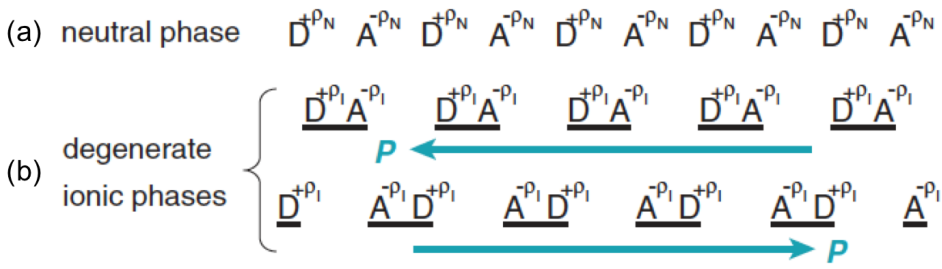

Figure 1.10: Distribution of a mixed stack of donor and acceptor molecules in the (a) centrosymmetric neutral phase and (b) the non-centrosymmetric degenerate ionic phases.[100]

site direction is equally possible by altering the arrangement of dimer pairs. As a result, the 'ionic' CT state in mixed stack CT complexes imparts two degenerate noncentrosymmetric phases, with opposing net polarizations.[100] The ability to switch between the net polarization moments using external forces, such as an external applied electric field, will be essential in the development of new electronic materials, a phenomenon that will be explored further in the coming sections.

1.3 LOCK-ARM SUPRAMOLECULAR ORDERING

Given the emergent properties of mixed stack charge transfer complexes, one of the major challenges when it comes to introducing CT co-crystals into technological settings is the production of high quality, air-stable, single-crystalline materials of appropriate sizes. Inspired by the advances made with regard to supramolecular D-A assemblies[101,102] in solution, Blackburn et al.[103] developed a (LASO) design strategy which takes advantage of the synergy between (i) CT interactions, (ii) hydrogen-bonding and (iii) solvophobic effects to produce ordered, close-packed, solvent-free and robust CT mixed stack co-crystals on a centimeter-length scale. This design motif was termed Lock-Arm Supramolecular Ordering (LASO).

The LASO design element consists (Figure 1.11a) of three major components – (i) complementary aromatic donor-acceptor cores, (ii) complementary hydrogen-bonding recognition units - flexible diethylene glycol (DEG) arms and functional groups (carbonyl, amino, imine and hydroxyl) capable of participating in intermolecular hydrogen-bonding interactions, and (iii) solvophobic forces

which promote the self-assembly/co-crystallization processes. It is noteworthy that the LASO strategy employs intrinsically flexible building blocks in concert with flat and rigid π-synthons in order to achieve molecular recognition involving orthogonal motifs. The dynamic stereochemical characteristics of the DEG arms - that is, their predisposition to adopt[104] an ensemble of conformations and co-conformations[105] - facilitates the hydrogen-bonding interactions between the complementary D-A components during the co-crystallization processes. While the propensity for hydrogen bonding is engineered into the supramolecular design, the specific hydrogen-bonding patterns in the superstructures cannot be programmed or predicted from first principles - that is, the hydrogen-bonded networks adopted in the LASO CT co-crystals are not designed de novo, but instead arise as a result of the molecular components engaging spontaneously in the most energetically favorable co-conformations in the solid state. The packing forces intrinsic to the co-crystals harness the conformational flexibility of the DEG arms to achieve intermolecular binding under co-conformational control in the lattice. This orthogonal source of molecular recognition distinguishes LASO complexes from other extended (super)structures utilizing rigid aromatic building blocks, e.g., coordination polymers[101,102] and metal-organic frameworks.[106–108]

The modularity of the LASO design motif allowed for the growth of nine different CT co-crystals from 12 available building blocks (Figure 1.12a). The building blocks themselves were divided into four groups based on their electronic and hydrogen bonding complementarity. It is worth noting that single crystals were grown using a liquid-liquid diffusion protocol, and that the crystals obtained remained air stable even after complete desolvation.

A close examination of the co-crystallization of the pyromellitic diimide (PMDI) acceptor $\mathbf{1}_A$ and the 1,5-diaminonaphthalene donor $\mathbf{9}_D$ reveals (Figure 1.11b,c) that acceptor $\mathbf{1}_A$ adopts two conformations (labeled $\mathbf{1}'_A$ and $\mathbf{1}''_A$) in the mixed stacks. The π-π interplanar separations between $\mathbf{9}_D$ and $\mathbf{1}'_A/\mathbf{1}''_A$ are consistent with those expected for the D-A interactions present, and are found to be 3.47 / 3.32 Å, respectively. These alternating D-A stacks are further reinforced by both intra- and inter-stack hydrogen bonds between (i) the amino functions of $\mathbf{9}_D$ with the carbonyl groups of $\mathbf{1}_A$,

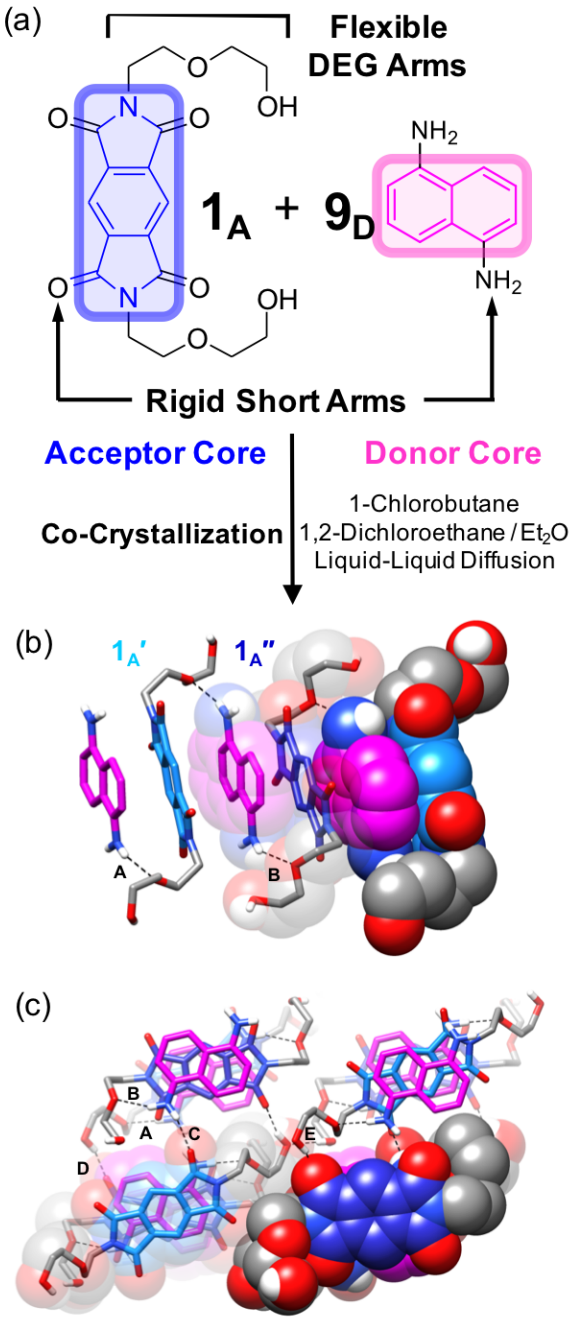

Figure 1.11: Cocrystallization of pyromellitic diimide derivative acceptor $\mathbf{1}_A$ and 1,5-diaminonaphthalene donor $\mathbf{9}_D$ by liquid–liquid diffusion to form a LASO complex. (b) Intermolecular recognition units in the cocrystal $\mathbf{1}_A \bullet \mathbf{9}_D$ that participate in donor–acceptor interactions shown in magenta and blue, respectively. (c) Superstructure of cocrystal $\mathbf{1}_A \bullet \mathbf{9}_D$.[103]

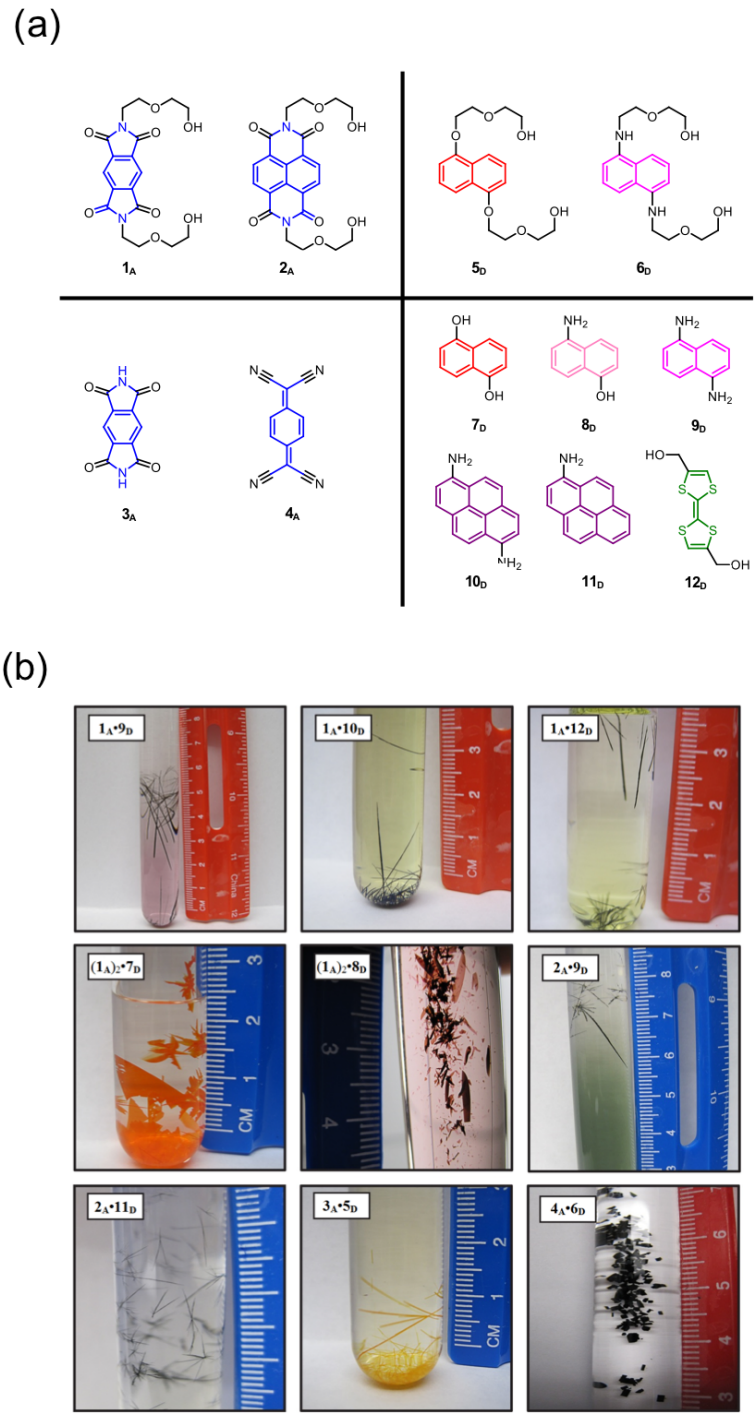

Figure 1.12: (a)Chemical structures of donor and acceptor molecules used to make the LASO library of mixed stack CT co-crystals. (b) Photographs of nine LASO co-crystals grown by liquid-liquid diffusion.[103]

(ii) the amino functions of $\mathbf{9}_D$ with the DEG arms of $\mathbf{1}_A$ and (iii) the DEG arms of $\mathbf{1}'_A/\mathbf{1}''_A$. As a result, the co-crystalline stacks are perfectly aligned so as to form an intricate three-dimensional network, where the D-A supramolecular components are tightly packed in the lattice and the co-crystal is devoid completely of any solvent molecules.

Although donors $\mathbf{7}_D$, $\mathbf{8}_D$ and $\mathbf{9}_D$ are naphthalene derivatives with similar constitutions, the minor differences in the functional groups (NH_2 versus OH) lead to dramatic differences in the resulting packing and optical properties of the co-crystals. While co-crystal $\mathbf{1}_A\bullet\mathbf{9}_D$ consists of one-dimensional mixed stacks with equal amounts of the donors and acceptors, the co-crystallizations of $\mathbf{1}_A$ with both $\mathbf{7}_D$ and $\mathbf{8}_D$ lead to (Figure 1.13) two isostructural co-crystals - $(\mathbf{1}_A)_2\bullet\mathbf{7}_D$ and $(\mathbf{1}_A)_2\bullet\mathbf{8}_D$ - which consist of two symmetrically nonequivalent acceptors and one donor component. Both crystallize in the triclinic space group $P\bar{1}$ and contain two halves of the acceptor and one half of the donor components in their asymmetric units. The PMDI acceptors in the $(\mathbf{1}_A)_2\bullet\mathbf{7}_D$ co-crystals are organized, (i) not only in a face-to-face fashion with the naphthalene donors along the [1 0 0] direction, (ii) but also in an edge-to-face manner along the [0 1 0] direction. This second CT interaction is stabilized by means of [C-H•••π] interactions between the naphthalene protons of the face-to-face mixed stack and the $\mathbf{1}_A$ PMDI aromatic cores of the second CT component. As in the one-dimensional LASO superstructures, an extensive hydrogen-bonding network is also present in the co-crystal, holding the three components together in a tight manner. Very similar interactions and long-range packing are observed for $(\mathbf{1}_A)_2\bullet\mathbf{8}_D$, where the only difference arises as a result of the constitutionally unsymmetrical nature of $\mathbf{8}_D$, wherein positions of the OH and NH_2 groups are disordered across one of two possible orientations throughout the lattice.

While the traditionally one-dimensional CT mixed stacks exhibit[43,51,109,110] strong absorbance of linearly polarized light oriented parallel to the CT axes, the absorption spectra of co-crystals $(\mathbf{1}_A)_2\bullet\mathbf{7}_D$ and $(\mathbf{1}_A)_2\bullet\mathbf{8}_D$ are much more complex. Both absorb (Figure 1.14) light preferentially along two directions in the (0 0 1) plane. The strongest absorption bands (476 and 490 nm in the case of $(\mathbf{1}_A)_2\bullet\mathbf{7}_D$ and $(\mathbf{1}_A)_2\bullet\mathbf{8}_D$, respectively) can be attributed to the CT interactions between face-

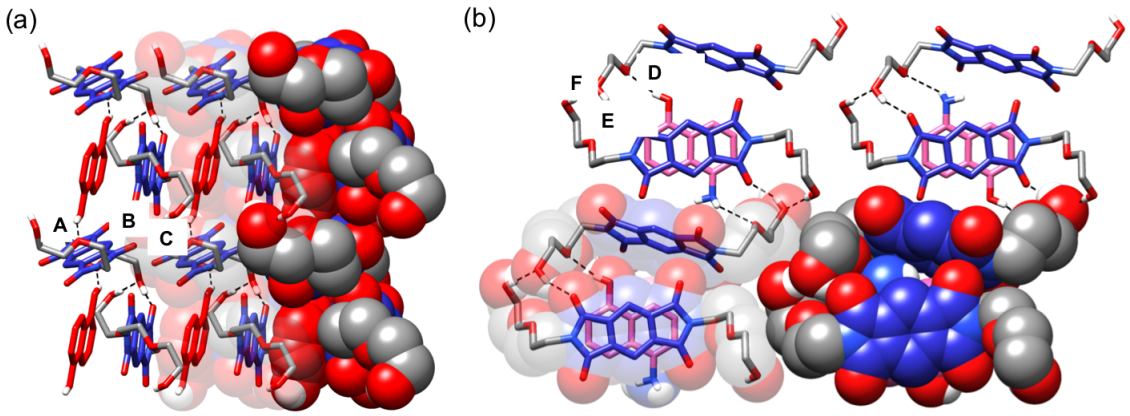

Figure 1.13: Space-filled superstructure of LASO co-crystal displaying a 1:2 D:A unit cell, and two axes of charge transfer. (a) $(\mathbf{1}_A)_2\bullet\mathbf{7}_D$ viewed from the side of the mixed stacks and (b) $(\mathbf{1}_A)_2\bullet\mathbf{8}_D$ viewed along the face-to-face π–π stacking direction. Hydrogen bonds are depicted as black dashed lines.[103]

to-face D-A complexes along the [1 0 0] direction, while the second absorption bands (530 and 595 nm in the case of $(\mathbf{1}_A)_2\bullet\mathbf{7}_D$ and $(\mathbf{1}_A)_2\bullet\mathbf{8}_D$, respectively) are oriented 42° and 29° from the [1 0 0] direction, respectively. The absorption spectra of the two chromophores within these two co-crystals suggest that acceptors in both the face-to-face and edge-to-face directions participate in CT interactions. In each co-crystal, the polarization angles associated with the two electronic transitions are neither parallel nor perpendicular to each other. They are a consequence of strong anomalous dispersion across the visible spectrum, coupled with the fact that the triclinic crystals have no fixed eigendirections at any wavelength. Moreover, since the axes of refraction and absorption ellipsoids are never parallel to each other, additional ellipticities which couple the electronic absorptions may arise, even during linearly polarized illumination.[111] The bidirectional CT in the co-crystals leads to (Figure 1.15) pleochroism[112] in polarized light – that is, the color of the co-crystal changes with the polarization angle of incident white light. With the addition of a second polarizer (analyzer), crossed with respect to the first one, both co-crystals $(\mathbf{1}_A)_2\bullet\mathbf{7}_D$ and $(\mathbf{1}_A)_2\bullet\mathbf{8}_D$ fail to extinguish (Figure 1.15) when rotated in the path of incident white light. The crystals are bright at all orientations and the colors transmitted vary across the visible spectrum.

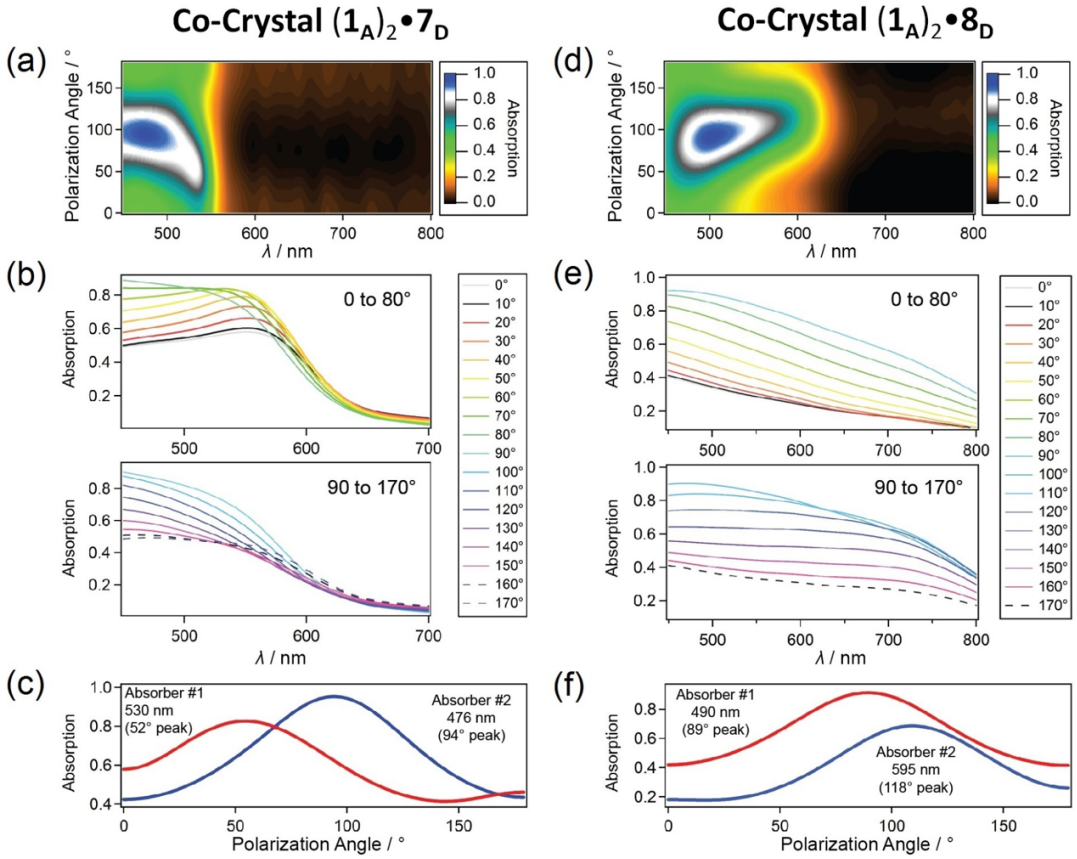

Figure 1.14: Polarized UV–visible spectra of (a,c) cocrystal $(1_A)_2$•7_D and (d,f) cocrystal $(1_A)_2$•8_D, revealing the presence of two distinct absorbance peaks arising from different CT pairs interactions the crossed-stack structure.[103]

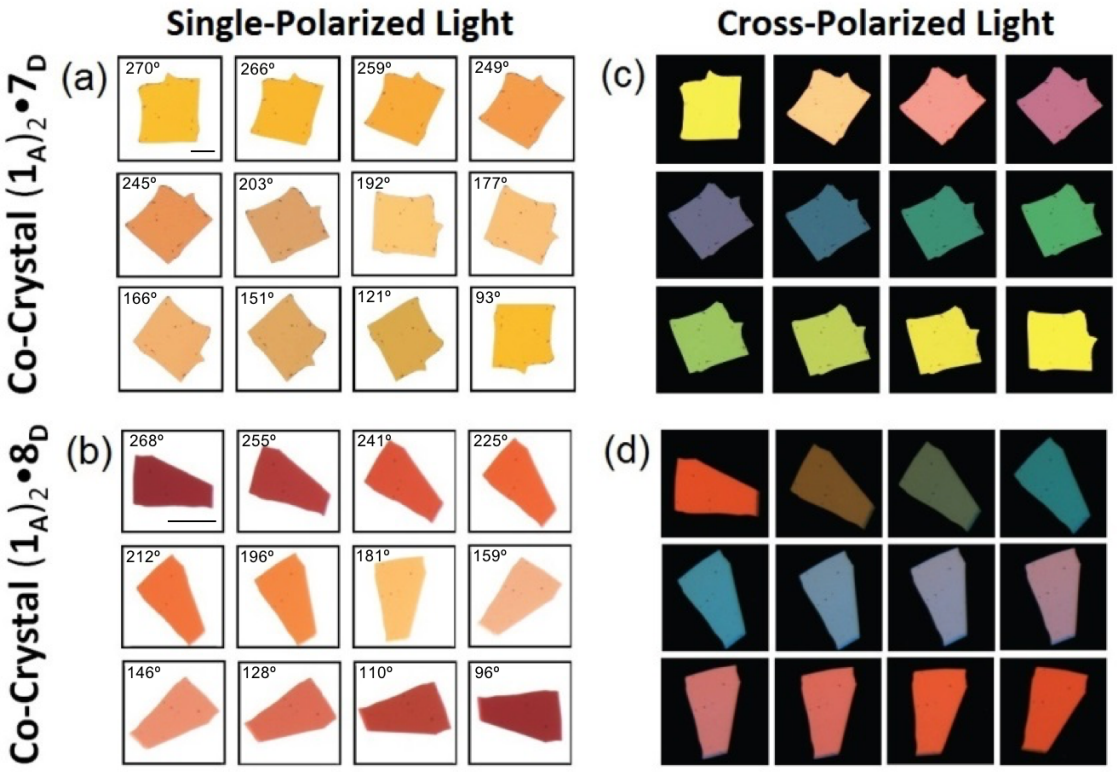

Figure 1.15: Images of single cocrystals $(\mathbf{1}_A)_2$•$\mathbf{7}_D$ and $(\mathbf{1}_A)_2$•$\mathbf{8}_D$ in (a,b) single-polarized mode and (c,d) cross-polarized mode. Cocrystals $(\mathbf{1}_A)_2$•$\mathbf{7}_D$ and $(\mathbf{1}_A)_2$•$\mathbf{8}_D$ exhibit bidirectional CT and, as a result, exhibit strong pleochroism. The scale bars (a,b) correspond to 50 μm for each crystal used in these experiments.[103]

Table 1.1: Structural Refinement of Co-Crystal $(\mathbf{1}_A)_2\bullet\mathbf{7}_D$ and $(\mathbf{1}_A)_2\bullet\mathbf{8}_D$

	$(\mathbf{1}_A)_2\bullet\mathbf{7}_D$		$(\mathbf{1}_A)_2\bullet\mathbf{8}_D$	
	Non-Centrosymmetric	Centrosymmetric	Non-Centrosymmetric	Centrosymmetric
Space Group	P1	$P\bar{1}$	P1	$P\bar{1}$
R[I>2.0σ(I)]	0.0518	0.0542	0.0507	0.0568
wR_2	0.1103	0.1219	0.1268	0.1528
Number of Restraints	3	0	162	0
Flack Parameter	-1(2)	-	-0.3(0.6)	-
Cif check alerts	ADDSYM suggests $P\bar{1}$ is correct space group (100% fit) Bad thermal paramters Low C-C bond precision Abnormal bond lengths	None	ADDSYM suggests $P\bar{1}$ is correct space group (100% fit) Bad thermal paramters Low C-C bond precision Abnormal bond lengths Poor data/parameter ratio	None
Parameter Correlations	>90%	<50%	>88%	<59%

Due to the low symmetry of the LASO co-crystals, crystallographic indexing of single crystals can be misleading, especially when it comes to refining the presence of an inversion center. It is evident that, when the structural data of the centrosymmetric superstructures are compared (Table 1.1 and Table 1.2) with the non-centrosymmetric refinements, that a centrosymmetric space group is the more appropriate crystallographic choice.[113] This situation is particularly evident when looking at the absolute configuration (Flack[114] parameter) of the non-centrosymmetric refinements, for which a value below 0 is abnormal and not realizable. Furthermore, a number of structural parameters are flagged as serious inconsistencies with what would be expected from the data set by CheckCIF, all of which arise from missing symmetry elements in the structures, as well as, in the case of a number of the structures, the inability of the refinements to converge in non-centrosymmetric space groups.

In all, the combination of charge transfer interactions and structurally flexible hydrogen-bonding motifs has been shown to constitute a good and reliable recipe for producing charge

Table 1.2: Structural Refinement of Co-Crystal $\mathbf{1}_A\bullet\mathbf{9}_D$, $\mathbf{1}_A\bullet\mathbf{10}_D$ and $\mathbf{1}_A\bullet\mathbf{12}_D$

	$\mathbf{1}_A\bullet\mathbf{9}_D$		$\mathbf{1}_A\bullet\mathbf{10}_D$		$\mathbf{1}_A\bullet\mathbf{12}_D$	
	Non-Centrosymmetric	Centrosymmetric	Non-Centrosymmetric	Centrosymmetric	Non-Centrosymmetric	Centrosymmetric
Space Group	P1	$P\bar{1}$	Pn	$P2_1/n$	P1	$P\bar{1}$
R[I>2.0σ(I)]	0.2219	0.0533	0.0484	0.0541	0.0810	0.0587
wR_2	0.5357	0.1318	0.1314	0.01463	0.2185	0.1605
Number of Restraints	326	0	3	0	888	0
Flack Parameter	-0.5(10)	-	-0.3(4)	-	-0.5(6)	-
Cif check alerts	ADDSYM suggests $P\bar{1}$ is correct space group (100% fit) Abnormal bond lengths and angles Low bond precision	None	ADDSYM suggests $P2_1/n$ is correct space group (100% fit) Abnormal hydrogen bond lengths	None	ADDSYM suggests $P\bar{1}$ is correct space group (97% fit) Abnormal hydrogen bond lengths Low bond precision	None
Parameter Correlations	>58%	<73%	>77%	<50%	>72%	<63%

transfer co-crystals that can grow up to several centimeters in length under ambient conditions. Although a limited number (twelve) of building blocks have been investigated and LASO-derived co-crystals (nine) have been realized, the concept of a molecular construction set extends as far as imagination allows. These features of the LASO design offer the possibility for the derived organic materials to acquire important functions in real-world applications related to a strong response to light or external fields.

1.4 FERROELECTRICITY AND FERROELECTRIC MATERIALS

In its most basic form, a material is said to be ferroelectric when it has two or more orientation states in the absence of an electric field, states that can switched from one to another in the presence of an external electric field.[115] These states should be enantiomorphous in crystal structure, and only differ in the orientation vector at null field. In ferroelectric materials, these orientation states are represented by dipole moments within a material. It follows that these changes in dipole moment cannot always be determined solely by crystallographic determination, requiring the use of a secondary measurement technique to probe the orientation state of the material. In this case, this probe is the measurement of net polarization, which is the linear combination of the dipolar orientations of each ferroelectric grain.

It was the discovery of ferroelectricity in sodium potassium tartrate tetrahydrate, commonly known as Rochelle salts,[116] that sparked academic discussion about ferroelectricity and the ability to switch and stabilize a net electrical polarization using an external electric field. Since then, inorganic materials[115] such as $BaTiO_3$ and polymers such as polyvinylidene fluoride[117] have dominated the push for functional electronic materials that make use of this unique property. This has paved the way for new ferroelectric materials that make use of a variety of polarization mechanisms, including order-disorder, hydrogen bonding, and even charge transfer.[78,83,118–124] This section will introduce ferroelectric materials from a basic theory perspective, followed by a brief walk through some of the unique ways in which ferroelectricity has manifested itself in inorganic as well as organic materials.

1.4.1 *Basic Concepts and Theory*

Phenomenological Theory

While atomistic theories exist[115] to explain the origin of ferroelectric transitions, they often require an assumption of the underlying mechanism behind the non-zero dipole moment stable in the absence of an electric field. Phenomenological or macroscopic theories,[115,121] however, treat the material in question as a continuum without regard for the underlying atomic structure. This postulation uses the underlying laws of thermodynamics and classical mechanics to describe the thermal, elastic and dielectric properties of the macroscopic system.

Before diving into the mathematical descriptions for ferroelectric transitions (full derivation in Appendix II), a fundamental consideration needs to be established: the linear relationship between electric displacement (D), applied electric field (E) and polarization (P):

$$\begin{aligned} D &= \varepsilon_0 E + P \\ &= \varepsilon_0 (1 + \chi) E \\ &= \varepsilon_0 \varepsilon_r E \end{aligned} \tag{2}$$

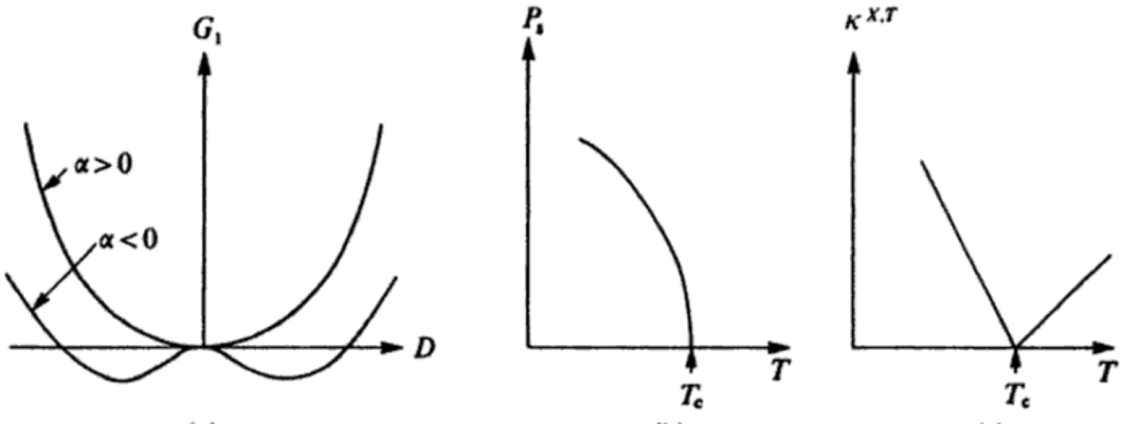

Figure 1.16: Qualitative depiction of relatioship between (a) Gibbs free energy and electric displacement, with changing α, (b) Polarization and temperature and (c) reciprocal isothermal permittivity and temperature, near the second-order ferroelectric phase transition.[115]

where ε_0 is the electric permittivity of free space, χ is the electric susceptibility, and ε_r is the relative permittivity.

The first phenomenological theory of ferroelectricity was developed by Ginzburg and subsequently Devonshire, based on Landau's theory of second-order phase transitions..[115,121] It expressed the Gibbs free energy in the Landau-Ginzburg polynomial form:

$$G = \frac{\alpha}{2}D^2 + \frac{\gamma}{4}D^4 + \frac{\delta}{6}D^6 \tag{3}$$

where γ and δ are temperature-independent constants. Assuming $\gamma > 0$ and $\delta > 0$, the shape of the Gibbs free energy curve is only dependent on the value of α (Figure 1.16). At positive values of α, the free energy curve has a single minimum at $D = 0$, which corresponds to a net zero polarization. This orientation state is know as the *paraelectric* phase. However when $\alpha < 0$, two distinct minima form with non-zero values of D, and by consequence P. In addition, since $E = \left(\frac{\partial G}{\partial D}\right)_T = 0$ at the gibbs free energy minima, the non-zero values of D describe the spontaneous polarizations stable at zero electric field, a requisite of the *ferroelectric* phase.

Since it is clear the ability of a material to hold two distinct polarization states is dependent on the sign of the constant α, the next step would be to deconstruct α as a function of measurable variables. Devonshire[125–127] asserted that α is related to temperature in the following manner:

$$\alpha = \beta(T - T_c) \approx \left(\frac{\partial^2 G}{\partial D^2}\right)_T = \kappa^{X,T}, \qquad T > T_c$$
$$\left(\frac{\partial^2 G}{\partial D^2}\right)_T = \frac{1}{\chi} \tag{4}$$

Where $\kappa^{X,T}$ is the inverse of the electric susceptibility χ, and T_c is the Curie-Weiss transition temperature at which the material switches from a zero spontaneous electrical polarization state (paraelectric) to a non-zero spontaneous polarization state (ferroelectric). Subsequently, we find that:

$$P^2 = \beta\frac{(T_c - T)}{\gamma} \qquad P \to 0$$
$$\kappa^{X,T} = 2\beta(T_c - T) \qquad T < T_c \tag{5}$$

Equations 3, 4 and 5 depict the phase transitions from a paraelectric, zero polarization state to a ferroelectric, finite spontaneous polarization state (Figure 1.16). It is worth noting that since there is no discontinuous jump in the electric displacement (or polarization) at the ferrelectric-paraelectric transition, it is referred to as a *second-order ferroelectric phase transition*. Materials that undergo this type of ferrelectric-paraelectric transition include triglycine sulfate (TGS).[128]

A similar mathematical analysis can be done (see Appendix II for full derivations) for the case when $\gamma = \gamma' < 0$. In this case, the relevant equations describing the ferroelectric behavior are as

follows:

$$G = \frac{\beta}{2}(T - T_c)D^2 + \frac{\gamma'}{4}D^4 + \frac{\delta}{6}D^6$$

$$P^2 = \frac{3\gamma'}{4\delta} \qquad T = T_c \tag{6}$$

$$\frac{1}{\chi} = \kappa^{X,T} = \frac{3\gamma'}{4\delta} + 8\beta(T_c - T) \qquad T \to T_c^-$$

$$\kappa^{X,T} = \frac{3\gamma'}{16\delta} + \beta(T - T_c) \qquad T \to T_c^+$$

From equation 6, one can immediately notice that the free energy diagram (Figure 1.17) has a third, local minimum at $D = 0$ at $T < T_c$ indicative of a metastable polarization state. The bigger difference, however, lies in the behavior of the polarization and electric susceptibility as a function of temperature. In this situation, both variable have finite but discontinuous values at the Curie-Weiss transition temperature (T_c), a hallmark that defines *first-order ferroelectric phase transitions*. Such first-order transitions are more commonplace among ferroelectric materials compared to second-order transitions, and have been a staple for ferroelectric ceramics and inorganic perovskites.[129]

In addition to the phase transition from paraelectric to ferroelectric, another hallmark of ferroelectric materials is the polarization hysteresis loop upon the application of external electric fields. This loop can be derived from the above phenomenological theory, but for the sake of simplicity a more qualitative argument will be proposed.[78]

It can be assumed that any material, ferroelectric or otherwise, originates with zero net polarization at zero electric field (Figure 1.18. On a polarization-electric field (P-E) graph, this state is represented at the origin. The application of an external electric field causes the dipole moments to align with the electric field vector, and as a result the material gains a net polarization (as described in equation 2). The maximum polarization attainable, defined by the number of dipolar domains in the material, is referred to as P_{max}. The hallmark of a ferroelectric material is that once this electric

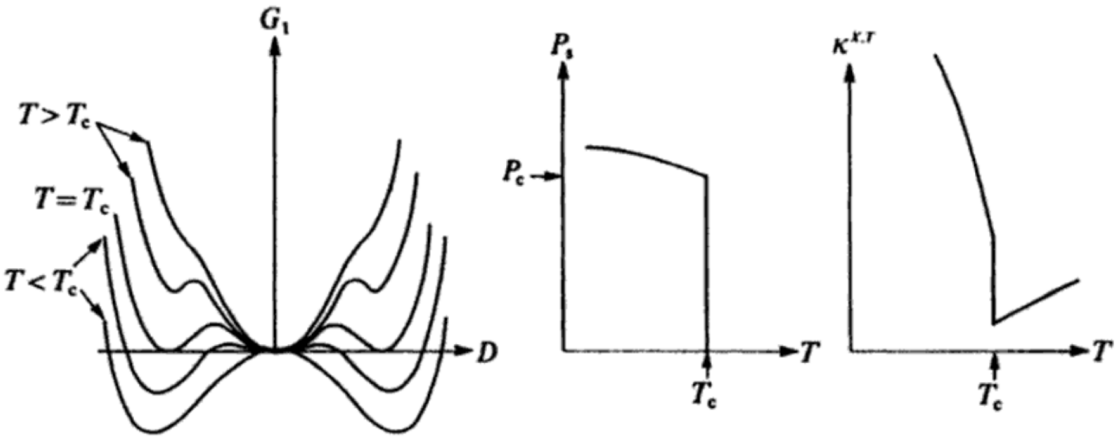

Figure 1.17: Qualitative depiction of relatioship between (a) Gibbs free energy and electric displacement, with changing α, (b) Polarization and temperature and (c) reciprocal isothermal permittivity and temperature, near the first-order ferroelectric phase transition.[115]

field is removed, the material retains some of that polarization (known as the remnant polarization P_R) defined by the Gibbs free energy minimum in the double well potential (Figures 1.16 and 1.17). This remnant polarization can be removed by the application of an electric field that opposes the direction vector of initial polarization. The electric field required to reset the remnant polarization to zero is known as the coercive field (E_C). At this point, the material can then be polarized in the opposite direction by applying the requisite electric field, and the whole cycle can be repeated symmetrically. The area under the P-E curve represented the work done the switch the polarization of the material from one vector to another, dependent on (i) how many dipolar domains are able to align with the electric field vector, and (ii) how thermodynamically stable these domains are.

The P-E hysteresis loop is arguably the most widely used and accepted experimental result to showcase ferroelectric behavior in a material. It is not only important from a scientific perspective, but it also plays a key role in the translation of these materials to memory or sensing device applications.[130,131] Care must be taken, however, to distinguish the difference between a ferroelectric hysteresis loop and that of a leaking dielectric material. Given the time-dependent nature of the ferroelectric measurement (typically a symmetrical triangular waveform), leakage currents inject

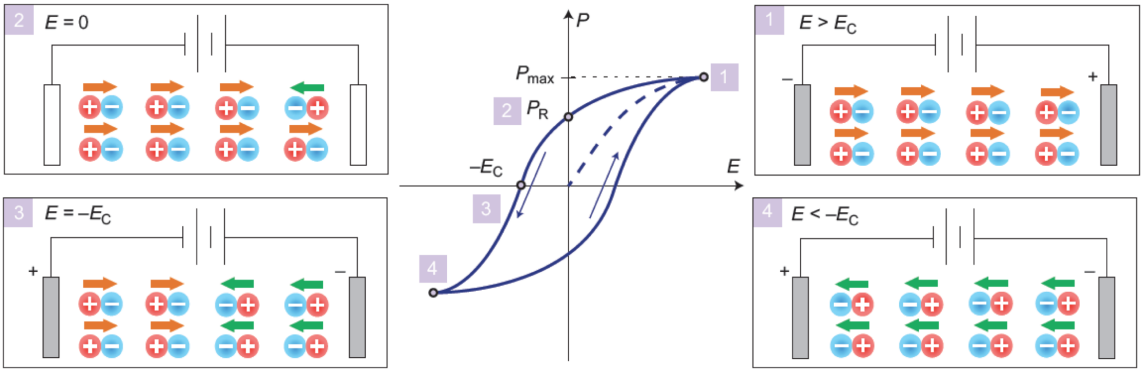

Figure 1.18: A polarization-electric field (P-E) hysteresis loop is one of the signature pieces of evidence for ferroelectric behavior in materials. (1) Applying an electric field to a ferroelectic material will rearrange the dipole moments of the material until they are all aligned with electric field and maximum polarization (P_{max}) is achieved. (2) Ferroelectric materials are able to retain this dipole vector orientation even upon the removal of the applied field, resulting in a remnant polarization P_R. (3) P_R can be removed by the application of an electric field in the opposite direction, the extent of which is known as the coercive field (E_C). (1) The entire top half of the ferroelectric hysteresis loop is symmetric upon the application of a field in the opposite direction, due to the degeneracy of the two dipole vectors in the ferroelectric material.[78]

charges to either electrode and artificially introduce a hysteretic response. The shape of the loop changes as well, where often the polarization saturates, and then *decreases* with increasing applied field. There is no clearly illustration of this discrepancy than that by J.F. Scott,[132] who compared (Figure 1.19 the hysteresis loops obtained from barium sodium niobate ($Ba_2NaNb_5O_{15}$), a known ferroelectric material, and that of a banana peel (clearly not ferroelectric).

Nonlinear Optics

An important feature of ferroelectric materials is that they lack a center of inversion. The lack of inversion symmetry is vital in defining a net dipole moment or polarization vector in the ferroelectric material, as it defines a dominant dipole moment orientation in the presence of an external field. In the context of thermodynamics and Gibbs free energy, this can be represented by a reduction in energy of one of the potential wells upon the application of an electric field vector to make that state

a global energy minimum. This defines a thermodynamically preferred electric displacement (and polarization) vector in the same direction as that of the applied field.

Not only is this noncentrosymmetry vital in the polarization state of ferroelectric materials, it also plays a key role in the non-linear optical behavior of ferroelectric materials. Non-linear optical phenomena, at its core, is the mixing of two or more optical waves. However, this mixing can go beyond the linear superposition of multiple waves, and can be described as follows:

Assume that light can be described as an electromagnetic wave. For the purpose of this discussion, we will ignore the magnetic and magneto-electric effects of light incident on ferroelectric materials, since their contribution is minimal. As a result, only the electric field (E) component of light need be considered. From equation 2, we know that the electric displacement (D) of a material varies linearly with the applied field (E). This can be written as a series expansion in tensor form:

$$D_i = \varepsilon_{ij}E_j + \chi^{(2)}_{ijk}E_jE_k + \chi^{(3)}_{ijkl}E_jE_kE_l... \tag{7}$$

where $\chi^{(2)}$ and $\chi^{(3)}$ represents the second- and third- order electronic susceptibilities, respectively. Now in centrosymmetric materials, all even-powered electronic susceptibilities (second, fourth, etc.) are forbidden, leaving only odd-powered susceptibilities (first, third, etc.). On the other hand for noncentrosymmetric materials, materials that do not have an inversion center, these even powered susceptibilities are allowed. Focusing on the second-order susceptibility, for an incident photon of light ($E_{in} = E_0\cos(\omega t)$), the corresponding electric displacement will be of the form

$$\begin{aligned} D &= \chi^{(2)}E_{in}^2 \\ &= \chi^{(2)}\big(E_0\cos(\omega t)\big)^2 \\ &= \chi^{(2)}E_0^2\left(\frac{1}{2} + \frac{1}{2}\cos(2\omega t)\right) \end{aligned} \tag{8}$$

where ω is the frequency of the incident photon, and t is time. As evident, an incident photon of frequency ω will incite an electric displacement in noncentrosymmetric materials with twice the frequency (2ω). This frequency doubling, or wavelength halving, is known as *second harmonic generation*, and is a phenomenon unique to materials that lack a center of inversion. In fact, detection of second harmonic responses (in the form of photons emitted from the material) in either powder,[133] thin film[134] or even using imaging techniques,[135] can be used to distinguish noncentrosymmetric materials from their centrosymmetric counterparts.[136]

1.4.2 *Inorganic Ferroelectrics*

The potential to create materials that are not only electronically (ferroelectric) but also optically (second harmonic) active has motivated the wide net of discovered and engineered ferroelectric materials. Among the most prevalent ferroelectric materials is the class inorganic perovskites that form a tetragonal crystal structure with degenerate polarization states..[131] These materials typically are of the form ABO_3, where A and B correspond to metal cations, and O the oxygen anion. Structurally (Figure 1.19a), the A atoms are typically located on the corners of the tetragonal cubic unit cell, B atoms in the body center, and O atoms centered on each face of the unit cell. In the ground (unpolarized) state, all the charged atoms are spatially arranged such that the net dipole moment from each unit cell is zero. However, upon the application of an external electric field, the B atom in the crystal can have the propensity to displace up or down relative to the O atoms depending on the vector of the applied field. This breaks the symmetry of charge distribution in the unit cell, therein imparting a net dipole vector. When the applied field is sufficient to align the dipole moments of all the crystal unit cells in congruency, a net stable polarization is defined, one that is reversible by the displacement of the central B atom in the opposite direction. Not all perovskite structures are capable of this ferroelectric mechanism of *atom displacement*, though prominent materials include $BaTiO_3$ and $PbTiO_3$.[115,130,131]

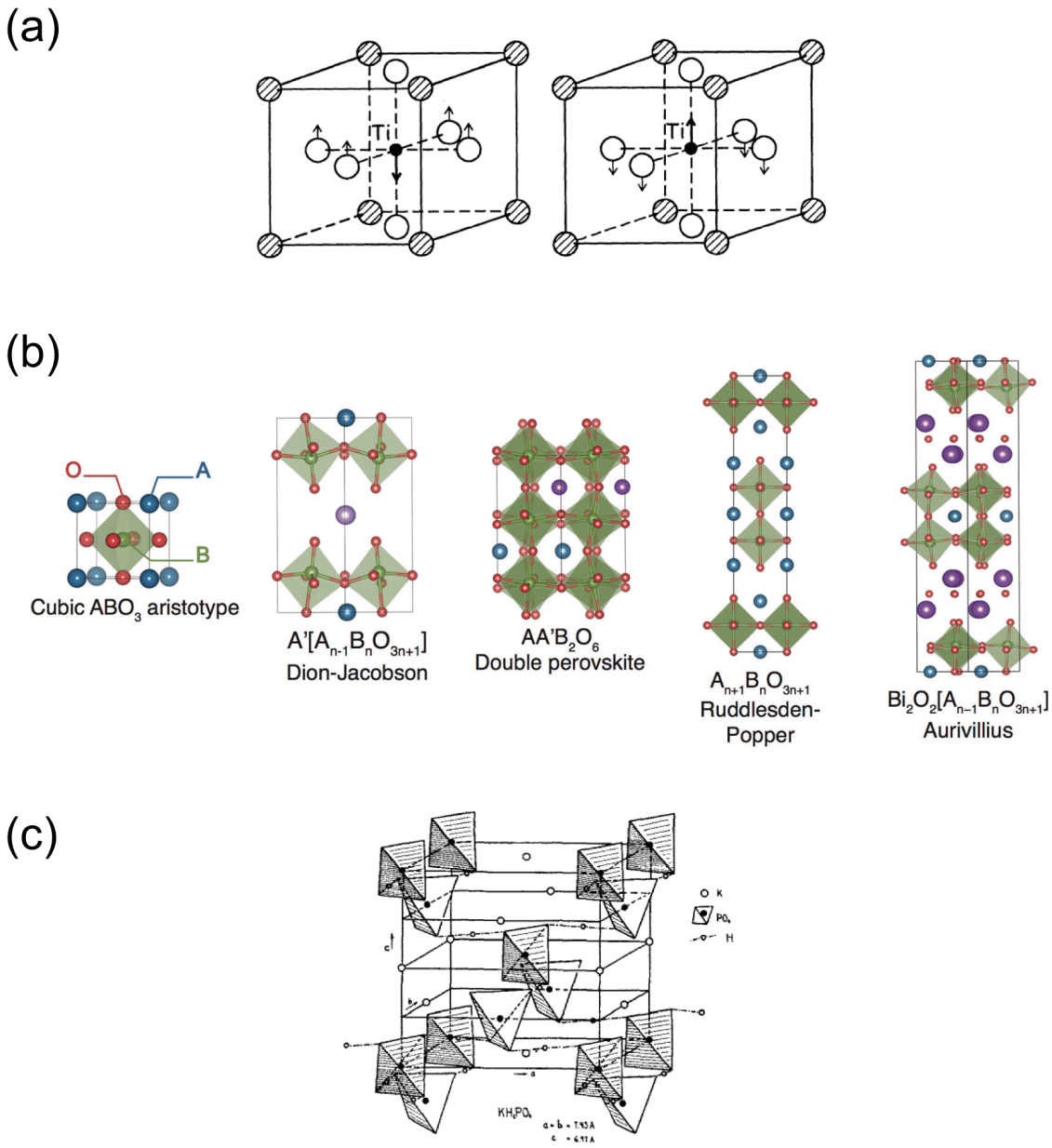

Figure 1.19: (a) Schematic of typical ABO_3 perovskite (shaded circles = A atoms, open circles = O atoms, black circle = B atoms), where atomic displacements of the body centered B atoms relative to the face centered O atoms result in a net dipole vector in the unit cell.[131] (b) Deviations from the traditional ABO_3 perovskite architype have been postulated to elucidate ferreoelctric behavior in a number of layered perovskite structures.[137] (c) Unit cell of potassium dihydrogen phosphate (KDP) salt, which displays a net dipole vector courtesy of the orientation hydrogens relative to phosphate groups in the unit cell.[138]

The limitation of ABO_3 perovskite ferroelectric materials is that only a small subset of the ABO_3 class is noncentrosymmetric, a prerequisite for ferroelectric behavior. Recently, however, Bousquet et al.[139] elucidated ferroelectric behavior from an artificial superlattice of layered $SrTiO_3$ and $PbTiO_3$. The source of this ferroelectric response was attributed to coupling of the rotational modes of the individual layers. Since then, a number of layered perovskite superlattices have been postulated (Figure 1.19b), wherein coupled non-polar lattice distortions (rotations or tilts) of the BO_6 octahedral result in noncentrosymmetric net dipole moment vectors capable of ferroelectric polarizations.[137,140,141]

A second common inorganic ferroelectric material are those whose polarization arises from *order-disorder transitions*. Coined by Slater,[142] this phenomenon is unique to dihydrogen phosphate crystals (such as KH_2PO_4, RbH_2PO_4 and CsH_2PO_4).[138] Contrary to the *atom displacement* ferroelectricity described above, *order-disorder* ferroelectricity relies on the orientation of the hydrogens relative to the phosphate groups (located on the corners of the unit cell), relying on dipole orientation of the $(H_2PO_4)^-$ anion, as opposed to the fixed positions of the metal cation (Figure 1.19c).

1.4.3 *Organic Ferroelectrics*

Order-Disorder Ferroelectrics

Much like their inorganic counterparts, the development of organic ferroelectrics has been driven by the potential applications as actuators and sensors. Indeed, organic polymers such as polyvinylidene fluoride (PVDF) have already found commercial use in acoustic transducers and microphones.[117,143,146] In this system, the overall dipole vector is determined by the relative orientation of the fluorine atoms in the $-CF_2$ unit (Figure 1.20a). Once again, this order-disorder ferroelectric mechanism relies on a cooperative orientation of all the individual $-CF_2$ units to result in a net overall polarization. As one can expect, the enthalpic and entropic energy required for such a mass polymeric reorganization is very high, which is why ferroelectric polymers such as PVDF suffer from abnormally high coercive fields.[78,143]

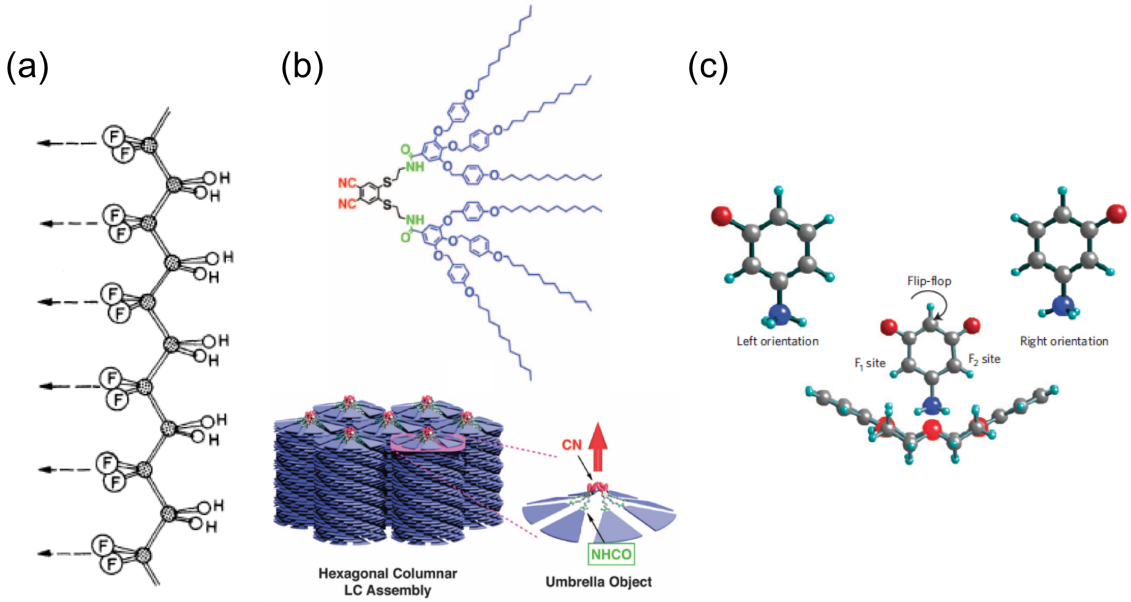

Figure 1.20: (a) Structure of PVDF ferroelectric polymer, with alighned -CF_2 units defining a net dipole moment for each monomer.[143] (b) Phthalonitrile-derived bent core molecules that form a hexagonal columnar liquid crystalline assembly. Homeotropic bowl inversion changes the orientation of the polar cyano groups, defining the polariazation vector in this liquid crystal ferroelectric system..[144] (c) Amphidynamic properties of asymmetric 4-fluoroanilinium molecules nested in a dibenzo[18]crown-6 complex define two degenerate polarization vectors by virtue of molecular rotation.[145]

In an effort to reduce the barrier for reorientation in these order-disorder ferroelectric materials, researchers turned to liquid crystals, with the hope that increased dynamics offered by liquid crystals would make molecular reorientation less energetically costly. Ferroelectricity in liquid crystals traditionally arises from the reorganization of chiral mesogens or intrinsic dipole moments within achiral molecules.[147] However, it was found that the covalent bonding and rigidity of early liquid crystalline ferroelectric hindered their dynamics and as a result their propensity to switch their net polarization. The solution, in a study by Miyajima et al.,[144,148] was to combine the supramolecular assembly of bent-core molecules into intrinsically noncentrosymmetric bowl-shaped structures with the added stability of hydrogen bonding to develop a supramolecular ferroelectric liquid crystal. The molecular design incorporates the use of amide hydrogen bonding to stabilize the bowl-shape assembly of phthalonitrile-derived molecules. Once again, ferroelectricity is determine by the orientation of the polar cyano groups, obtainable through homeotropic bowl inversion (Figure 1.20b) in the presence of an external electric field. This system is among the first to demonstrate liquid crystalline ferroelectricity with any processing or device treatment.

In an attempt to further minimize the motion of key dipolar components in order-disorder ferroelectrics, Akutagawa et al.[145] demonstrated ferroelectric polarization by the motion of a single host molecule in a host-guest complex system (Figure 1.20c). In this case, the authors utilized the amphidynamic - the rotation of molecules in a crystalline lattice - properties of the asymmetric 4-fluoroanilinium in a dibenzo[18]crown-6 complex to define two distinct but degenerate dipole vectors in what the authors termed a "flip-flip supramolecular rotor" ferroelectric.

Hydrogen Bonding Ferroelectrics

While the ordering or physical reorientation of dipolar molecules can be one method to develop a material with ferroelectric properties, achieving a dipole vector by either the displacement of protons or electrons offers a simpler, pseudo-static polarization mechanism with a lower energy barrier towards polarization switching.[78] The advent of hydrogen bonding in ferroelectric mate-

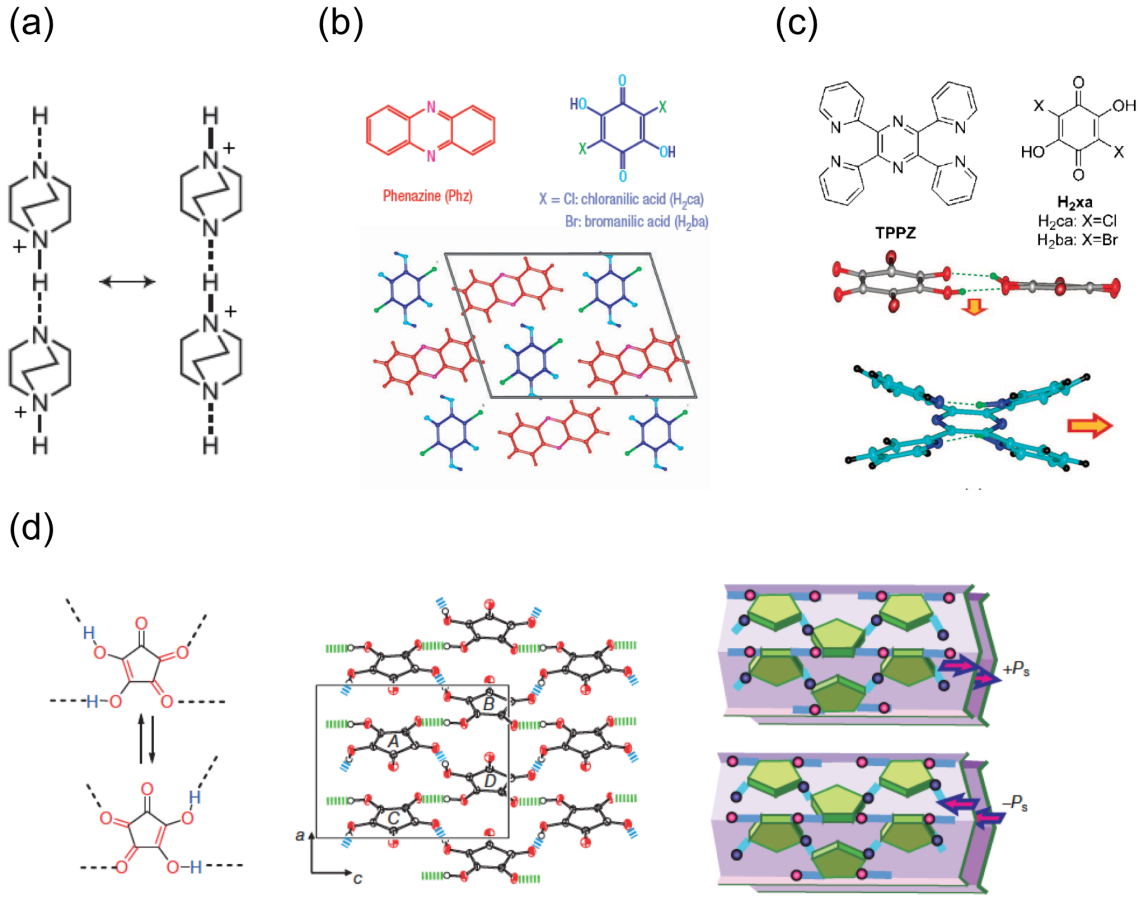

Figure 1.21: (a) Single-component ditopic dabcoHClO$_4$ that assemble in an anti-parallel manner. The polarization vector is defined by hydrogen bonding interactions along the anti-parallel stacking arrangement.[149] (b) Two-component co-crystal of Phz and H_2ca (or H_2ba), where ferroelectric dipoles are defined by the asymmetric displacement of hydrogen bonding molecules in the presence of an electric field..[150] (c) Two-component co-crystal of TPPZ and H_2ca (or H_2ba) display ferroelectric properties due to TPPZ acting as a 'proton sponge'.[151] (d) Proton tautomerization of croconic acid result in inter- and intra-molecular hydrogen bonding interactions to define an extended supramolecular crystal with polarization vectors in the plane of the molecules.[152]

rials has already been alluded to, with the KH_2PO_4 set of order-disorder ferroelectric materials, in that the binding orientation of hydrogen atoms to the phosphate anions. *Hydrogen bonding* ferroelectrics, in contrast, rely on the explicit interactions between a proton acceptor and proton donor. Specifically, hydrogen bonding creates a dipole between these acid-base pairs, wherein the proton donor becomes partially negative, and the proton acceptor partially positive. An early example[149] of a single-component ditopic hydrogen bonding ferroelectric material was that of 1,4-diazabicyclo[2.2.2]octane (dabcoHClO$_4$). In the solid-state, the hydrogen bonding chains of dabco molecules crystallized (Figure 1.21a) in an anti-parallel manner, defining an axis of polarization that was later exploited[153] as a room-temperature ferroelectric response.

The success of the dabco-based single component hydrogen bonding system spurred research into the development of more complicated and intricate hydrogen bonding ferroelectric materials. A prominent case would be the use of a two-component hydrogen bonding system, where one aromatic molecule was functionalized with hydrogen bonding donors, and the other with hydrogen bonding acceptors. Such is the case with the two-component crystal of chloranillic acid H_2ca (or bromanillic acid H_2ba) with phenazine (Phz).[150] While structurally (Figure 1.21b) centrosymmetric at room temperature, the alternating nature of the Phz and H_2ca (or H_2ba) molecules, combined with the similar pKa's ($pKa_{Phz} = 1.20, pKa_{H_2ca} = 0.73, pKa_{H_2br} = 0.80$) ensures that the hydrogens are shared equally between the two component molecules. Below 253 K, however, the hydrogen-bonding molecules displace in a manner that breaks inversion symmetry and produces a net dipole vector. In similar vein, a co-crystal between H_2ca (or H_2ba) and 2,3,5,6-tetra(2-pyridinyl)pyrazine (TPPZ) (Figure 1.21c) has been shown[151] to display ferroelectric properties at temperatures above room temperature. In this case, however, the two molecules do not partake in intermolecular hydrogen bonding exchange. Instead, the TPPZ molecule acts as a "proton sponge", and the dynamic shuttling of the proton between the neutral and protonated pyridinyl rings acts as the source of ferroelectric polarization in the co-crystal.

While most hydrogen bonding ferroelectric materials rely on the relative motion of protons from a proton donor to a proton acceptor, proton tautomerization in single component molecular crystals have been shown[82,152] to lead to dipole vectors that are ferroelectric. Tautomerization is characterized by intramolecular proton migration, typically observed between ketone and enol, or imine and enamine functional groups. In this case, inter- and intra-molecular hydrogen bonding was observed (Figure 1.21d) for single crystals of croconic acid. This, combined with aromatic π-π interactions between neighboring molecules ensured the growth a stabilization of planar layered supramolecular crystals. In the presence of an electric field, the migration of a proton from the β position of the enol to the ketone, inverts the symmetry between neighboring molecules, and with it the dipole vector.

Charge Transfer Ferroelectrics

Much like hydrogen bonding ferroelectric materials *charge transfer* (CT) ferroelectrics also require the motion of a charged particle from one functional position to another. In this case, however, the particle of choice is an electron, instead of a proton. As alluded to in Section 1.2.2, the structural orientation of CT complexes that most suits ferroelectric behavior is the mixed stack, wherein the electron donor and electron acceptor alternate in a linear stack along the direction of charge transfer. A prior discussion in Section 1.2.2 illustrated the capability of mixed stack CT complexes to undergo symmetry-breaking dimerization due to Peierls instability, forming two discrete degenerate states characterized by an aligned dipole vector. We now know that this "ionic" state is crucial for ferroelectric applications, as the aligned dipole vectors add up to discrete ferroelectric polarizations.

One of the most prominent ferroelectric material that relies on CT interactions is the co-assembly of tetrathiafulvalene (TTF) and halogenated quinones. The TTF-QCl_4 co-crystal, which has previously been studied from the perspective of crystallography,[97] and vibrational[99] and absorption spectroscopy,[97] displays (Figure 1.22a) a neutral-to-ionic transition at 81 K. This was

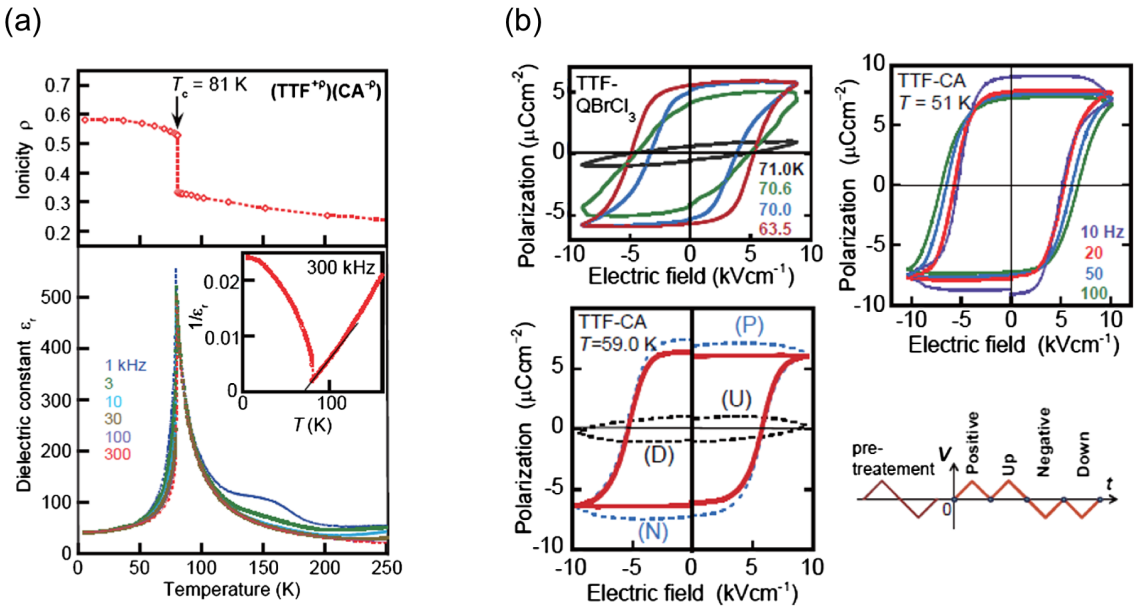

Figure 1.22: (a) Anomalous changes in ionicity and dielectric constant for TTF-QCl_4 (also known as TTF-CA) co-crystals indicative of ferroelectric-paraelectric phase transition at 81 K for CT co-crystal. (b) Ferroelectric hysteresis observed in TTF-QCl_4 and TTF-$QBrCl_3$ (independent of the applied switching frequency), above and below the phase transition temperature. Novel positive-up-negative-down (PUND) method was used to eliminate non-hysteretic contributions, where the 'up' and 'down' cycles elucidated non-hysteretic signals while the 'positive' and 'negative' cycles displayed a linear combination of the hysteretic and non-hystereric contributions to the polarization signal.[154]

deduced by the observation of a large anomalous spike in the dielectric constant at 81 K, indicative of a phase transition as per equation 5 and 6, implying that at temperatures above the observed transition, the co-crystal displayed a centrosymmetric orientation, with little or no charge transfer from the donor molecules to the acceptor molecule. Below the transition temperature, however, the co-crystal switches to a non-centrosymmetric orientation with a sharp increase in charge transfer, attributed to displacive dimerization between the donor and acceptor.[120,122] While elucidating bulk ferroelectric measurements proved initially difficult for the co-crystal TTF-QCl_4, extensive studies on the conductivities[155] of the co-crystal (a hindrance to ferroelectricity) as well as the mesoscale dipole vector domains[156] pushed the field forward in understanding these complex CT co-crystals. The bulk ferroelectric polarization of TTF-QCl_4 and it's sister TTF-$QBrCl_3$ was finally realized (Figure 1.22b) by eliminating non-hystereric contributions (such as leakage currents) in the P-E loop. Specifically, Kobayashi et al.[154] used a double triangular waveform, referred to as a positive-up-negative-down (PUND) procedure, where the 'positive' and 'negative' inputs reverse the polarity, and the 'up' and 'down' elucidate any nonhysteretic contributions such as current and capacitive contributions. Elimination of these artifacts from the 'positive' and 'negative' inputs resulted in well-defined parallelogram hysteresis loops at cryogenic temperatures. Further studies expanded the library of TTF-quinone complexes, where ferroelectricity was elucidated in TTF-QBr_4,[157] TTF-QBr_2I_2[158] and 4,4-dimethyltetrathiafulvalene complexes (DMTTF-QBr_4),[159] pressure and magnetic fields to influence the spin-Peierls system and the ferroelectric properties of the co-crystals. While fascinating to study from an academic standpoint, these series of co-crystals were limited in the translational applicability since their ferroelectric properties were only addressable at cryogenic temperatures.

In the push to develop functional charge transfer ferroelectrics, there still remained a the need for materials that can function at room temperatures and pressures without altered chemistry or changes in physical environment. Tayi et al.[79] developed arguably the first system of charge transfer ferroelectrics that displayed ferroelectric hysteresis at both cryogenic and room temperatures at at-

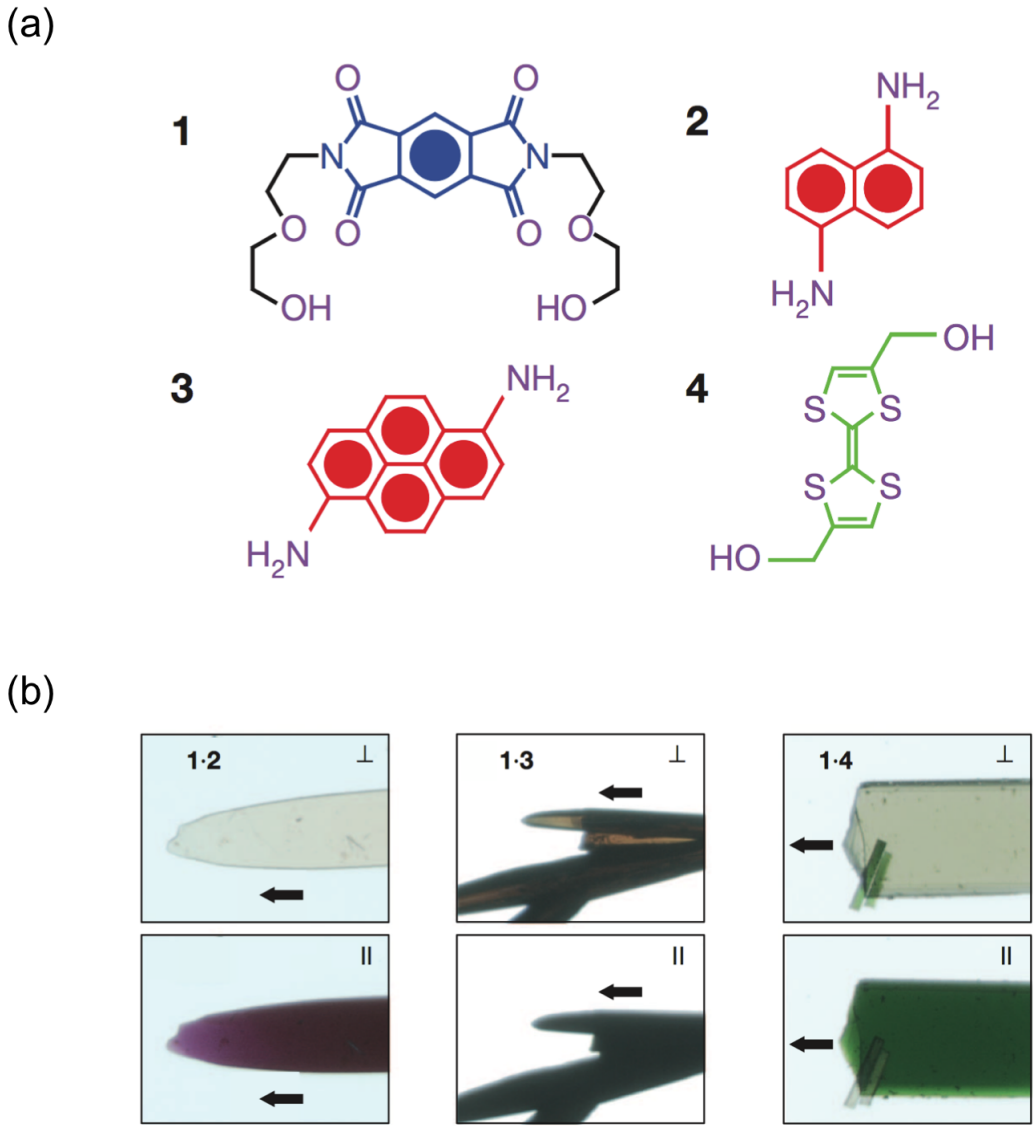

Figure 1.23: (a) Chemical structures of LASO ferroelectric co-crystals, incorporating a PMDI acceptor (**1**) co-assembled with either a naphthalene-based (**2**), pyrene-based (**3**) or]ceTTF-based (**4**) donor molecule. (b) Optical microscopy of LASO co-crystals under linearly polarized light either perpendicular or parallel to length of co-crystal. Strong absorbance along the length of crystals assert that CT (and by consequence the mixed stack direction) occurs along the physical length of the co-crystals.[79]

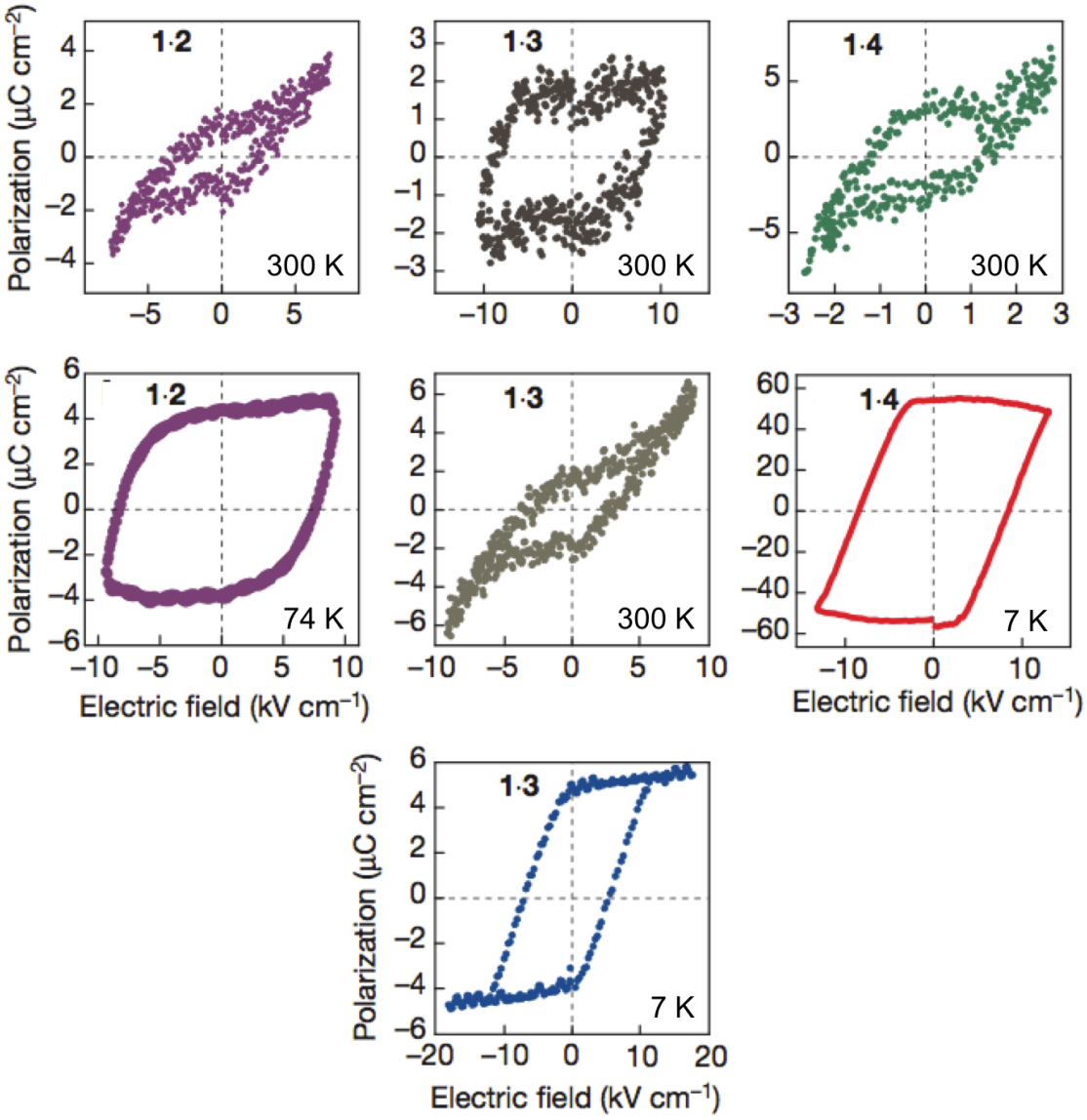

Figure 1.24: Polarization hysteresis loops at room temperature as well as crogenic temperatures for supramolecular LASO co-crystals. All hysteresis measurements were performed with a switching frequency $f = 0.1$Hz.[79]

mospheric conditions. This was achieved used the previously described (Section 1.3) LASO motif for charge-transfer co-crystals, where aromatic donor and acceptor molecules were functionalized with complementary hydrogen bonding diethylene glycol 'arms' to form large, robust and air stable single co-crystals of donor and acceptor molecules. It was hypothesized that the combination of hydrogen bonding, solvophobic interactions and charge transfer helped stabilize the mixed stack arrangement of donor and acceptor molecules into a three-dimensional supramolecular network. Tayi et al. focused on three sets of co-crystals (Figure 1.23), with a pyromellitic diimide (PMDI) based acceptor and naphthalene (NP), pyrene (Py) and tetrathiafulvalene (TTF) based donor molecules. The supramolecular network of donor and acceptor molecules grew to form long, linear crystals, with the direction of charge transfer and the alignment of the mixed stack along the long-axis of the crystal (Figure 1.23), which made for easy electrical measurements. What set these co-crystals apart from their predecessors was the observation (Figure 1.24) of ferroelectric polarization at room and cryogenic temperatures for these co-crystals. While the exact mechanism of ferroelectric polarization in these systems is currently under study, the hypothesis of a combination of charge and proton transfer interactions, along the direction of the applied electric field, contributing to the overall polarization observed at room temperature stands to this day.

1.5 THESIS OVERVIEW

The research presented in this thesis illustrates the versatility of charge transfer complexes in a variety of different morphologies that drive their applications. In the solid state, these molecules crystallize in a number of unique combinations and conformations, from a 1:1 linear stack of donor and acceptor molecules to a 2:1 sheet of mixed and crossed stack orientations. The assembly, in turn, defines their photophysical and electronic properties due the combination and orientation of complementary hydrogen bonding and charge transfer interactions. Solution-phase CT interactions will also be explored, due to their diversity in morphology and function. The interplay between hydrogen bonding, solvophobic interactions and charge transfer in both organic and aqueous sol-

vents is key in delineating and understanding the applications, in both static and dynamic systems, of these CT complexes. In addition, the difference between assemblies in solution and on a substrate provides an avenue of further study, one that is conveniently omitted in much research on solution-processable CT complexes. Finally, using CT interactions as a medium for studying the dynamics of exchange between assembled nanostructures provides insight on how supramolecular systems interact with each other, especially when the positive driving force for interaction can be tuned through variations in chemistry and morphology.

2 Ferroelectric Polarization and Second Harmonic Generation in Supramolecular Co-Crystals with Two Axes of Charge Transfer

2.1 OBJECTIVES AND SIGNIFICANCE

Serendipity has always been at the forefront of scientific discovery. Not only did it motivate and drive our research front on charge transfer ferroelectric materials, but it also played a large role in motivating this chapter of research. While traditional charge transfer LASO complexes assembly in a perfectly alternating 1:1 stack of donor and acceptor molecules, we stumbled across one particular series that assembled in a 1:2 donor to acceptor motif, wherein each donor molecule had two acceptor molecules within the crystalline lattice. In this co-crystal, charge transfer occurred along not one but two axes. This bidirectional charge transfer drives the growth of the superstructure along two axes to form rectangular plate-like single crystals, instead of the needle-like crystal morphologies observed in traditional 1:1 LASO co-crystals. In addition, these unique co-crystals exhibit room-temperature ferroelectric polarization along two independent axes. That the two polarization axes are largely independent of each other is a landmark observation, as it suggests that the single crystal is able to hold and stabilize two independent modes of polarization at room temperature. This opens up the potential for these materials to be used in high density storage applications, an ever-growing need in this age of computing and industry.

2.2 BACKGROUND

Materials that possess non-linear optical (NLO) as well as ferroelectric properties with switchable spontaneous electrical polarization hold great promise in electronic memory and optoelectronic applications.[130,131] Inorganic ferroelectric materials, such as the prototypical $BaTiO_3$, are composed of two ionic sublattices that experience a spontaneous breaking of inversion symmetry by

atomic displacement along one direction at a time.[115,160] This implies that while it is possible for inorganic ferroelectric materials to display ferroelectric properties in multiple directions,[82,161,162] the magnitude and mechanism under which polarization occurs is identical. The atomic displacement, in turn, gives rise to a non-linear optical response, characterized by second harmonic generation (SHG).[163,164]Recent breakthroughs in organic crystals, hybrid frameworks, and liquid crystalline materials have drawn attention to organic ferroelectric materials that have performances approaching those of their inorganic counterparts.[20,78,79,83,165]

Mixed stack charge-transfer (CT) complexes,[43] in which electron donor and acceptor molecules assemble face-to-face in an alternating mixed stack, are promising candidates for ferroelectric organic materials on account of their tunable neutral and ionic ground states.[96] We have developed[103] a motif termed Lock-Arm Supramolecular Ordering (LASO) to obtain ordered, close-packed, solvent-free and robust crystalline materials by leveraging a combination of charge-transfer, π-π stacking, van der Waals, and complementary hydrogen bonding interactions. In three of the LASO co-crystals, we observed room temperature ferroelectric hysteresis.[79] We hypothesized that the spontaneous polarizations observed at room temperature, rather than solely at cryogenic temperatures, are enabled by the complementary hydrogen bonding and charge-transfer interactions that stabilize the polar, dimerized donor-acceptor supramolecular network. In our efforts to probe structure-property relationships in these co-crystals, we obtained a thin sheet-like LASO co-crystal characterized by two crystallographically unique axes, indicative of two preferred directions of crystal growth. Polarized absorption spectra of the co-crystal suggests CT interactions in both the face-to-face and edge-to-face directions. This is in direct contrast to traditional LASO needle-like co-crystals, which have one preferred directon of crystal growth due to a single direction of charge transfer.[103]

This chapter focuses on the optical and electronic properties of the unique LASO CT co-crystal. The co-crystal (Figure 2.1a) incorporates a 2:1 ratio of pyromellitic diimide acceptor **1** to 5-amino-1-naphthol donor **2**. The crystal structure (Figure 2.1b) of $(\mathbf{1})_2\bullet\mathbf{2}$, obtained by single crystal X-ray

diffraction, reveals[103] that each donor molecule engages in (i) face-to-face CT interactions, reminiscent of a conventional mixed stack CT complex along the [100] crystallographic axis, and (ii) edge-to-face CT interactions with additional acceptor molecules along the [010] direction. In the following discussion, the face-to-face stacking [100] direction will be referred to as the mixed stack axis and the edge-to-face [010] stacking direction as the crossed stack axis. Given the nature of the crystal structure, we have explored here the possibility of anisotropic ferroelectric behavior as well as signatures for noncentrosymmetry using second harmonic microscopy and spectroscopy.

2.3 RESULTS AND DISCUSSION

2.3.1 *Room and Cryogenic Temperature Ferroelectric Polarization*

Evidence for ferroelectricity in co-crystal $(\mathbf{1})_2\bullet\mathbf{2}$ was obtained along both the mixed stack and crossed stack axes (Figure 2.1b) at 300 K and 10 K by measuring (Figure 2.1c-f) polarization hysteresis curves of electric displacement as a function of applied electric field. The individual co-crystals were face-indexed before (Figure 2.2) and after (Figure 2.3) the application of electric fields to ensure that the mixed stack [100] and crossed stack [010] axes corresponded to the long and short axis of the co-crystal. Depolarization fields,[166,167] typically observed in thin film devices, were assumed to be negligible since the ferroelectric device lengths (Table 2.1) were on the order of hundreds of micrometers. The mixed stack axis [100] has a maximum room temperature polarization (Pmax) of 3.5 μC/cm^2 and a remnant polarization (Pr) of 2.4 μC/cm^2, while the crossed stack axis [010] has a Pmax of 1.1 μC/cm^2 and a Pr of 0.5 μC/cm^2. Lowering the temperature to 10 K allowed us to bias the crystals at higher electric fields and observe curves having larger hysteresis with Pr values of 10 μC/cm^2 and 4.5 μC/cm^2 along the [100] and [010] axes, respectively. Dielectric breakdown of the crystals at high voltages limits the maximum observable polarization, and as a result the hysteresis curves measured are under-saturated. Joule heating and crystal degradation at high voltages are possible causes for this observed effect.7 Nonetheless, we found that at both 10 K and room temper-

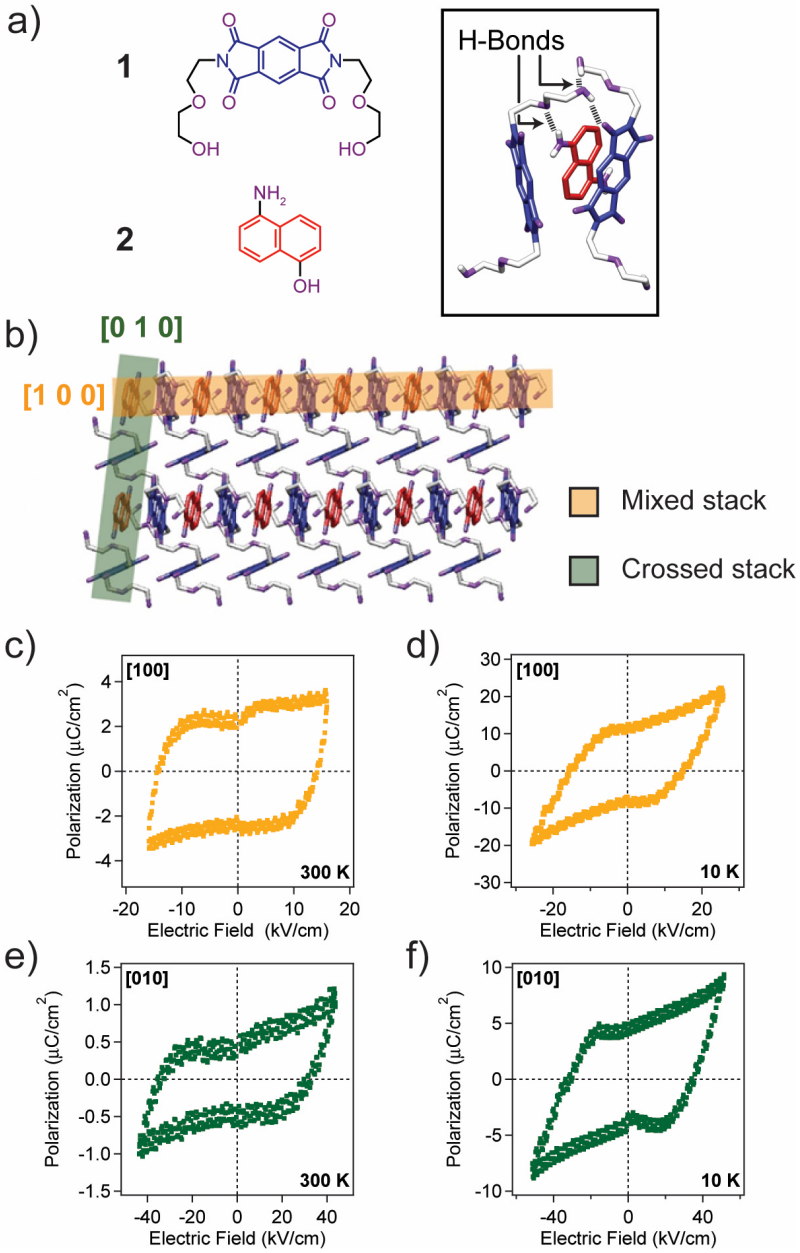

Figure 2.1: (a) Structural formulas of electron acceptor **1** (blue) and electron donor **2** (red) with hydrogen bond donors (OH and NH_2) and hydrogen bond acceptors (C=O and OCH_2CH_2). Crystal structure of $(\mathbf{1})_2$•**2** (inset a). The heteroatoms (purple) that participate in noncovalent bonding interactions as well as the hydrogen bonds (black hatched lines) between atoms are identified. (b) The superstructure of co-crystal with the mixed stack and crossed stack axes are highlighted in orange and green, respectively. Polarization versus electric-field curves measured along the (c,d) [100] stack and (e,f) [010] axes. Polarization hysteresis loops along the [100] axis were observed at (c) 300 K and (d) 10 K, and along the [010] axis at (e) 300 K and (f) 10 K. All hysteresis measurements were performed at f = 0.1 Hz.

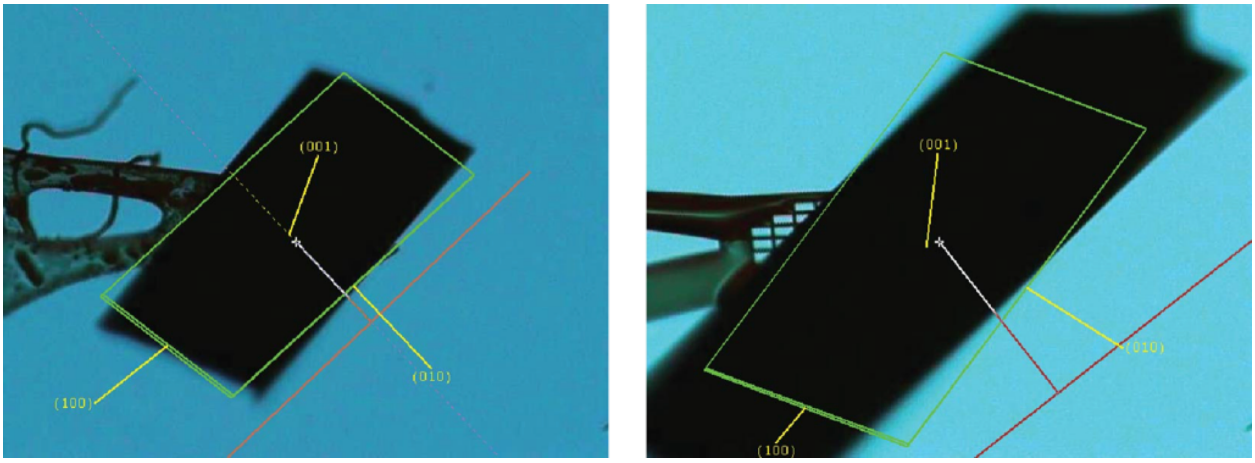

Figure 2.2: Two examples of indexing single crystal samples of co-crystal $(\mathbf{1})_2\bullet\mathbf{2}$. The [100] and [010] directions are approximately normal to the short and long edges of a typical single crystal, respectively.

Table 2.1: Average device dimensions across the [100] and [010] axes of co-crystal $(\mathbf{1})_2\bullet\mathbf{2}$.

Device Orientation	Average Length (μm)	Average Width (μm)	Average Thickness (μm)
[100]	757.2	244.1	21.8
[010]	276.7	742.9	25.5

ature the polarization curves measured for $(\mathbf{1})_2\bullet\mathbf{2}$ do not resemble the banana loops that are often observed for materials as a false-positive indication of ferroelectricity.[132]

The ferroelectric axes in co-crystal $(\mathbf{1})_2\bullet\mathbf{2}$ are nearly orthogonal (84°) and, as a consequence, applying a field along any one axis would result in a far smaller projection on the second axis (Figure 2.4). This electric field component (Table 2.2) along the second axis is an order of magnitude smaller than the applied field. The lower parasitic field results in a negligible polarization along the second axis. As a result, the second non-orthogonal axis does not contribute to the remnant polarization observed. The unique geometry of the two ferroelectric axes, along with the two observed directions of charge-transfer,[103] suggest that the two polarization states in co-crystal $(\mathbf{1})_2\bullet\mathbf{2}$ are decoupled. This decoupling and asymmetry between the two non-equal ferroelectric polarizations are unique among ferroelectric materials. Ferroelectricity across multiple axes has traditionally been limited to materials that form ferroelectric vortices, or have multiple crystallographically equivalent

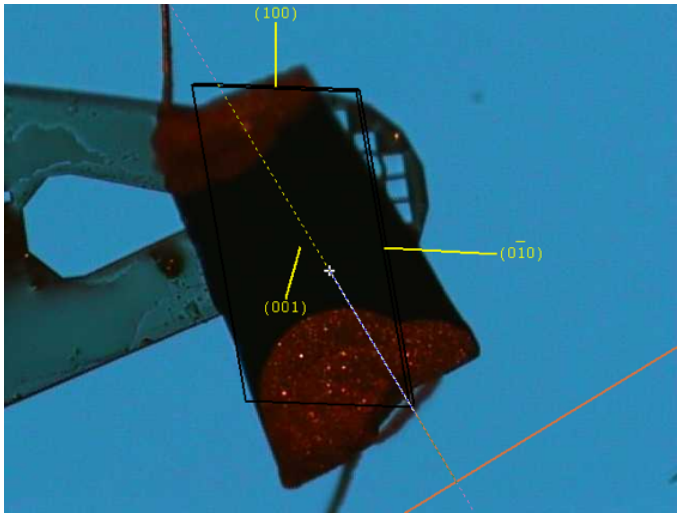

Figure 2.3: The device measured in Figure 2.1(c,d) was indexed and found to be along the mixed stack axis [100].

polarization axes. Ferroelectric vortices are topological defects in ferroelectric materials, characterized by closure domains where adjacent in-plane polarizations align head-to-tail with a domain angle less than 180°, resulting in a closed polarization loop.[168–171] Although examples of naturally occurring[172] and induced[162] ferroelectric vortices have been reported, the sizes of these vortices are restricted to the nanoscale due to their metastable nature. Ferroelectric materials with multiple crystallographically equivalent axes are also candidates that can display ferroelectric polarization across multiple axes. One such material is the organic crystal 2-methylbenzimidazole, wherein ferroelectric behavior arises from proton tautomerization.[82] In this compound, tetragonal crystal symmetry allows for ferroelectric polarization of equal magnitude across two crystallographically equivalent axes. What distinguishes the ferroelectric co-crystal reported here from these examples is that co-crystal $(\mathbf{1})_2\bullet\mathbf{2}$ displays anisotropic, single crystal ferroelectric polarizations across two crystallographically unique axes. We believe this phenomenon can be attributed to the combined effects of charge-transfer along more than one axis and the existence of a three-dimensional hydrogen bonding network in the donor-acceptor co-crystal.

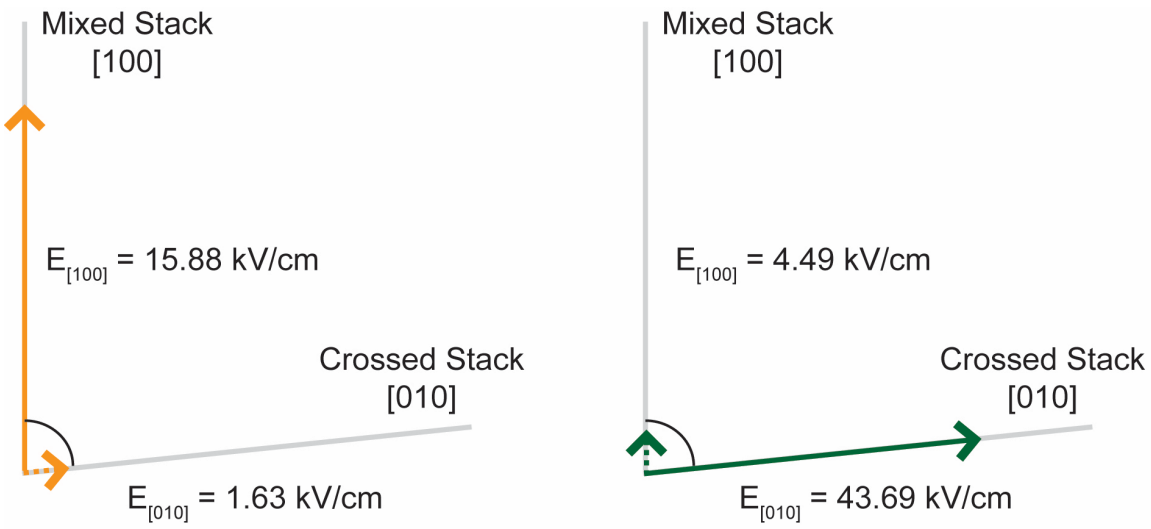

Figure 2.4: Vector diagrams illustrating the components of electric field along the two ferroelectric axes for co-crystal $(\mathbf{1})_2\bullet\mathbf{2}$. a) An electric field of 15.88 kV/cm is required to induce room temperature ferroelectric hysteresis along the mixed stack axis of the crystal. This electric field results in a 1.63 kV/cm component across the non-orthogonal crossed stack axis of the co-crystal. b) An electric field of 43.69 kV/cm is required to induce room temperature ferroelectric hysteresis along the crossed stack axis of the co-crystal. This electric field results in a 4.49 kV/cm component across the non-orthogonal mixed stack axis of the co-crystal

Table 2.2: Applied electric fields across the mixed stack and crossed stack axes, as well as their components along the mixed stack and crossed stack axes, respectively

Measurement at 300K			Projection along second axis			
Measured Polarization Axis	Applied Electric Field (kV/cm)	Remnant Polarization (μC/cm^2)		Applied Electric Field (kV/cm)	Remnant Polarization (μC/cm^2)	Calculated Parasitic Remnant Polarization (μC/cm^2)
Mixed Stack [100]	15.88	2.4	[100]	-	-	0.019*
			[010]	1.63	0.19*	-
Crossed Stack [010]	43.69	0.5	[100]	4.49	0.68*	-
			[010]	-	-	0.070*

*The parasitic remnant polarization calculated was small across both axes of co-crystal $(\mathbf{1})_2\bullet\mathbf{2}$. It is believed that the incident electric field is not high enough to induce dipolar switching.

2.3.2 *Variable-Temperature Dielectric Spectroscopy*

In an effort to determine the ferroelectric Curie temperature (T_c) of the co-crystal $(\mathbf{1})_2\bullet\mathbf{2}$, we measured (Figure 2.5) dielectric constants along the two ferroelectric axes as a function of temperature. In both cases, the expected discontinuity, characteristic of a ferroelectric-to-paraelectric phase transition,[115] was not observed within the 7 K to 400 K temperature range. This observation suggests that the T_c lies outside the range of this measurement and close to the decomposition temperature of the co-crystal. The lack of an observable Curie temperature is likely the result of the stable hydrogen bonding network in this system. Other examples[173–176] of ferroelectric materials are known for which a Curie temperature is not observed. One such material is poly(vinylidene fluoride) (PVDF), where the T_c has been estimated by extrapolation from copolymer samples since PVDF melts before undergoing any ferroelectric-to-paraelectric transition. The frequency dependence of the dielectric constants of co-crystal $(\mathbf{1})_2\bullet\mathbf{2}$ can be attributed to the dynamics of domain wall motion along mixed and crossed stacked axes, a phenomenon not uncommon among mixed-stack charge transfer complexes.[81,177] This is especially apparent at lower temperatures, where the frequency-dependent dielectric response slows down enough to be observed in the measured frequency ranges.

2.3.3 *Effects of Temperature and Electric Field on Crystal Structure*

An intriguing aspect of these results is the fact that we previously reported the crystal structure of $(\mathbf{1})_2\bullet\mathbf{2}$ to be centrosymmetric.[103] This property is, of course, not consistent with the observed ferroelectric behavior. We compared diffraction data of co-crystal $(\mathbf{1})_2\bullet\mathbf{2}$ collected at (i) cryogenic and (ii) room temperatures, as well as (iii) after the application of electric fields. In all three cases, the crystallographic data for the co-crystals refine (Table 2.3) to the centrosymmetric space group $P\bar{1}$. Attempts to assign a noncentrosymmetric space group $P\bar{1}$ consistently yielded multiple checkCIF[178,179] alerts. Based on indications of ferroelectric behavior in co-crystal $(\mathbf{1})_2\bullet\mathbf{2}$, we decided

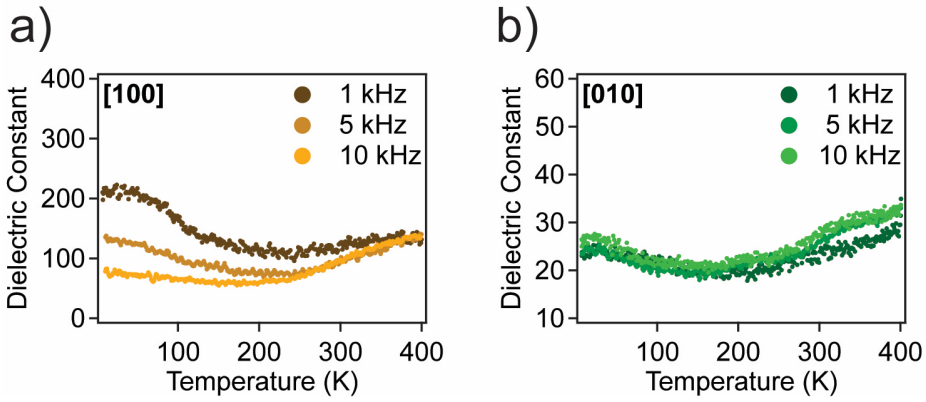

Figure 2.5: Dielectric constant measurements between 7 K and 400 K on co-crystal $(\mathbf{1})_2\bullet\mathbf{2}$ along the a) mixed stack [100] and b) crossed stack [010] axes. No ferroelectric Curie transition is observed along either axis, indicative of ferroelectric-paraelectric phase transition that is outside the measurement range. All dielectric measurements were performed at 2 V with f = 1 kHz, 5 kHz and 10 kHz.

to assess the hypothesis that X-ray crystallography alone is unable to resolve the source of noncentrosymmetry in these co-crystals.

2.3.4 *Nonlinear Optical and Second Harmonic Activity*

Second harmonic generation is a nonlinear optical effect that is well established as a tool for elucidating structure and detecting noncentrosymmetry in electronic and magnetic crystals.[136,180–182] Specifically, SHG refers to the process where two photons undergo frequency doubling (wavelength halving) when incident on a material. SHG is distinct from other photoexcitation processes in that it does not require a photoinduced excited state, and is unique to materials that lack a crystallographic inversion center. This nonlinear optical phenomenon has been previously demonstrated in organic crystals[183–185] and biological samples[135] as well as in organic ferroelectric materials.[82,134,186]

Two-photon Confocal Microscopy

Two-photon confocal microscopy is a technique traditionally used by to image live cells deep within intact tissue.[135] The mechanism for two-photon involves the simultaneous incidence of two

Table 2.3: Crystal Data and Structure Refinement

	$(\mathbf{1})_2$•**2**	$(\mathbf{1})_2$•**2**	$(\mathbf{1})_2$•**2** (post-polarization)
Empirical formula	C46H49N5O17	C46H49N5O17	C46H49N5O17
Formula weight	943.90	943.90	943.90
Crystal	Red plate	Red plate	Red plate
Temperature	84(2) K	299(2) K	100(2) K
Wavelength	1.54178 Å	1.54178 Å	1.54178 Å
Crystal system	Triclinic	Triclinic	Triclinic
Space group	$P\bar{1}$	$P\bar{1}$	$P\bar{1}$
Unit cell dimensions	a = 6.7603(7)	a = 6.8413(2)	a = 6.7670(5)
	b = 10.8522(11)	b = 11.0012(4)	b = 10.8796(8)
	c = 15.785(2) Å	c = 15.8978(5) Å	c = 15.7609(12) Å
	α = 71.882(9)	α = 71.153(2)	α = 71.775(4)
	β = 81.810(9)	β = 82.265(2)	β = 81.966(4)
	γ = 84.105(8)°	γ = 84.224(2)°	γ = 83.780(4)°
Volume	1087.3(2) $Å^3$	1119.97(6) $Å^3$	1088.75(14) $Å^3$
Z	1	1	1
ρ calcd	1.441	1.399	1.440
2θmax	59.131	63.490	27.508
Absorption coefficient, μ	0.938 mm^{-1}	0.911 mm^{-1}	0.111 mm^{-1}
Crystal size	0.722 x 0.238 x 0.094 mm^3	0.3 x 0.158 x 0.03 mm^3	0.338 x 0.332 x 0.044 mm^3
Reflections collected	3058	3579	4983
Independent reflections	2259	3169	4238
Data / restraints / parameters	3058 / 0 / 305	3579 / 0 / 310	4983 / 0 / 310
R[I >2.0σ(I)]	R1 = 0.0568	R1 = 0.0347	R1 = 0.0395
wR2 (all data)	0.1692	0.0979	0.1048
CCDC number	986214	986216	986215

photons in a single quantized event.[180,187] The benefit of two-photon confocal microscopy lies in its provision of three dimensional optical scanning without photobleaching or sample degradation above and below the focal plane. In this chapter, on a single crystal of $(\mathbf{1})_2\bullet\mathbf{2}$ under ambient conditions at zero applied field allowed us to image (Figure 2.6) a second harmonic response. The lack of an inversion center in co-crystal $(\mathbf{1})_2\bullet\mathbf{2}$ results in frequency doubling (wavelength halving) of the incident two-photon radiation. Consequently, the co-crystal is only 'seen' by the detector that possesses a detection range within half the incident multiphoton wavelength. To delineate this observation from potential photoexcitation processes, the co-crystal was excited at multiple incident wavelengths. Tuning the incident two-photon wavelength from 850 to 950 nm results in the detection of co-crystal $(\mathbf{1})_2\bullet\mathbf{2}$ changing from Detector 1 to Detector 2 because the second harmonic wavelength falls beyond the detection limit of Detector 1 and into the detection range of Detector 2. This behavior proves that the detected photons arise solely due to SHG within the co-crystal, suggestive of a noncentrosymmetric crystal structure. The same pattern was observed (Figure 2.7) with the two-photon confocal microscope in transmission mode, albeit with some crystal degradation due to the higher laser power necessary in transmission mode to detect second harmonic photons. This result limits the possibility of surface-mediated SHG, and corroborates the previous hypothesis of noncentrosymmetry in the bulk co-crystal $(\mathbf{1})_2\bullet\mathbf{2}$.

Nonlinear Optical Spectroscopy

To further elucidate noncentrosymmetry in co-crystal $(\mathbf{1})_2\bullet\mathbf{2}$, we measured the spectroscopic SHG of powdered crystals under ambient conditions at zero applied field. SHG signals were observed (Figure 2.8) for co-crystal $(\mathbf{1})_2\bullet\mathbf{2}$ at second harmonic wavelengths greater than 650 nm, corresponding to the optically transparent region of the co-crystal. This spectroscopic evidence of SHG, combined with the second harmonic images obtained by two-photon confocal microscopy, prove that the co-crystal does indeed have a noncentrosymmetric structure. It is important to note the difference in the detected second harmonic wavelengths using spectroscopic versus microscopic tech-

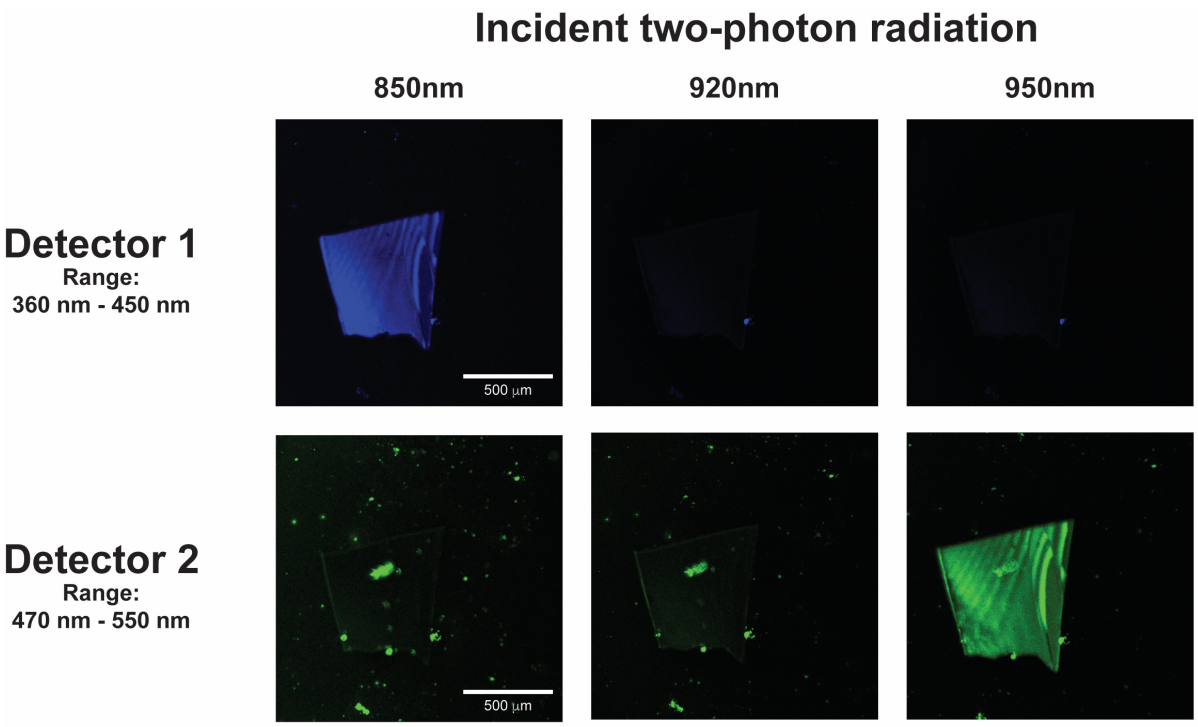

Figure 2.6: Two photon confocal microscopy of co-crystal $(\mathbf{1})_2 \bullet \mathbf{2}$, which can only be detected when the induced second harmonic response falls within the detector range. For example, incident two-photon radiation at 850nm induced a second harmonic response at 425nm, which can only be imaged by Detector 1. Tuning the incident radiation screens the detection of co-crystal $(\mathbf{1})_2 \bullet \mathbf{2}$ based on the wavelength of the second harmonic response.

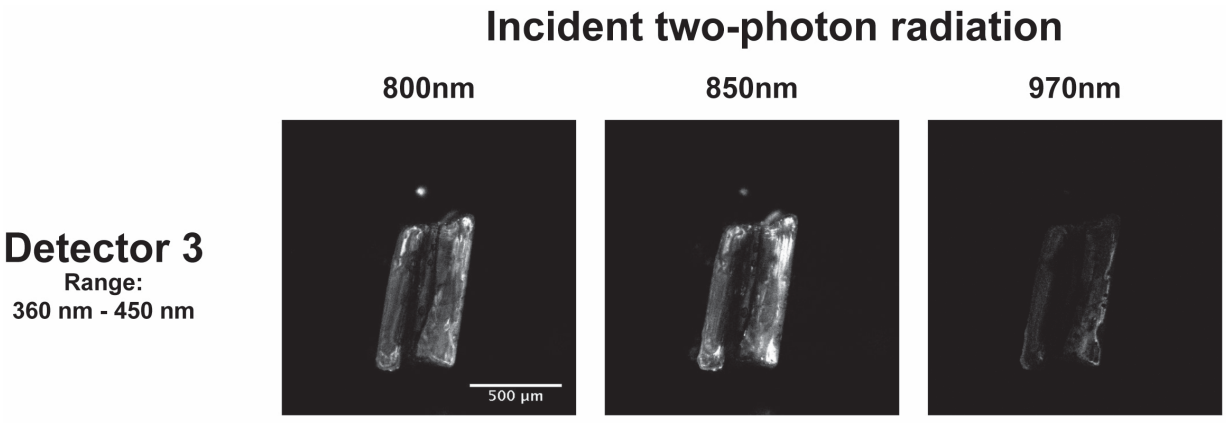

Figure 2.7: Two-photon confocal microscopy on single crystals of $(\mathbf{1})_2 \bullet \mathbf{2}$ in transmission mode.

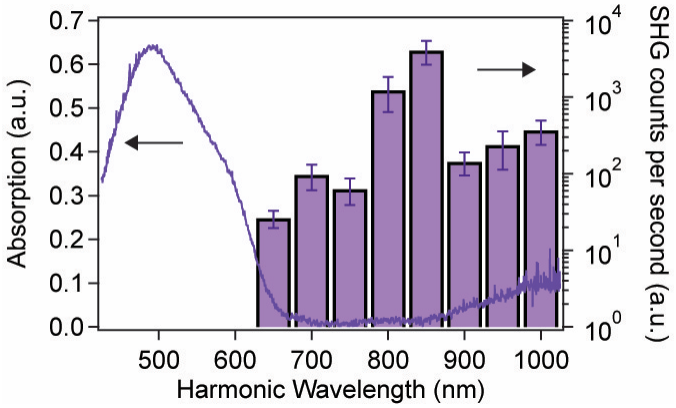

Figure 2.8: Spectroscopic second harmonic generation (right axis, bar plot) in relation to the optical absorption (left axis, line plot) of co-crystal $(\mathbf{1})_2\bullet\mathbf{2}$. The optical absorption spectrum is adapted from Blackburn et al.[103]

niques. Using spectroscopy, we only observed SHG at harmonic wavelengths longer than 650 nm, whereas we observed a second harmonic response at 425 nm when using two-photon microscopy. This disparity can be attributed to the absorption of second harmonic photons. Absorption is more important in the powder than in single crystals because the optical path length through the sample is longer in the spectroscopic than in the microscopic measurements. At shorter second harmonic wavelengths, the co-crystals absorb the emitted second harmonic photons, and therefore SHG signals cannot be detected. This feature, combined with the microscope's higher numerical aperture and the 106 faster repetition rate of the microscope laser over that of the laser used for SHG spectroscopy, makes two-photon microscopy, which sacrifices detection range, far more sensitive in detecting second harmonic photons than the laser set-up used for spectroscopic measurements. As a result, we were able to observe SHG using two-photon microscopy at wavelengths where the co-crystal absorbs a significant fraction of the emitted second harmonic photons.

We also compared (Figure 2.9) the second harmonic activity of co-crystal $(\mathbf{1})_2\bullet\mathbf{2}$ to a commercial $AgGaSe_2$ reference sample. The chalcopyrite $AgGaSe_2$ has been extensively studied[188] for its non-linear optical properties, and serves as a benchmark to compare the nonlinear optical properties of materials.[189] Co-crystal $(\mathbf{1})_2\bullet\mathbf{2}$ displays weaker second harmonic generation than $AgGaSe_2$

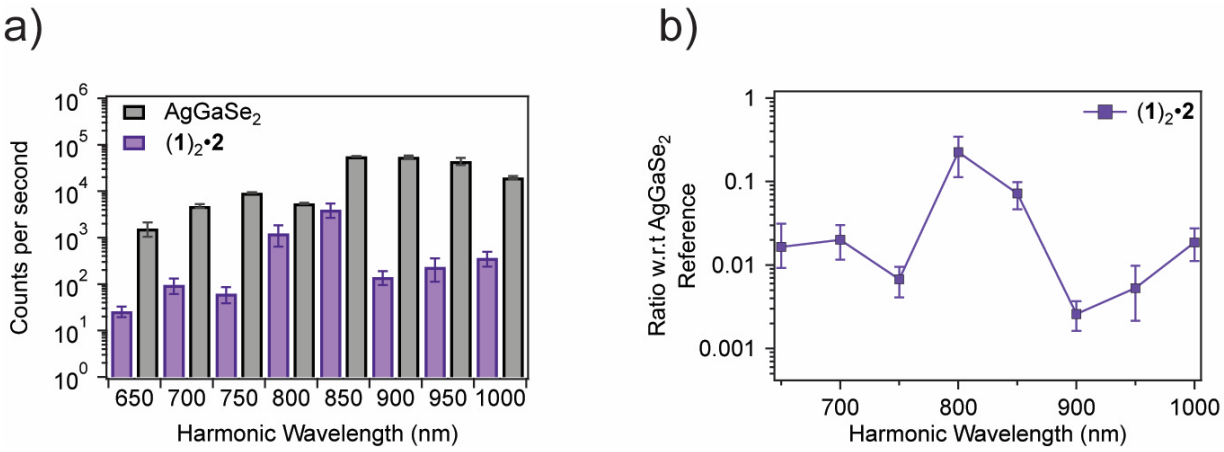

Figure 2.9: Comparative second harmonic generation intensities between $AgGaSe_2$ and co-crystal $(\mathbf{1})_2\bullet\mathbf{2}$. a) Side-by-side comparison. b) Co-crystal $(\mathbf{1})_2\bullet\mathbf{2}$ as a fraction of $AgGaSe_2$

at all harmonic wavelengths measured, suggesting that the organic co-crystal has weaker second harmonic generation efficiencies and smaller nonlinear susceptibility than the inorganic chalcopyrite reference. This difference could arise from higher second harmonic generation efficiencies in the inorganic chalcopyrite crystal compared to the organic co-crystal $(\mathbf{1})_2\bullet\mathbf{2}$. In addition, crystal degradation, as noted in the transmission-mode two-photon confocal microscopy experiments, could also reduce the second harmonic generation output of co-crystal $(\mathbf{1})_2\bullet\mathbf{2}$.

2.3.5 *Origin of Ferroelectric Polarization in CT Co-Crystal*

We suggest that there are three possible reasons for observing spontaneous ferroelectric polarization and SHG in the crystallographically centrosymmetric co-crystal $(\mathbf{1})_2\bullet\mathbf{2}$. Firstly, hydrogen bonding interactions play a significant role in the observed spontaneous polarization. The potentially symmetry-breaking hydrogen atoms cannot be located crystallographically, due to their weakly diffracting electron shells. Secondly, space group averaging of multiple noncentrosymmetric space groups across a crystal has been reported[190] to lead to a centrosymmetric refinement, but this possibility is unlikely given the quality of the X-ray diffraction data obtained. A third explanation for the origin of noncentrosymmetry in co-crystal $(\mathbf{1})_2\bullet\mathbf{2}$ could be a result of the asymmetry

in the π electron cloud distribution between the donor and acceptor molecules arising from intermolecular charge-transfer interactions.[191–193] In any case, it is clear that the molecular or atomic displacements that break the center of inversion have not been resolved using conventional X-ray crystallography.

Theoretical studies have attempted to predict the remnant polarization and phase transitions in LASO co-crystals. Chen et al.[194] combined density functional theory geometry optimization with polymorph predictors to predict the packing structure and spontaneous polarizations obtainable from LASO co-crystals consisting of tetrathiafulvalene donors and pyromellitic diimide-based acceptors. These authors correctly predicted the mixed stack packing arrangement of the LASO co-crystals,[103] and calculated spontaneous polarizations of up to 127 μC/cm^2. They attribute these high polarizations to the collective contributions of π-π stacking, charge-transfer and hydrogen bonding. A different computational study on the ferroelectricity of the LASO co-crystals was carried out by D'Avino et al.[195] using the Peierls-Hubbard model in addition to first-principles calculations. These authors compared the results from their theoretical study to the experimental evidence of ferroelectricity in both LASO as well as other charge-transfer ferroelectric co-crystals.[80,96] Their predictions differed considerably from the experimental data. We believe this difference could be a consequence of an incomplete analysis of the role of hydrogen bonding on the ferroelectric polarization in these charge-transfer complexes. Future theoretical work that takes into account all the noncovalent bonding interactions would help enumerate the origin and mechanism of room temperature ferroelectricity in these co-crystals.

2.4 CONCLUSION

We have described crystalline alternating stacks of acceptor and donor molecules that exhibit room temperature ferroelectric behavior along two nearly orthogonal crystallographic axes. We attribute this phenomenon to the combined effects of three-dimensional hydrogen-bonding networks

and charge-transfer along more than one axis. These supramolecular materials could offer platforms to design devices with high density and non-volatile information storage.

2.5 MATERIALS AND METHODS

Purification of Compounds

N,N′-Ethoxy(ethanol)-pyromellitic diimide (**1**) was synthesized following previously reported procedures. The solids obtained were dissolved in a minimum volume of hot THF and the solution was allowed to gradually cool back to RT under ambient conditions. After 6 h, filtration of the crystallization mixture yielded analytically pure **1** as a colorless crystalline powder. A second crop of large, colorless single crystals was obtained after the mother liquor was allowed to stand open to the atmosphere in the filtration flask for several days. Both crops were satisfactory for LASO co-crystallization.

5-Amino-1-naphthol (**2**, Aldrich, 97%) was dissolved in a minimum volume of hot ethanol and the solution was allowed to gradually cool back to RT under ambient conditions to yield a dark purple solution. The flask containing this solution was placed in a – 20 °C fridge overnight to initiate crystallization. Cold filtration of this mixture yielded analytically pure 5-amino-1-naphthol as a dark crystalline powder.

Crystallization

Recrystallized 5-amino-1-naphthol (13 mg 82 μmol) was dissolved in a 20-mL scintillation vial containing 11 mL of a 10:1 mixture of 1,2-dichloroethane (Aldrich) and diethyl ether (Aldrich). Subsequently, **1** (17 mg, 43 μmol) was added to the solution and the mixture was sonicated at 45 °C to fully solubilize **1**. Once this solution was cooled to room temperature, it was passed through a 0.45 μm PTFE syringe filter (Pall Corporation) into a 16×150mm borosilicate test tube (VWR) that was washed with Me_2CO and dried in a glassware drying oven for 3 days prior to use. Subsequently, 10

mL of 1-chlorobutane (Aldrich) was slowly passed through a fresh 0.45 μm PTFE syringe filter (Pall Corporation) and layered very carefully on top of the 1,2-dichloroethane mixture. The tube was capped with a rubber septum and allowed to crystallize for 3 d to yield dark purple plate-like crystals that can be several centimeters long and several millimeters wide. The crystals were collected by filtration and washed with n-hexane or hexanes prior to being stored in glass vials.

A detailed list of observations made during the optimization of the crystallization of $(\mathbf{1})_2\bullet\mathbf{2}$ follows:

1. The use of strictly anhydrous solvent is not vital to obtaining high quality single crystals. However, the crystals that were evaluated in this report were all prepared using anhydrous solvents from Aldrich Sure-Seal bottles.

2. If non-recrystallized batches of **1** or **2** are utilized, a portion of the solids remain insoluble in 1,2-dichloroethane even after extended heating and sonication. While these solids can be removed during the syringe filtration steps, crystallization using solutions made from unpurified starting materials only yield a microcrystalline powder that sometimes crashes out of solution even before the layering of 1-chlorobutane.

3. It is not required to wait for the 1,2-dichloroethane solution to reach room temperature prior to filtration and layering of 1-chlorobutane. However, if the solutions are too warm then diffusion between the solvent layers occurs more rapidly, leading to faster nucleation.

4. It is crucial to conduct the layering in a slow and controlled manner. It was found that flowing the 1-chlorobutane down the side of the test tube slowly could minimize the mixing between solvent layers. Excessive turbulence during the layering process leads to fast nucleation and precipitation of a microcrystalline powder.

5. Crystallization often begins immediately, with thin plates being observed between 5 min and 4 hours after the initial layering. Crystals will become thicker and more robust if they are given at least 3 days to grow.

6. Exposure to light during the crystallization process does not appear to adversely affect crystal growth. Typically, the crystals were left to grow in a cabinet or covered by aluminum foil.

7. A gentle stream of n-hexane or hexanes from a squirt bottle can be used to dislodge crystals that are adhered to the test tube surface.

8. Crystals that have been stored for 2 or 3 years in 20-mL glass vials or plastic petri dishes without any protective blanket of inert gas have similar device characteristics as crystals that were freshly grown.

9. Crystals of $(\mathbf{1})_2 \bullet \mathbf{2}$ tend to display a preferred growth axis in the [100] direction.

X-Ray Crystallography

X-Ray diffraction data were obtained on Bruker Platform and Kappa diffractometers, equipped with a MoKα or CuKα sealed-tubesource and an APEX II CCD detector. Intensity data were collected using ω and φ scans spanning at least a hemisphere of reciprocal space for all structures (data were integrated using SAINT). Absorption effects were corrected on the basis of multiple equivalent reflections (SADABS). Structures were solved by direct methods (SHELXS[196]) and refined by full-matrix least-squares against F2 (SHELXL[196]). The structures were solved and refined using Olex2. Hydrogen atoms were assigned using riding isotropic displacement parameters and constrained to idealized geometries, including those bound to oxygen, as no hydrogen atoms could be located in the difference Fourier map.

Two-Photon Confocal Microscopy

Two-photon confocal microscopy images were obtained using a Nikon A1R MP+ Multiphoton Confocal Microscope, equipped with a Coherent Ti:Sapphire Chameleon Vision S Laser, mode locked at 80 MHz with a 75 fs pulse duration. The incident laser wavelength was tunable from 690 nm to 1040 nm. Reflected and transmitted photons were detected by detectors above and below

the sample plane, with detection windows from 380 nm to 450 nm and 470 nm and 500 nm. The irradiation power across all incident wavelengths was set at 800 mW. Single crystals of $(\mathbf{1})_2\bullet\mathbf{2}$ were sandwiched between a glass microscope slide and cover slip, to separate the crystals from the water immersion microscope objective lens. All samples were irradiated in the dark at room temperature under ambient conditions.

Non-Linear Optical Measurements

We performed spectroscopic second harmonic generation measurements[133] using a Nd:YAG laser pulsed at 10 Hz with a (54 ± 5) ps pulse duration. This irradiation frequency was tripled (355 nm) and was used to pump a homemade optical parametric amplifier (OPA). A filter passing the longer wavelength was used to remove the signal beam, and the idler beam was focused onto the samples with a 100 mm focal length N-BK7 lens with a spot size of order 1 mm. In order to check the SHG efficiency as a function of the excitation energy, we tuned the wavelengths of the idler light from 1100 to 2000 nm. In this range, the spectral bandwidth of the linearly polarized light from the OPA is rather broad, about 2 meV full width at half-maximum. The SHG signal was collected off axis and focused onto a fiber optic bundle. The output of the fiber optic bundle coupled to the entrance slit of an Andor 300i spectrometer and detected using a DU420-BX2-DD CCD camera. The data collection time was 10 seconds.

As-grown crystals of $(\mathbf{1})_2\bullet\mathbf{2}$ were crushed and sieved to achieve a size distribution of less than 63 μm. Material was placed into borosilicate capillary tubes (1.5–1.8 mm × 90 mm) and measured at ambient conditions in the dark.

Polarization and Dielectric Measurements

Temperature-dependent dielectric constant and ferroelectric hysteresis measurements were performed on single co-crystals of $(\mathbf{1})_2\bullet\mathbf{2}$. Gold paste (Ted Pella) electrodes were applied to each co-crystal along either the [100] or [010] axis. Gold wires (12.5 μm diameter) were fixed to the two gold

paste contacts and then connected to the ferroelectric tester. All measurements were performed in a He atmosphere within a temperature controlled Physical Properties Measurement System (PPMS 6000, QuantumDesign).

The dielectric constant was measured using an Agilent E4980A from 8 to 400 K at 2 V at frequencies of 1, 5, or 10 kHz. All ferroelectric measurements were performed with a Radiant Technologies Precision LC, coupled to a Trek Inc. 609A high voltage amplifier.

3 Expanding the Library of LASO Ferroelectric Materials: Co-Crystals with a Series of 1,5-Difunctionalized Naphthalenes

3.1 Objectives and Significance

The ability to influence macro-scale properties of materials by tuning chemical functionality at an atomic scale has always been the hallmark of materials science. Through years of trial and error, we previously established a design motif (termed Lock Arm Supramolecular Ordering, or LASO) for the development of robust and solvent-free charge transfer co-crystals that are stabilized by electron transfer between complementary aromatic electron donor and electron acceptor molecules, hydrogen bonding, solvophobic and van der Waals interactions. These co-crystals, displaying either a 1:1 or 1:2 alternating stack of donor and acceptor molecules, have displayed room-temperature ferroelectric behavior along one or two axes due to symmetry-breaking dimerization of the aromatic donor/acceptor pairs. An understanding, however, of the specific structure-property relationships for LASO co-crystals has been limited, due to the esoteric physics behind organic ferroelectric polarization. Studies that attempt to systematically uncover design rules that govern ferroelectricity in these complex materials will, as a result, be highly beneficial towards progress in this field. Not only will it lead to a better understanding of how to harness and manipulate the molecular chemistry to achieve supramolecular function, it will expand the library of organic ferroelectric materials with broad translational possibilities.

3.2 Background

In the drive to move away from toxic ferroelectric[115,130,131,160] materials, organic ferroelectrics[78,83,122] have gained interest for their low cost, light weight, and tunability. Within the class of organic ferroelectrics, intermolecular charge transfer complexes,[43] in which a π-electron donor

(D) on one molecule transfers some of its charge to a π-electron acceptor (A) on another molecule, have been garnered interest for their synthetic and functional modularity.[78,120] Specifically, the assembly of these complementary molecules in a mixed-stack arrangement, where each electron donor and acceptor molecule assemble in an alternating, face-to-face arrangement, have been shown to dimerize upon a neutral-to-ionic (NIT) transition ($D^0\ A^0\ D^0\ A^0 \rightarrow D^{\delta+}\ A^{\delta-}\ D^{\delta+}\ A^{\delta-}$), resulting in a net electrical dipole that is additive to a macroscopic polarization along the stacking direction.[80,96,97,100] Switching this polarization using an external electric field defines the ferroelectric properties that are unique to these mixed-stack CT complexes.[78,83] More recently, it was reported that room-temperature ferroelectricity could be observed in a number of charge-transfer (CT) co-crystals as a consequence of either one[79] or two[197] directions and charge transfer and crystal growth. These co-crystals were designed based on the design principles of lock-arm supramolecular ordering (LASO),[103] where complementary donor and acceptor molecules are functionalized with flexible hydrogen bonding 'arms' to stabilize the formation of a mixed stack assembly. It is hypothesized that the intermolecular CT and hydrogen-bonding interactions synergistically stabilize the solvent-free crystal growth, as well as the ferroelectric polarization of the co-crystals.

This chapter presents a systematic study of the interplay between molecular chemistry and supramolecular structure and electronic properties in LASO co-crystals. However in contrast to the original series of LASO ferroelectric co-crystals,[79] the electron donor molecules (Figure 3.1) are functionalized with the flexible diethylene glycol 'arms', with the complementary hydrogen-bonding 'short arms' located on the electron acceptor. It must be noted that while traditional LASO co-crystals had to be grown in freshly dried, strictly anhydrous solvents in order to produce high quality single crystalline materials, the co-crystals grown in this work could be crystallized from *aqueous* dimethylformamide (DMF), significantly improving the ease at which co-crystals can be grown and translational devices fabricated using this molecular design. It was envisioned that systematically changing the electron donor core from 1,5-diaminonaphthalene (**2**) to 1-amino-5-naphthol (**3**) or

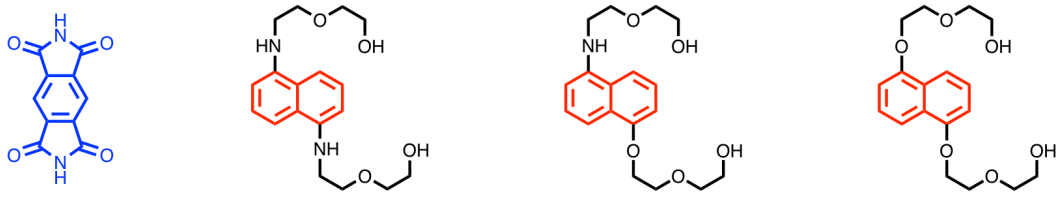

Figure 3.1: Structural formulae of pyromellitic diimide acceptor **1** as well as series of 1,5-difunctionalized naphthalene donors functionalized with diethylene glycol 'arms': 1,5-diaminonaphthalene (**2**), 1-amino-5-naphthol (**3**) and 1,5-dioxynaphthalene (**4**)

1,5-dioxynaphthalene (**4**) in turn changes the extent of CT interactions in a co-crystal with pyromellitic diimide (**1**) as a consequence of varying the electron donating capacity of the donor molecules. This in turn would influence the supramolecular packing arrangement and electronic properties of the binary (as well as ternary) donor/acceptor co-assemblies, aspects that this chapter will explore in great detail.

3.3 RESULTS AND DISCUSSION

3.3.1 *Binary and Ternary Co-Crystallization*

The pyromellitic diimide acceptor **1** co-crystallized readily with donor naphthalene derivated **2**,**3** and **4** (Figure 3.1) to yield co-crystals **1**•**2**, **1**•**3** and **1**•**4**. **1**•**3** crystallizes (Figure 3.2) in same $P2_1/c$ space group, with similar unit cell parameters as that reported[103] on the co-crystals, with the only exception that the oxygen and nitrogen atoms in the asymmetric donor **3** are disordered over the two crystallographic sites equally. Specifically, the electron donor and acceptor molecules are arranged in a periodic alignment with alternating donor and acceptor molecules along the direction of the face-to-face aromatic stacking and charge transfer. In addition, hydrogen bonding between the terminal hydroxyl (OH) groups on the flexible diethylene glycol 'arms' on the donor molecules

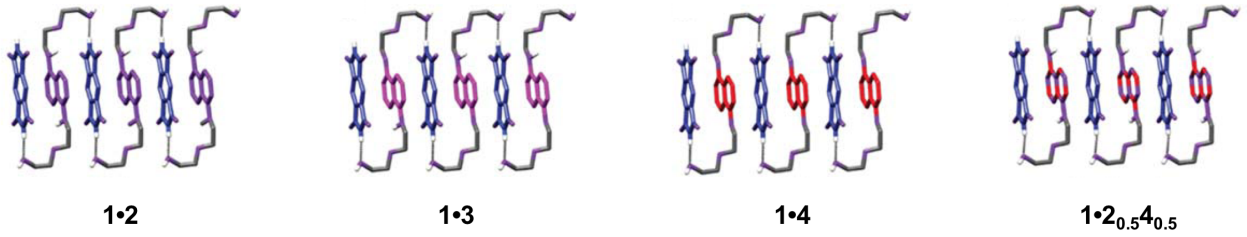

Figure 3.2: Crystal superstructures of isostructural co-crystals **1•2**,**1•3**, **1•3** and **1•2**$_{0.5}$**4**$_{0.5}$. In co-crystal **1•3**, the N and O atoms in **3** are disordered over their two respective sites equally. The heteroatoms that participate in noncovalent bonding interactions are identified in purple and the interstack hydrogen bonds between atoms are depicted as black lines.

and the secondary amine (NH) of the pyromellitic diimide acceptor further stabilizes the long-range stacking order of the resulting co-crystal.

In comparison to the binary co-crystals above, ternary co-crystals were also prepared by crystallizing mixtures of electron donors **2** and **4** with acceptor **1**. Crystallizations were prepared varying the mole fraction (x) of **4** from zero (binary co-crystals **1•2**) to one (binary co-crystal **1•4**), yielding needle-like crystals (Figure 3.3)for all ternary co-assemblies. A comparative nuclear magnetic resonance (NMR) spectroscopic study of the crystallization solutions with the co-crystals dissolved in deuterated dimethyl sulfoxide (DMSO-d_6) was performed to understand the influence of the composition of the crystallization solution on the structure of grown crystals. Integrating the relevant proton signals from **2** and **4** revealed (Figure 3.4a) a linear 1:1 relationship between the crystallization solution and the grown co-crystals, indicating that the composition of the solution has a direct and proportional effect on the structure of the grown ternary co-crystal.

X-ray diffraction of the single crystals of **1•2**$_{1-x}$**4**$_x$ reveals (see Section 3.5 for details) that all the ternary crystals are isostructural to their binary ($x = 0$ or $x = 1$) counterparts, with near-identical unit cell parameters. X-ray diffraction further suggests that the compounds **2** and **4** are disordered randomly throughout the ternary crystals. The only observable difference in crystal structure manifested itself in the β angle of the unit cells (Figure 3.4b). As the mole fraction of **4** in the ternary co-crystal increases, the β angle decreases from 106.2° in binary **1•2** to 104.6° in **1•4**.

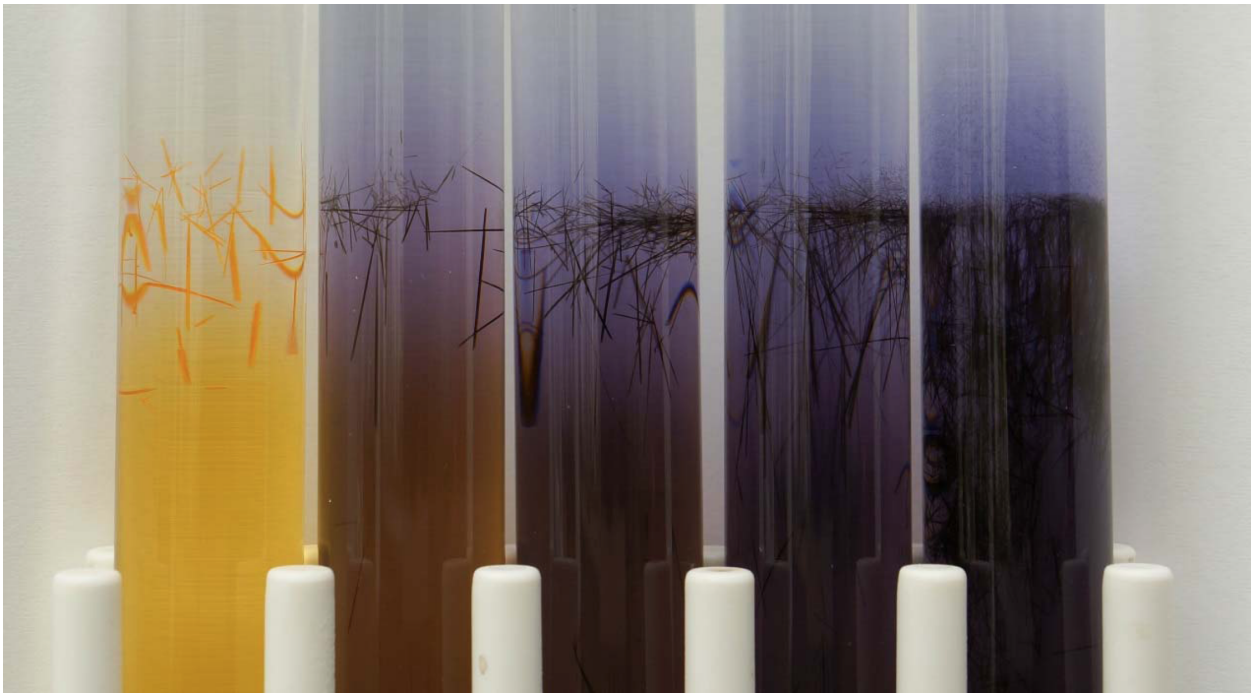

Figure 3.3: A photograph of ternary LASO co-crystals $\mathbf{1}\bullet\mathbf{2}_{1-x}\mathbf{4}_x$. (Left to Right) Photographs, taken after five days of crystallization, of ternary solutions where $x = 1, 0.75, 0.5, 0.25, 0$, respectively.

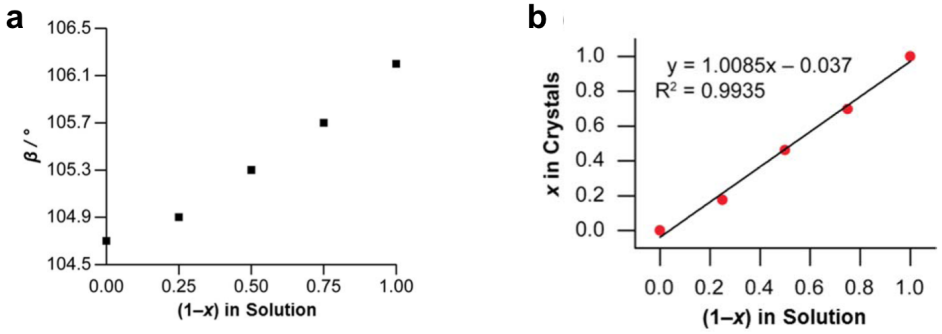

Figure 3.4: (a) A comparison of mole fraction (x) of **4** between crystallization solutions and single crystal diffraction of $\mathbf{1{\bullet}2}_{1-x}\mathbf{4}_x$. The ratios of the two naphthalene derivates in solution are determined by integration of the corresponding proton signals, which reveal a linear relationship between the ratio of **2** and **4** in crystallization solutions and in LASO co-crystals. (b) The β angle in the ternary co-crystal unit cell varies linearly with x, indicative of solution solution mixing.

These differences are likely attributed to the differing splay angles at the point of attachment between the glycol linker and the donor naphthalene core. That both NMR and X-ray show a continuous linear transition in the composition of the ternary co-crystal $\mathbf{1{\bullet}2}_{1-x}\mathbf{4}_x$ as a function of x is further proof of non-interacting, randomized solid solution of the donors **2** and **4** upon co-assembly and co-crystallization with acceptor **1**. Interestingly, the β angle for the ternary co-crystal $\mathbf{1{\bullet}2}_{0.5}\mathbf{4}_{0.5}$ (Figure 3.2) ($\beta = 105.3°$) is nearly identical to that found in asymmetric donor co-crystal **1•3** ($\beta = 105.2°$), despite the obvious chemical structural differences in the donor molecules, therein motiving further studies on the structure-property relationships in these isostructural but chemically dissimilar LASO co-crystals.

3.3.2 *Polarized Absorption Spectroscopy*

Polarized absorption spectroscopy has been employed to validate the direction of charge transfer absorption along the longest dimension of the physical needle-like LASO co-crystal.[79,103] In similar fashion, polarized UV-Vis spectroscopy was employed (Figure 3.5) to confirm the CT anisotropy in LASO co-crystals presented in this chapter. Maximum absorption was observed when the polar-

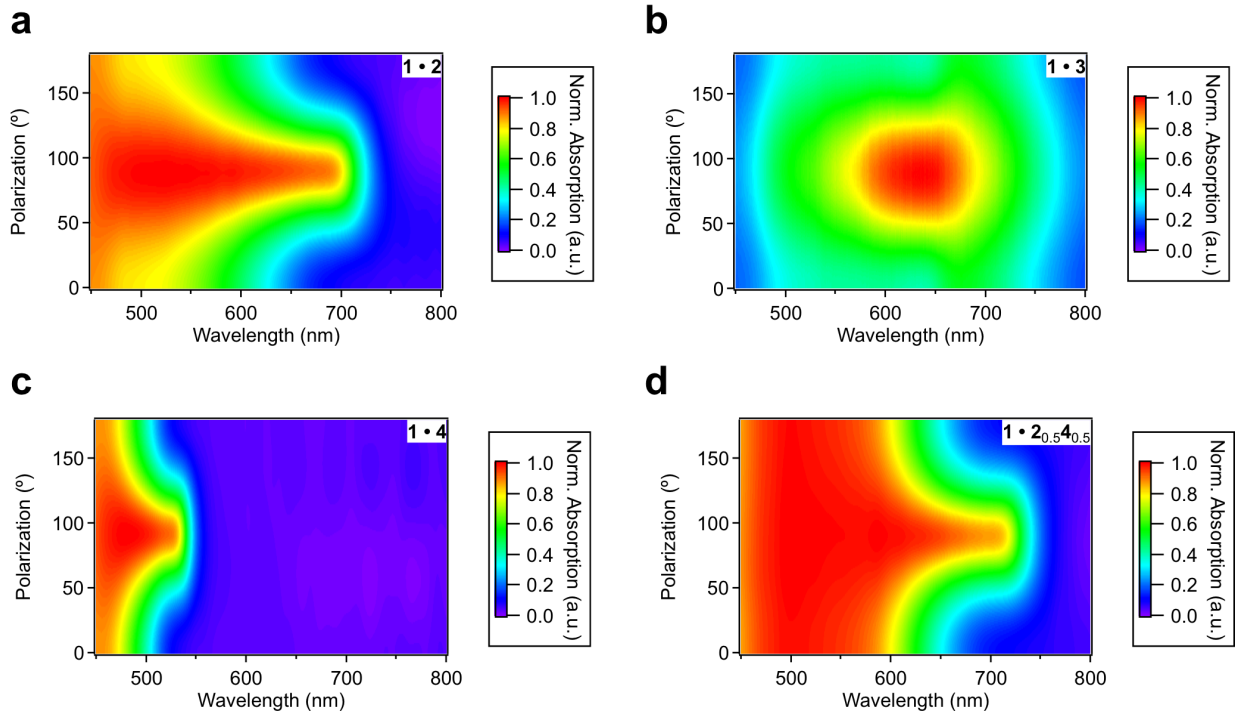

Figure 3.5: Polarized UV-Vis spectra of binary co-crystals (a) **1•2**, (b) **1•3**, (c) **1•4**, and ternary co-crystal (d) **1•2**$_{0.5}$**4**$_{0.5}$. Maximum absorption occurs when the incident light is polarized along the long dimension of the co-crystal, which corresponds to the direction of charge transfer along the mixed stack assembly of donor and acceptor molecules.

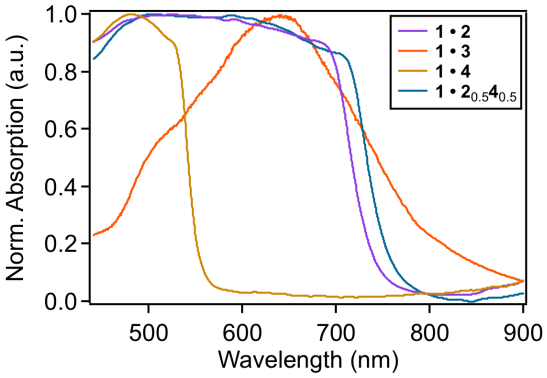

Figure 3.6: Normalized absorption bands, taken from the indicent light polarization at which maximum absorption is observed, of binary co-crystals **1•2**, **1•3** and **1•4** and ternary LASO co-crystal $\mathbf{1{\bullet}2}_{0.5}\mathbf{4}_{0.5}$. Changing the functionality of the naphthalene donor from amine to alkoxy groups results in a blue shift of the maximum absorption peak or band in the binary co-crystal system, indicative of less charge transfer interactions between the donor and pyromellitic diimide acceptor molecules. The absorption band of ternary co-crystal $\mathbf{1{\bullet}2}_{0.5}\mathbf{4}_{0.5}$ is a linear combination of that of **1•2** and **1•4**, with the absorption of **1•2** dominating the shape of the spectrum.

ization the incident light was parallel to the long dimension of the co-crystal, whereas minimum absorption was observed when the polarization was perpendicular. Since the wavelength of CT absorbance is a metric for the extent of charge transfer interactions and resonance stabilization (Section 1.2) the differences observed in the absorption profiles (along the long dimension of the crystals) provide some insight as to the influence of chemical modifications to the naphthalene electron donor on the degree and stability of CT interactions with the pyromellitic diimide electron acceptor. Specifically, co-crystal **1•2** exhibits (Figure 2.6) a saturated absorption band that drops off beyond 700 nm, while **1•3** and **1•4** exhibits bands that center at 650 nm and 490 nm respectively. This difference can be attributed to the changes in electron density in the naphthalene donor as a result of amine or alkoxy functionalization. Since amine groups are known to have a stronger electron donating capacity than alkoxy groups,[198] it is unsurprising that functionalizing the donor with more amine groups (as in **2** and **3**) results in more stable charge transfer interactions, and a red-shifted absorption band. Interestingly, the absorption spectrum of the ternary co-crystal $\mathbf{1{\bullet}2}_{0.5}\mathbf{4}_{0.5}$

(Figure 3.5c) appears as a linear summation of that of **1•2** and **1•4**, proof of non-interaction randomized CT domains of **1•2** and **1•4** in the ternary co-crystal.

3.3.3 *Variable-Temperature Dielectric Spectroscopy*

Given the precedence for ferroelectric behavior in LASO co-crystals,[78,79,197] variable temperature dielectric spectroscopy was adopted to elucidate the presence of a ferroelectric Curie temperature (T_c) in these LASO binary and ternary co-crystals. In all cases (Figure 3.7), the dielectric constant does not display the characteristic discontinuity indicative of a second-order ferroelectric phase transition. The observation suggests that T_c for all the binary and ternary co-crystals lie outside the range of measurement, and instead close to the decomposition temperature of the crystals. This result is hardly surprising, as previous LASO co-crystals[79,197] have also failed to display a phase transition up to 400 K, despite ferroelectric polarization at room and cryogenic temperatures. This trend can be attributed to the combination of strong CT interactions between aromatic electron donor and acceptor molecules, as well as stabilizing hydrogen bonding from the diethylene glycol 'arms' functionalized to the electron donors.

3.3.4 *Room-Tempearture Ferroelectric Polarization*

Polarization hysteresis loops were obtained (Figure 2.8) for co-crystals **1•2**, **1•3** and **1•4** by applying a large AC electric field ($f = 0.1Hz$) along the long dimension of the crystals, which correspond to the direction of charge transfer. Ferroelectric behavior was observed for co-crystal **1•2**, with a near-saturation remnant polarization (P_r) of 5.1 $\mu C/cm^2$ and a coercive field (E_c) of 6.4 kV/cm. On the other hand, the polarization-hysteresis loop for co-crystal **1•4** cannot be attributed to ferroelectric behavior, and is instead indicative of a canonical lossy dielectric material.[132] Such a large change in electronic behavior between the isostructural co-crystals **1•2** and **1•4** can only be attributed to the differing degrees of charge transfer as a result of the change in donor functionalization. Increasing the electron density of the donor naphthalene molecule, and as a result the

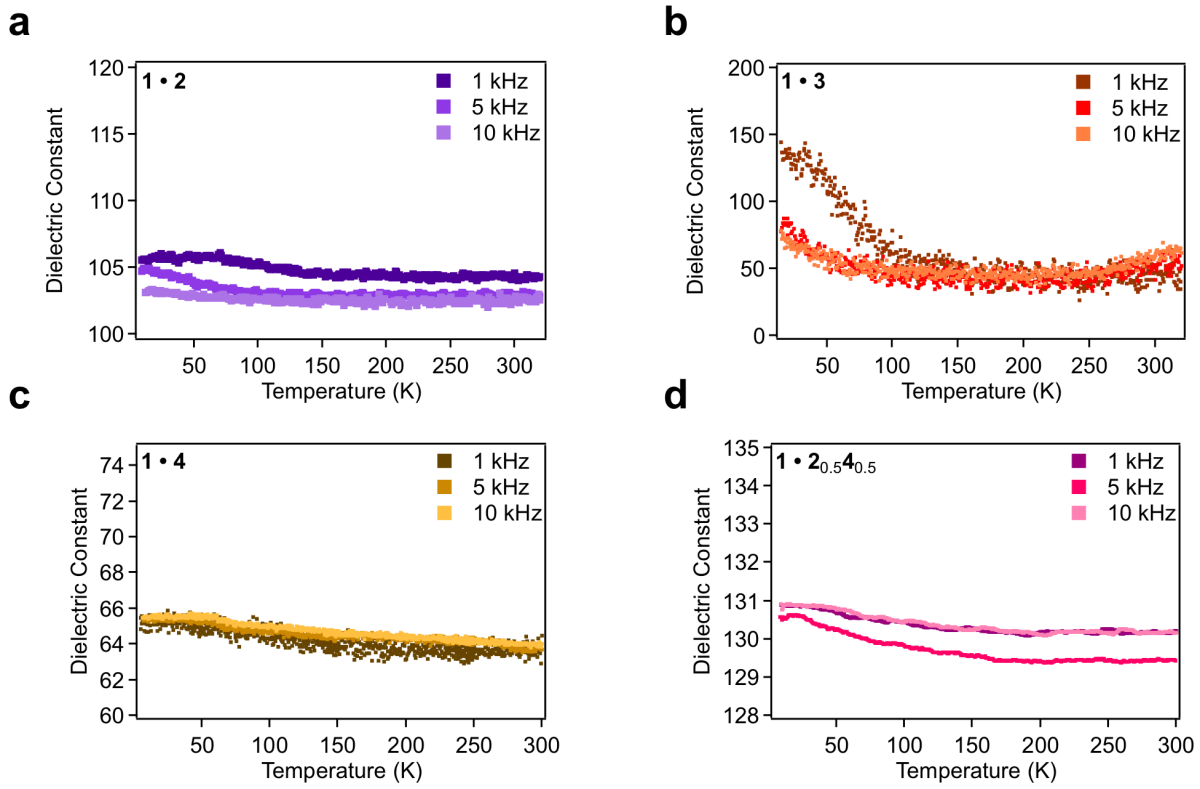

Figure 3.7: Variable-temperature dielectric spectroscopy of binary co-crystal (a) **1•2**, (b) **1•3**, (c) **1•4**, and ternary co-crystal (d) **1•2**$_{0.5}$**4**$_{0.5}$. The lack of a frequency-independent dielectric discontinuity suggests that the LASO co-crystals do not display a ferroelectric-paraelectric Curie transition at temperatures up to 400 K.

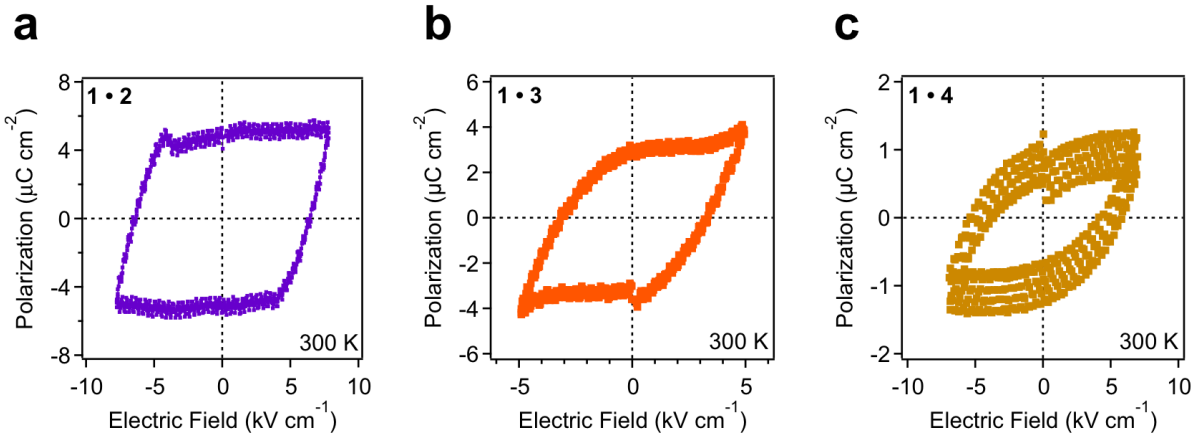

Figure 3.8: Room-temperature polarization hysteresis of binary co-crystal (a) **1•2**, (b) **1•3** and (c) **1•4**. While co-crystal **1•2** exhibits a polarization hysteresis loop indicative of ferroelectric behavior, co-crystal **1•4** exhibits classic lossy dielectric behavior, with co-crystal **1•3** exhibiting components of both ferroelectric and lossy dielectric behavior. The loss of ferroelectric character upon changing the donor in the LASO CT complex from **2** to **4** can be attributed to the reduction in electron donor strength, highlighting the use of molecular chemistry to modulate supramolecular ferroelectricity.

degree of charge transfer, through amine functionalization shifts the resulting co-crystal from lossy paraelectric dielectric to ferroelectric. This hypothesis is further validated when considering the polarization hysteresis loop of **1•3**, which displays a combination of ferroelectric and lossy paraelectric character.

3.3.5 *Two-photon Confocal Microscopy*

To further understand the interplay between the chemical structure and ferroelectric polarization of the LASO co-crystals reported here, two photon confocal microscopy was used. As reported previously,[197] two photon confocal microscopy can be used to determine second harmonic activity and noncentrosymmetry in organic co-crystals. It has been established (Section 1.4.1) that the lack of an inversion center results in the frequency doubling (wavelength halving) of incident two-photon radiation. In the context of two-photon confocal microscopy, this second harmonic generation can be detected by the observation of materials in a detector whose range falls within the gen-

erated second harmonic wavelength. The benefit, specifically of two-photon confocal microscopy, lies in its provision of three-dimensional optical scanning without photobleaching or sample degradation above and below the focal plane. In this study, **1•2** (Figure 3.9, 3.10) and **1•3** (Figure 3.11) exhibited a second harmonic response under ambient conditions at zero applied field. This is characterized by the ability to 'see' the co-crystal by the detector whose range lies within half the incident multiphoton wavelength (indicative of second harmonic generation). To delineate this observation from possible photoexcitation processes, the excitation wavelength was changed, and the detection of the co-crystals switches from Detector 1 to Detector 2 as the second harmonic wavelength falls beyond the detection limit of Detector 1 and into that of Detector 2. This suggest that co-crystals **1•2** and **1•3** lack a center of inversion as a consequence of second harmonic activity. A similar observation, however, was not observed (Figure 3.12) for co-crystal **1•4**, where no second harmonic activity was observed. This in turn suggests that co-crystal **1•4** does not lack a center of inversion. The possibility of surface-related symmetry-breaking or second harmonic activity (or lack thereof) was eliminated by collecting z-stack images (Figure 3.13) of the second harmonic photons emitted by co-crystals **1•2** and **1•3**. This indicates second harmonic activity, and by association noncentrosymmetry, is a property of the bulk co-crystals, and not a surface-related effect. No z-stack was collected for **1•4** since the co-crystal did not emit any second harmonic photons on account for its lack of inversion symmetry.

3.3.6 *Correlating Molecular Chemistry to Supramolecular Ferroelectricity*

That the structurally centrosymmetric co-crystals display second harmonic activity is not new,[197] and could be due to a number of reasons. First, hydrogen bonding interactions, which play a significant role in the observed ferroelectric polarization, may not be accurately located crystallographically, due to their weakly diffracting electron shells. Second, space group averaging[182,190] of multiple noncentrosmmetric space groups leads to a crystallographic refinement. Lastly, asymmetry in the π electron cloud distribution between the donor and acceptor molecules could

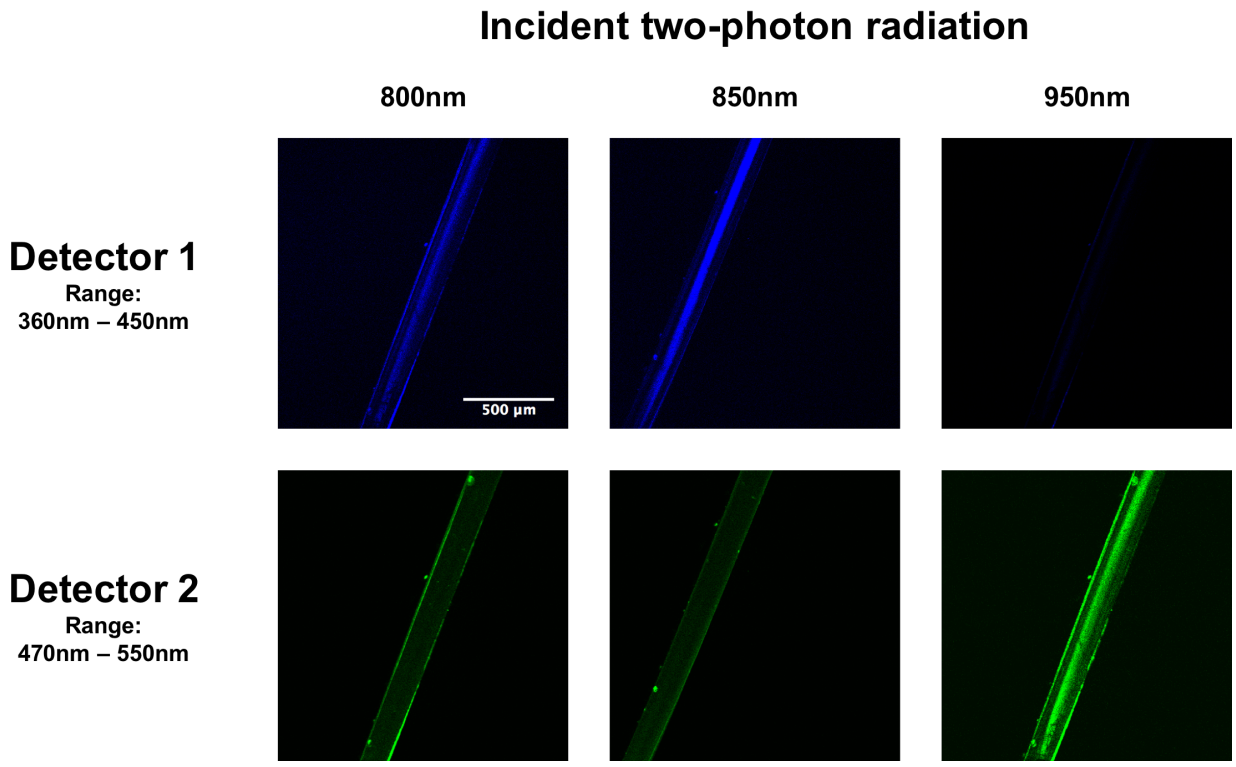

Figure 3.9: Two-photon confocal microscopy on co-crystal **1•2**. The crystal can only be detected when the induced second harmonic response falls within the detector range. For example, incident two-photon radiation at 850nm induced a second harmonic response at 425nm, which can only be imaged by Detector 1. Tuning the incident radiation screens the detection of co-crystal **1•2** based on the wavelength of the second harmonic response. An autofluorescence response can also be detected in Dectector 2 at wavelengths where the second harmonic response is picked up by Detector 1.

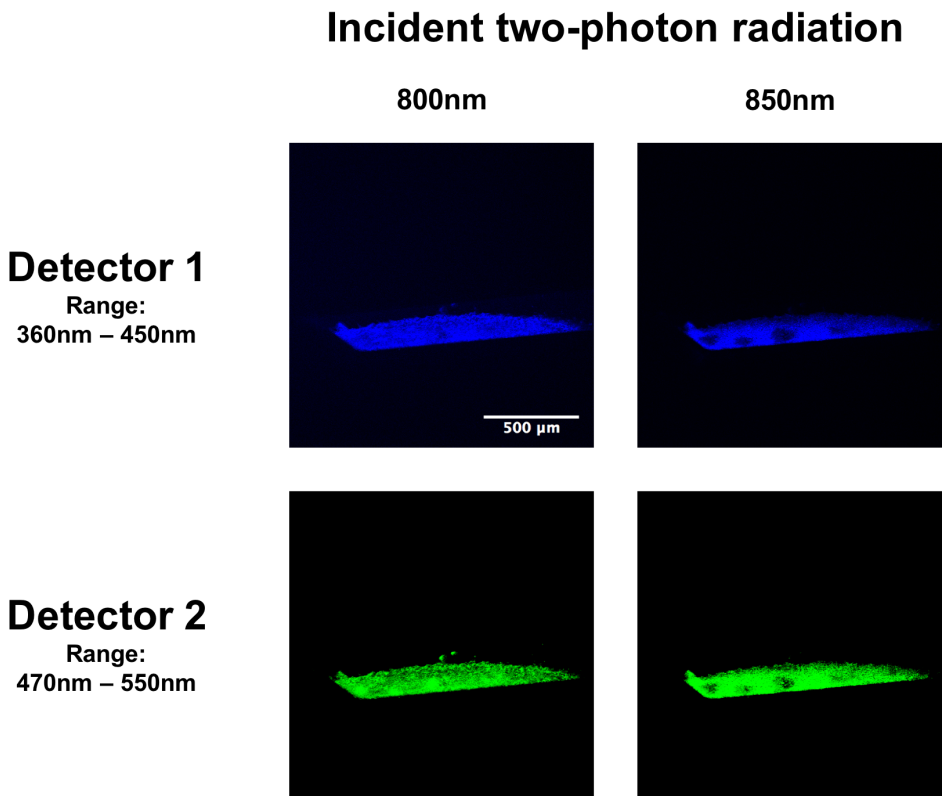

Figure 3.10: Additional two-photon confocal microscopy on co-crystal **1•2**. The same principles of crystal detection apply here. For example, incident two-photon radiation at 850nm induced a second harmonic response at 425nm, which can only be imaged by Detector 1. In addition, photodegredation of the crystal can be observed at incident wavelengths of 850nm (dark spots on the image) due to high laser power required to observe second harmonic effects. An autofluorescence response can also be detected in Dectector 2 at wavelengths where the second harmonic response is picked up by Detector 1.

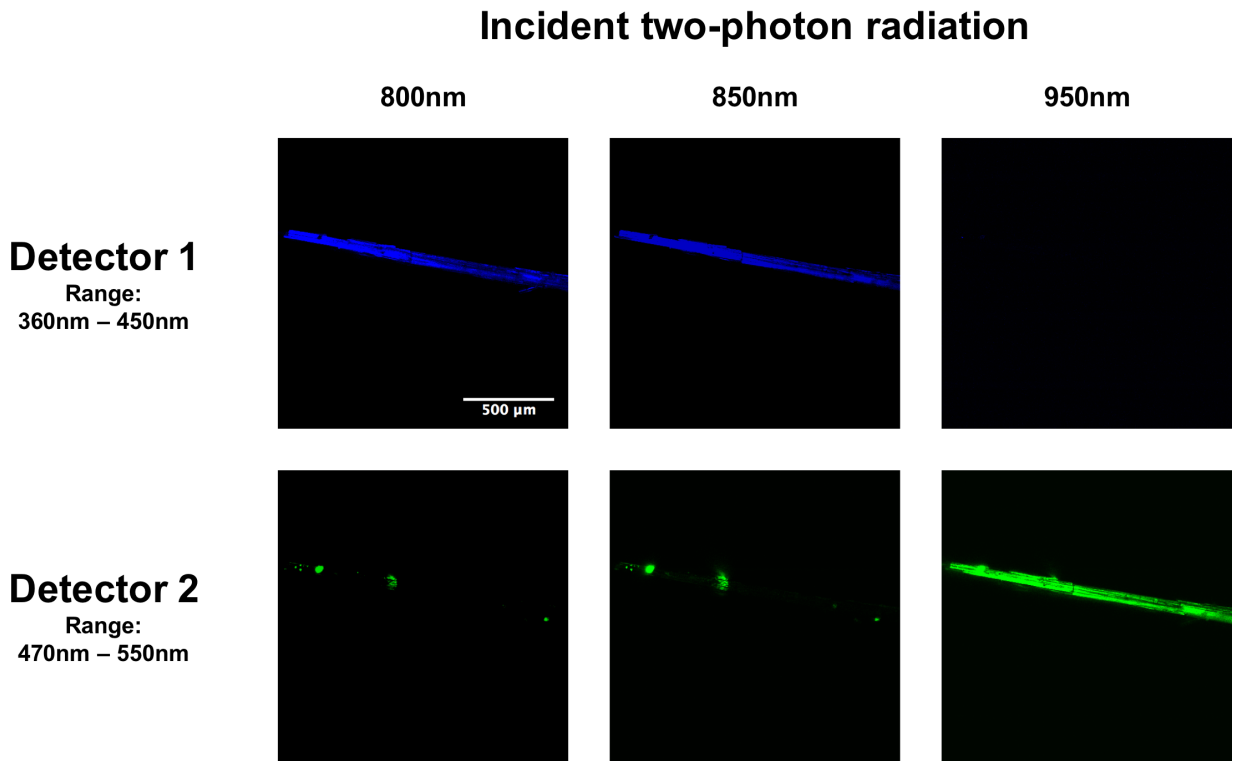

Figure 3.11: Two-photon confocal microscopy on co-crystal **1•3**. The crystal can only be detected when the induced second harmonic response falls within the detector range. For example, incident two-photon radiation at 850nm induced a second harmonic response at 425nm, which can only be imaged by Detector 1. Tuning the incident radiation screens the detection of co-crystal **1•3** based on the wavelength of the second harmonic response. An autofluorescence response can also be detected in Dectector 2 at wavelengths where the second harmonic response is picked up by Detector 1.

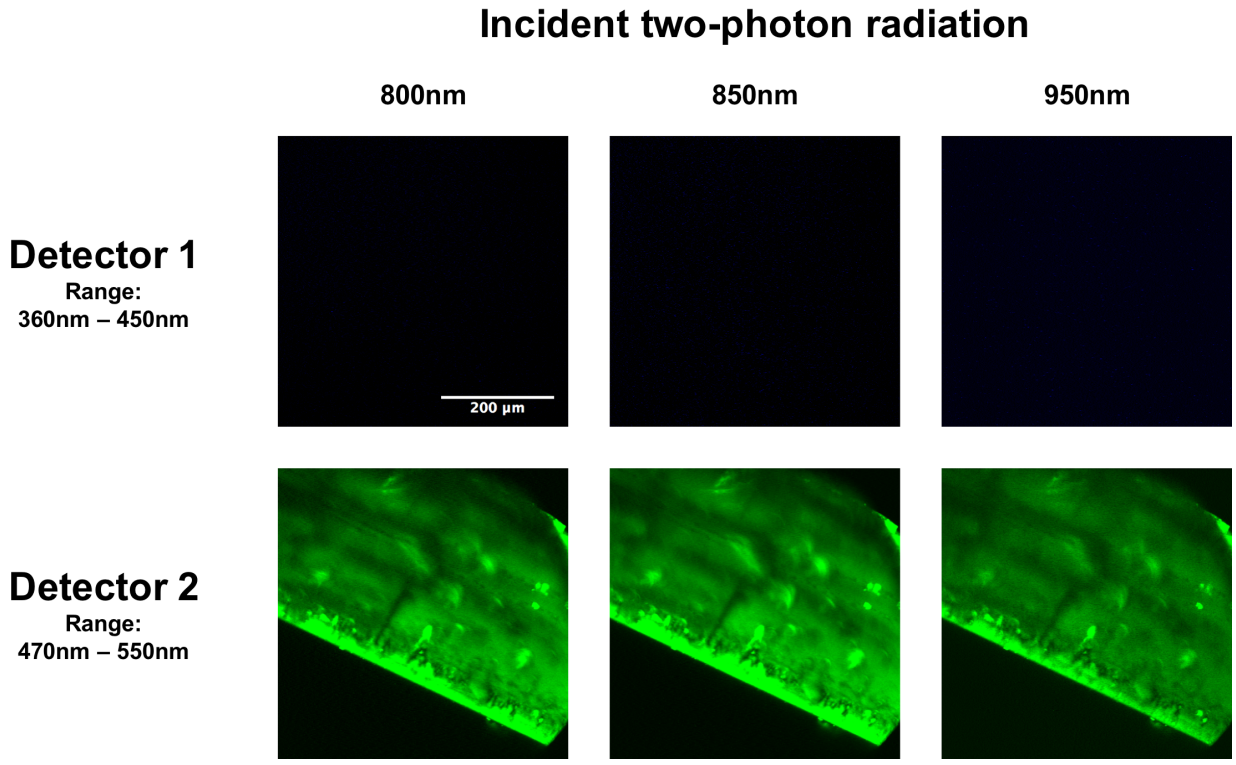

Figure 3.12: Two-photon confocal microscopy on co-crystal **1•4**. he crystal can only be detected when the induced second harmonic response falls within the detector range. Unlike co-crystals **1•2** and **1•3**, no second harmonic photons were observed with varying incident two-photon wavelengths. This suggests that co-crystal **1•4** does not possess non-centrosymmetric character necessary for ferroelectric activity. An autofluorescence response, however, can be detected in Dectector 2 at all incident wavelengths.

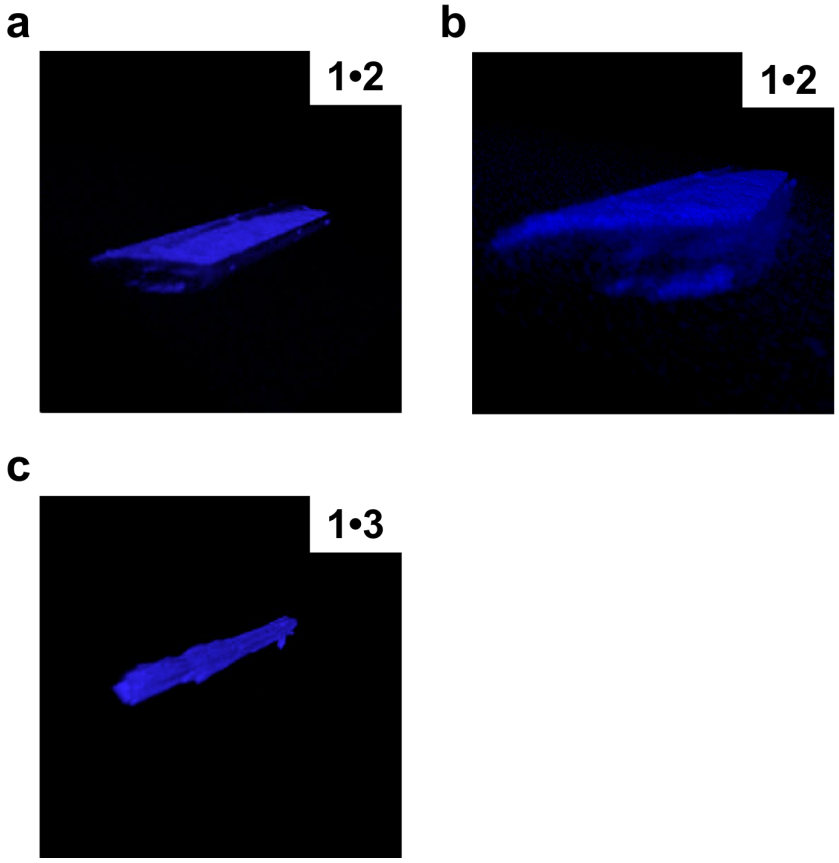

Figure 3.13: Two-photon confocal z-stack images of second harmonic photons emitted from LASO co-crystals (a,b) **1•2** and (c) **1•3**. That second harmonic photons are observable through the entire cross-section of the co-crystals precludes the notion that a breaking of intersion symmetry only occurs on the surface of the co-crystals. Incident two-photon wavelength = 850 nm; Detector range = 360 nm - 450 nm.

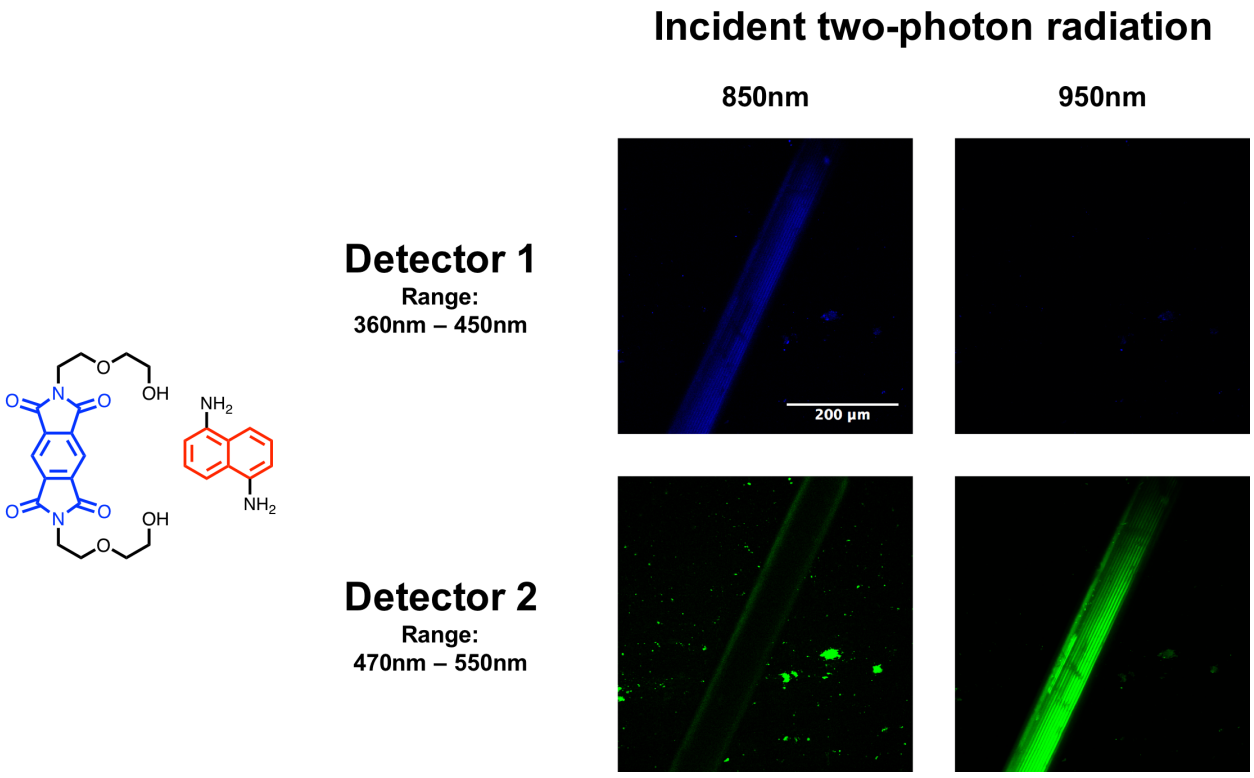

Figure 3.14: Two-photon confocal microscopy on diaminonaphthalene LASO ferroelectric co-crystal.[79] The crystal can only be detected when the induced second harmonic response falls within the detector range. For example, incident two-photon radiation at 850nm induced a second harmonic response at 425nm, which can only be imaged by Detector 1. Tuning the incident radiation screens the detection of co-crystal based on the wavelength of the second harmonic response.

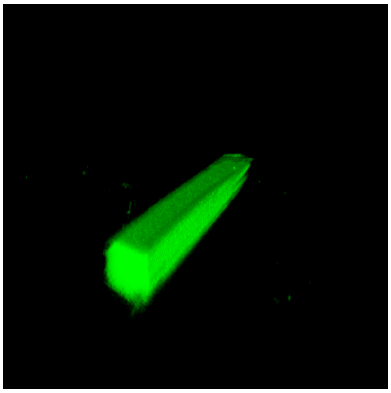

Figure 3.15: Two-photon confocal z-stack images of second harmonic photons emitted from diaminonaphthalene original LASO co-crystals. That second harmonic photons are observable through the entire cross-section of the co-crystals precludes the notion that a breaking of intersion symmetry only occurs on the surface of the co-crystals. Incident two-photon wavelength = 950 nm; Detector range = 470 nm - 550 nm.

lead to noncentrosymmetry that is not detected or refined through tradtitional crystallographic means.[191–193]

The trend in second harmonic activity observed for the co-crystals mirrors their ferroelectric behavior, wherein the co-crystals that display second harmonic activity (**1•2** and **1•3**) are the ones that exhibit some element of ferroelectric polarization. In fact, second harmonic activity was also observed (Figures 3.14, 3.15 and 3.16) in two of the original LASO co-crystals (synthetic difficulties hampered efforts to measure second harmonic effects for the third co-crystal), all of which display room-temperature ferroelectricity. The inverse is true for **1•4**, which does not exhibit any second harmonic behavior nor is it ferroelectric. This suggests that, in this series of LASO co-crystals, changing functionalization of the electron donor molecule to achieve stronger CT interactions between the donor and the pyromellitic diimide acceptor **4** pushes the co-crystal out of a centrosymmetric alignment into a dimerized polarized state the exhibits ferroelectric behavior.

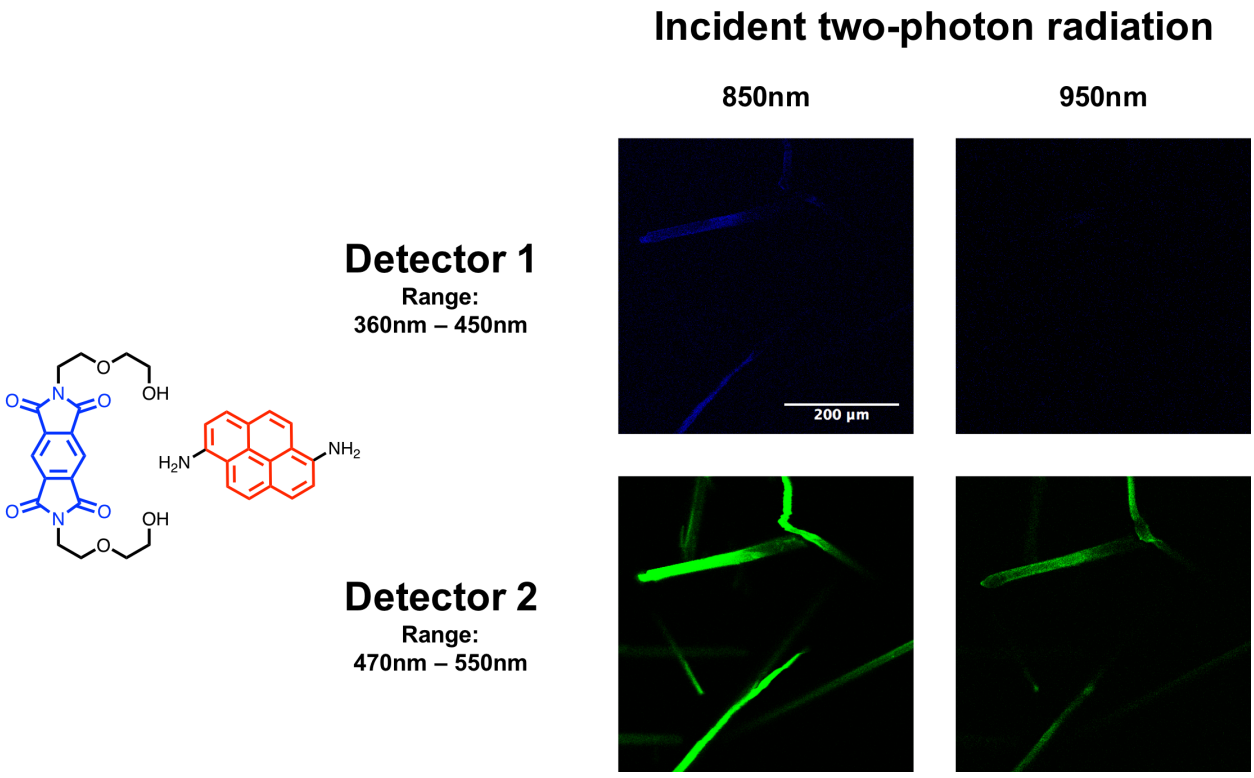

Figure 3.16: Two-photon confocal microscopy on diaminopyrene LASO ferroelectric co-crystal.[79] The crystal can only be detected when the induced second harmonic response falls within the detector range. For example, incident two-photon radiation at 850nm induced a second harmonic response at 425nm, which can only be imaged by Detector 1. Tuning the incident radiation screens the detection of co-crystal based on the wavelength of the second harmonic response.

3.4 CONCLUSION

We have described in great detail the crystalline assembly and room-temperature ferroelectric properties of a series of LASO co-crystals. Binary co-assemblies of difunctionalized naphthalene donor molecules with pyromellitic diimide form isostructural needle-like crystals, and ternary co-assemblies form solid solution-like random distributions of binary domains. Ferroelectric properties in the binary co-assemblies are only observed in mono- or diamino-functionalized donors, attributed to inversion symmetry breaking as a consequence of strong charge transfer interactions between the donor and acceptor molecules. The systematic study of these LASO co-crystals not only expand the library of possible room-temperature ferroelectric organic crystals, but also shed light onto the design parameters required to tune the molecular chemistry to affect supramolecular ferroelectricity.

3.5 MATERIALS AND METHODS

General Methods

Compounds and **2**[199] and **4**[200] were prepared following literature methods.[103] Unless otherwise stated, compounds and solvents were purchased from commercial vendors (Sigma Aldrich) and were used as supplied without further purification.

Single Crystal X-ray Crystallography

X-Ray diffraction data were obtained on Bruker Platform and Kappa diffractometers, equipped with a MoKα or CuKα sealed-tubesource and an APEX II CCD detector. Intensity data were collected using ω and ϕ scans spanning at least a hemisphere of reciprocal space for all structures (data were integrated using SAINT). Absorption effects were corrected on the basis of multiple equivalent reflections (SADABS). Structures were solved by direct methods (SHELXS[196]) and refined by full-matrix least-squares against F2 (SHELXL[196]). The structures were solved and refined using Olex2.

Hydrogen atoms were assigned using riding isotropic displacement parameters and constrained to idealized geometries, including those bound to oxygen, as no hydrogen atoms could be located in the difference Fourier map.

Polarized Absorption Spectroscopy

The absorption spectra were taken using a polarization microscopy setup. A Nikon TE2000 inverted microscope and Prior ProScan II stage were used to manipulate the sample position. The microscope halogen lamp was used as the source for the absorption spectra. Spectra were recorded using an Ocean Optics USB 2000 miniature spectrometer in both single polarizer and double-polarizer modes.

Two-Photon Confocal Microscopy

Two-photon confocal microscopy images were obtained using a Nikon A1R MP+ Multiphoton Confocal Microscope, equipped with a Coherent Ti:Sapphire Chameleon Vision S Laser, mode locked at 80 MHz with a 75 fs pulse duration. The incident laser wavelength was tunable from 690 nm to 1040 nm. Reflected and transmitted photons were detected by detectors above and below the sample plane, with detection windows from 380 nm to 450 nm and 470 nm and 500 nm. The irradiation power across all incident wavelengths was set at 800 mW. Single crystals were sandwiched between a glass microscope slide and cover slip, to separate the crystals from the water immersion microscope objective lens. All samples were irradiated in the dark at room temperature under ambient conditions.

Polarization and Dielectric Measurements

The LASO crystals are mechanically robust and can be handled with vacuum tweezers. Gold wire electrodes (12.5 μm) were attached on either end using gold paint (Ted Pella PELCO Conductive Gold Paste). The resulting devices were tested for ferroelectricity in a physical properties

measurement system (Quantum Design PPMS 6000) under an inert atmosphere. The temperature-dependent dielectric constants of LASO complexes were measured at 2 V with f = 1, 5 or 10 kHz frequency. These measurements were performed using an Agilent E4980A LCR meter. Polarization hystereses were measured using a ferroelectric tester (Radiant Technologies Precision LC with Trek 609A Amplifier).

Synthesis of **3**

Synthesis of 1-napthylamine-5-alkoy-diethylene glycol: A mixture of 5-acetamido-1-naphthol[201] 587 (11.0 g, 54.7 mmol), 2-(2- chloroethoxy)ethanol (7.50 g, 60.3 mmol), K_2CO_3 (22.8 g, 165 mmol), and KI (500 mg, 3.01 mmol) in MeCN (250 mL) was refluxed for 60 h, at which point TLC indicated complete consumption of the starting material. The reaction mixture was cooled to RT and the insoluble inorganic salts removed by filtration. The solvent was evaporated to yield an oil which foams under low pressure. A mixture of the crude residue, EtOH (200 mL), and conc. HCl (25 mL) was refluxed for 3 h. The reaction mixture was then cooled to RT, neutralized carefully with aq. K_2CO_3, and the aqueous extracted with CH_2Cl_2. The organic layer was dried ($MgSO_4$), filtered, and solvent evaporated. The residue was recrystallized from iPrOH/hexanes to yield (7.25 g, 53%) pink crystals. ^{1}H NMR (500 MHz, CD_3SOCD_3): δ = 7.60 (d, J = 8.5 Hz, 1H), 7.37 (d, J = 8.2 Hz, 1H), 7.24 (dd, J = 8.6, 7.5 Hz, 1H), 7.16 (dd, J = 8.3, 7.4 Hz, 1H), 6.87 (d, J = 7.5 Hz, 1H), 6.67 (d, J = 7.5 Hz, 1H), 5.64 (s, 2H), 4.65 (t, J = 5.4 Hz, 1H), 4.23 – 4.19 (m, 2H), 3.89 – 3.84 (m, 2H), 3.70 – 3.48 (m, 4H); ^{1}3C NMR (125 MHz, CD_3SOCD_3): δ = 154.01, 144.49, 126.05, 125.86, 123.53, 114.63, 109.03, 108.07, 104.85, 72.59, 69.03, 67.54, 60.25; HR MS (ESI): m/z calcd for $C_{14}H_{17}NO_3$: 270.1101 $[M + Na]^+$; found: 270.1098.

Synthesis of 3: A mixture of 1-napthylamine-5-alkoy-diethylene glycol (1.41 g, 5.70 mmol), 2-(2-chloroethoxy)ethanol (1.42 g, 11.4 mmol), K_2CO_3 (1.57 g, 11.4 mmol), and KI (95 mg, 0.57 mmol) in EtOH (50 mL) was refluxed for 12 d at which point TLC indicated complete consumption of the starting material. The reaction mixture was cooled to RT, diluted with

Ch_2Cl_2, and washed carefully with sat. NH_4Cl. The organic layer was dried ($MgSO_4$), filtered, and solvent evaporated. The residue was purified by column chromatography on silica gel using CH_2Cl_2/EtOAc/MeOH/NH_4OH (49 : 49 : 1.75 : 0.25 (v/v)) to yield **3** (1.33 g, 70%) as pink crystals. ^{1}H NMR (500 MHz, CD_3SOCD_3): δ = 7.66 (d, J = 8.6 Hz, 1H), 7.42 (d, J = 8.3 Hz, 1H), 7.29 (dd, J = 8.1, 7.9 Hz, 1H), 7.26 (d, J = 8.1, 7.7 Hz, 1H), 6.92 (d, J = 7.6 Hz, 1H), 6.56 (d, J = 7.5 Hz, 1H), 5.97 (t, J = 5.4 Hz, 1H), 4.67 (dt, J = 7.4, 5.3 Hz, 2H), 4.22 (dd, J = 5.7, 3.5 Hz, 2H), 3.93 – 3.80 (m, 2H), 3.70 (t, J = 6.0 Hz, 2H), 3.60 – 3.46 (m, 8H), 3.41 – 3.35 (m, 2H); ^{1}3C NMR (125 MHz, CD_3SOCD_3): δ = 154.11, 143.73, 125.99, 125.82, 124.03, 123.85, 113.74, 109.14, 105.17, 103.58, 72.59, 72.22, 69.02, 68.45, 67.59, 60.25, 60.20, 43.03; HR MS (ESI): m/z calcd for $C_{18}H_{25}NO_5$: 358.1625 $[M + Na]^+$; found: 358.1628.

General Crystallization Procedure

The naphthalene donors (60 mg, 0.18 mmol) and pyromellitic diimide **1** (20 mg, 0.093 mmol) were dissolved in N-methyl-2-pyrrolidone (NMP) (10 mL). For ternary co-crystals, the appropriate ratio of compound **2** to **4** was employed (60 mg, 0.18 mmol). The resulting solution was passed through a 0.2 μm PTFE syringe filter into a 20-mL test tube. Fresh Milli-Q water (10 mL) was layered carefully on top of the NMP solution. Needles were observed to grow within 1 d.

Crystallographic Data

The crystallographic data, for the co-crystals **1•2** and **1•4** has been previously reported, but for the sake of convenience is reproduced here.[103]

Crystal Parameters for **1•2**

$C_{28}H_{30}N_4O_8$; purple needle, 0.681 × 0.10 × 0.04 mm^3; monoclinic, space group $P2_1/c$; a = 6.67, b = 23.36, c = 8.36 Å; α = 90, β = 104.6, γ = 90°; V = 1260.65 Å^3; Z = 2; ρ_{calcd} = 1.452 g cm^{-3};

$2\theta_{max}$ = 61.35°; T = 100(2) K; 1966 reflections collected, 1220 independent, 193 parameters; μ = 0.71073 mm^{-1}; R_1 = 0.0455 [$I > 2.0\sigma(I)$], wR_2 = 0.1101 (all data).

Crystal Parameters for **1•3**

$C_{28}H_{29}N_3O_9$; red needle, 0.52 × 0.08 × 0.06 mm^3; monoclinic, space group $P2_1/c$; a = 6.68, b = 23.39, c = 8.35 Å; α= 90, β = 105.2, γ= 90°; V = 1258.61 $Å^3$; Z = 2; ρ_{calcd} = 1.455 g cm^{-3}; $2\theta_{max}$ = 63.52°; T = 100(2) K; 6261 reflections collected, 1952 independent, 190 parameters; μ = 1.54178 mm^{-1}; R_1 = 0.0356 [$I > 2.0\sigma(I)$], wR_2 = 0.0923 (all data).

Crystal Parameters for **1•4**

$C_{28}H_{28}N_2O_{10}$; orange needle, 0.21 × 0.20 × 0.10 mm^3; monoclinic, space group $P2_1/c$; a = 6.68, b = 23.42, c = 8.37 Å; α= 90, β = 106.2, γ= 90°; V = 1257.99 $Å^3$; Z = 2; ρ_{calcd} = 1.459 g cm^{-3}; $2\theta_{max}$ = 30.53°; T = 100(2) K; 17663 reflections collected, 3828 independent, 189 parameters; μ = 0.71073 mm^{-1}; R_1 = 0.0508 [$I > 2.0\sigma(I)$], wR_2 = 0.1229 (all data).

Crystal data for $\mathbf{1•2}_{0.25}\mathbf{4}_{0.75}$

$C_{28}H_{28}N_2O_{10}$; purple needle, 0.69 × 0.17 × 0.04 mm^3; monoclinic, space group $P2_1/c$; a = 6.68, b = 23.37, c = 8.36 Å; α= 90, β = 105.7, γ= 90°; V = 1256.28 $Å^3$; Z = 2; ρ_{calcd} = 1.460 g cm^{-3}; $2\theta_{max}$ = 30.02°; T = 100(2) K; 39632 reflections collected, 3634 independent, 198 parameters; μ = 0.71073 mm^{-1}; R_1 = 0.0364 [$I > 2.0\sigma(I)$], wR_2 = 0.1042 (all data).

Crystal data for $\mathbf{1•2}_{0.5}\mathbf{4}_{0.5}$

$C_{28}H_{29}N_3O_9$; purple needle, 0.78 × 0.23 × 0.14 mm^3; monoclinic, space group $P2_1/c$; a = 6.68, b = 23.41, c = 8.36 Å; α= 90, β = 105.3, γ= 90°; V = 1259.65 $Å^3$; Z = 2; ρ_{calcd} = 1.454 g cm^{-3}; $2\theta_{max}$ = 66.83°; T = 100(2) K; 8536 reflections collected, 2206 independent, 187 parameters; μ = 1.54178 mm^{-1}; R_1 = 0.0314 [$I > 2.0\sigma(I)$], wR_2 = 0.0796 (all data).

Crystal data for $\mathbf{1}\bullet\mathbf{2}_{0.75}\mathbf{4}_{0.25}$

$C_{28}H_{28}N_4O_8$; purple needle, 0.69 × 0.17 × 0.06 mm^3; monoclinic, space group $P2_1/c$; a = 6.66, b = 23.38, c = 8.35 Å; α= 90, β = 104.9, γ= 90°; V = 1256.64 $Å^3$; Z = 2; ρ_{calcd} = 1.450 g cm^{-3}; $2\theta_{max}$ = 30.02°; T = 100(2) K; 3305 reflections collected, 3634 independent, 194 parameters; μ = 0.71073 mm^{-1}; R_1 = 0.0415 [$I > 2.0\sigma(I)$], wR_2 = 0.1209 (all data).

4 Co-Assembly and Phase Separation in Semiconducting Hydrogen-Bonded Charge Transfer Complexes

4.1 OBJECTIVES AND SIGNIFICANCE

Translational function drives much of scientific research today. The ability to take a concept or idea, validated by experiments, and bring it to a form that is commercially viable plays a key role in innovation. Such is the case with the field of charge transfer (CT) complexes, where foundational work focused on the single-crystalline complexes of donor and acceptor molecules. It is through this understanding that established theories of inter- and intra-molecular charge transfer, as well as the variety of assembly architectures and their properties over the decades. The downsides, however, of using entirely crystalline complexes lies in their low-throughput production, and brittle mechanical properties. The promise of solution (or roll-on-roll) processing of organic electronic materials has opened the door to studying materials that mimic the properties of their single-crystalline counterparts with the added benefit of a liquid or solution-based morphology. This chapter focuses on exactly that transition, where inspiration is taken from the LASO CT design criteria to develop solution-based complementary donor/acceptor molecules that assemble and exhibit semiconducting properties. While the aromatic units of the donor and acceptor molecules are the same as that used in the LASO crystals, additional hydrogen bonding units as well as solubilizing groups are added to promote assembly in solutions. This chapter will study both the assembly and properties of the CT complexes in solution as well as once cast onto a substrate (from whence function is derived), and the interplay between the two based on the changing driving forces for inter- and intra-molecular association.

4.2 BACKGROUND

Materials garnered from supramolecular chemistry offer great promise in the development of innovative technologies that span the field of thin-film electronics.[14,19,202,203] The ability to control the chemistry, assembly and functional electronic properties of supramolecular materials sets it apart from its bulk polymeric counterpart, limited by the size and distribution of crystalline domains, as well as molecular electronics, hampered by device dimensions and molecular sterics.[202] In this vein, intermolecular charge transfer interactions, in which an electron donor transfers some of its charge to an electron acceptor, have been renowned for the unique assembly-driven electronic properties.[43,69] Specifically, the assembly of these complementary molecules in a mixed-stack arrangement, where each electron donor and acceptor molecule assemble in an alternating, face-to-face arrangement, have been shown to dimerize and exhibit ferroelectric polarization.[78–80,83,96,97,100] Alternatively, the assembly of charge transfer complexes into segregated stacks, where the molecules assemble in linear arrays of donor and acceptor molecules, has been shown to result in metal-like conductivities for organic CT co-crystals, attributed to the delocalization of charge carriers along the partially ionized donor and acceptor arrays.[45,85,90,204]

More recent efforts have focused on translating the physics and electronic properties of crystalline CT complexes to a more solution-processable form.[101,205] Introducing solubilizing groups to the complimentary aromatic cores have opened new doors to understanding the interplay between solvophobic and hydrogen bonding interactions in conjunction with charge transfer.[72,75,95,206,207] This in turn has expanded the library of applications of CT complexes, ranging from exploiting the unique optical characteristics,[208–213] to using CT complexes as vehicles for molecular capture or recognition,[214–219] to exploring the ambipolar semiconducting properties of the co-assembled *p*-type donor and *n*-type acceptor molecules.[220–227]

The work in this chapter probes the interplay between hydrogen bonding and charge transfer in co-assembled CT complexes, and their influence on thin-film electronic properties. Inspiration for this work originates from the previously-reported LASO co-crystal motif,[103] where complemen-

tary donor and acceptor molecules are functionalized with hydrogen bonding 'arms' to stabilize the formation of a mixed stack assembly. Complementary electron donor (1,5-dialkoxynaphthalene) and electron acceptor (pyromellitic diimide) moieties are functionalized with urea and sulfonamide hydrogen-bonding groups respectively. The urea/sulfonamide complementary hydrogen bonding groups were chosen for their propensity to heterodimerize in solution (Figure 4.2b).[228,229] This intermolecular hydrogen bonding is more favorable since the sulfonamide proton is the most acidic hydrogen bond donor in the system, with the carbonyl of the urea as the most basic hydrogen bond acceptor. This selective binding, in conjunction with the CT interactions, should drive the dimerization of the donor and acceptor molecules in solution (Figure 4.2c). This chapter probes the intermolecular interaction and properties of donor and acceptor molecules, both in solution and on a substrate. The distinction between the two is key, as the balance of forces that lead to association and assembly, and therefore the semiconducting properties, are vastly different between the two.

4.3 RESULTS AND DISCUSSION

4.3.1 *Molecular Design Considerations*

Initial efforts into building a supramolecular solution-based CT complex incorporated (Figure 4.1a) a symmetric diethylene glycol linker between the donor/acceptor molecules and the hydrogen bonding moieties. A linear octyl tail was added at the end of the molecule to impart solubility in organic solvents. Issue of solubility, especially in the acceptor ($\mathbf{0}_A$) molecule, hindered co-assembling efforts to observe CT interactions. In fact, $\mathbf{0}_A$ was only found to be soluble in an excess of 1-bromonaphthalene ($\mathbf{0}_D$), with a charge transfer absorption band observed (Figure 4.1b) at 475 nm. The excess $\mathbf{0}_D$ likely disrupted the strongly-associating $\mathbf{0}_A$ through CT interactions, therein promoting the dissolution of $\mathbf{0}_A$.

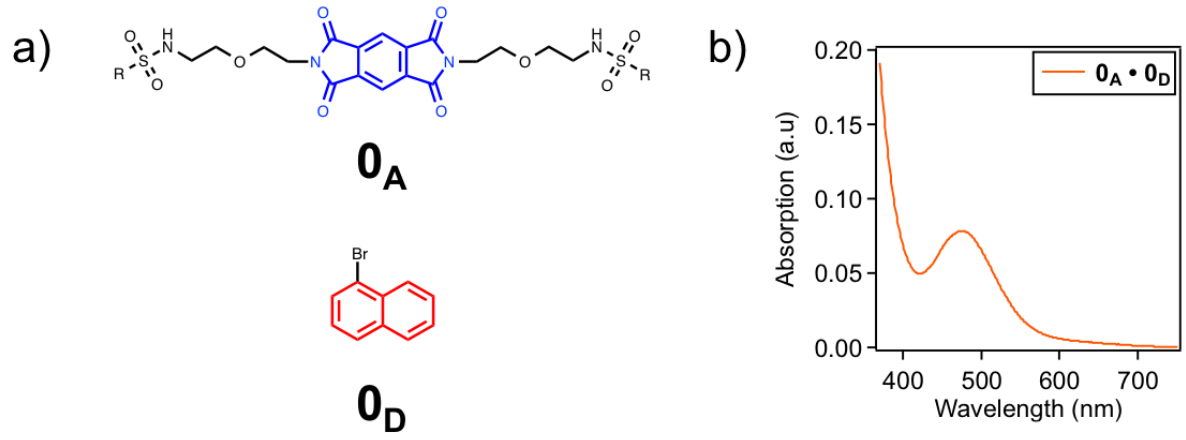

Figure 4.1: (a) Initial molecular design for pyromellitic diimide-based electron acceptor molecule (0_A), soluble only in excess 1-bromonaphthalene ($mathbf 0_D$). (b) Absorption spectrum of 0_A dissolved in excess $mathbf 0_D$, highlighting a broad absorption band at 475 nm indicative of charge transfer between the aromatic donor and acceptor small molecules.

4.3.2 *Solution Characterization*

Buoyed by these results, a second iteration (Figure 4.2a) of the donor/acceptor molecules was explored, this time increasing the length of the diethylene glycol spacer to tetraethylene glycol. This proved to dramatically increase the solubility of both the acceptor **1** and the donor **2** in organic solvents. When the donor and acceptor molecules are dissolved in toluene with the brief application of heat, a broad CT absorption band is observed (Figure 4.3a) at 450 nm when the solution cools to room temperature. This band is a fingerprint of the CT interactions between the napthalene donor and pyromellitic diimide acceptor moieties. This result is further corroborated by the quenching (Figure 4.3b) of the naphthalene monomer fluorescence emission (from the donor **2**) upon co-assembly with acceptor **1**. Tracking the absorption of the CT absorption peak of **1•2** upon cooling the solution temperature from 353 K to 298 K reveals (Figure 4.3c) two features: (i) The intensity of the CT absorption peak dramatically increases upon cooling, indicative of CT interactions upon cooling the system from a high energetic state (high temperature) to a lower energetic state (room temperature). (ii) The sigmoidal shape of the absorption curve suggests an *isodesmic*

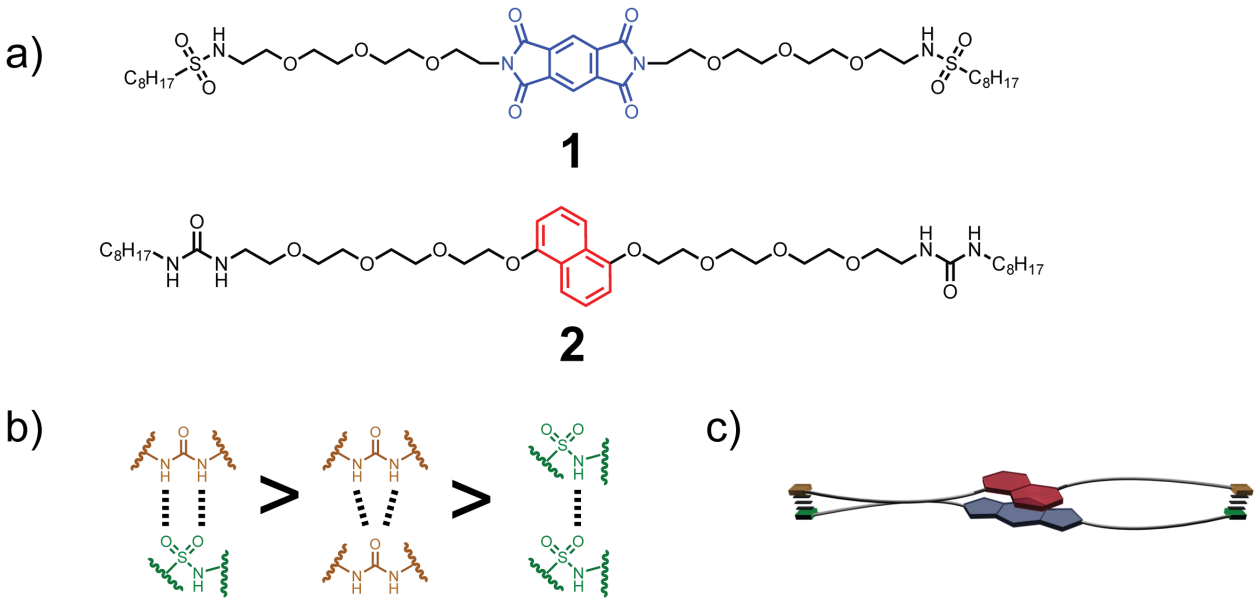

Figure 4.2: (a) Molecular design for pyromelletic diimide-based electron acceptor (**1**) and naphthalene-based electron donor (**2**), functionalized with complementary urea and sulfonamide hydrogen bonding moieties. (b) Intermolecular hydrogen bonding favors the heterodimerization of sulfonamide and urea moieties, as the sulfonamide proton is the most acidic hydrogen bond donor, and the carbonyl of the urea the most basic hydrogen bond acceptor.[228,229] (c) The combination of intermolecular charge transfer and hydrogen bonding should promote the dimerization of **1** and **2** upon co-assembly in organic solvents.

Table 4.1: Diffusivities of **1**, **2** and **1•2** in d-toluene

	MW (Da)	Total conc. of dissolved species (mM)	D (cm^2/s) $(\times 10^{-6})$
1	919	5	3.89
2	814	5	3.59
1•2	-	5	3.74

mechanism of supramolecular polymerization,[230–233] where association between the donor and acceptor molecules is governed by a single association constant. Lastly, the stoichiometry of association between **1** and **2** can be ascertained from the fluorescence quenching of **2** using a method of continuous variation.[234,235] Figure 4.3c that the fluorescence quenching (normalized for the mole fraction of **2**) is at its maximum when the mole fraction of **1** is 0.5, indicative of a 1:1 association ratio between the donor and acceptor molecules, similar to that observed in CT co-crystals with the same aromatic donor/acceptor moieties.[103]

Nuclear Magnetic Resonance (NMR) spectroscopy in deuterated toluene reveals further details about the nature of co-assembly and association between **1** and **2**. Upfield shifts (Figure 4.4) of both the naphthalene H_α and pyromellitic diimide H_β proton signals upon co-assembly are indicators of increased electron density in the vicinity of the aromatic protons, likely due to face-to-face association between the aromatic donor and acceptor moieties. Hydrogen bonding between the donor and acceptor molecules is also evident from the downfield shifts of the sulfonamide (H_γ) proton, further corroborating the hypothesis of cooperative dimerization between **1** and **2** upon co-assembly. In addition, Diffusion Ordered (DOSY) NMR reveals that the diffusivity (Table 4.1) of the dissolved molecules changes upon co-assembly. While the diffusivities of **1** (Figure 4.5) and **2** (Figure 4.6) are $3.89 \pm 0.06 \times 10^{-6}\ cm^2/s$ and are $3.59 \pm 0.04 \times 10^{-6}\ cm^2/s$ respectively, **1•2** exhibits a diffusivity of $3.74 \pm 0.09 \times 10^{-6}\ cm^2/s$. That the diffusivity of **1•2** (Figure 4.7) is an intermediate of that of **1** and **2**, represented by a single Gaussian distribution (as opposed to a bimodal distribution expected for non-interacting particles) is further proof that of cooperative assembly between **1** and **2** upon co-assembly to **1•2**.[236–239]

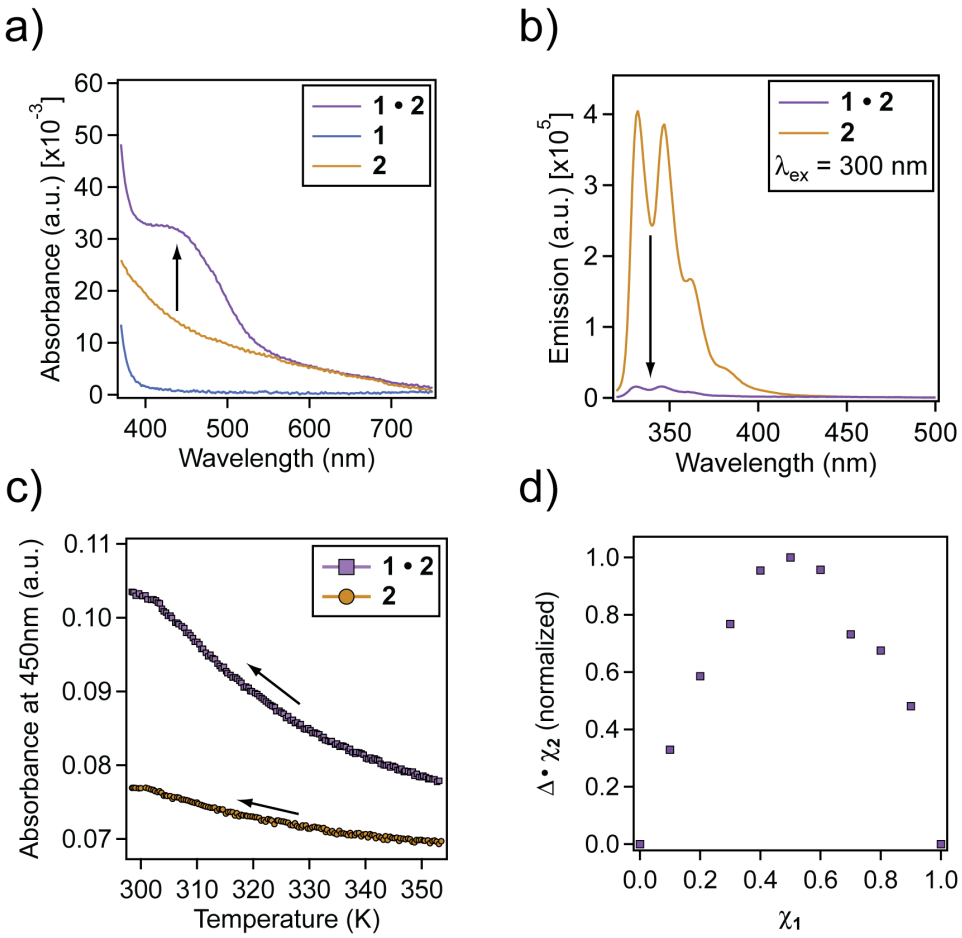

Figure 4.3: Co-assembly of **1** and **2** results in (a) a broad charge transfer absorption band at 450 nm, distinct from the absorption of **1** and **2**, as well as (b) the quenching of naphthalene monomer fluorescence. (c) Variable-temperature UV-Vis absorption of a **1•2** solution illustrates that the charge transfer band grows upon cooling the solvent from high temperatures. The absorption-temperature profile is indicative of an isodesmic assembly of **1** and **2** upon cooling from a high to a low energetic state. (d) The stoichiometry of assocaition of **1** and **2**, elucidated by tracking fluorescence quenching (normalized for the mole fraction of **2**) as a function of the mole fraction of **1**, implies a 1:1 association between the donor and acceptor small molecules.

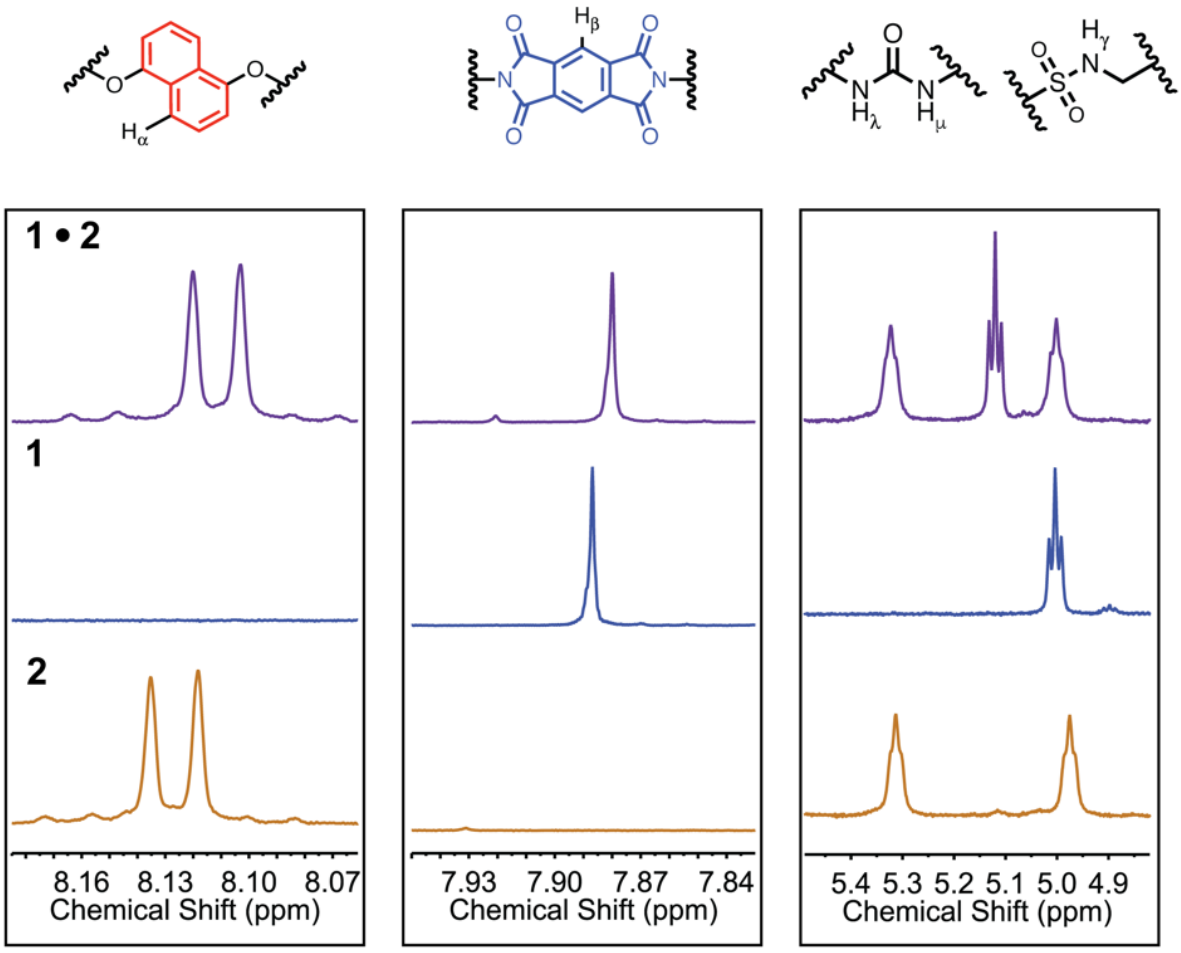

Figure 4.4: Solution NMR Spectra of **1**, **2** and **1•2**. Upfield shifts of the naphthelene and pyromellitic diimide proton signals are likely due to face-to-face assocation between the donor and acceptor moieties. The presence of hydrogen bonding in solution between **1** and **2** can be ascertained by the downfield shift of the sulfonamide proton.

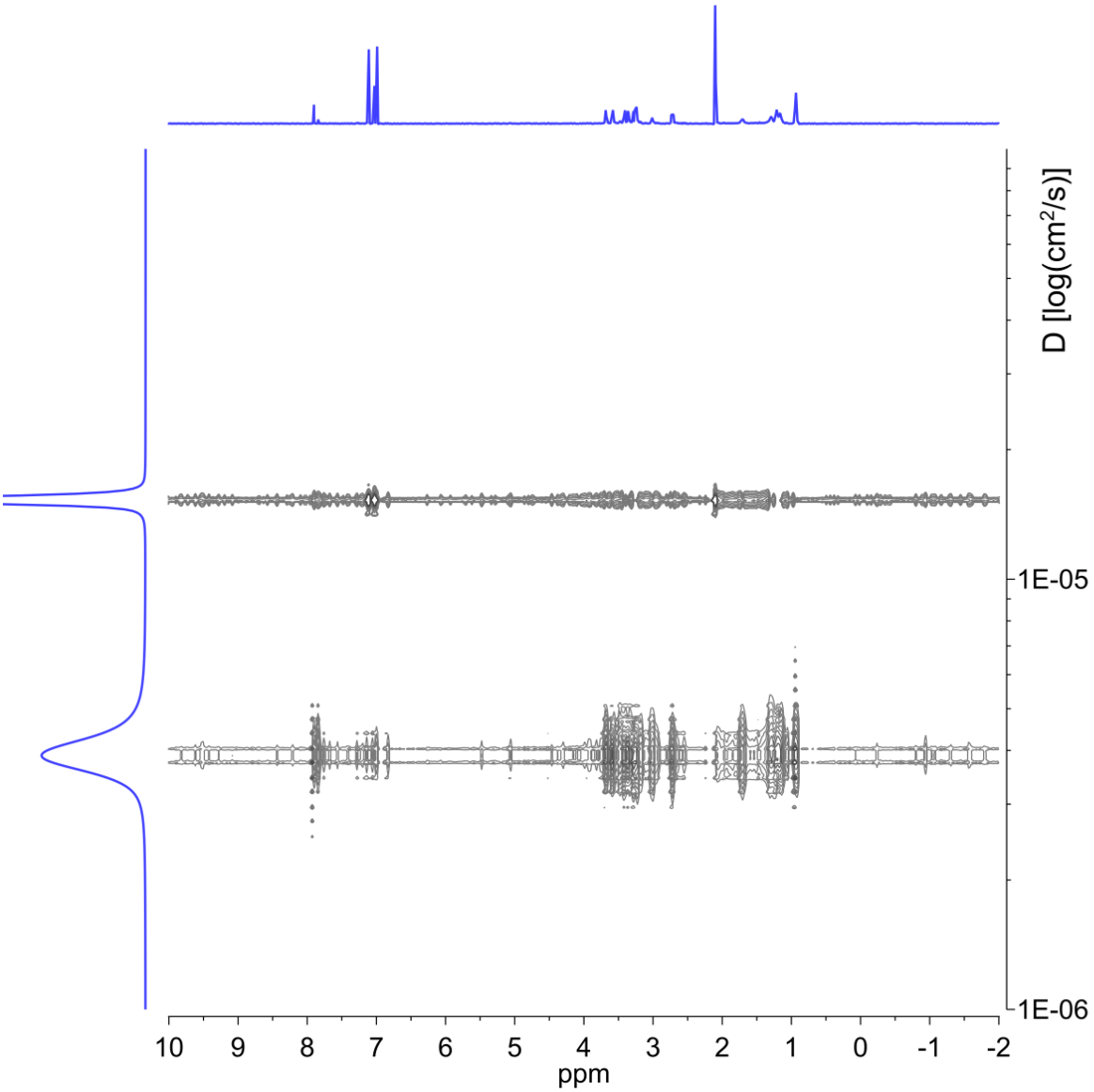

Figure 4.5: DOSY Spectrum of **1**, which has a diffusivity of $3.89 \pm 0.06 \times 10^{-6}\ cm^2/s$. Residual free toluene has a diffusivity of $1.53 \times 10^{-6}\ cm^2/s$.

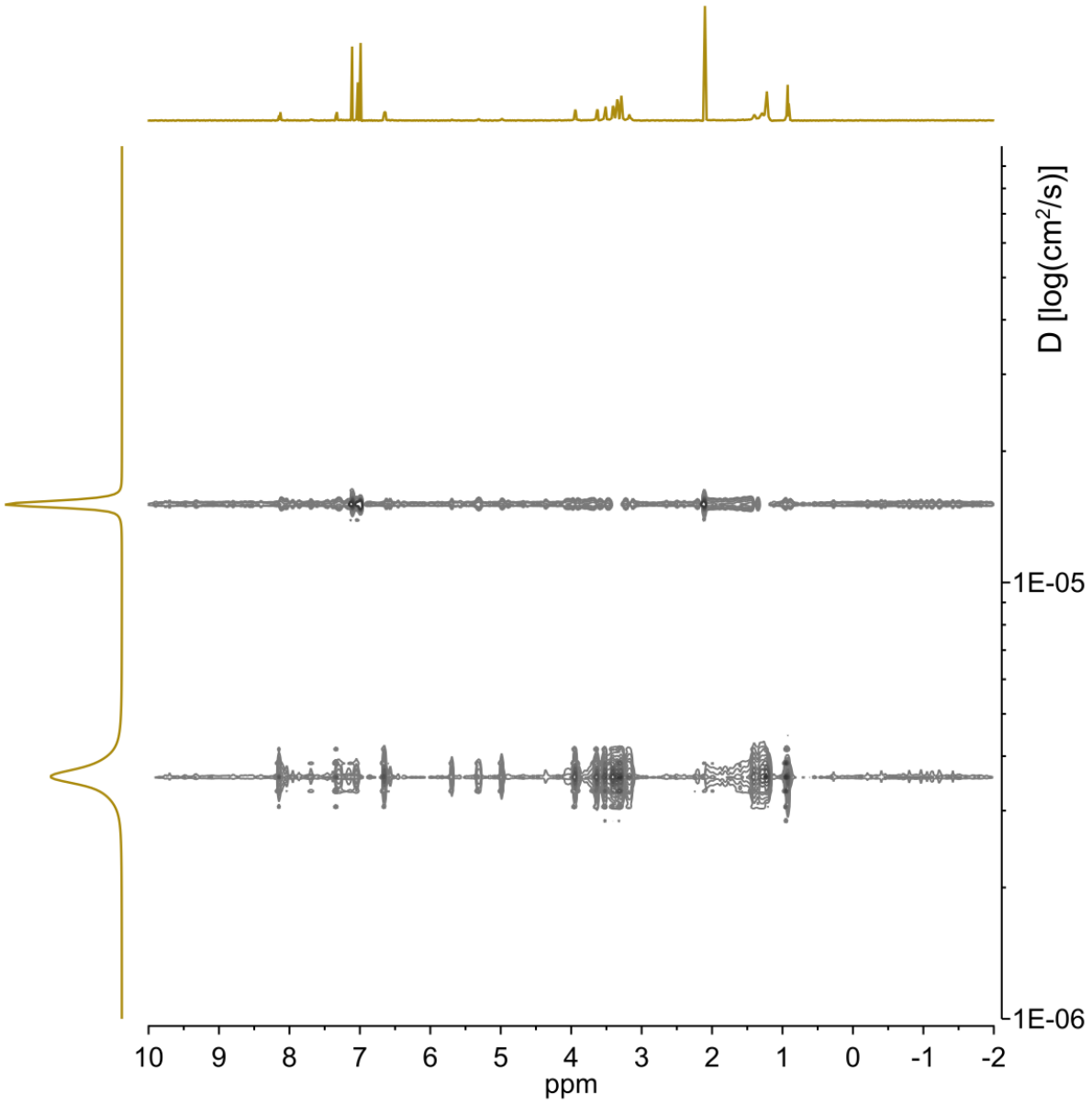

Figure 4.6: DOSY Spectrum of **2**, which has a diffusivity of $3.59 \pm 0.04 \times 10^{-6}\ cm^2/s$. Residual free toluene has a diffusivity of $1.51 \times 10^{-6}\ cm^2/s$.

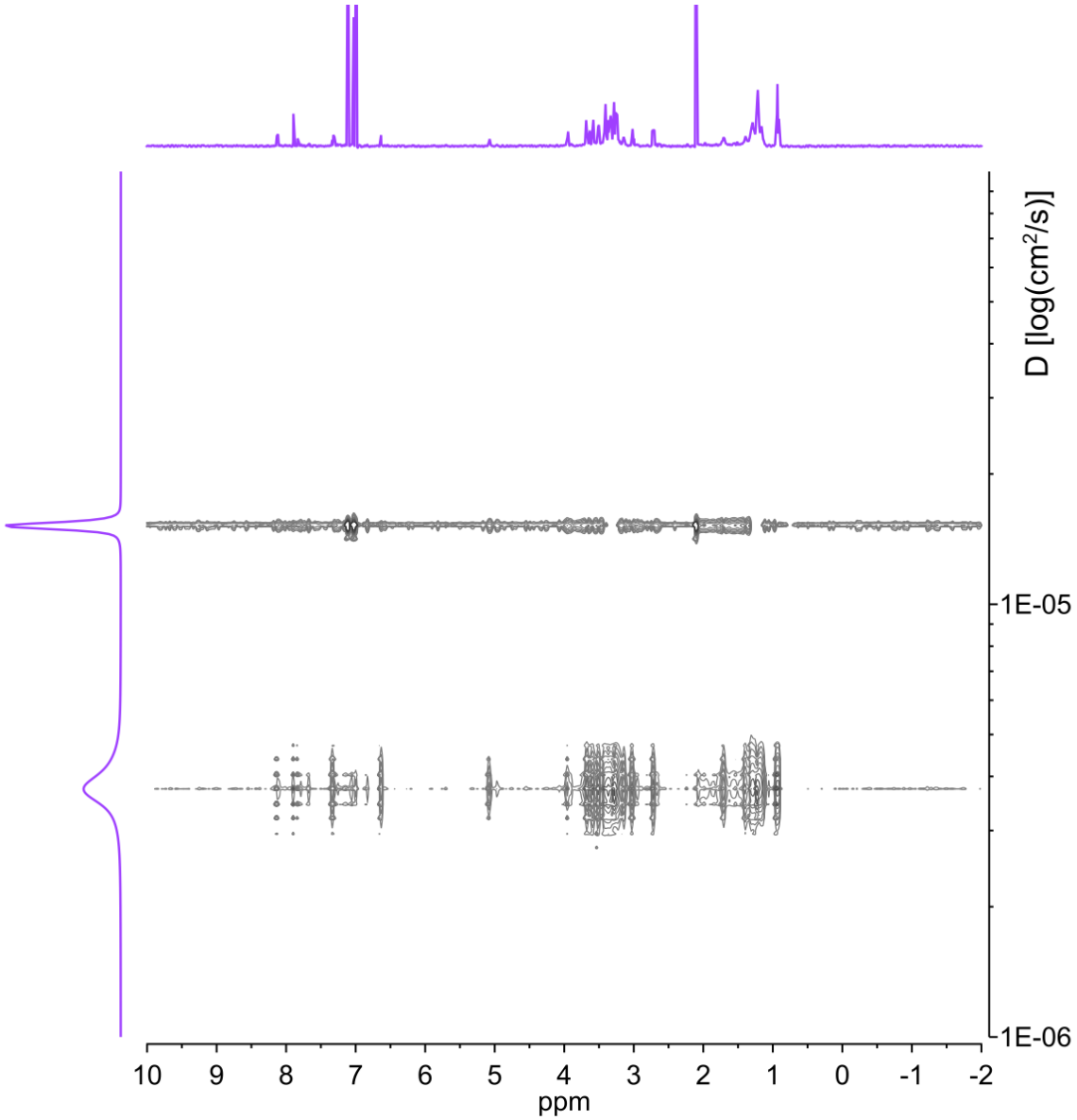

Figure 4.7: DOSY Spectrum of **1•2**, which has a diffusivity of $3.74 \pm 0.09 \times 10^{-6}\ cm^2/s$. Residual free toluene has a diffusivity of $1.52 \times 10^{-6}\ cm^2/s$.

4.3.3 *Surface Characterization*

While the association between **1** and **2** points towards a 1:1 dimerization between the donor and acceptor molecules in solution, the morphology and assembly on surfaces paints a very different picture. Atomic force microscopy (AFM) images if **1** point (Figure 4.8a) to the formation of fibrous nanostructures. Since nanostructures of **1**, **2** or **1•2** were not observed by any electron microscopic or solution-based small angle X-ray spectroscopic technique, it can be assumed that the assemblies observed result from nucleation and growth of the nanostructured elements on the surface of the substrate. In contrast to the fibrous surface nanostructure morphology of donor **1**, acceptor **2** forms (Figure 4.8b) regular platelet structures with repeat heights of 4 nm. Interestingly, the surface profiles (Figure 4.8c) of **1•2**, which in solution was just shown to form a cooperative 1:1 assembly, illustrates the presence of both fibrous nanostructures and well-defined platelets, suggestive of phase segregation of **1** and **2** when cast on a substrate. This hypothesis was corroborated by grazing incidence X-ray scattering (GIXS) of the assemblies (Figure 4.9c,d), where the horizontal and vertical linecuts of the 2D X-ray micrographs of co-assembled **1•2** system suggested a linear superposition of that of the donor (Figure 4.9a) and acceptor (Figure 4.9b) assemblies. This definitely proves that while co-operatively associating in solution, the two molecules undergo phase separation and form segregated arrays of donor and acceptor molecules when cast on a surface.

Interestingly, despite phase separation when cast in a thin film, the co-assembled **1•2** retains (Figure 4.10a) its charge transfer absorption band. In fact, the absorption intensity of the CT band is highest (Figure 4.10b) in equimolar mixtures of **1** and **2**, indicative that even upon phase separation, **1•2** is able to retain its charge transfer character and 1:1 association. A number of reasons could explain this observation. For one, the presence of dopant **1** or **2** molecules in the bulk surface assemblies of **2** and **1** respectively could result in residual charge transfer character while not influencing the overall crystallinity of the bulk nanostructure. The number of dopant molecules would, of course, scale with the molar fractions of **1** and **2**, which would explain the trends in thin film CT absorption intensity upon varying donor/acceptor co-assembly ratios. A second possibility could

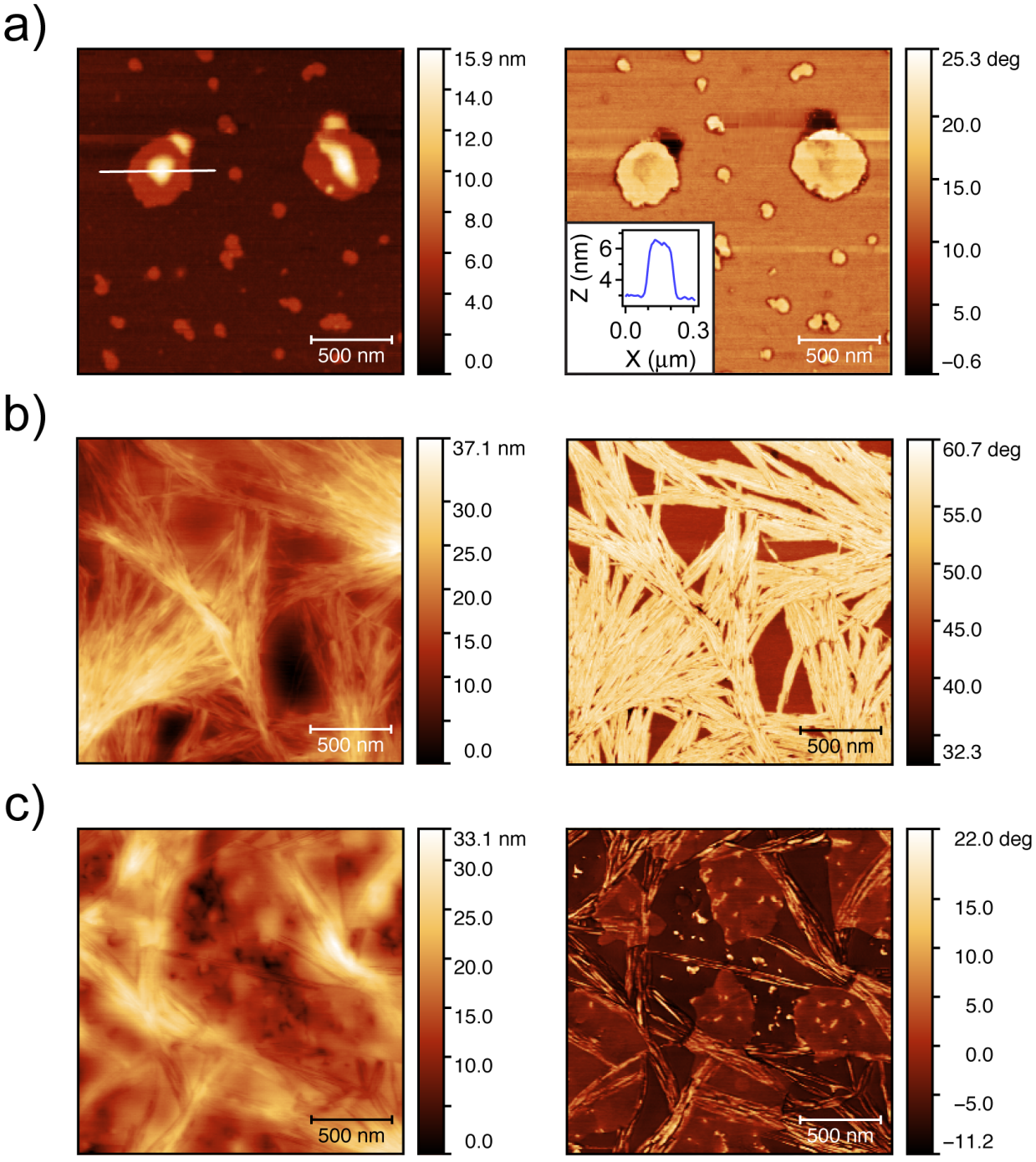

Figure 4.8: AFM profiles of cast films of (a) **2**, which assembles into fibrous nanostructures, (b) **1**, which assembles into platelet structures with 4 nm heights, and (c) **1•2**, which phase separatates into platelets (**1**) and fibrous nanostructures (**2**).

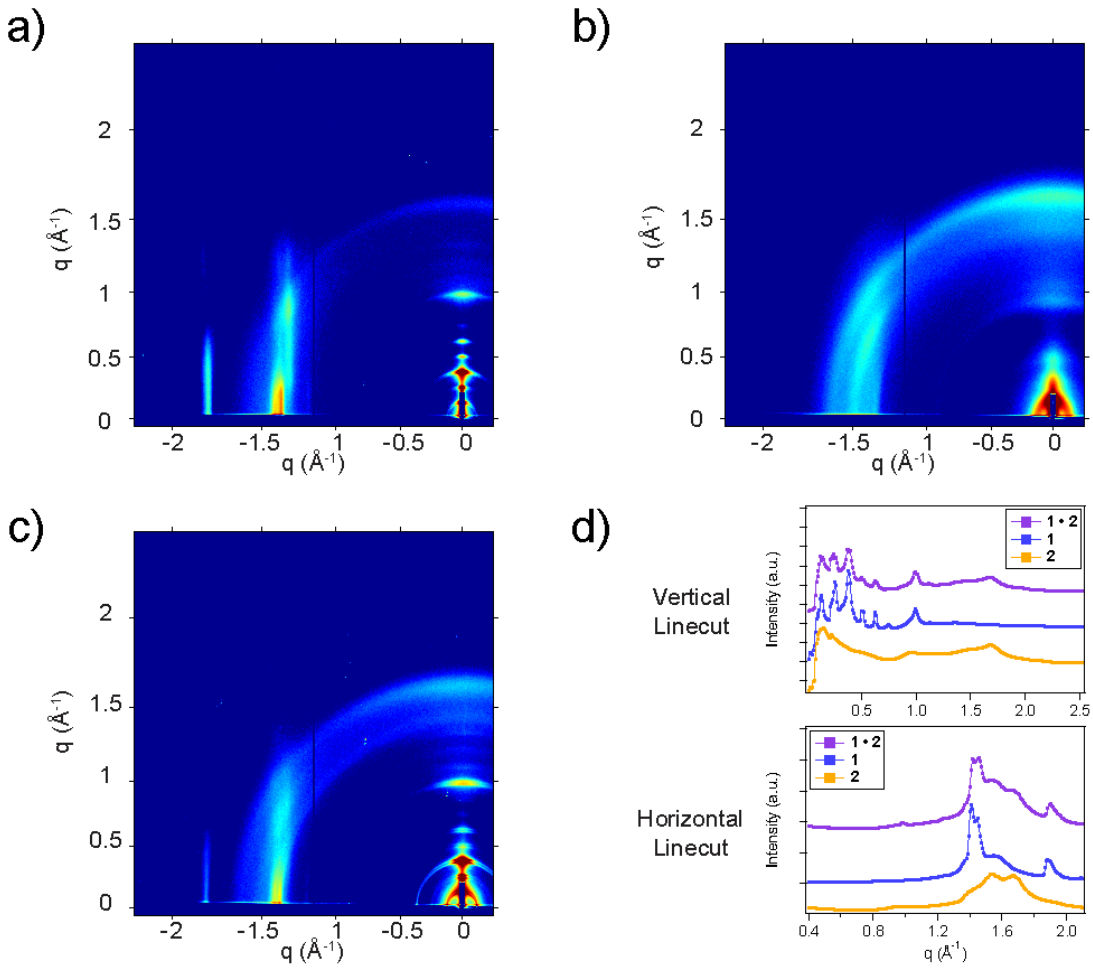

Figure 4.9: GIXS profiles of (a) **2**, (b) **1** and (c) **1•2**. (d) Vertical (left) and horizontal (right) linecuts of GIXS profiles indicate that the crystallinity of **1•2** is a linear superposition of that of **1** and **2**.

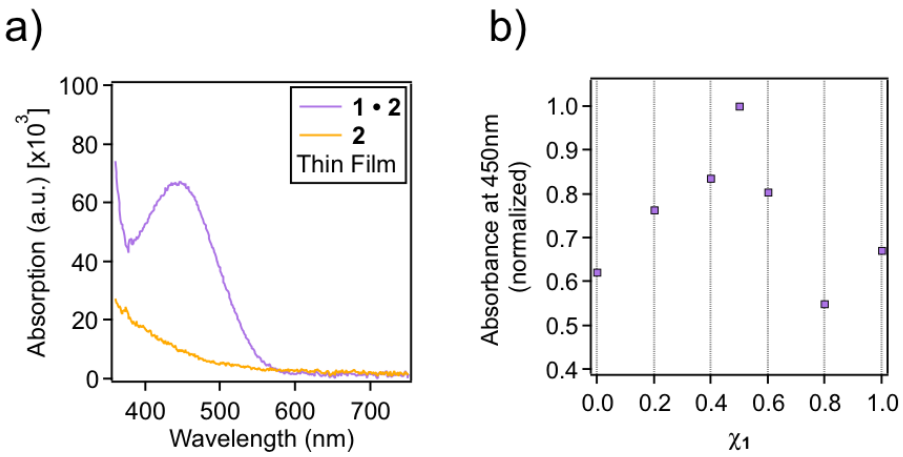

Figure 4.10: Thin-film absorption of **1**, **2** and **1•2**, where (a) a broad charge transfer absorption band is observed upon co-assembly. (b) Highest CT absorption is observed in films of **1•2** when the mole fraction of **1** is 0.5, indicative that **1•2** retains its 1:1 charge transfer association when cast into a thin film.

be that assemblies of **1** and **2** retain their partially ionized state obtained from association and co-assembly in solution. This in turn would preserve the CT energy levels in **1•2** upon co-assembly in solution, and would explain the presence and trends in CT absorption observed in films of **1•2**.

Ultraviolet Photoelectron Spectroscopy (UPS) of the films further corroborates the hypothesis of remnant charge transfer despite phase separation. UPS on the co-assembled **1•2** illustrates (Figure 4.11) an increase in the ionization potential of the complex, indicative of a reduction in the highest occupied molecular orbital (HOMO) level of the complex. This is a fingerprint of CT interactions, as electron transfer, in a Huckel-like picture,[240,241] results in intermolecular resonance stabilization (Section 1.2) of donor/acceptor complex, therein lowering the HOMO energy level. The extent of this resonance stabilization (referred to as the resonance or charge-transfer integral) can be gleaned from the difference between the lowest unoccupied molecular orbital (LUMO) of the acceptor molecule and the LUMO of the corresponding charge transfer complex.[240]

The persistence of charge transfer in the phase-separated **1•2** can also be alluded to using Fourier transform infrared (FTIR) spectroscopy. Specifically, the position of the carbonyl (C=O) peak of the acceptor has been used as a metric to measure the degree of ionization, or ionicity,

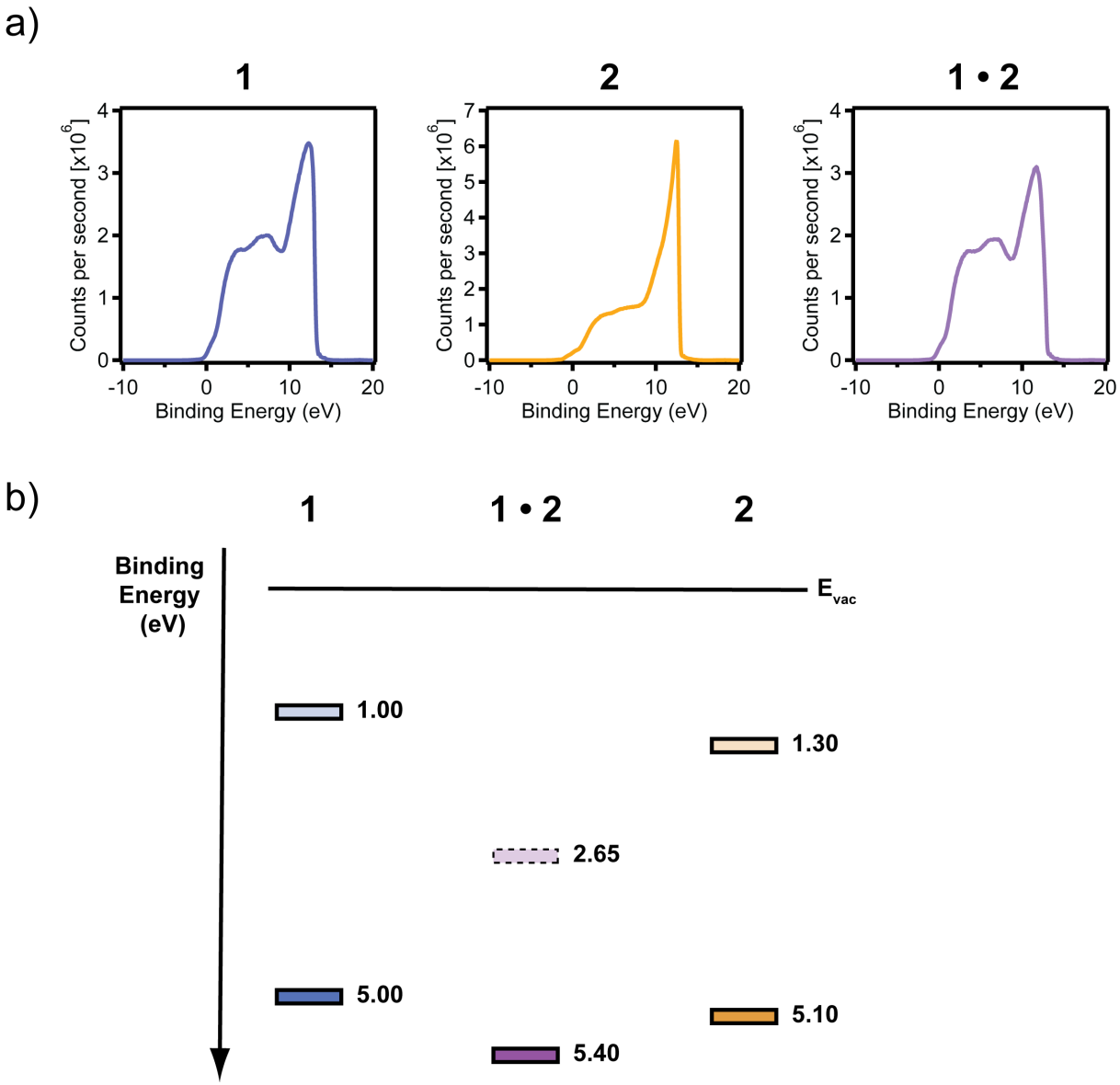

Figure 4.11: (a) UPS spectra and (b) simulated band energy diagrams for **1**, **2** and **1•2**. While the HOMO energy levels can be ascertained from the UPS spectra, the LUMO levels were estimated from the naphthalene and pyromelletic diimide absorption peaks of **1** and **2** respectively, and the CT absorption peak for **1•2**.

of the acceptor molecule as a metric for the extent of CT interactions.[154,242,243] While popularized with quinone-derived acceptor molecules, this technique has not been widely utilized with the pyromellitic diimide family of acceptor molecules. Indeed in this case, acceptor **1** shows (Figure 4.12) a strong peak at 1718 cm^{-1}, which can be assigned to the stretching mode of the imide carbonyl (C=O) bond. Upon co-assembly to **1•2**, the position of the C=O stretching mode does not change, but its intensity increases significantly. Since there is no anomalous change in the PMDI C=O bond density upon co-assembly, this increase in absorption intensity can only be due to an increase in the transition dipole moment of the C=O bond, since a changing dipole moment potentiates the absorption of the acceptor molecule.[43,244–247] One possibility for this increase could be the increase in electron density in the C=O bond due to electron transfer to the aromatic acceptor **1**.[43] A similar pattern can be observed (Figure 4.13) for the co-assembly of **3** and **4**, where the peak intensity of the C=O stretching band (1720 cm^{-1}) increases in intensity upon co-assembly. While not quantitative, this result also points to the presence of CT interactions between co-assembled donor and acceptor molecules, even after they phase separate on a surface.

To understand the interplay between charge transfer and hydrogen bonding interactions in the small molecules presented here, control donor/acceptor molecules were designed and synthesized (Figure 4.13a), where the hydrogen-bonding urea and sulfonamide moieties were omitted to leave naphthalene donor and pyromellitic diimide acceptor cores symmetrically functionalized with just tetraethylene glycol units. Acceptor molecules **3** assembles (Figure 4.13b) to form large sheet-like structures of 4 - 6 nm repeat heights. That the assembly (on a substrate) for both molecules **1** and **3** are similar in profile suggests that for the acceptor molecule, the presence of the sulfonamide hydrogen-bonding functional group does not influence the supramolecular assembly, and that instead the π-π stacking, van der Waals, solvophobic, as well as surface interactions are responsible for directing supramolecular assembly. This is not the case, however, for the assembly of **4** (Figure 4.13c), where instead the morphology largely consists of small aggregates. This indicates that for the donor molecule, hydrogen bonding of the urea moiety is highly consequential

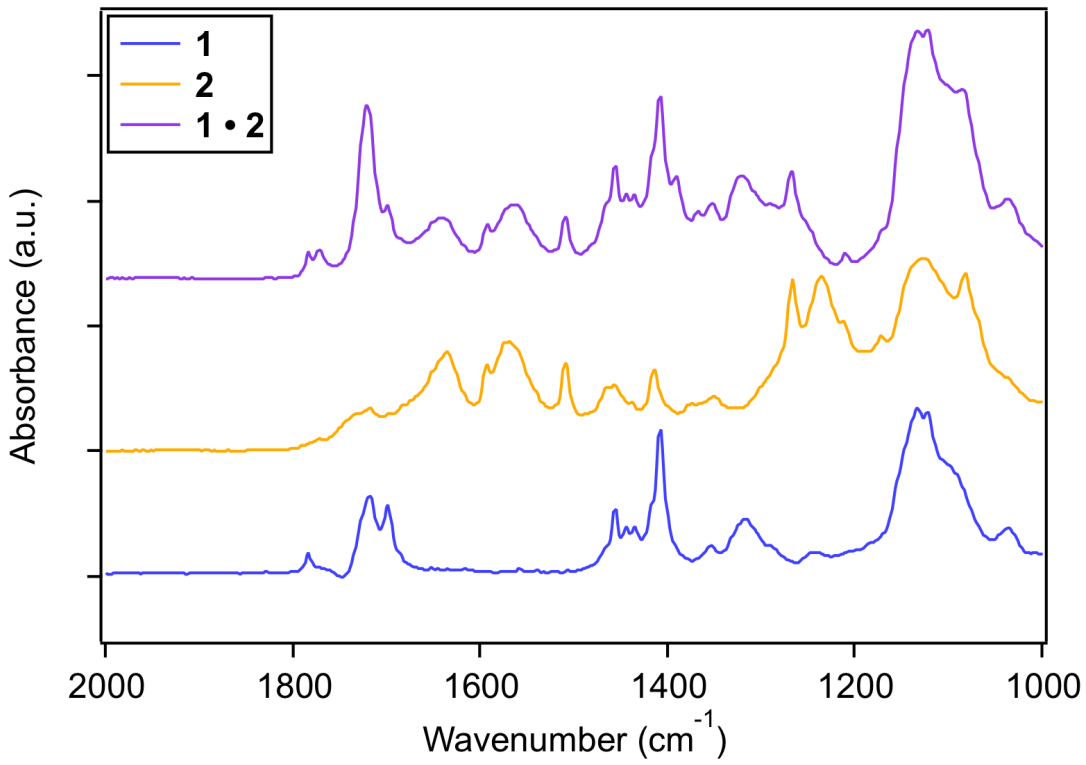

Figure 4.12: ATR-FTIR Spectra on films of **1**, **2** and **1•2**

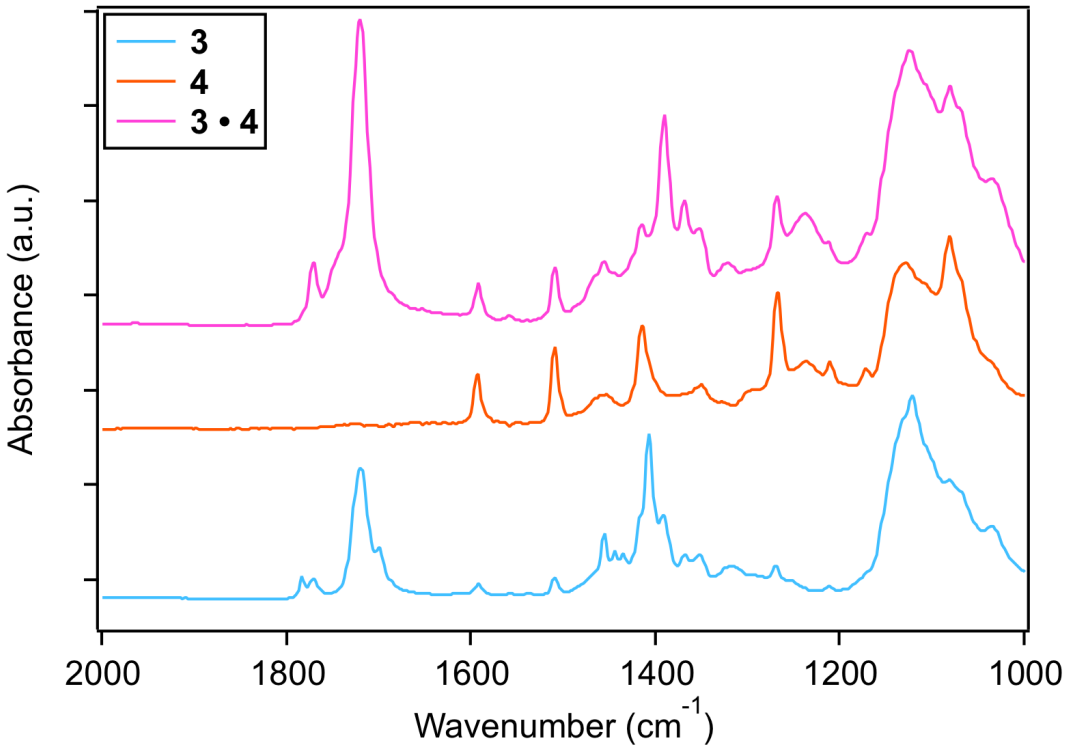

Figure 4.13: ATR-FTIR Spectra on films of **3**, **4** and **3•4**

towards supramolecular assembly. This is hardly surprising, as urea-functionalized groups have been known[102,248–251] to promote large, hierarchical assemblies due to their propensity to form directional intermolecular hydrogen bonds. The co-assembly **3•4** does not display any signs of morphologies that differ from that of **3** and **4**, which could either be due to phase separation or the lack of long-range assembling order for the intercalated assembly of **3•4**.

4.3.4 *Electronic Properties*

To understand the electronic properties of these co-assembled but surface-segregated arrays of donor and acceptor molecules, a thin film device was constructed (Figure 4.14a), where 50 nm of Au was evaporated on top of a film of **1•2** spuncoat on top of a silicon wafer with a 300 nm of amorphous silicon dioxide dielectric layer. Applying a transverse linear direct current (DC) field to the device consistently saw a much more pronounced (Figure 4.14b) electronic response for the co-assembled **1•2** device than that for the individual **1** and **2** devices. Measuring the resistivity of the thin-film devices from the ohmic portion of the current-voltage (I-V) curve highlighted (Figure 4.14c) that the film of co-assembled **1•2** exhibited conductivities of $2.1 \pm 0.1 \times 10^{-3}$ S/m, which is orders of magnitude greater than that of **1** ($7.3 \pm 4.4 \times 10^{-5}$ S/m) and **2** ($6.1 \pm 5.2 \times 10^{-6}$ S/m). Consistent with this observation are the measured conductivities of cast films prepared with solutions containing several different molar ratios of donor **1** and acceptor **2**, where the highest conductivity was observed (Figure 4.7d) for 1:1 donor:acceptor co-assemblies. This mirrors the previous observation that the 1:1 assembly (in solution) displayed the strongest charge transfer absorption, and suggests that charge transfer interactions play a role in influencing the electronic properties of the resulting thin-film device.

Further proof of the importance of CT interactions on the thin-film conductivity of **1•2** can be elucidated by comparing the DC conductivity of **1•2** (where CT interactions are present) with that of a layered film of **1** and **2** (devoid of any CT interactions). In this device, solutions of **1** and **2** were prepared separately, and spuncoat on top of each other to create a layered thin-film device

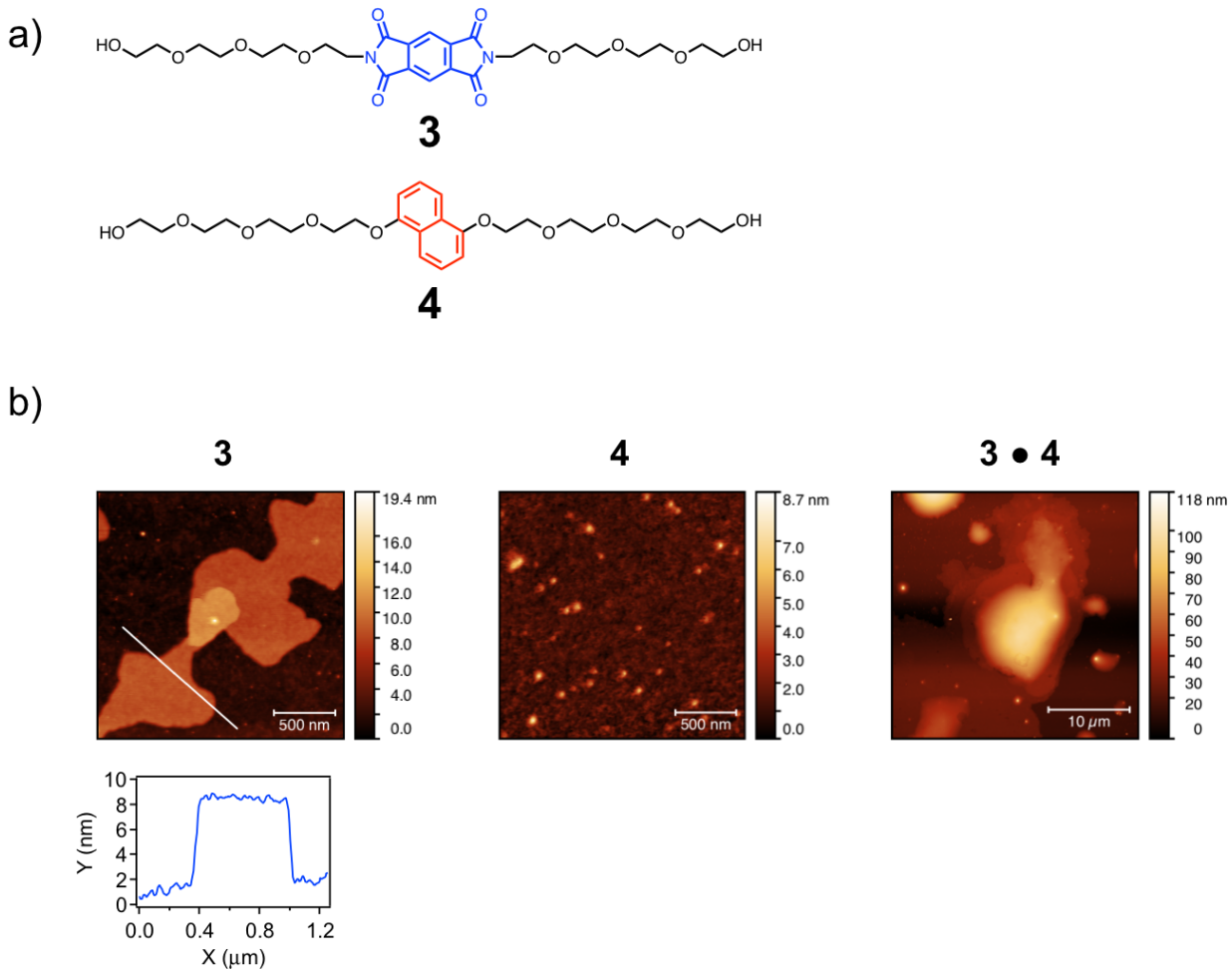

Figure 4.14: (a) Molecular design of **3** and **4**, which utilizes the same aromatic complementary electron poor and rich cores, without the urea and sulfonamide functionality. (b) AFM profiles of **3**, **4** and **3•4**. While **3** forms platelet-like structures similar to **1**, both **4** and **3•4** do not exhibit long-range order due to their lack of hydrogen bonding capabilities.

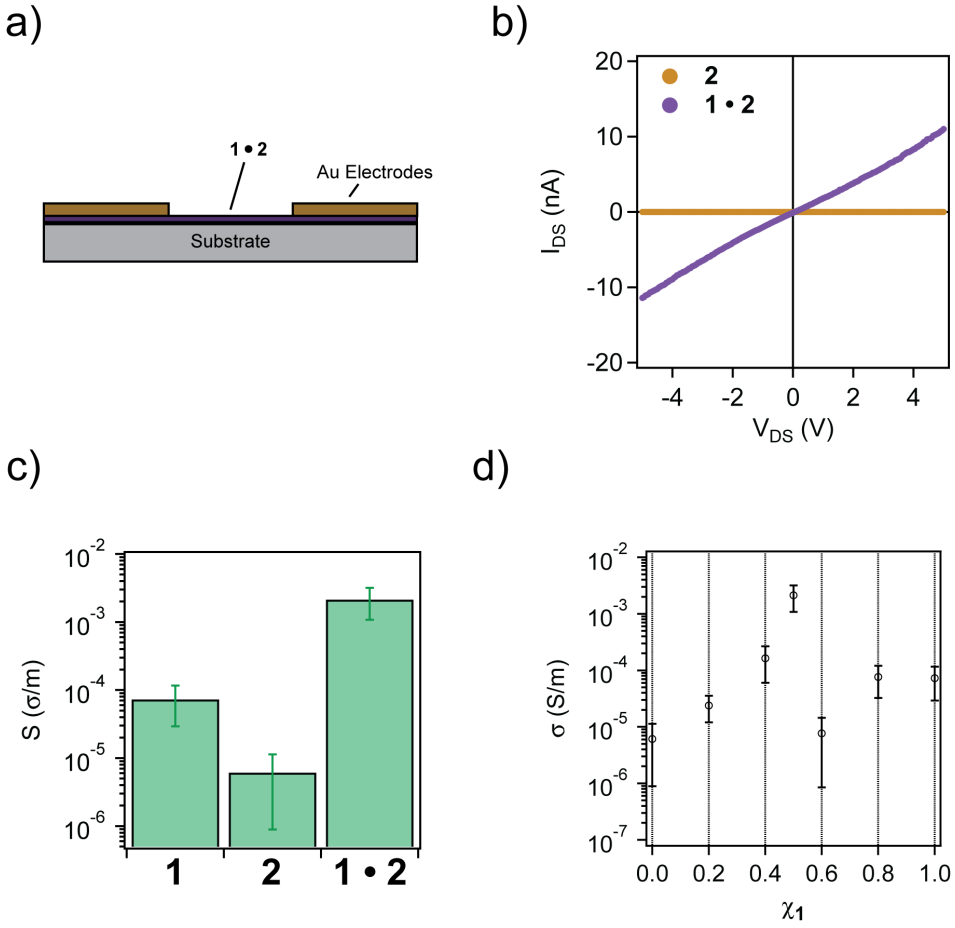

Figure 4.15: (a) Schematic of top-electrode thin film device use to measure conductivity and field effect mobility of **1**, **2** and **1•2**. (b) Representative current-voltage (I-V) curve of **1** and **1•2**. (c) Linear conductivities (measured from the ohmic region of corresponding I-V curves), highlighting the increased conductivity upon co-assembly of **1** and **2**. (d) Variation of conductivity as a function of the mole fraction of **1**.

(Figure 4.15a). The surface profile of the layered device illustrates (Figure 4.15b) the presence of both donor fibers and acceptor platelets, which imitates that observed for the co-assembled **1•2**. In this case, the measured conductivity ($8.4 \pm 7.4 \times 10^{-7}$ S/m) (Figure 4.15c) was significantly lower than that of the co-assembled **1•2**, further suggesting that the electron transfer upon co-assembly in solution is key in defining the electronic properties of the CT complex.

The changes in conductivity of the co-assembled **1•2** also translate to changes in electron and hole field effect mobility (Figure 4.16, Table 4.2) of the co-assembled CT complex. Co-assembly of the electron poor **1** and the electron rich **2** compounds should result in ambipolar behavior in response to a gated electric field.[203,252] Indeed, the device of co-assembled **1•2** does exhibit gated output current (I_{DS}) (Figure 4.16a) akin to that of a thin-film field effect transistor (TFT), albeit with no current saturation observed. This can be explained by the fact that many organic TFTs do not have a carrier threshold voltage (V_T) due to the absence of localized trap or defect states, and as a result induced charges are necessarily mobile.[253,254] A minimal or lack of a carrier V_T, in turn, implies that the saturation regime of electron transport is minimal, if not negligible. Further current-voltage relations of the co-assembled **1•2** can be understood from the transfer curve (Figure 4.16b) which illustrates regions of hole-dominant, electron-dominant, as well as ambipolar charge transport. Given this ambipolar behavior, the charge carrier mobilities can be calculated using the following equations:[203,252,255]

$$\mu_{FET,linear} = \frac{L}{W C_{ox} V_{DS}} \frac{\partial I_{DS}}{\partial V_G} \tag{1}$$

$$\mu_{FET,saturated} = \frac{2L}{W C_{ox}} \frac{\partial \left(I_{DS}\right)^{1/2}}{\partial V_G} \tag{2}$$

where $\mu_{FET,linear}$ and $\mu_{FET,saturated}$ correspond to the carrier mobilities in the linear and saturated carrier transport regime, V_{DS} the applied voltage across the source and drain electrodes, V_G the gate voltage, L the electrode spacing, W the width of the electrodes and C_{ox} the capacitance of the dielectric oxide layer. Table 4.2 contains the electron and hole mobilities, calculated across

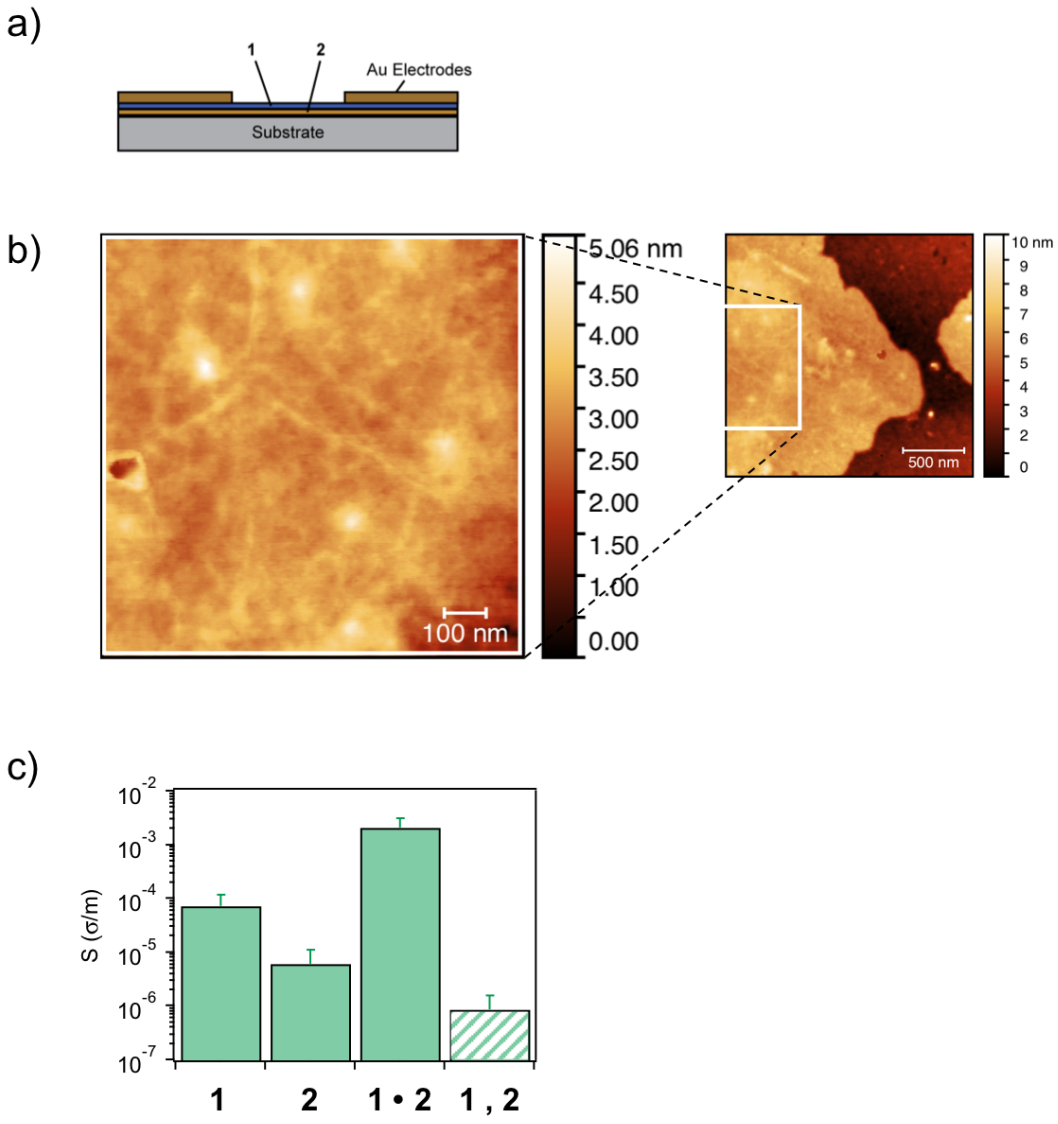

Figure 4.16: (a) Schematic of top-electrode thin film device used to measure conductivity in layered films of **1** on **2** (**1**,**2**). (b) AFM surface profiles of **1**,**2**, confirming the presence of fibrous **1** underneath platelets of **2**. (c) Linear conductivities of the layered **1**,**2** compared to **1**, **2** and **1•2**

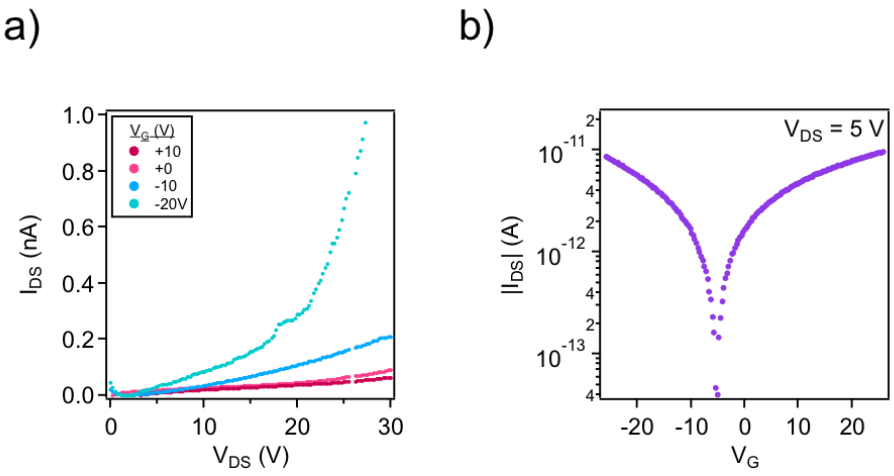

Figure 4.17: (a) Representative output curve and (b) transfer curve for a thin-film field-effect transistor device of **1•2**.

both the linear and saturated regime, for **1•2**, as well as that of **1** and **2** for comparison. A large increase in both the electron and hole mobility in the linear and saturated transport regime upon co-assembly of **1** and **2** rationalizes the increased conductivity observed for **1•2**, as now both charge carriers contribute to the electronic conductivity of the thin-film device.

The role of hydrogen bonding on the electronic properties of the studied donor/acceptor co-assemblies was studied by measuring the conductivities (Figure 4.17) of **3**, **4** and the respective co-assembly **3•4**. When cast on a surface, **3** exhibited DC conductivity values of $3.7 \pm 3.0 \times 10^{-5}$

Table 4.2: Field-Effect Mobilities of **1**, **2** and **1•2**

	1	**2**	**1•2**
$\mu^{h}_{FET,linear}$ $(cm^2/V \cdot s)$ (10^{-7})	6.72 ± 2.56	3.30 ± 0.95	24.78 ± 6.61
$\mu^{e}_{FET,linear}$ $(cm^2/V \cdot s)$ (10^{-7})	5.51 ± 1.57	2.92 ± 0.73	26.37 ± 8.95
$\mu^{h}_{FET,saturated}$ $(cm^2/V \cdot s)$	1.00 ± 0.13	0.52 ± 0.08	3.77 ± 0.91
$\mu^{e}_{FET,saturated}$ $(cm^2/V \cdot s)$	0.93 ± 0.17	0.53 ± 0.09	3.52 ± 0.72

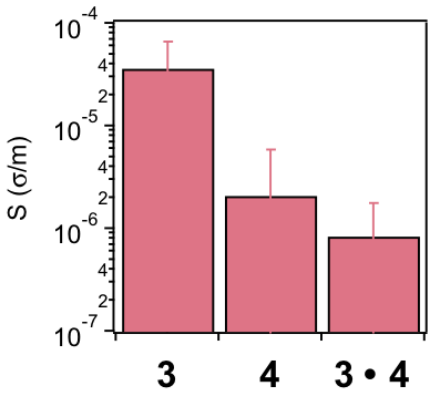

Figure 4.18: Linear conductivities of **3**, **4** and **3•4**

S/m, which is similar to that observed for **1**. That both the electrically active moiety, as well as the supramolecular morphology, is similar for both **1** and **3**, suggests that the DC linear conductivity values should be similar. In contrast, **4** exhibits lower conductivity ($2.1 \pm 3.7 \times 10^{-6}$ S/m) compared to that of **2**, likely due to the lack of long-range order. The largest difference, however, was observed for the conductivity of **3•4** ($8.4 \pm 9.3 \times 10^{-6}$ S/m), which is three orders of magnitude smaller than that of **1•2**. This implies that co-assembly of **3** and **4** negatively impacts the electronic properties of the resulting thin film complex, in contrast to that observed for the co-assembly of **1** and **2**. Since the only molecular difference between **1•2** and **3•4** is the presence of hydrogen bonding units, it can be hypothesized that the observed difference can be due to the stabilizing forces as well as the long-range order that the intermolecular hydrogen bonding provided between urea and sulfonamide functional groups. Fully delineating the electronic contributions of hydrogen bonding and charge transfer may be difficult, however, as hydrogen bonding and long-range order can not only provide conducting pathways for the motion of charge carriers, but also stabilize CT interactions. That said, it can be said that hydrogen bonding and CT interactions work cooperatively in the co-assembly of **1** and **2** to significantly improve the thin-film semiconducting properties of the CT complex.

4.4 CONCLUSION

This chapter describes the co-assembly of complementary donor and acceptor molecules that, while associated in solution, phase separate when cast onto a substrate. The cast thin-films, however, display electrical conductivities and ambipolar charge mobilities that are significantly higher than that of the component donor and acceptor molecules. This difference can be attributed to dopant donor or acceptor molecules that maintain the partially ionized state of the bulk acceptor or donor assemblies through residual charge transfer interactions despite phase separation. Functionalizing the molecules with hydrogen-bonding units further improves the electronic properties of the resulting thin film. These supramolecular complexes could open new doors to the large-scale development of electronics entirely comprised of supramolecular interactions between electro-active small molecules.

4.5 MATERIALS AND METHODS

General Methods

All reagents were purchased from commercial suppliers and used without further purification unless stated otherwise. Column chromatography was carried out on silica gel 60F (Merck 9385, 0.040-0.063 mm. Nuclear magnetic resonance (NMR) spectra were recorded on a Bruker Avance III 600 MHz, Bruker Avance III 500 MHz, and Agilent 500 MHz spectrometers, with working frequencies of 600, 500, and 500 MHz (^1H NMR), respectively, and at 150, 125, and 125 MHz (^{13}C NMR), respectively. Chemical shifts are reported in ppm relative to the signals corresponding to the residual non-deuterated solvents ($CDCl_3$: $\delta H = 7.24 ppm$ and $\delta C = 77.23 ppm$. High-resolution mass spectra (HRMS) were measured on an Agilent 6210 Time-of-Flight (TOF) LC-MS, using an ESI source, coupled with Agilent 1100 HPLC stack.

All samples were prepared by dissolving the requisite mass (or moles) of material into toluene, and ultrasonicating the solution to break up any aggregates. Finally, the solutions were heated gently

(using a heat gun) until the boiling point of toluene, after which they were allowed to cool under ambient conditions. For the co-assemblies **1•2** and **3•4**, heat caused the solutions to turn clear colorless, and orange (due to CT interactions) upon cooling to room-temperature.

All substrates (with the exception of cleaved mica) were cut from a four-inch wafer into 2×2 cm squares using a diamond cutter, scrubbed with soapy water, cleaned by ultrasonication in a 1:1:1 mixture of Me_2CO/MeOH/iPrOH and then blown dry in a stream of N_2 gas. Finally, the substrates were UV-ozone cleaned for 30 minutes before material was deposited onto the surface.

Synthesis of **1** *and* **3**

TsOPEG4OH (**I**). To a solution of tetraethylene glycol (16.5 g, 109 mmol), triethylamine (15.0 mL, 108 mmol) and 4-dimethylaminopyridine (DMAP, 0.665 g, 5.44 mmol) in DCM (100 mL) was slowly added p-toluenesulfonyl chloride (20.8 g, 109 mmol). The reaction was stirred for 2 hrs before diluting in ethyl acetate and filtering out the amine salt. The ethyl acetate washings were concentrated under vacuum and the product purified by column chromatography (DCM, then 2% MeOH/DCM, then 5% MeOH/DCM) to give a colorless liquid (13.3 g, 35%). ^{1}H NMR (400 MHz; $CDCl_3$): δ 7.81 (d, 2H), 7.34 (d, J = 8.0 Hz, 2H), 4.17 (dd, J = 5.4, 4.3 Hz, 2H), 3.72-3.70 (m, 4H), 3.69 (t, J = 3.2 Hz, 2H), 3.65 (t, J = 3.3 Hz, 2H), 3.61 (q, J = 4.2 Hz, 6H), 2.45 (s, 3H), 1.58 (d, J = 9.2 Hz, 1H). ^{13}C NMR (126 MHz; $CDCl_3$): δ 129.9, 129.2, 128.1, 126.4, 72.5, 71.7, 70.79, 70.75, 70.54, 70.36, 69.3, 68.8, 61.9. HRMS calc m/z for $C_{15}H_{24}O_7S$: $[M + Na]^+$ 371.1135, found 371.1146.

TsOPEG4OTs (**II**). This product was obtained from the reaction to make compound **I**, it eluted in 2% MeOH/DCM in the column and was obtained as a colorless liquid (18 g, 33%). ^{1}H NMR (499 MHz; $CDCl_3$): δ 7.80-7.78 (d, 4H), 7.34 (d, J = 8.0 Hz, 4H), 4.15 (dd, J = 5.4, 4.3 Hz, 4H), 3.68 (t, J = 4.8 Hz, 4H), 3.58-3.54 (m, 8H), 2.44 (s, 6H). ^{13}C NMR (126 MHz; $CDCl_3$): δ 129.9, 129.3, 128.1, 126.5, 70.83, 70.64, 69.3, 68.8, 60.9. HRMS calc m/z for $C_{22}H_{30}O_9S_2$: $[M + Na]^+$ 525.1223, found 525.1238.

N3PEG4OH (III). To a solution of **I** (16.46 g, 47.3 mmol) in DMF (30 mL) was added sodium azide (3.90 g, 60.0 mmol) and left heating at 60°C for 3 hrs. After cooling to room temperature, the crude was diluted in ethyl acetate and the precipitate filtered off. The solvent was then removed under vacuum to give a colorless liquid in quantitative yield. ^{1}H NMR (400 MHz, $CDCl_3$): δ 3.75 – 3.71 (m, 2H), 3.70 – 3.65 (m, 10H), 3.62 (ddd, J = 5.8, 3.2, 1.2 Hz, 2H), 3.40 (t, J = 5.1 Hz, 2H). ^{13}C NMR and HRMS have been previously reported[256] (reference Compound 37). The previously reported[256] ^{1}H NMR matches that of the synthesized **III**.

N3PEG4N3 (IV). To a solution of **II** (16.46 g, 32.75 mmol) in DMF (30 mL) was added sodium azide (6.39 g, 98.0 mmol) and left heating at 60°C for 3 hrs. After cooling to room temperature, the crude was diluted in ethyl acetate and the precipitate filtered off. The solvent was then removed under vacuum to give a colorless liquid in quantitative yield. ^{1}H NMR (400 MHz; $CDCl_3$): δ 3.68 (q, J = 3.6 Hz, 12H), 3.39 (t, J = 5.0 Hz, 4H). ^{13}C NMR (126 MHz; $CDCl_3$): δ 70.8, 70.1. HRMS has been previously reported[257] (reference Compound A7). The previously reported[257] ^{1} and ^{13}C NMR matches that of the synthesized **IV**.

NH2PEG4OH (V). To a solution of **III** (8.50 g, 38.7 mmol) in THF/water (50/5 mL) was added triphenylphosphine (12.6 g, 47.7 mmol). The reaction was left stirring for 2 hrs before concentrating under vacuum. The crude was partitioned between water (10 mL) and toluene (200 mL), and the aqueous layer was then collected and dried under vacuum to give a light yellow liquid (7.10 g, 95%). ^{1}H NMR (499 MHz, $CDCl_3$): δ 3.75 – 3.70 (m, 2H), 3.69 – 3.62 (m, 8H), 3.62 – 3.55 (m, 4H), 2.93 – 2.87 (m, 2H). ^{13}C NMR spectra[258] (reference compound 31) and HRMS spectra[259] (reference compound 6) have been previously reported. The previously reported[258,259] ^{1}H NMR matches that of the synthesized **V**.

NH2PEG4NH2 (VI). To a solution of **IV** (9.47 g, 38.8 mmol) in THF/water (50/5 mL) was added triphenylphosphine (23.0 g, 87.6 mmol). The reaction was left stirring for 2 hrs before concentrating under vacuum. The crude was partitioned between water (10 mL) and toluene (200 mL), and the aqueous layer was then collected and dried under vacuum to give a light yellow liquid (7.08

g, 95%). ^{1}H NMR (400 MHz; $CDCl_3$): δ 3.66-3.62 (m, 8H), 3.52-3.49 (m, 4H), 2.84 (q, J = 5.4 Hz, 4H), 1.82 (b, 4H). ^{13}C NMR (126 MHz; $CDCl_3$): δ 72.7, 70.41, 70.27, 61.6. HRMS calc m/z for $C_8H_{20}N_2O_3$: $[M+H]^+$ 193.1547, found 193.1542.

C8SNHPEG4NH2 (**VII**). To a solution of **VI** (2.00 g, 10.4 mmol) and triethylamine (1.45 mL, 10.4 mmol) in DCM (15 mL) was added 1-octanesulfonyl chloride (1.02 mL, 5.20 mmol) and left stirring for 1 hr before concentrating under vacuum, diluting in ethyl acetate and filtering the precipitate off. The product was purified by column chromatography (5% MeOH/DCM, then 10% MeOH/5% Et_3N/DCM) to give a light yellow liquid (1.84 g, 48%). ^{1}H NMR (400 MHz; $CDCl_3$): δ 6.20-6.14 (m, 1H), 3.77-3.69 (m, 4H), 3.67-3.57 (m, 9H), 3.52-3.45 (m, 1H), 3.26 (dt, J = 9.6, 4.8 Hz, 2H), 3.02-2.93 (m, 2H), 1.85-1.76 (m, 2H), 1.63-1.51 (m, 2H), 1.44-1.35 (m, 2H), 1.33-1.20 (m, 8H), 0.88-0.82 (m, 3H). ^{13}C NMR (126 MHz; $CDCl_3$): δ 70.2, 69.91, 69.74, 69.5, 66.8, 53.0, 42.7, 39.9, 31.8, 29.12, 29.05, 28.4, 24.9, 23.5, 22.6, 14.1. HRMS calc m/z for $C_{16}H_{36}N_2O_5S$: $[M+H]^+$ 369.2418, found 369.2428.

PMDIPEG4NHSC8 (**VIII**) (Molecule **1**). To a solution of compound **VII** (0.520 g, 1.41 mmol) in anhydrous DMF (5 mL) was added pyromellitic dianhydride (0.123 g, 0.565 mmol) and stirred for 12 hrs at 100°C under nitrogen. After cooling to room temperature, the solvent was evaporated under vacuum and the product purified by column chromatography (5% MeOH/DCM) to give a slightly brown solid (0.156 g, 30%). ^{1}H NMR (400 MHz; $CDCl_3$): δ 8.28-8.26 (m, 2H), 4.98 (q, J = 5.5 Hz, 2H), 3.97 (t, J = 5.5 Hz, 4H), 3.79 (t, J = 5.5 Hz, 4H), 3.66 (dd, J = 5.6, 3.0 Hz, 4H), 3.61 (t, J = 4.1 Hz, 16H), 3.27 (q, J = 5.2 Hz, 4H), 3.01 (dd, J = 14.6, 6.7 Hz, 4H), 1.83-1.76 (m, 4H), 1.44-1.38 (m, 4H), 1.38-1.20 (m, 16H), 0.90-0.84 (m, 6H). ^{13}C NMR (126 MHz; $CDCl_3$): δ 166.3, 137.3, 118.3, 70.62, 70.56, 70.38, 70.14, 70.09, 67.8, 52.8, 43.2, 38.0, 31.8, 29.18, 29.07, 28.4, 23.7, 22.7, 14.2. HRMS calc m/z for $C_{42}H_{70}N_4O_{14}S_2$: $[M+Na]^+$ 941.4222, found 941.4227

PMDIPEG4OH (**IX**) (Molecule **3**). To a solution of compound **V** (5.00 g, 25.9 mmol) in anhydrous DMF (30 mL) was added pyromellitic dianhydride (2.60 g, 11.8 mmol) and stirred for 12 hrs at 100°C under nitrogen. After cooling to room temperature, the solvent was evaporated under vac-

uum and the product purified by column chromatography (5% MeOH/DCM) to give a white solid (2.22 g, 33%). ^{1}H NMR (499 MHz, $CDCl_3$): δ 8.28 (s, 2H), 3.96 (s, 4H), 3.78 (s, 4H), 3.64 (s, 8H), 3.59 (s, 12H), 3.55 (s, 4H). ^{13}C NMR (101 MHz, CDCl3) δ 166.35, 137.37, 118.34, 72.61, 70.71, 70.60, 70.38, 70.17, 67.79, 61.78, 38.07. HRMS calc m/z for $C_{26}H_{36}N_2O_{12}$: $[M + Na]^+$ 591.2166, found 591.2163.

Synthesis of **2** *and* **4**

NphOPEG4OH (**X**) (Molecule **4**). A solution of 1,5-dihydroxynaphthalene (0.500 g, 3.12 mmol), compound **I** (2.40 g, 6.89 mmol) and cesium carbonate (2.50 g, 7.67 mmol) in anhydrous DMF (10 mL) was heated at 100° for 12 hrs under nitrogen. After cooling, the reaction was diluted in ethyl acetate and the precipitate filtered off. The solvent was removed under vacuum and the product purified by column chromatography (5%MeOH/DCM) to give a light brown liquid (0.620 g, 36%). ^{1}H NMR (400 MHz; $CDCl_3$): δ 7.86 (d, J = 8.6 Hz, 2H), 7.34 (dd, J = 8.2, 7.8 Hz, 2H), 6.85 (d, J = 7.6 Hz, 2H), 4.30 (t, J = 4.9 Hz, 4H), 4.00 (t, J = 4.9 Hz, 4H), 3.82-3.80 (m, 4H), 3.73-3.64 (m, 16H), 3.59-3.57 (m, 4H), 2.01 (d, J = 4.8 Hz, 2H). ^{13}C NMR (126 MHz; $CDCl_3$): δ 154.4, 126.9, 125.2, 114.7, 105.8, 72.6, 71.1, 70.7, 70.4, 69.9, 68.0, 61.8. HRMS calc m/z for $C_{26}H_{40}O_{10}$: $[M + H]^+$ 513.2694, found 513.2700.

NphPEG4OTs (**XI**). To a solution of **X** (1.91 g, 3.73 mmol), triethylamine (1.10 mL, 7.90 mmol) and DMAP (0.100 g, 0.818 mmol) in DCM (10 mL) was added p-toluenesulfonyl chloride (1.42 g, 7.45 mmol) and the reaction was stirred for 2 hrs before diluting in DCM (50 mL) and partitioning the solution in dilute citric acid. The organic layer was collected, dried under magnesium sulfate and dried under vacuum to give a dark brown liquid (2.37 g, 77%). ^{1}H NMR (499 MHz; $CDCl_3$): δ 7.86-7.84 (d, 2H), 7.81-7.76 (d, 4H), 7.34 (d, 2H), 7.32 (d, 4H), 6.85-6.82 (m, 2H), 4.29 (t, J = 4.9 Hz, 4H), 4.12 (q, J = 4.6 Hz, 4H), 3.98 (t, J = 4.8 Hz, 4H), 3.78 (dd, J = 5.8, 3.7 Hz, 4H), 3.67-3.65 (m, 8H), 3.61-3.59 (m, 4H), 3.57 (dd, J = 5.5, 3.3 Hz, 4H), 2.40 (s, 6H). ^{13}C NMR (126 MHz; $CDCl_3$):

δ 154.4, 144.9, 133.1, 129.3, 126.8, 126.5, 125.2, 114.7, 105.8, 71.1, 70.84, 70.81, 70.66, 69.9, 69.3, 68.8, 68.0, 21.7. HRMS calc m/z for $C_{40}H_{52}O_{14}S_2$: $[M + Na]^+$ 843.2691, found 843.2701.

NphOPEG4N3 (**XII**). Compound **XI** (2.38 g, 2.88 mmol) was dissolved in DMF (10 mL) and sodium azide (0.562 g, 8.64 mmol) was added, then the reaction was heated at 60°C for 2 hrs. The crude was diluted in ethyl acetate, filtered, and the washings were collected and dried under vacuum to give a brown liquid (1.60 g, 98%). ^{1}H NMR (499 MHz; $CDCl_3$): δ 7.86 (d, J = 8.4 Hz, 2H), 7.34 (t, J = 8.0 Hz, 2H), 6.84 (d, J = 7.7 Hz, 2H), 4.30 (t, J = 4.9 Hz, 4H), 4.00 (t, J = 4.9 Hz, 4H), 3.80 (dt, J = 5.9, 3.3 Hz, 4H), 3.71 (dd, J = 5.6, 3.8 Hz, 4H), 3.69-3.68 (m, 4H), 3.65 (td, J = 5.9, 3.2 Hz, 8H), 3.35 (t, J = 5.0 Hz, 3H). ^{13}C NMR (126 MHz; $CDCl_3$): δ 154.4, 126.9, 125.2, 114.7, 105.8, 71.1, 70.89, 70.81, 70.11, 69.92, 68.0, 50.8. HRMS calc m/z for $C_{26}H_{38}N_6O_8$: $[M + H]^+$ 585.2643, found 585.2646.

NphOPEG4NH2 (**XIII**). To a solution of **XII** (0.800 g, 1.42 mmol) in THF/water (10/1 mL) was added triphenylphosphine (0.931 g, 3.55 mmol) and let stir for 2 hrs. The reaction was concentrated under vacuum and used without purification for the next step.

NphOPEG4NHCONHC8 (**XIV**) (Molecule **2**). The crude of **XIII** (assuming full conversion) was dissolved in pyridine (10 mL) and octylisocyanate (0.551 mL, 3.21 mmol) was added, then the reaction was refluxed for 12 hrs before cooling and concentrating under vacuum. The product was purified by column chromatography (5% MeOH/DCM) to give a white solid (0.560 g, 48%). (^{1}H NMR (499 MHz; $CDCl_3$): δ 7.85 (d, J = 8.5 Hz, 2H), 7.34 (t, J = 8.0 Hz, 2H), 6.84 (d, J = 7.7 Hz, 2H), 4.30 (t, J = 4.7 Hz, 4H), 4.01 (t, J = 4.7 Hz, 4H), 3.84-3.83 (m, 4H), 3.70-3.69 (m, 4H), 3.63-3.58 (m, 8H), 3.51 (q, J = 4.4 Hz, 4H), 3.30 (t, J = 4.9 Hz, 4H), 3.07-3.04 (m, 4H), 1.40-1.38 (m, 4H), 1.27-1.25 (m, 4H), 1.22 (s, 14H), 0.88-0.85 (m, 6H). ^{13}C NMR (126 MHz; $CDCl_3$): δ 159.1, 154.3, 126.8, 125.3, 114.7, 105.9, 71.1, 70.8, 70.51, 70.46, 70.2, 69.9, 68.0, 40.6, 31.9, 30.3, 29.4, 27.0, 22.7, 14.2. HRMS calc m/z for $C_{44}H_{76}N_4O_{10}$: $[M + Na]^+$ 843.5454, found 843.5455

Optical Absorption Spectroscopy

UV-vis absorbance spectra were recorded using a Perkin Elmer Lambda 1050 spectrophotometer. The path length of the cuvette in all cases was 0.1 mm. Thin-film absorption measurements were performed on the by Perkin Elmer Lambda 1050 spectrophotometer by utilizing a 150 mm integrating sphere. The samples were prepared by drop-casting 40 μl of material onto cleaned glass slides, and allowed to dry completely in ambient conditions before measurement.

Variable temperature absorbance experiments were performed using a CaryWin spectrometer with a temperature controlled stage. For the temperature ramp experiments, the cuvette was heated at 1°C / min using the built-in "Thermal" software package and data point were recorded every 0.5°C at 450 nm.

Fluorescence Spectroscopy

Fluorescence spectra were recorded using an ISS PC1 spectrofluorimeter. The path length of the cuvette was 3 mm. Emission spectra were recorded at an excitation wavelength of 300 nm. To control the number of emitted photons incident on the photodetector, neutral density filters were placed in the path of the emitted photon beam.

Diffusion Ordered Nuclear Magnetic Resonance Spectroscopy

DOSY experiments were performed on an Agilent DD2 500 Mhz system. The Dbppste_cc (bipolar pulse pair stimulated echo with convection correction) pulse sequence was used with a defocusing time of 2 ms, and diffusion delay of 50 ms. The gradient was varied from 0 to 95% (max gradient strength 60 G/cm) in 32 increments. MestreNova's Bayesian DOSY transform was used to process these data.

Atomic Force Microscopy

All tapping-mode atomic force microscopy (AFM) measurements were performed in air using a TESPA-V2 probe (Bruker AFM Probes). The samples were either mounted on cleaved mica or cleaned transistor-grade silicon (for later device measurements) by spin-coating 20 μl of the relevant solution onto the relevent substrates. The spin conditions used were a spin speed of 5000 r.p.m, accelerating at 1000 r.p.m/s, for a duration of 59 s.

Grazing Incidence X-ray Scattering

Grazing Incidence X-ray Scattering was collected at Argonne National Lab's Advanced Photon Source, Sector 8-ID-E. The beam energy was 7.35 KeV, with an incident angle of 0.3°. Samples were prepared by drop casting a 20 μL of prepared solution onto a precleaned silicon wafer and allowing the solution to dry under ambient conditions.

Ultraviolet Photoelectron Spectroscopy

Ultraviolet Photoelectron Spectroscopy (UPS) data was used to determine the HOMO level of the organic molecules. UPS data was collected using a Thermo Scientific ESCALAB 250Xi with a -8.0 V sample bias and a He I ($h\nu$ = 21.2 eV) source. The spectrum width of UPS data is related to the work function, ϕ, according to the equation $\phi = h\nu - BE$. The edges of the spectrum were fit in order to determine the binding energy.[260] In the inelastic cutoff region, the intercept between the tangent to the main peak and a linear fit to the background level was used as the edge of the spectrum. At the Fermi edge, the onset of the peak was determined as energy at which the intersection between the local tangent to the spectrum and a linear fit to the background level occurs. The difference in energy between the Fermi edge and the inelastic cutoff region was then subtracted from the incident energy (21.2 eV) in order to determine the HOMO level of the material.

Fourier Transform Infrared Spectroscopy

Attenuated total reflectance Fourier transform infrared spectroscopy (ATR-FTIR) was performed on a ThermoNicolet Nexus 870 spectrometer equipped with a Harrick GATR module. Spun coat thin films of samples on silicon substrates were pressed against the germanium crystal for ATR spectra acquisition. Substrate signals were used for background subtraction from the sample signals.

Conductivity and Mobility Measurements

Four-inch Silicon Quest International Si wafers with a 300 nm oxide surface coating were used as substrates on which devices were fabricated. The wafers were cleaned before a thin film of material was deposited onto the surface using the spin-coating methods described above. Electrodes (spaced at 10 μm) were patterned onto the surface of the wafer by thermally evaporating 50 nm of Au through a TEM grid shadow mask at a pressure of 10^{-6} mbar. DC conductivity and field-effect mobility measurements were performed at a Signatone probe station, in conjunction with an Agilent 4155C semiconductor parameter analyzer. Current output was measured at room temperature for DC voltage sweeps from -5 to +5 V. All measurements were carried out in a US FED STD 209E Class 100 (ISO 5) clean room.

A list of the average device dimensions used in all thin-film electrical measurements is reported in Table 4.3.

Table 4.3: Average device dimensions for all thin-film conductivity and field-effect mobility measurements reported

	1•2							**3**	**4**	**3•4**
χ_1	0	0.2	0.4	0.5	0.6	0.8	1			
Length between electrodes (L) (μm)	10	10	10	10	10	10	10	10	10	10
Electrode width (W) (μm)	200	200	200	200	200	200	200	300	300	300
Average film thickness (t) (nm)	17.0	13.9	11.7	15.6	14.2	11.1	12.5	13.1	10.3	15.6
Devices measured (n)	8	7	7	8	7	6	8	7	7	7

5 Intermolecular Charge-Transfer and Molecular Exchange Between Complementary Donor/Acceptor Peptide Amphiphiles

5.1 objectives and significance

Supramolecular systems exist, by definition, on a spectrum of thermodynamics and kinetics. Deriving function from supramolecular systems involves understanding the dynamic behavior of molecules within the constraints of their environment. Within the context of charge transfer (CT) interactions, dynamics and reversibility of CT between neighboring crystalline donor and acceptor molecules within a three-dimensional architecture are what define the ferroelectric and semiconducting behavior of these systems. Understanding the molecular kinetics and interactions between bio-inspired molecules can inspire knowledge about natural systems, and drive the development of translational artificial supramolecular materials. This chapter takes inspiration from previous work on hydrogen-bonded CT complexes to understand the exchange between complementary donor and acceptor moieties in aqueous solvents, when functionalized with hydrogen-bonding peptides.

5.2 background

Adaptive supramolecular interactions are ubiquitous in nature, controlling and defining function through the kinetics and thermodynamics of assembly driven by non covalent interactions. To that end, peptide amphiphiles (PAs) have long been heralded for applications based on their chemistry and assembling morphologies.[19,20,28,261] The combination of hydrophobic effects, electrostatic interactions and hydrogen bonding interactions that drive the formation of supramolecular β-sheets help these small molecules self-assemble in aqueous conditions into the unique architectures from which their functions are derived. As an example, covalent attachment of biological epitopes to the hydrophilic segment of the PA molecules have enabled the expression of biological signals

and mediated specific cell growth and interactions.[30–34,37] The use of these materials in inherently dynamic systems therefore warrants study into the nature and kinetics of these interactions.

Understanding the kinetics of molecular and supramolecular interactions has, for a long time, utilized Förster resonance energy transfer (FRET), which measures the intermolecular distance between a complementary pair of donor and acceptor fluorophores,[262] X-ray absorption and scattering,[263] as well as radical-labelled moieties.[39] Most of these studies, while able to understand molecular dynamics on an aggregated scale, fail to resolve exchange at a molecular level. A recent study[42] examined the kinetics of molecular and supramolecular exchange using stochastic optical reconstruction microscopy (STORM) to resolve exchange dynamics between pre-assembled supramolecular structures, and revealed a molecular exchange mechanism involving the motion of clusters of molecules. The limitation in these studies, however, is their focus on the dynamics of non-interacting supramolecular assemblies with no intrinsic driving force for co-assembly. Studying the dynamics of multi-component supramolecular systems, where intermolecular association of *functional moieties* can be monitored, offers a fresh perspective on dynamics of supramolecular systems in biological and electronic applications, where interactions between systems of molecules are modulated by an intrinsic non-zero driving force.

The incorporation of intermolecular charge transfer (CT),[43] the positive association between complementary donor and acceptor moieties, is one way to investigate dynamics of functional supramolecular systems with a driving force towards association. CT interactions have been known to give rise to a myriad of supramolecular architectures, each with unique functional electronic properties. The strong association between the donor and acceptor moieties have enabled the diffusion-driven growth of millimeter-scale single co-crystals of perfectly alternating stacks of donor and acceptor molecules.[103] Many of these crystals have exhibited pleochroic[103] and room-temperature ferroelectric[78,79,197] behavior by virtue of their assembly and electronic structure. Translating this unique supramolecular motif to an aqueous medium through the incorporation of short peptide sequences has revealed[102,264–273] unique supramolecular assemblies due to the balance between charge

transfer, aromatic π-π stacking, hydrophobic, van der Waals, and hydrogen bonding non-covalent interactions. The ability to tune these intermolecular forces through chemistry and processing conditions have opened a variety of applications for these peptide CT complexes, from their use as energy transfer probes,[272,273] to elucidating conductivity by virtue of their CT energy levels,[225,274] to aiding biocatalytic reactions.[218]

The work in this chapter describes in great detail the self- and co-assembly of intermolecular charge transfer complexes, each functionalized with a short peptide sequence to impart amphiphilicity and structure-driving hydrogen bonding motifs. The introduction of CT interactions to the hydrophobic core of existing architectures alters the thermodynamics of assembly, and kinetics of association between molecules within, as well as between, supramolecular assemblies. Specifically, this work will focus on the intrinsic photophysical properties of the organic donor and acceptor molecules to study the assembly and kinetics of exchange between supramolecular nanostructures with a positive driving force towards association.

5.3 RESULTS AND DISCUSSION

5.3.1 *Molecular Design Considerations*

Taking inspiration from previous work[103] on LASO CT complexes, initial efforts into developing an amphiphilic charge transfer (CT) small molecule involved either adding a trialanine (Figure 5.1a) or alternating valine-glutamic acid (VEVE) tetrapeptide (Figure 5.1b) sequence to of complementary donor/acceptor moieties. The VEVE peptide sequence was chosen for its propensity to laterally aggregate through dimerization of carboxyl groups on the glutamic acid moieties on neighboring PA molecules, forming wide sheet-like bilayer structures.[22] This supramolecular morphology would aid the assembly of aromatic charge transfer moieties, which tend to associate in a rigid face-to-face stacking arrangement.[275] Solubility limitations in aqueous, however, hindered the use of the trialanine CT peptides. The peptides in Figure 5.1b too, were limited in their use, since

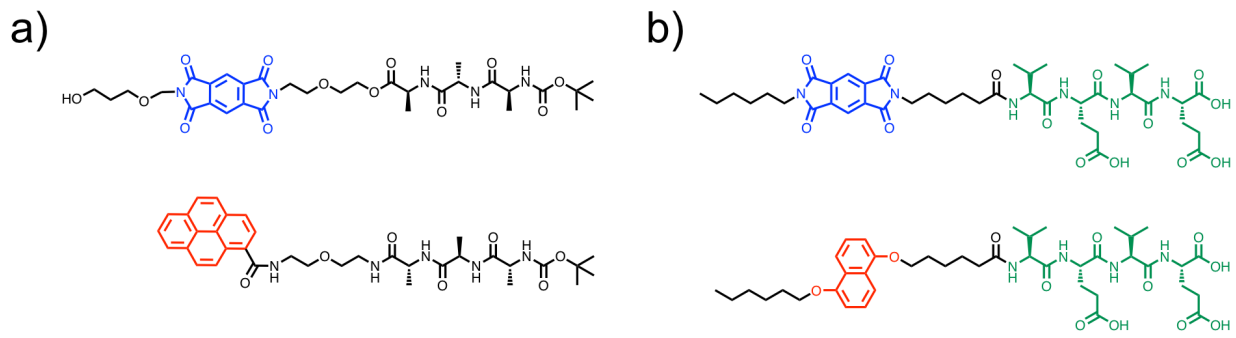

Figure 5.1: Initial molecular design for acceptor/donor peptide amphiphiles incorporating pyromellitic diimide (PMDI) acceptor moieties. This molecular design was scrapped due to solubility issues. (a) PMDI acceptor and pyrene donor molecules, incorporating a trialanine peptide sequence. (b) PMDI acceptor and naphthalene donor molecules, incorporating alternating hydrophobic valine (V) and negatively charged glutamic acid (E) residues. This design failed due to the instability of the PMDI core to basic HPLC purification conditions.

the pyromellitic diimide (PMDI) acceptor core underwent ring-opening hydrolysis upon purification by High-Performance Liquid Chromatrography (HPLC) under basic conditions. While steps could be taken to re-close the imide ring, re-purification would result in the same issues. As a result, these two initial designs were discarded.

This chapter employs a peptide amphiphile design (Figure 5.2) that incorporates an alternating valine-lysine tetrapeptide sequence as the β-sheet assembling and the hydrophilic section of the amphiphile. At the N-terminus of the peptide sequence, naphthalene diimide (NDI) acceptor (**1**) or naphthalene donor (**2**) was attached, with brached or linear aliphatic tails, respectively, to impart solubility in aqueous solvents. In addition, a hexyl liner was added between the last amino acid and the donor/acceptor aromatic moiety, to allow flexibility in CT association and orientation. Finally, a control peptide amphiphile (**VKVK**) was designed, with the same tetrapeptide sequence, but with a 16-carbon linear aliphatic tail to impart amphiphilicity without donor/acceptor functionality.

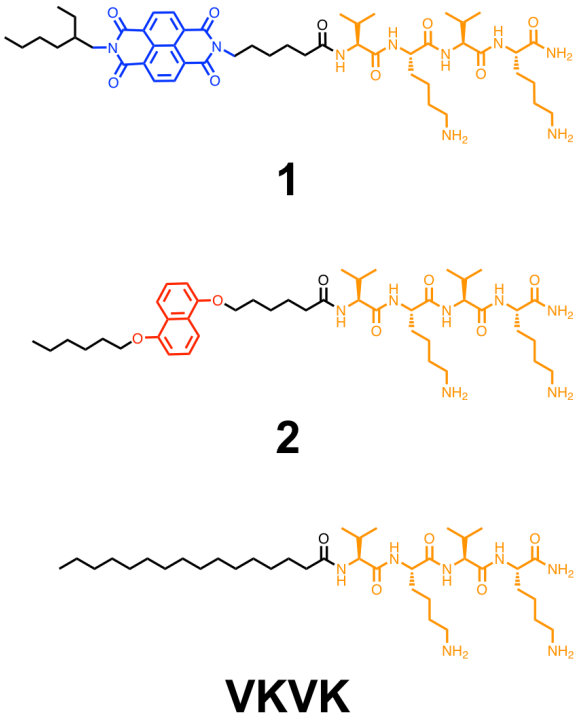

Figure 5.2: Amphiphiles incorporating a napthalene diimide (NDI) electron acceptor **1**, dioxynaphthalene **2**, or linear palmitic acid (**VKVK**) hydrophobic core to an alternating hydrophobic valine (V) and positively charged lysine (K) amino acid residues.

5.3.2 *Self-Assembly of* **1** *and* **2**

This work first investigates the influence of pH on the self-assembly of **1** and **2** by cryogenic transmission electron microscopy (cryo-TEM), atomic force microscopy (AFM), circular dichroism (CD) and small angle X-ray scattering (SAXS). Cryo-TEM of **1**, dissolved in Milli-Q water (pH ≈ 5) or Tris-buffered water (pH ≈ 8) illustrate (Figure 5.3a,b) the formation of long, one-dimensional nanostructures in solution. Specifically, at pH 5 these molecules self-assemble into (Figure 5.3a) twisted ribbons, a morphology that is corroborated by AFM images (Figure 5.3c) of the nanostructures under the same assembly conditions. This twisted morphology is unsurprising, as naphthalene diimide derivatives often assemble in a helical structure as a consequence of offset π-π interactions between neighboring NDI molecules.[268,270,276–281] Increasing the pH results (Figure 3.3b,d) in the assembly of shorter and wider supramolecular nanostructures. Indeed, SAXS illustartes a change in power law slope in the low-q Guinier regime, from (-1) at pH 5 to (-2) and pH 8. This in turn corresponds to a transition from ensemble averaged one-dimensional cylindrical nanostructures to two-dimensional ribbon-like structures with increasing pH,[282] corroborating the change in morphology observed using electron microscopy (Figure 5.3b) and surface imaging (Figure 5.3d) techniques.

Where microscopy and X-ray scattering illustrate this change in external nanostructure morphology, CD documents the change in *internal* supramolecular order upon changing pH. at pH 5, a negative Cotton effect is observed (Figure 5.3f) from 300 nm - 400 nm, corresponding to the π-π^* absorption (Figure 5.5a) polarized along the long-axis of the NDI chromophore.[279] Where a negative Cotton effect is indicative[279,283] of a left-handed helical NDI assembly, chiral inversion to a right-handed helical assembly, coupled with a hypochromic absorption change (Figure 5.5a) is observed (Figure 5.3f) when increasing the pH from 5 to 8.

It is abundantly clear that small changes in pH greatly influences the supramolecular assembly of the acceptor amphiphile **1**. Since the assembly of amino acids can shift their pKa transitions,[284,285] it can be envisioned that small changes in the pH of the solution can alter the protonation state of the assembled lysines in **1** and **2**, with a higher protonation state at mildly acidic pH, and lower

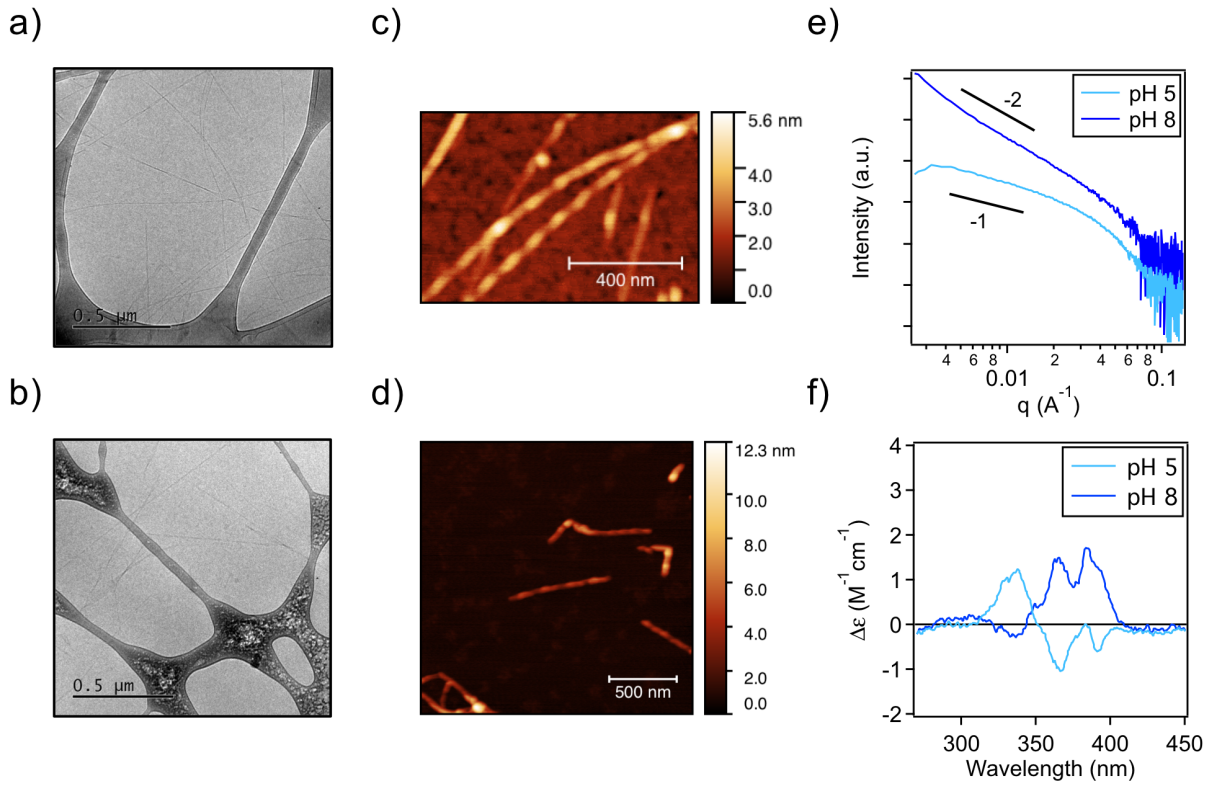

Figure 5.3: Representative cryogenic transmission electron microscopy of **1** assembled at (a) mildly acidic (pH 5) and (b) Tris-buffered mildly basic (pH 8) aqueous conditions. Surface characterization under (c) mildly acidic and (d) mildly basic conditions were carried out using atomic force microscopy. (e) Small angle X-ray scattering illustrates a change in the slope of the low-q Guinier scattering region upon increases in pH. (f) Circular dichroism indicates an inversion of NDI chiralitywhen the pH of the assembling solution is increased.

protonation state at mildly basic pH. In the context of the supramolecular assembly of **1**, mildly acidic pH and a higher lysine protonation state promotes the left-handed helical assembly of NDI, which dominates the non-covalent supramolecular interactions and drives the assembly of helical nanostructures. The small pitch of the helices explains why SAXS estimates the ensemble average of these structures to be cylindrical. At mildly basic pH, and lower lysine protonation state, intermolecular association and hydrogen bonding between the uncharged amino acid sequences dominates supramolecular assembly, driving right-handed helical NDI chirality and lateral aggregation to form wider and shorter.

The assembly of **2** depicts a similar story of pH-dependent supramolecular assembly. Cryo-TEM of **2** at pH 5 illustrates (Figure 5.4a) the formation of long fibrous nanostructures, a morphology that is maintained (Figure 5.4b) at Tris-buffered pH 8. This morphology is corroborated with AFM images of the PA assembly at both pH 5 (Figure 5.4c) and pH 8 (Figure 5.4d). In addition, SAXS of **1** exhibited (Figure 5.4e) minimal changes to the slope in the low-q Guinier region for both mildly acidic and mildly basic conditions, adding further evidence to suggest that changing the protonation state of the lysine amino acids does not influence the exterior supramolecular morphology.

Changes to the interior supramolecular order upon changes in pH can, however, be observed using CD (Figure 5.4f). At mildly acidic pH, a negative Cotton effect is observed at 195 nm, indicative of a random coil amino acid assembly. No CD band attributed to the aromatic naphthalene chromophore in **1**, however, was observed. Since naphthalene is intrinsically achiral, this suggests that at mildly acidic pH, there is little rigid association and assembly between neighboring naphthalene moieties, resulting in no observed chirality. Increasing the pH, however, results in a positive Cotton effect observed between 300-320 nm, as well as a negative Cotton effect between 227-203 nm. The peaks at 300-320 nm correspond to the π-π^* absorption (Figure 5.5b) polarized along the short axis of the naphthalene chromophore.[279] Similarly, the peaks at 227-238 nm can be attributed to the naphthalene long axis polarized transition. While the peak at 203 nm can be attributed to chirality arising from the peptide secondary structure, a definitive understanding of the structural motif is challenging due to interference from the aromatic naphthalene transitions. Regardless, it can be concluded that increases in pH induces chirality in the assembly of naphthalene moieties in **1**, likely due to stronger packing and chiral assembly of the small molecules upon deprotonation of lysine residues.

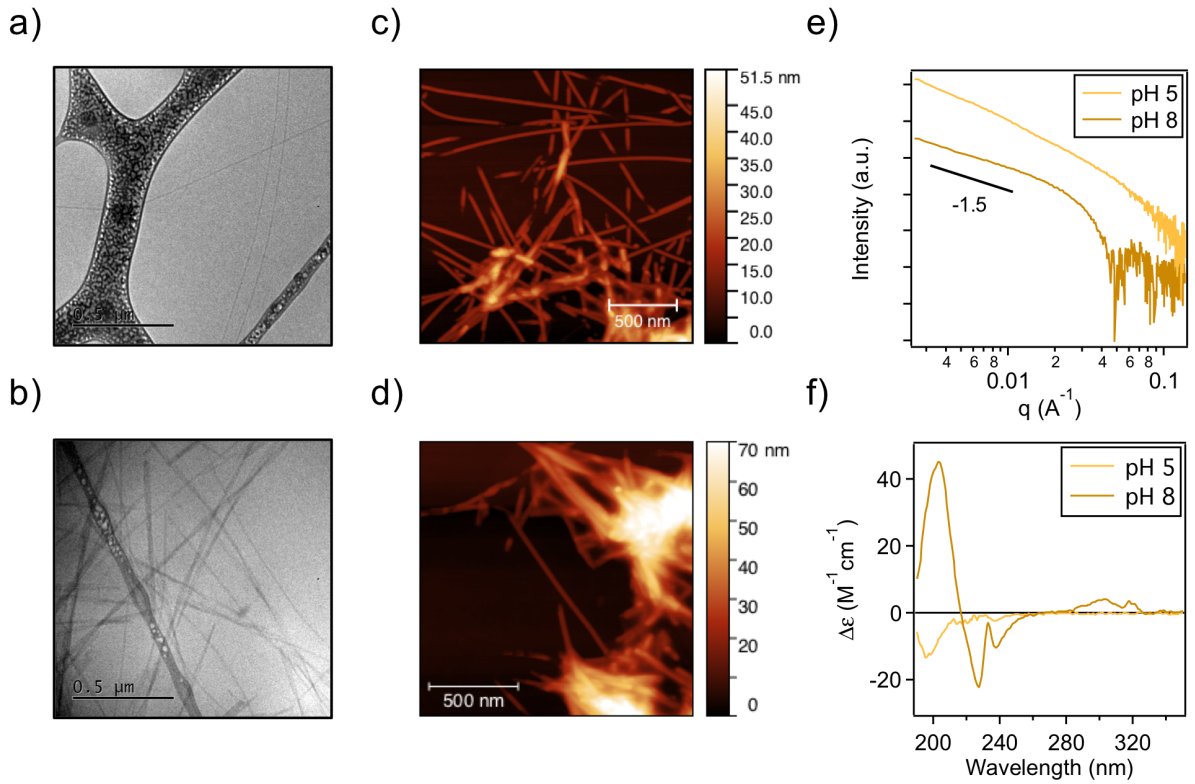

Figure 5.4: Representative cryogenic transmission electron microscopy of **2** assembled at (a) mildly acidic (pH 5) and (b) Tris-buffered mildly basic (pH 8) aqueous conditions. Surface characterization under (c) mildly acidic and (d) mildly basic conditions were carried out using atomic force microscopy. (e) Small angle X-ray scattering illustrates no significant change to the slope of the low-q Guinier scattering region upon changes in solution pH. (f) Circular dichroism indicates an induction of naphthalene chirality with increasing pH.

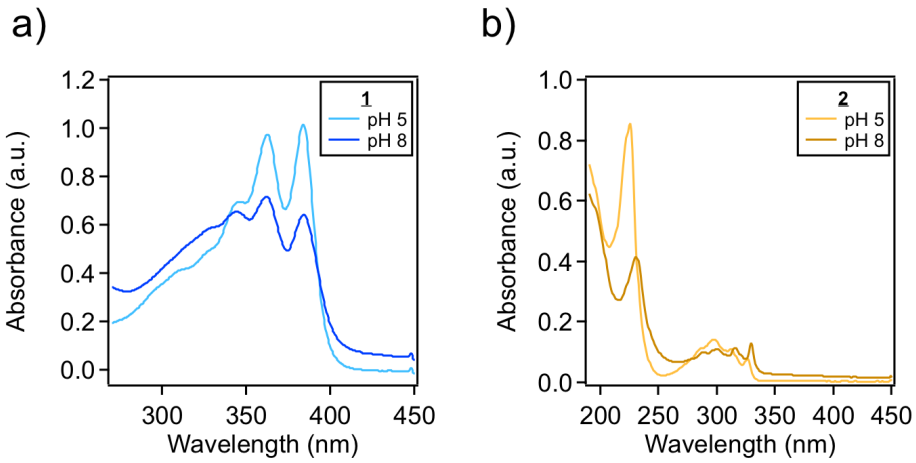

Figure 5.5: Absorption spectra of (a) **1** and (b) **2** at mildly acidic and Tris-buffered mildly basic conditions.

5.3.3 *Initial Co-Assembly and Charge Transfer Studies*

Having established the interplay between aromatic core and amino acid interactions in **1** and **2**, intermolecular interactions between co-assemblies of the amphiphilic acceptor/donor and small molecular donor/acceptors were studied using absorption spectroscopy. The co-assembly of donor amphiphile **2** and small molecular acceptor 7,7,8,8-tetracyanoquinodimethane (TCNQ) resulted in the appearance (Figure 5.6a) of a broad charge transfer absorption band at 500 nm, with a reduction of the TCNQ monoanion peak at 730 nm.[286] Similarly, the co-assembly of **2** with tetrachloro-1,4-benzoquinone (chloranil) also illustrates (Figure 5.6b) the presence of a broad charge transfer band at 400 nm. That these small donor and acceptor molecules are able to co-assemble with the acceptor and donor peptide amphiphiles lends credence to the possibility of forming a stable CT complex between complimentary donor/acceptor PAs in aqueous solvents, warranting further study on their co-assembly in aqueous solvents.

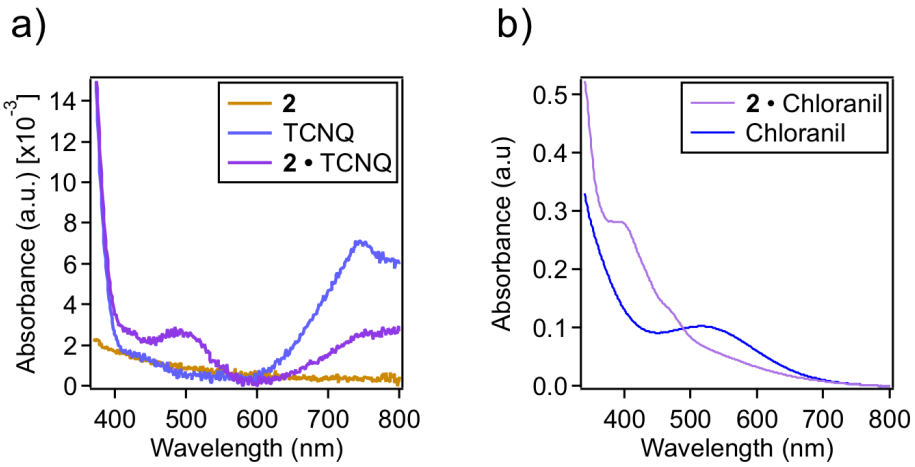

Figure 5.6: Absorption spectroscopy on co-assembly of (a) TCNQ and **2**, with a CT absorption at 500 nm, and a reduction of the TCNQ anion absorption upon co-assembly, and (b) Chloranil and **2**, with a CT absorption band at 400 nm.

5.3.4 *Co-Assembly of* **1** *and* **2**

The photophysical properties of the co-assembly between acceptor **1** and donor **2** peptide amphiphiles was examined using fluorescence emission, visible light absorption, and circular dichroism spectroscopy. Tracking the naphthalene fluorescence emission of **2** before and after co-assembly at pH 5 (Figure 5.7a) and pH 8 (Figure 5.7b) illustrates significant quenching upon co-assembly with electron acceptor **1**, suggestive of intermolecular interactions between the aromatic donor and acceptor chromophores. That the ratio of the naphthalene monomer emission peaks (at 333 nm and 347 nm) to the dimer emission peak (at 415 nm) is larger for co-assembly at pH 5 compared to pH 8 points to stronger intermolecular packing in the co-assembled **1•2** upon increasing pH and deprotonation of lysine residues. Absorption spectroscopy also reveals (Figure 5.7c) a broad charge transfer band at 500 nm for the co-assembled **1•2**, at both acidic and basic conditions, indicative of persistant CT interactions in **1•2** regardless of the local dielectric and electrostatic environment. The internal structure of the co-assemblies show (Figure 5.7d) show no difference in chirality between pH 5 and pH 8, where the chirality of the co-assembled **1•2** mimics the left-handed helical structure of **1** under mildly basic conditions. This observation

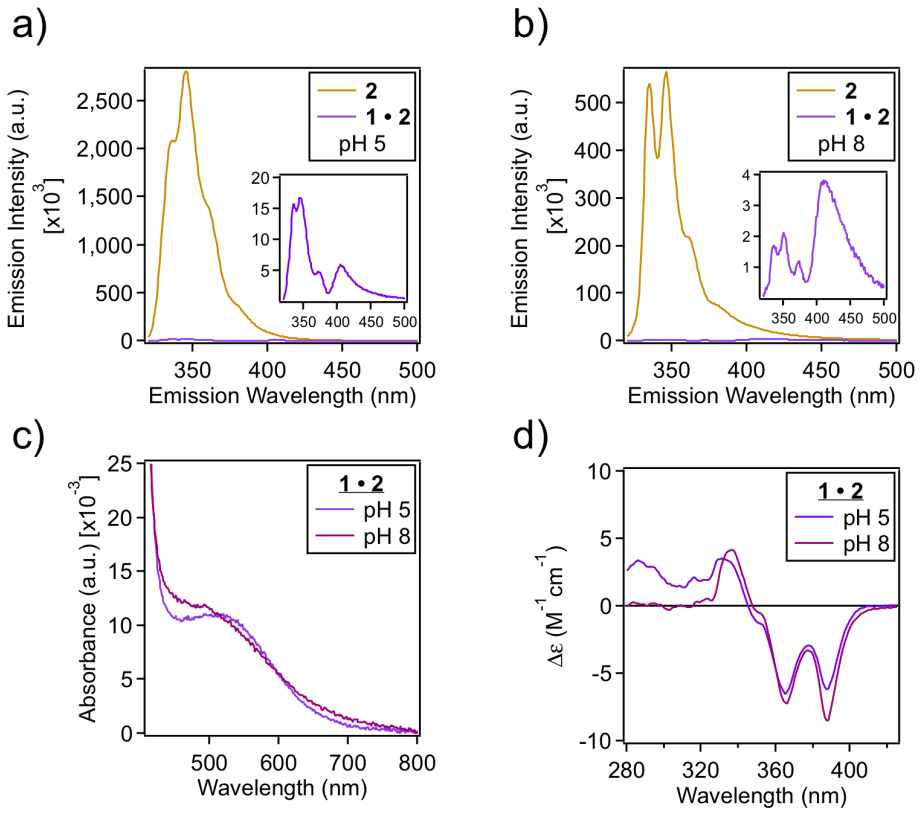

Figure 5.7: Fluorescence emission spectroscopy indicative of quenching of napthalene monomer fluorescence upon co-assembly of **1** and **2** at (a) pH 5 and (b) pH 8. (c) Co-assembly also results in a CT absorption band at 500 nm at both pH ranges. (c) Circular dichroism suggests that co-assembly at both pH 5 and pH 8 induce a packing structure that promotes left-handed NDI chirality

is in direct contrast with that for the self-assembly of **2**, where the chirality of the NDI core is dependent on the interplay between the π-π stacking of the aromatic cores and hydrogen bonding and secondary structure of the peptide sequence. In the co-assembled **1•2**, that the aromatic chiral handedness is independent of pH indicates that the driving force for supramolecular assembly is dominated by aromatic and charge transfer interactions in the hydrophobic core of the PA.

To distinguish whether the observed CT interactions are a consequence of aromatic association (between the NDI acceptor and naphthalene donor) or peptide interactions, co-assemblies of the donor **2** and the control **VKVK** were prepared. Fluorescence spectroscopy shows (Figure 5.7) no change in the naphthalene donor emission spectra upon co-assembly at either mildly acidic

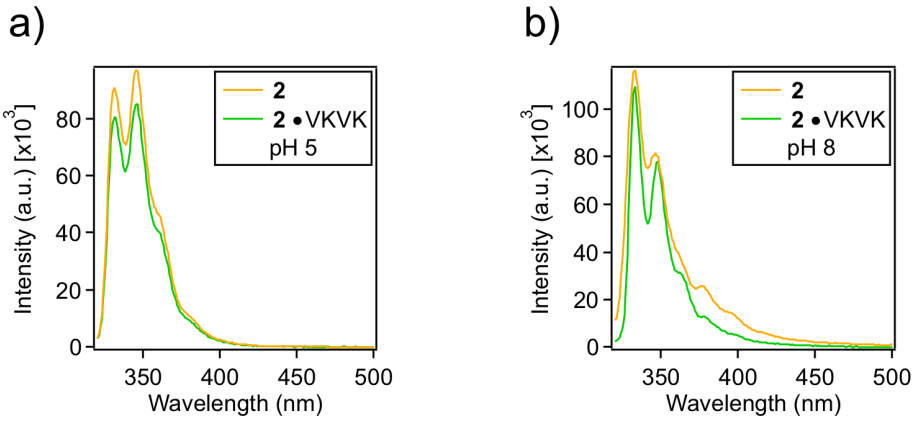

Figure 5.8: Fluorescence emission spectroscopy highlighting no change in the emission intensity of the napthalene monomer fluorescence upon co-assembly of **2** and **VKVK** at (a) pH 5 and (b) pH 8. This suggests that the emission quenching noticed in **1•2** is entirely due to CT interactions between aromatic donor and acceptor cores, and independent of amino acid interactions.

or mildly basic conditions, indicative of non-interacting association between **2** and **VKVK**. This result confirms intermolecular charge transfer interactions between NDI and naphthalene upon co-assembly of the acceptor **1** and donor **2** peptide amphiphiles.

Morphological characterization of **1•2** by cryo-TEM illustrates (Figure 5.9a,b) the formation of long nanostructures with no qualitative difference between co-assembly at pH 5 and pH 8. This suggests that co-assembly of **1** and **2**, while forming a stable CT complex, does not disrupt the supramolecular assembly of the amphiphilic molecules in the cooperative association required for a stable CT complex. To further illustrate this point, no significant changes were observed to low-q power law SAXS slopes (Figure 5.9c) of the self- and co-assembled amphiphilic molecules molecules. Broad peaks were observed for **1•2** at $q = 0.011$ Å^{-1} ($d = 57$ nm)and $q = 0.024$ Å^{-1} ($d = 26$ nm), suggestive of long-range spatial correlation[282] exclusive to the co-assembled **1•2**.

5.3.5 *Exchange Kinetics Between* **1** *and* **2**

Since intermolecular charge transfer requires close spatial proximity of the electron acceptor and donor molecules, CT interactions can be used as a metric to understand molecular mixing and

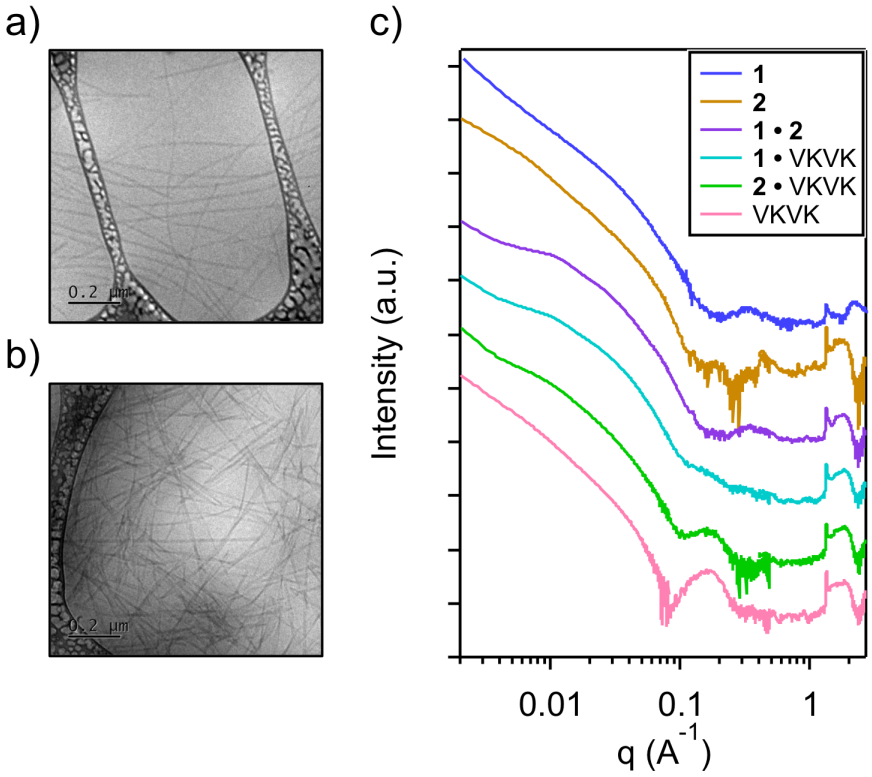

Figure 5.9: Cryo-TEM of **1•2** and (a) pH 5 and (b) pH 8, indicative that co-assembly does not disrupt supramolecular, hierarchical order. (b) Small angle X-ray scattering of **1**, **2**, **VKVK** and all the respective co-assemblies, where the dimensionality of nanostructure formation remains largely unchanged through all possible co-assembly permutations.

exchange between two assembled nanostructures. Here, the fluorescence emission of **2** is used as a metric for association between donor and acceptor nanostructures, since it was established that changes in emission only occur as a consequence of charge transfer interactions between the donor and acceptor amphiphilic molecules. Specifically, tracking the fluorescence emission of **2** provides real-time information about the mixing of **1** and **2**. As a proof of concept, injecting an equimolar solution of **1** into **2** (henceforth defined as **1 + 2**) resulted in significant fluorescence quenching (Figure 5.10a) after ageing the mixture at room temperature for an hour. To differentiate the effects of CT between **1** and **2** from that of dilution, an equimolar solution of **VKVK** into **1** was injected into **2** (defined as **VKVK+2**). In this control mixing experiment, the fluorescence emission intensity at 335 nm and 346 nm was halved over the course of an hour, indicative of dilution effects between non-interacting species. In contrast, that the mixed system **1 + 2** displayed significantly more quenching suggests CT interactions drive mixing between the donor and acceptor nanostructures.

Tracking the fluorescence quenching (defined as the difference in fluorescence emission between **VKVK+2** and **1 + 2**) shows (Figure 5.10b) that the bulk of this fluorescence quenching in **1 + 2** occurs within the first few seconds of mixing. This is unprecedented, as mixing of two identical non-interacting supramolecular nanostructures have been shown to occur over the course of hours or days.[42] This implies that charge transfer between the donor and acceptor amphiphiles is the driving force for the rapid inter-fiber exchange and intermolecular mixing, likely involving molecular or cluster dissociation,[42] followed by re-assembly and association of donor and acceptor moieties. To conform this hypothesis, the emission intensity of **2** quenches at a much slower rate when mixed with non-intearcting **VKVK**. Observed quenching is likely due to diffusion effects, as well as photobleaching and photodegradation of the aromatic naphthalene moieties in the presence of CO_2.[287–290]

Attempts to modulate the mixing kinetics of **1 + 2** involved reducing the mole fraction of **1** and **2** in solution. This required the co-assembly of the donor or acceptor molecule non-interacting **VKVK** before annealing the solution to form a homogeneous supramolecular assembly

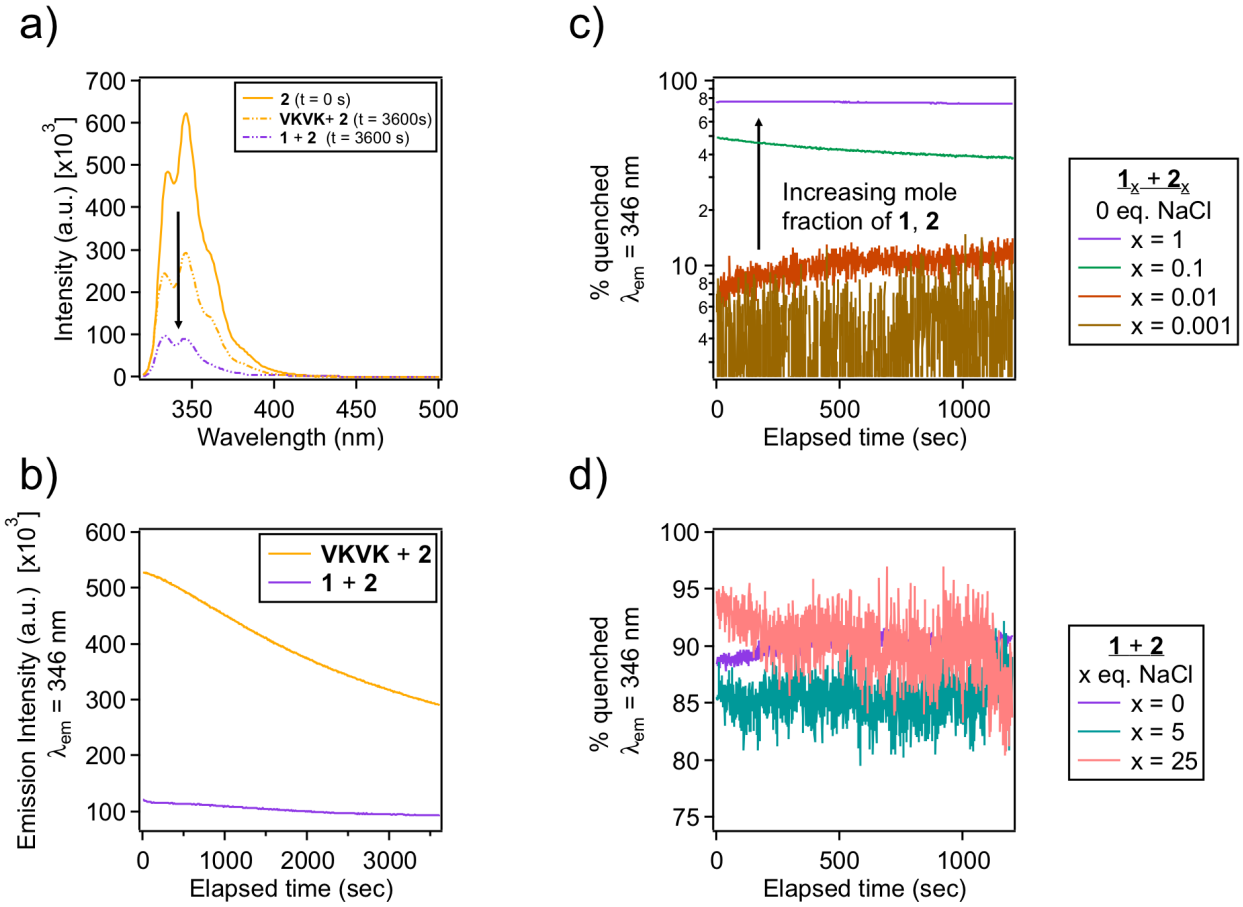

Figure 5.10: Fluorescence mixing experiments between **1** and **2** to understand the kinetics of association. All mixing experiments were done by pre-assembling solutions of **1**, **2** or **VKVK**, and injecting one into the other at t = 0s. (a) Fluorescence emission spectra of **2** at the start of the mixing experiments (t = 0s), with the addition of **VKVK** or **2** and subsequent ageing at room tempearture for an hour (t = 3600s). (b) Tracking the emission intensity at 346 nm for the mixing of non-interacting supramolecular assemblies **VKVK+2**, as well as CT-driven assemblies **1** + **2**. (c) Tracking the time-dependent fluorescence quenching, expressed as a fraction of the emission intensity of **VKVK+2**$_x$ while changing the mole fractions of donor and acceptor molecules (x). (d) Tracking the time-dependent fluorescence quenching, expressed as a fraction of the emission intensity of **VKVK+2**, while changing the amount added NaCl.

of $\mathbf{1}_x$•VKVK$_{1-x}$ and $\mathbf{2}_x$•VKVK$_{1-x}$, where x =mole fraction of **1** or **2** in solution. This modulated the number of acceptor and donor molecules without changing the total concentration of PA in solution. Decreasing the mole fraction of **1** and **2**, in turn, decreased (Figure 5.10c) magnitude of quenching in the mixed $\mathbf{1}_x + \mathbf{2}_x$ (due to the reduction in the number of donor and acceptor moieties). However, the rate at which the quenched emission equilibrates is large independent of the mole fraction of **1** and **2**. Namely CT interactions between the aromatic donor and acceptor molecules drives the rapid assembly and CT-mediated fluorescence quenching, regardless of the mole fraction of donor and acceptor molecules in solution.

Changing the ionic strength of the mixing solution is another way to alter the association between the acceptor and donor molecules. Increasing the ionic strength through the addition of NaCl should increase mixing dynamics, as the Cl^- ions should screen the protonated lysine molecules, resulting in less electrostatic repulsion between neighboring supramolecular nanostructures, therein promoting more molecular mixing.[12,20,29,261,263,291,292] This was not observed , however, as increasing the salt concentration did not appreciably alter the fluorescence quenching of the $\mathbf{1} + \mathbf{2}$ system (Figure 5.10d).

5.4 CONCLUSION

This chapter describes the design and supramolecular assembly of electron acceptor and donor peptide amphiphiles. The aromatic components within the hydrophobic core of the amphiphile introduce pH sensitivity to the chirality and morphology of self-assembly, due to the introduction of and competition between π-π stacking, hydrogen bonding and hydrophobic non-covalent bonding interactions. Mixing assembled structures of electron acceptor with electron donor molecules resulted in charge transfer, due to inter-fiber exchange and intermolecular association, at a rate far higher than that of non-interacting supramolecular assemblies. This lays the groundwork for the kinetics of association and charge transfer of supramolecular amphiphiles, shedding light onto the

energy landscape of exchange between assembled systems with a non-zero driving force for association.

5.5 MATERIALS AND METHODS

General Methods

All reagents were purchased from commercial suppliers and used without further purification unless stated otherwise. Column chromatography was carried out on silica gel 60F (Merck 9385, 0.040-0.063 mm. Nuclear magnetic resonance (NMR) spectra were recorded on a Bruker Avance III 600 MHz, Bruker Avance III 500 MHz, and Agilent 500 MHz spectrometers, with working frequencies of 600, 500, and 500 MHz (^{1}H NMR), respectively, and at 150, 125, and 125 MHz (^{13}C NMR), respectively. Chemical shifts are reported in ppm relative to the signals corresponding to the residual non-deuterated solvents ($CDCl_3$: $\delta H = 7.24 ppm$ and $\delta C = 77.23 ppm$. High-resolution mass spectra (HRMS) were measured on an Agilent 6210 Time-of-Flight (TOF) LC-MS, using an ESI source, coupled with Agilent 1100 HPLC stack, using direct infusion (0.6 mL min^{-1}).

All samples were prepared by dissolving the requisite amount of PA into either Milli-Q Water or 5 mM Tris-buffered solution. The samples were then ultrasonicated and vortexed to ensure complete dissolution, and annealed in a water bath set at 80˚C for 30 minutes, followed by a slow cool (achieved by turning off the water bath and letting the system equilibriate) to room-temperature overnight. For co-assemblies, the a small molecules were first dissolved in 1,1,1,3,3,3,-hexafluoro-2-propanol (HFIP) in a 1:1 molar ratio. Once complete dissolution was ensured through sonication and vortexing, the samples were placed in a vaccuum chamber, and a small vacuum was pulled to ensure the co-assembled samples are completely dry. The dried samples are then rehydrated in either Milli-Q water or 5 mM Tris-buffered solution, and annealed using the same protocols described above.

Synthesis of **1**, **2** *and VKVK*

EtHexNDIC5COOH (**I**). A suspension of 1,4,5,8-Naphthalenetetracarboxylic dianhydride (9.86 g, 36.8 mmol), 2-ethyl-1-hexylamine (6.55 mL, 40.0 mmol) and 6-aminohexanoic acid (5.25 g, 40 mmol) in anhydrous DMF (50 mL) was heated at 100°C for 12 hrs under nitrogen. Acetic anhydride (7.56 mL, 80.0 mmol) was then injected and the reaction was stirred for an additional 2 hrs at 100°C under nitrogen. After cooling to room temperature, the crude was poured in cold dilute citric acid. The precipitate was filtered, collected and the product purified by column chromatography (5% THF/DCM) to give a slightly pink solid (3.30 g, 18%). ^{1}H NMR (400 MHz; $CDCl_3$): δ 8.76 (s, 4H), 4.21 (t, J = 7.5 Hz, 2H), 4.15 (t, J = 7.4 Hz, 2H), 2.39 (t, J = 7.5 Hz, 2H), 1.94 (s, 1H), 1.80-1.72 (m, 4H), 1.54-1.49 (m, 2H), 1.43-1.37 (m, 3H), 1.37-1.27 (m, 5H), 0.96-0.86 (m, 6H). ^{13}C NMR (126 MHz; $CDCl_3$): δ 176.2, 163.3, 163.0, 131.1, 126.77, 126.63, 44.7, 40.7, 38.0, 33.3, 30.8, 28.7, 27.8, 26.5, 24.4, 24.1, 23.1, 14.2, 10.7.

C6NphOH (**II**). A solution of 1,5-dihydroxynaphthalene (5.00 g, 31.2 mmol), 1-bromohexane (2.38 mL, 15.0 mmol) and potassium carbonate (2.07 g, 15.0 mmol) in anhydrous DMF (20 mL) was heated at 100°C for 2 hrs under nitrogen. After cooling, the reaction was diluted in water (300 mL) and 4 M HCl (10 mL) was added. The precipitate was collected and the product purified by column chromatography (DCM) to give a dark brown solid (2.74 g, 36%). ^{1}H NMR (400 MHz; $CDCl_3$): δ 7.89 (d, J = 8.5 Hz, 1H), 7.71 (d, J = 8.5 Hz, 1H), 7.38 (dd, J = 8.3, 7.8 Hz, 1H), 7.32-7.28 (m, 1H), 6.85-6.83 (m, 2H), 5.21-5.14 (m, 1H), 4.13 (t, J = 6.4 Hz, 2H), 1.96-1.89 (m, 2H), 1.61-1.53 (m, 2H), 1.44-1.34 (m, 4H), 0.96-0.91 (m, 3H). ^{13}C NMR (126 MHz; $CDCl_3$): δ 155.0, 151.2, 127.2, 125.4, 125.1, 115.0, 113.4, 109.5, 105.3, 68.3, 31.7, 29.4, 26.0, 22.7, 14.2.

C6NphOC5COOH (**III**). A suspension of **II** (2.74 mmol, 11.2 mmol), 6-bromohexanoic acid methyl ester (2.38 mL, 15.0 mmol) and potassium carbonate (2.07 g, 15.0 mmol) was heated in anhydrous DMF (20 mL) at 100°C under nitrogen for 2 hrs. After cooling to room temperature, the crude was diluted in water (200 mL) and 4M HCl was added (10 mL). The precipitate was collected and dissolved in isopropanol/3M NaOH (100/20 mL) and heated overnight at 80°C. After cooling

to room temperature, the reaction was concentrated under vacuum, diluted in water and the precipitate filtered. The filtrate was then washed with DCM and air dried to give a light brown solid (2.30 g, 57%). ^{1}H NMR (499 MHz; $CDCl_3$): δ 4.12 (q, J = 7.1 Hz, 4H), 2.43 (t, J = 7.4 Hz, 2H), 1.93 (dquintet, J = 19.8, 7.0 Hz, 4H), 1.78 (quintet, J = 7.6 Hz, 2H), 1.68-1.63 (m, 2H), 1.55 (q, J = 6.9 Hz, 2H), 1.39-1.35 (m, 4H), 0.92 (t, J = 7.0 Hz, 3H). ^{13}C NMR (126 MHz; $CDCl_3$): δ 178.4, 154.80, 154.63, 126.91, 126.84, 125.22, 125.10, 114.3, 114.0, 105.4, 68.3, 67.8, 33.8, 31.7, 29.4, 29.1, 26.05, 25.93, 24.6, 22.7, 14.2.

All PAs were synthesized using fluorenylmethyloxycarbonyl (Fmoc) solid-phase peptide synthesis on Rink Amide MBHA resin and purified by reverse phase high performance liquid chromatography (RP-HPLC). Deprotection of Fmoc was achieved using piperidine in N,N-dimethylformamide (DMF). Coupling reaction of amino acid and **EtHexNDIC5COOH** (for **1**), **C6NphOC5COOH** (for **2**) or palmitic acid (for **VKVK**) consisted of 1.2 molar eq. of the protected amino acid or palmitic acid, 1.1 eq. PyBOP, and 6 eq. of N,N-diisopropylethylamine (DIEA) in a 1:1 solvent mixture of DMF:dichloromethane (DCM). The synthesized products were cleaved from the resin using a mixture of 95% trifluoroacetic acid (TFA), 1% water, 1% triisopropylsilane (TIPS) and 3% DCM. Rotary evaporation was used to remove TFA and then the product was precipitated with cold diethyl ether, and purified using preparative scale reverse phase high performance liquid chromatography on a Waters Prep 150 HPLC, equipped with a Phenomenex Kinetex column (C_{18} stationary phase, 5 μm, 100 Åpore size, 30.0 × 150 mm.

The pure precipitate was dissolved in water with 0.1% TFA (added to aid PA solubility) and purified fractions were separated out in a linear gradient of acetonitrile (35% to 65%). ESI mass spectrometry (Agilent 6520 Q-TOF LC/MS) was used to identify the PAs of interest and the pure fractions were then combined for rotary evaporation to remove excess acetonitrile. The pure fractions were then lyophilized with varying quantities of HCl to remove any excess TFA and exchange the counter-ion on the positively charged PA to Cl^-. This lyophilization step helped remove (Table 5.1) over 90% of TFA from the PAs. Purified PAs were stored at -20°C until future use.

Table 5.1: Post-synthetic lyophilization of purified **1** and **2** with HCl, and its effect on the number of remnant TFA anions bound to each PA

	1	**2**	
[HCl] added	20	0	20
TFA per PA	0.119	1.45	0.053
% removed	-	-	96.4%

Determination of TFA Concentration with NMR

A solution of 1 mM d3-toluene in d6-DMSO was prepared for use as an internal standard. Approximately 2-3 mg of PA was dissolved in 700 μL of this DMSO solution, and a 600 μL aliquot of this transferred to an NMR tube. Fluorine T1 relaxation time for the trifluoroacetic acid and d3-toluene was determined to be 1.2 and 1.6 seconds respectively, so an 8 second delay was used for ^{19}F experiments. A 10 second delay was used for ^{1}H experiments. From the ^{1}H data, the terminal methyl peak (0.8 ppm) was integrated relative to whichever d3-toluene peak was least overlapping other peaks (usually the meta-carbon protons at 7.6 ppm). In the ^{19}F data, the trifluoroacetic acid peak (-75 ppm) was integrated relative to the d3-toluene peak (-60 ppm). By normalizing the integrals with the number of nuclei associated with each peak, the relative concentration of trifluoroacetic acid to PA was determined. To corroborate this analysis, the concentration of PA was calculated based on the mass added, and the concentration of trifluoroacetic acid was determined relative to the known concentration of d3-toluene (1mM) as described above.

Optical Absorption Spectroscopy

UV-vis absorbance spectra were recorded using a Perkin Elmer Lambda 1050 spectrophotometer. The path length of the closed demountable quartz cuvette was 0.1 mm (Starna Cells). Absorption measurements were taken with a scan speed of 1 nm/sec.

Fluorescence Spectroscopy

Fluorescence spectra were recorded using an ISS PC1 spectrofluorimeter. The path length of the cuvette was 3 mm. Emission spectra were recorded at an excitation wavelength of 300 nm. To control the number of emitted photons incident on the photodetector, neutral density filters were placed in the path of the emitted photon beam.

Tracking supramolecular mixing using fluorescence was performed by preparing separate 1mM solutions of **1**, **2** and **VKVK** as described in Section 5.5. 100 μl of **2** was placed in the fluorescence cuvette, forming the basis for the naphthalene emission intensity at t = 0s. 100 μl of either **1** or **VKVK** was injected into the bottom of the cuvette, immediately removing the micropipette tip and starting collection of the emission intensity at 346 nm. The elapsed time from the point of injection to the start of data collection (once the fluorimeter equilibrates and the software calibrates) is approximately 10 seconds.

Mixing experiments involving various mole fractions of donor or acceptor molecules involved first dissolving **1**, **2** and **VKVK** in HFIP, before mixing **1** or **2** with **VKVK** at the correct ratios to obtain a series of $\mathbf{1}_x$•$\mathbf{VKVK}_{1-x}$ and $\mathbf{2}_x$•$\mathbf{VKVK}_{1-x}$ mixtures. The mixtures were then dried, rehydrated to a final solution concentration of 1mM, and annealed as per Section 5.5.

In this study, fluorescence quenching is defined as the difference in emission intensity between $\mathbf{1}_x$+**VKVK** and **1** + **2**, expressed as a fraction of the intensity of $\mathbf{1}_x$+**VKVK**.

Atomic Force Microscopy

All tapping-mode atomic force microscopy (AFM) measurements were performed in air using a TESPA-V2 probe (Bruker AFM Probes). The samples were either mounted on cleaved mica or cleaned transistor-grade silicon (for later device measurements) by spin-coating 20 μl of the relevant solution onto the relevent substrates. The spin conditions used were a spin speed of 5000 r.p.m, accelerating at 1000 r.p.m/s, for a duration of 59 s.

Small Angle X-ray Spectroscopy

SAXS measurements were performed at the Synchrotron Research Center at the Advanced Photon Source, Argonne National Laboratory using the beamline 5 ID-D DuPont-Northwestern-Dow Collaborative Access Team (DND-CAT). 10 mM PA solution in water or 5mM Tris solution was placed in 1.5 mm quartz capillaries (Charles Supper, 1.50 mm wall thickness). An incident photon energy of 10 keV corresponding to a wavelength λ = 1.24 Å was selected using a double-crystal monochromator, samples were exposed for 1.5 s, and the scattering data was collected using CCD cameras (MAR) positioned 850.6 cm, 101.4 nm and 201.0 cm behind the sample. Samples were either stationary or oscillated with a syringe pump during exposure to prevent beam damage. Two-dimensional scattering data was reduced to one dimensional intensity profile by radial integration using the program FIT2D, and plotted on a relative scale (I) as a function of the wave vector $q = (2\pi/\lambda)sin(\theta/2)$, where θ is the scattering angle. Background subtracted scattering profiles were obtained by subtraction of the 1D profile from a capillary containing only solvent from the 1D profile obtained for each sample. No attempt was made to convert the units to an absolute scale. Fitting of SAXS spectra was done using software provided by NIST (NCNR SANS package on IGOR); a polydisperse core-shell cylinder model was used to fit the spectra as described previously.

Circular Dichroism

CD measurements were performed on a Jasco J-815 spectropolarimeter. Annealed PA solutions at 1 mM were first sonicated to break up fibers and minize linear dichroism artifacts, and then added to a quartz cuvette of 1.0 mm path length. Spectra were collected at RT over a wavelength range of 450 - 190 nm with a step size of 1 nm. The data was averaged over three spectra for each sample.

6 Tuning Supramolecular Assembly by Amino Acid Hydrophobicity

6.1 objectives and significance

Supramolecular assembly and materials science is hinged on the ability to use chemistry to tune hierarchical order and function. In this vein, peptide amphiphiles offer remarkable versatility in the ability to tune non covalent hydrogen bonding and solvophobic reactions between small molecule subunits to derive a vast array of morphologies and function. This chapter builds on that capacity to understand the assembly of a series of amphiphiles, where the hydrophobicity of the amino acid sequences are changed. This not only helps expand the functional understanding of these supramolecular systems, but also provides inspiration for further studies on the dynamics of exchange between complementary peptide amphiphiles, as started in Chapter 5.

6.2 background

Self-assembly and supramolecular chemistry relies on the interplay between weak intermolecular interactions to drive hierarchical order and, by extension, function. In this vein, biology inspired the development of the peptide amphiphile (PA) molecule, which has long been established[12,19,20,29,261] as a useful building block for to construct a diverse array of supramolecular assemblies. Their known capacity[27] to impart directional assembly and long-range order through hydrogen bonding, hydrophobic and π-π interactions sets PAs apart from other supramolecular building blocks. In aqueous solution, these molecules assemble into one-dimensional nanofibers, largely driven by intermolecular hydrogen bonding between neighboring peptide segments. Specifically, the propensity of the supramolecular assembly to form a β-sheet secondary structure is heavily dependent on the hydrophobicity of the non-charged amino acids. Tuning this weak non-covalent interaction by changing the number,[40] order,[41] and chemistry[21,22,292] of the peptide

sequence within these amphiphiles has opened new doors to the development of novel synthetic architectures that can impart and control biological function.[38,293]

The work in this chapter builds on the exploration of charge transfer peptide amphiphiles described in Chapter 5, where aromatic charge transfer complexes were coupled to short peptide linkers to impart amphiphilicity and hydrogen bonding to the small molecule. In Chapter 5, the peptide sequence of choice was a tetrapeptide with alternating valines (V) and lysines (K). Exploring this hypothesis further, this chapter focuses on a series of peptide amphiphiles that incorporate a similar design strategy, with the exception of systematically modulating the hydrophobicity of the peptide sequence. Specifically, three tetrapeptide sequences: alternating glycine-lysine (**GKGK**), valine-lysine (**VKVK**) and phenylalanine-lysine (**FKFK**) were chosen, and coupled to a 16-carbon linear alkyl tail to provide amphiphilicity (Figure 6.1). This chapter then focuses on the influence of the hydrophobic amino acid on the morphology as well as the strength of supramolecular assembly in these PAs. While the morphology can be easily estimated using molecular simulations, and experimentally determined by a number of microscopic techniques, the strength of the assembly, in this work, is measured through the apparent pKa of the supramolecular system.

6.3 RESULTS AND DISCUSSION

6.3.1 *Molecular Dynamics Simulations*

Coarse grained molecular dynamics (CG-MD) of a series of PAs with varying hydrophobicity help illustrate (Figure 6.2) the effect of the hydrophobic side chain on the self-assembly of the amphiphilic molecules. Setting the net charge on the PA at (+1) by protonating the terminal lysine residue, simulations of the least hydrophobic peptide amphiphile, C_{16}−GKGK−NH_2, depict the formation of globular micellar structures. Increasing the hydrophobicity of the amino acid from G to A saw a change in assembly morphology to elongated structures. That the orientation of the simulated amphiphile (Figure 6.2, purple) follows that of the corresponding hydrophobic segments (Fig-

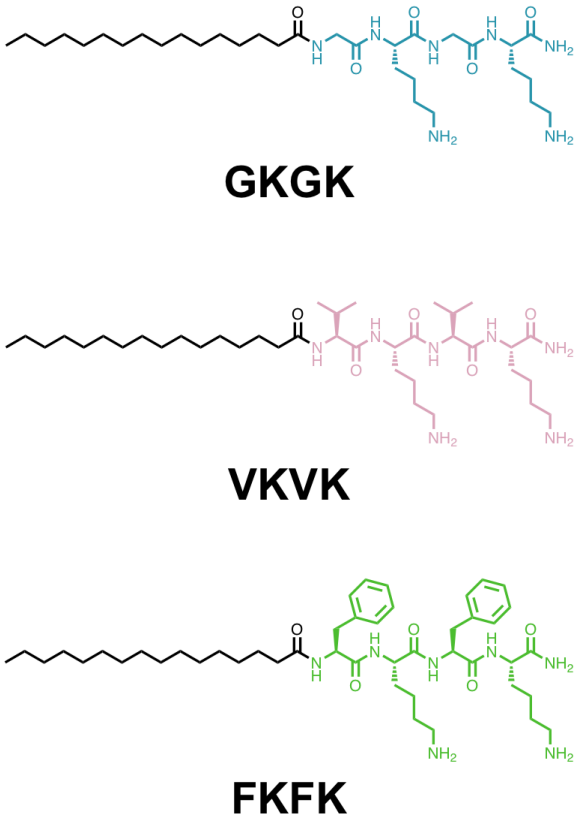

Figure 6.1: Molecular designs for peptide amphiphiles containing a 16-carbon hydrophobic tail, coupled to an alternating XKXK tetrapeptide amino acid sequence, where lysine (K) residues impart amphiphilicity and solubility in aqueous conditions (X = glycine (G), valine (V), phenylalanine (F).

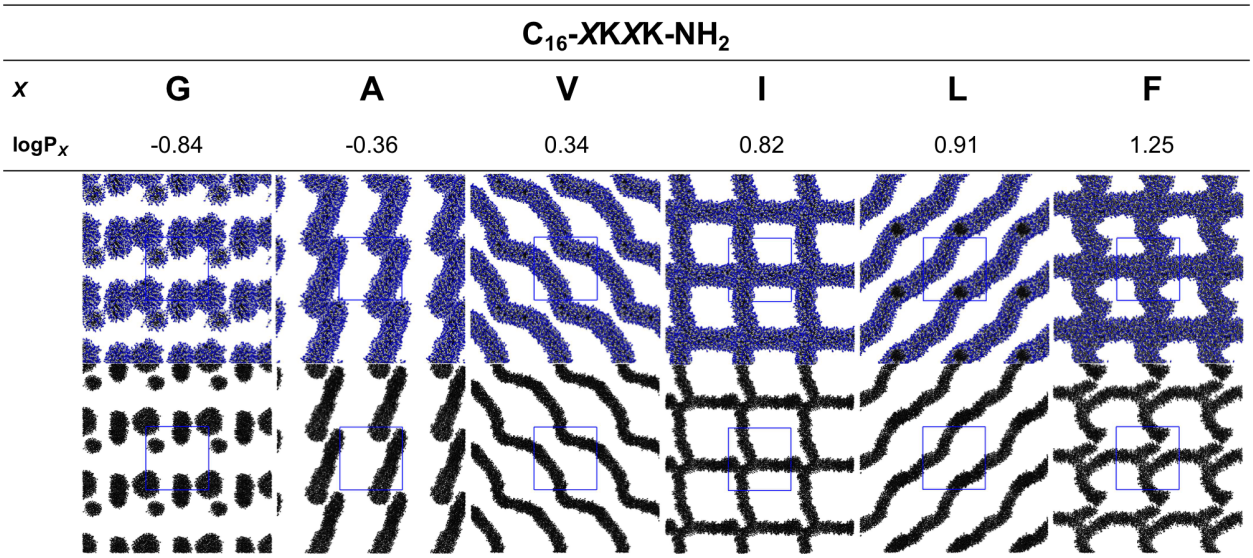

Figure 6.2: Molecular dynamics simulations of a series of tetrapeptide amphiphiles (C_{16}−XKXK) with varying hydrophobic amino acids. Energy minimized simulations of the PAs highlight the supramoelcular locations and orientation of the peptide residues (purple) as well as the hydrophobic alkyl talks (black). The charges on all PAs were set to (+1) by protonating the terminal lysine, therein standardizing electrostatic effects.

ure 6.2, black) suggests that C_{16}−AKAK−NH_2 forms cylindrical nanostructures. This nanostructure morphology is maintained through C_{16}−VKVK−NH_2, C_{16}−IKIK−NH_2, C_{16}−LKLK−NH_2 and C_{16}−FKFK−NH_2, with the length of the nanostructured assembly increasing with increasing amino acid hydrophobicity. In addition, inter-fiber interactions are observed for C_{16}−IKIK−NH_2 and C_{16}−FKFK−NH_2, indicative of lateral aggregation between assembled nanostructures. It is clear that increasing the hydrophobicity of the amino acids increases the propensity of the amphiphiles to assemble into cylindrical nanostructures with high aspect ratio, likely due to intermolecular hydrogen bonding and the formation of β-sheet supramolecular assemblies. Further increases in hydrophobicity introduce lateral aggregation *between* assembled nanostructures, likely to minimize exposed hydrophobic surfaces and, in the case of C_{16}−FKFK−NH_2, due to π-π stacking interactions between phenyl groups on amphiphilic molecules on neighboring nanostructures.

The interation between water molecules and PAs are mediated by the chemistry and geometry of the PA-water molecules. It has been established[291] that fast dynamics of water molecules

in the hydrophobic core of the PA mimic that of bulk-like water, whereas slow dynamics at the charged surface of the PA mimic that of structural water. In the context of this work, PA-water interactions are used as a metric to probe the strength of supramolecular interactions. Here, each PA molecules was condensed into a number of 'beads', comprised of hydrophilic and hydrophobic segments, with the backbone of each PA comprising 8 'beads' (Figure 6.3a). The specific interaction potentials of the beads were modulated based on their location, with electrostatic interactions only allowed for the hydrophillic bead that encompassed the charged terminal lysine. PA-water contacts, were, in turn, defined by the number of water molecules within a radius of 1.1 nm away from each bead. Figure 6.3b illustrates that for all simulated tetrapeptide PAs, the least PA-water contacts occur by the most hydrophobic bead (Residue -3), with the most PA-water contacts occurring by the charged hydrophilic bead (Residue +4). While amino acid hydrophobicity has little effect on the PA-water contacts in the hydrophilic Residue +4, significant changes can be elucidated in the hydrophobic Residue -3. Specifically, Residue -3 on C_{16}−GKGK−NH_2 PAs are calculated to have the most water contacts among the PAs tested, with that of C_{16}−FKFK−NH_2 having the least. This difference can be attributed the hydrophobicity of the PA core, with the most hydrophobic core (C_{16}−FKFK−NH_2) having the least PA-water interactions, and the least hydrophobic core (C_{16}−GKGK−NH_2) having the least PA-water interactions. The number of PA-water contacts can, in turn, be viewed as inversely related to the strength of PA assembly, as fewer PA-water contacts implies more PA-PA intermolecular interactions driving stronger association and more stable assembly. The inverse is true for more PA-water contacts, which can be seen as disrupting the PA-PA intermolecular interactions and driving weaker association. As a result, the trend of decreasing PA-water contacts in the hydrophobic residues with increasing amine hydrophobicity can be attributed to stronger PA-PA intermolecular interactions driving stronger supramolecular assemblies.

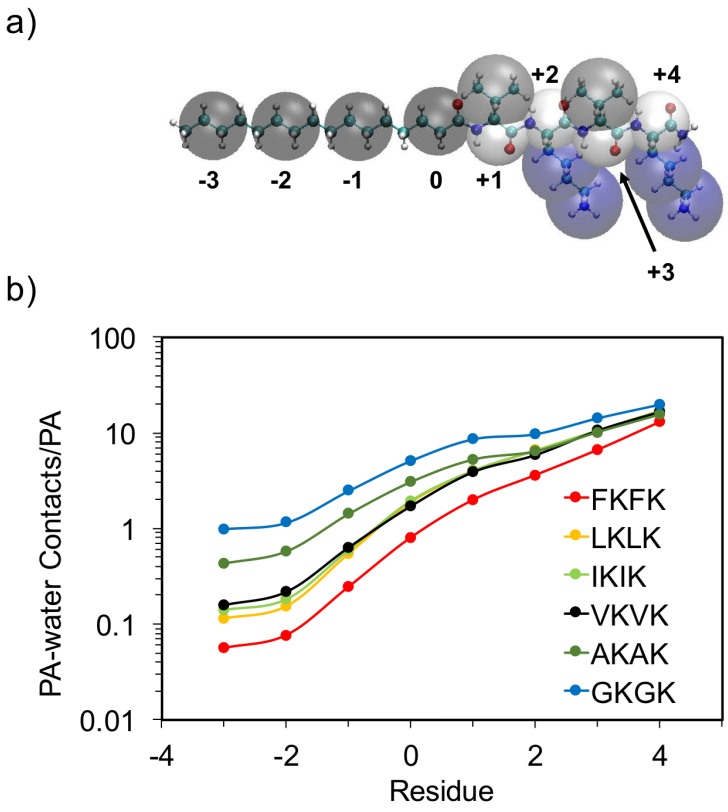

Figure 6.3: Coarse-grained molecular dynamics simulations of C_{16}–XKXK, where (a) the backbone of the PA molecular structure is condensed into a series of 8 'beads' with defined interaction potentials.(b) PA-water contacts (defined as the number of water molecules within a 1.1 nm radius of each bead) for the assembled supramolecular structures, with fewest water contacts in the most hydrophobic bead (Residue -3) and most water contacts in the terminal charged hydrophillic bead (Residue +4). Changes in the number of water contacts as a function of amino acid hydrophobicity can be used as a metric to understand the strength of inter-PA assembly interactions.

6.3.2 *Morphological Characterization*

The relationship between supramolecular morphology and protonation state of the PA series was established by imaging the surface profiles of the assembled PAs using atomic force microscopy (AFM). **GKGK**, with no added equivalents of NaOH, does not appear (Figure 6.4a) to assembly into any structure with long-range order. This is unsurprising, considering the lack of structure-directing hydrophobic amino acids to aid β-sheet formation and drive the long-range order. The addition of 2 equivalents of base, however, does result (Figure 6.4b) in nanostructured assembly in the **GKGK** PA, likely due to the deprotonation of lysine residues leading the additional hydrophobic collapse driving the supramolecular assembly of the PA. In contrast, the assembly of **VKVK** under acidic conditions (with no added NaOH) illustrates (Figure 6.4c) the formation of fibrous nanostructures, likely aided by the hydrophobicity of the valine amino acids. Increasing the equivalents of NaOH, in turn, results in the formation of wider nanostructures (Figure 6.4d), similar to that noted for **GKGK** under the same assembly conditions. This implies that under low degrees of lysine protonation, the assemblies of both **GKGK** and **VKVK** are not dependent on the hydrophobicity of the first and third amino acid. The assembly of **FKFK**, which contains the most hydrophobic amino acids, paints a different picture. At low pH, **FKFK** assembles (Figure 6.4e) into fibrous structures, akin to **VKVK**. At 2 equivalents of NaOH, however, **FKFK** assembles (Figure 6.4f) into well-defined ribbon structures, characterized by the lateral aggregation of smaller nanostructured domains. This is likely due to aromatic π-π stacking interactions between phenylalanine amino acids on neighboring PAs, driving the lateral assembly of the nanostructures.

Cryo-TEM of the PA assemblies with 2 equivalents of NaOH corroborate (Figure 6.5) the morphologies observed by AFM. Specifically, the assembly of **GKGK** depicts (Figure 6.5a) the formation of twisted ribbon-like nanostructures, with aspect ratios that mimic that observed by AFM. Granted, observing the rotational twisting of supramolecular nanostructures is often difficult in surface profile measurements such as AFM, where the hydrydrated supramolecular nanostructures has to be dried completely before imaging, resulting in a collapse of some of the structural nuances

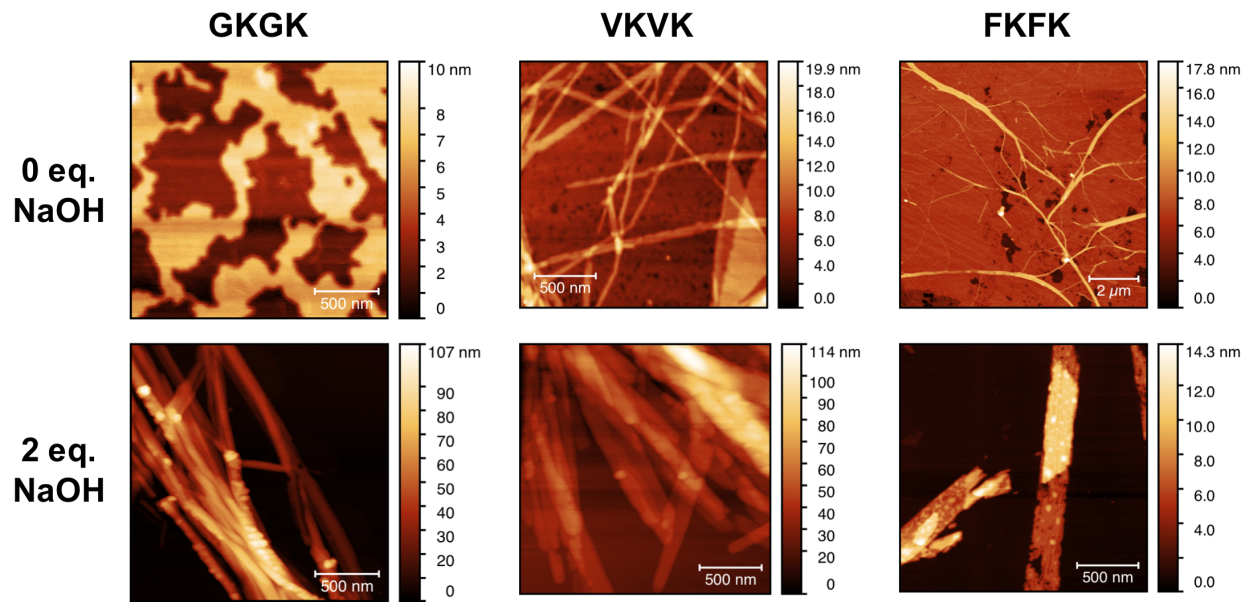

Figure 6.4: Atomic force microscopy images on the assembly of (a,b) **GKGK** with 0 and 2 equivalents of NaOH, (c,d) **VKVK** with 0 and 2 equivalents of NaOH and (e,f) **FKFK** with 0 and 2 equivalents of NaOH. All PAs were initially dissolved in 2 equivalents of HCl to ensure complete dissolution and protonation of lysine residues

such as chiral twisting. Representative Cryo-TEM of **VKVK** depict (Figure 6.5b) a dense network of ribbon-like nanostructures, similar to that observed by AFM. Finally, images (Figure 6.5c) of **FKFK** corroborated the assembly of wide ribbon-like structures, likely due to lateral aggregation of adjacent **FKFK** PAs due to aromatic π-π stacking of phenylalanines on neighboring PAs.

6.3.3 *pH Titrations*

pH titrations of the PAs also give insight as to the strength and stability of supramolecular assembly under different electrostatic environments. Shifts in the apparent pKa of charged amino acids in supramolecular assemblies[284,285] have been attributed to differences in the local environment surrounding assembled amino acids as well as structural transitions in supramolecular assembly due to changes in protonation state. In the context of this chapter, pH titrations offer a window into the effect of amino acid hydrophobicity on the supramolecular assembly of PAs. "Titrations" were done

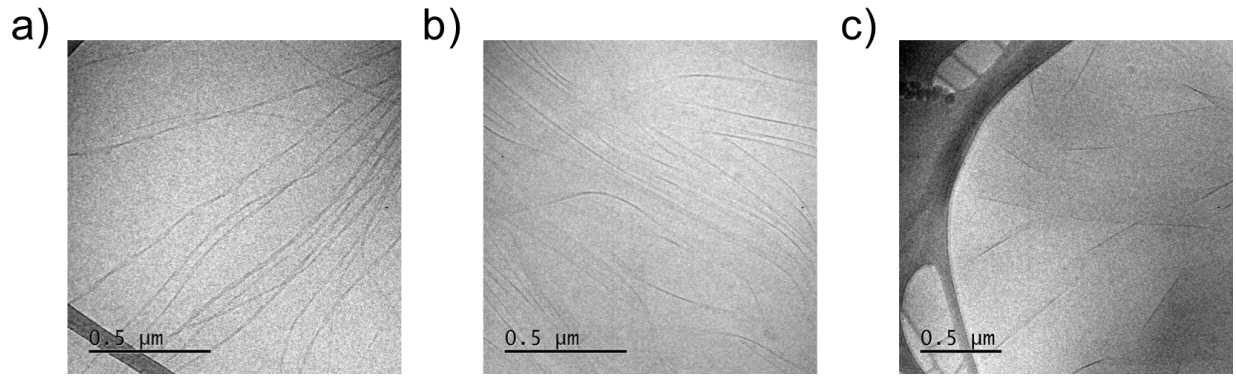

Figure 6.5: Cryo-TEM of the assembly of (a) **GKGK**, (b) **VKVK** amd (c) **FKFK** with 2 equivalents of NaOH. All PAs were initiall dissolved in 2 equivalents of HCl to ensure complete dissolution and protonation of lysine residues

by first pre-dissolving the PA molecules in 2 equivalents of HCl, to ensure complete dissolution and protonation of the lysine amino acids ($pKa = 10.67$). The solutions were then split into a number of solutions, with varying amounts of NaOH added. To homogenize the distribution of OH^- ions around the supramolecular assemblies and minimize kinetically trapped states, each solution was then annealed (see Section 6.5 for protocol) and cooled to room-temperature. While measuring the pH of all PA solutions saw (Figure 6.6) an initial buffering region, likely due to excess free H^+ ions in solution, the titration of the assembled **FKFK** solutions saw two transitions at $pH = 5.7$ and $pH = 9.7$, before PAs began precipitating above $pH = 10$. Far lower than the pKa of lysine, these transitions can be attributed to the deprotonation of the lysine residues in the interior of the assembled nanostructure, where the local concentration of H^+ and OH^- ions could differ dramatically from that in free solution. Both **VKVK** and **GKGK** saw a similar first transition at $pH = 6.4$ and $pH = 7.8$ respectively, once lower than that of free lysine. That the shift in pKa increases with increased amino acid hydrophobicity is a marker of the strength of supramolecular asssembly, as stronger and more tightly bound assemblies are likely to present a local amino acid dielectric environment that is far different from that of the free amino acid, therein resulting in larger shifts in pKa. Weaker supramolecular assemblies where the molecules are not as tightly bound, on the

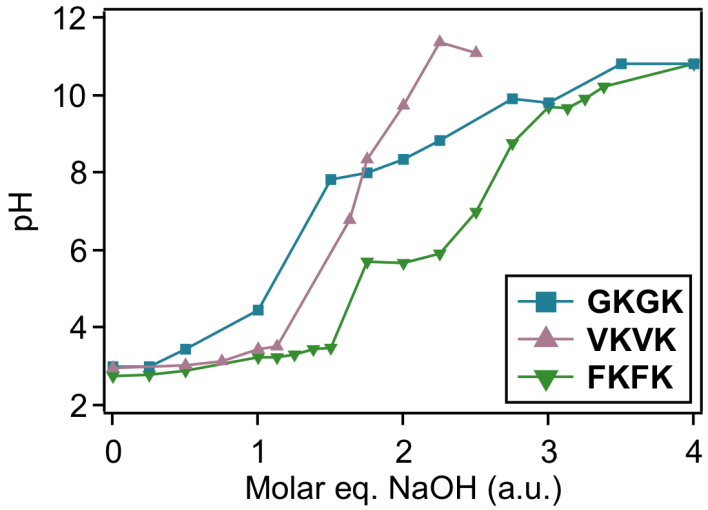

Figure 6.6: pH titrations of pre-assembled **GKGK**, **VKVK** and **FKFK**. Note that each data point represents a different PA sample, annealed after the addition of base to ensure pH measurements are representative of the thermodynamic assembly of PAs. (Initial [PA] = 1 mM; HCl = 2 mM)

other hand, are likely to offer a local dielectric environment that is closer to that of the free amino acid, resulting in smaller shifts in pKa. In addition, the titration of **FKFK** presents much sharper and more defined transitions compared to that of **GKGK**, likely due to the observed pH stability in supramolecular morphology for **FKFK**, compared to a changing supramolecular morphology of **GKGK**.

6.4 CONCLUSION

This chapter describes the assembly of a series of tetrapeptide amphiphiles, with varying amino acid hydrophobicities. Molecular dynamics simulations cast a wide net on the morphology of (+1) charged PA assemblies, ranging from globular micelles to fiber-like structures with signs of lateral aggregation. The interaction between PA hydrophobic residues and water molecules too, show an increase in PA-water contacts with decreasing hydrophobicity, attributed to weaker simulated assemblies with less hydrophobic amino acid residues. Indeed, experimental microscopy and sur-

face profiling of the PA assemblies corroborate simulations, with **GKGK** transitioning from non-assembled to fibrous structures with increasing equivalents of NaOH, and **FKFK** forming ribbon-like structures with evidence of lateral aggregation with increasing NaOH. This interplay between chemistry and supramolecular assembly, where amino acid hydrophobicity significantly changes the morphology and strength of supramolecular assembly, opens new doors to the development of novel nanostructured functional architectures (akin to Chapter 5).

6.5 MATERIALS AND METHODS

General Methods

Rink Amide MBHA resin, Fmoc-protected amino acids and HBTU were purchased from Novabiochem. Palmitic acid was obtained from Acros Organics. All other reagents were purchased from Sigma-Aldrich, and used as received. Nuclear magnetic resonance (NMR) spectra were recorded on a Bruker Avance III 600 MHz, Bruker Avance III 500 MHz, and Agilent 500 MHz spectrometers

For the experiments highlighted in this chapter, all PA molecules were dissolved in Milli-Q water at a concentration of 1 mM. 2 equivalents (eq.) of HCl was added to the PA solutions. The solutions were sonicated and vortexed to ensure solubility, and various additions of NaOH as deemed necessary was added. The solutions were then annealed at 80°C for 30 minutes, and slow cooled overnight.

*Synthesis of **GKGK**, **VKVK** and **FKFK***

All PAs were synthesized using fluorenylmethyloxycarbonyl (Fmoc) solid-phase peptide synthesis on Rink Amide MBHA resin and purified by reverse phase high performance liquid chromatography (RP-HPLC). Deprotection of Fmoc was achieved using piperidine in N,N-dimethylformamide (DMF). Coupling reaction of amino acid and palmitic acid consisted of 4 molar eq. of the protected amino acid or palmitic acid, 3.95 eq. HBTU, and 6 eq. of N,N-diisopropylethylamine (DIEA) in a

Table 6.1: Post-synthetic lyophilization of purified **GKGK**, **VKVK**, **FKFK** with HCl, and its effect on the number of remnant TFA anions bound to each PA

	VKVK		**GKGK**	**FKFK**
[HCl] added	0	20	20	20
TFA per PA	1.66	0.12	0.20	0.12
% removed	-	93%	-	-

1:1 solvent mixture of DMF:dichloromethane (DCM). The synthesized products were cleaved from the resin using a mixture of 95% trifluoroacetic acid (TFA), 1% water, 1% triisopropylsilane (TIPS) and 3% DCM. Rotary evaporation was used to remove TFA and then the product was precipitated with cold diethyl ether, and purified using preparative scale reverse phase high performance liquid chromatography on a Waters Prep 150 HPLC, equipped with a Phenomenex Kinetex column (C_{18} stationary phase, 5 μm, 100 Åpore size, 30.0×150 mm.

The cure precipitate was dissolved in water with 0.1% TFA (added to aid PA solubility) and purified fractions were separated out in a linear gradient of acetonitrile (35% to 65%). ESI mass spectrometry (Agilent 6520 Q-TOF LC/MS) was used to identify the PAs of interest and the pure fractions were then combined for rotary evaporation to remove excess acetonitrile. The pure fractions were then lyophilized with varying quantities of HCl to remove any excess TFA and exchange the counter-ion on the positively charged PA to Cl^-. This lyophilization step helped remove (Table 6.1) over 90% of TFA from the PAs, with only 0.20 eq. TFA present per PA molecule after lyophilizing. Purified PAs were stored at -20°C until future use.

Determination of TFA Concentration with NMR

A solution of 1 mM d3-toluene in d6-DMSO was prepared for use as an internal standard. Approximately 2-3 mg of PA was dissolved in 700 μL of this DMSO solution, and a 600 μL aliquot of this transferred to an NMR tube. Fluorine T1 relaxation time for the trifluoroacetic acid and d3-toluene was determined to be 1.2 and 1.6 seconds respectively, so an 8 second delay was used for ^{19}F exper-

iments. A 10 second delay was used for ^{1}H experiments. From the ^{1}H data, the terminal methyl peak (0.8 ppm) was integrated relative to whichever d3-toluene peak was least overlapping other peaks (usually the meta-carbon protons at 7.6 ppm). In the ^{19}F data, the trifluoroacetic acid peak (-75 ppm) was integrated relative to the d3-toluene peak (-60 ppm). By normalizing the integrals with the number of nuclei associated with each peak, the relative concentration of trifluoroacetic acid to PA was determined. To corroborate this analysis, the concentration of PA was calculated based on the mass added, and the concentration of trifluoroacetic acid was determined relative to the known concentration of d3-toluene (1mM) as described above.

Atomic Force Microscopy

All tapping-mode atomic force microscopy (AFM) measurements were performed in air using a TESPA-V2 probe (Bruker AFM Probes). The samples were either mounted on cleaved mica or cleaned transistor-grade silicon (for later device measurements) by spin-coating 20 μl of the relevant solution onto the relevent substrates. The spin conditions used were a spin speed of 2000 r.p.m, accelerating at 1000 r.p.m/s, for a duration of 59 s.

Cryogenic Transmission Electron Microscopy

Transmission electron microscopy (TEM) images were obtained using a Hitachi model HT-7700 electron microscope operating at 80 kV, equipped with an Orius SC 1000A camera. Plunge-freezing for cryogenic TEM samples were performed using a FEI model Vitrobot Mark IV.

6.5 μl of sample solution was deposited onto a Cu specimen grid covered with holey carbon support film (300 mesh, Electron Microscopy Science) and held in place with tweezers mounted on the Vitrobot. The specimen was blotted in an environment with 100% humidity at 22 °C (Blot time: 1 second, wait time: 1 second, drain time: 1 second, blot force: 3 or 5, blot total: 3 or 5) and plunged into a liquid ethane reservoir cooled by liquid N_2. The vitrified samples were stored in liquid nitrogen and then transferred to a Gatan cryo-TEM holder.

pH Titrations

All pH titration measurements were conducted on a Mettler Toledo SevenCompact pH meter with an InLab Semi-Micro pH electrode (working range = pH $0 - 12$).

A stock solution of 400 μl, 1 mM PA was prepared by dissolving in Milli-Q water, with the addition of 2 mM HCl. The stock solution was then equally divided into a number of different samples, and stepwise addition of NaOH was added to each sample. The samples were then vortexed to ensure thorough mixing, and annealed as per the protocol above. That each samples was annealed with a different molar quantity of NaOH ensures that the PA is able to reach a thermodynamically favourable supramolecular assembly given the electrostatic and dielectric conditions imparted by the equivalence of HCl and NaOH in solution. In addition, this method dramatically improves the stability of the measured pH.

Molecular Simulations

The PAs for the simulations were created in Avogadro[294] and transformed to MARTINI force field[295–298] CG representation using a modified version of martinize.py to include the aliphatic tail,[299] and using coiled coil as choice for secondary structure. The PAs have a total charge of $(+1)$ situated on their last K, because preliminary simulations of C_{16}-VKVK-NH_2 showed that this is the optimum protonation state to reproduce the fiber formation observed experimentally, therefore, the first K deprotonated and the second protonated. Initial structures consist on 600 molecules disposed randomly and spaced a minimum of 3 Å, solvated with CG water and enough ions were added to neutralize the system in a cubic box $17.1 \times 17.1 \times 17.1$ nm^3. This corresponds to a concentration of 200 mM (12 wt%) which is around 10 times higher than the experimental systems, which is commonly used to speed up self-assembly simulations.[266,300,301] All visualizations were rendered using VMD.[302]

Coarse grained Molecular Dynamic (CG-MD) Simulations were performed in GROMACS 5.0.4,[303] which was also used for the analysis of the simulations. A cut-off of 1.1 nm was used

for intermolecular interactions using reaction field with a relative dielectric constant of 15 for electrostatics and potential-shift for Lennard-Jones interactions.[304] All systems were minimized for 5000 steps or until the forces in atoms converged below 2000 pN. Self-assembly simulations were run using a 25 fs time step in NPT ensemble using V-rescale algorithm for the temperature (303 K, τ_T = 1 ps)[305] and Berendsen for the pressure (1 bar, τ_P = 3 ps).[306] Simulations were run for 5,000,000 steps corresponding to 5 μs effective time.[295,296]

7 Semiconducting Single Crystals Comprising Segregated Arrays of Complexes of C_{60}

7.1 OBJECTIVES AND SIGNIFICANCE

One of the challenges in developing small molecule electronic materials is the ability to impart directionality towards function. The intrinsic disparity between the effective size of these electronic molecules (on the order of nanometers) and the dimensions of a working device (on the order of micrometers) presents an obstacle in translating the unique and highly modular properties of small molecules towards practical use in devices. Self-assembly can help alleviate some of these issues, due to the capacity to harness intermolecular interactions, such as hydrogen bonding, charge transfer, and solvophobic interactions to drive the alignment of small molecules into higher-order architectures. Previous chapters have detailed the use of these supramolecular interactions to drive the association of neighboring molecules towards linear arrays of crystals or nanostructures. This chapter introduces a different form of molecular assembly and supramolecular order: host-guest chemistry. Here, a host molecule is able to stabilize and bind and enclose a smaller guest molecule, an interaction driven through intermolecular forces described above. Doing so an also aligns the guest molecule through supramolecular assembly, driving the formation of millimeter-scale aligned arrays of the guest molecule. In this chapter, the small molecule of choice is C_{60}, an increasingly popular *n*-type semiconductor that has a tremendous breadth of applications, from photovoltaics to transistors. Within the context of small molecules, however, the application of C_{60} is limited due to the isolated arrangement of the individual molecules. Encapsulating the molecules within a small molecule host, and aligning the co-assembled system across electrodes overcomes the limitations of native C_{60}, and allows one to exploit the intrinsic properties within.

7.2 BACKGROUND

Since the early discoveries[307,308] of C_{60}, research on fullerenes has blossomed rapidly, and considerable effort has been expended with a view to understanding and exploiting the band structure[309,310] of doped[311,312] and undoped[313–317] fullerenes in order to capitalize on their electronic properties in devices such as organic field effect transistors[318,319] (OFETs) and organic photovoltaic (OPV) solar cells.[320,321] Host-guest chemistry has been employed in an effort to introduce solution-based techniques for the isolation and processing of C_{60}. Some of the objectives of this work have been to obtain pure fullerenes on a large scale[322] and to control the packing arrangement of one C_{60} molecule with respect to others on surfaces.[323,324] The more commonly used hosts, such as calixarenes,[322,325] γ cyclodextrin,[326,327] porphyrin-based cyclic dimers,[328,329] cyclotriveratrylenes,[330,331] and cycloparaphenylenes,[332] have all been shown to bind C_{60}, usually through enthalpy driven mechanisms,[314] such as donor-acceptor interactions where the host is the donor and C_{60} is the acceptor. Although these hosts bind C_{60} with high affinities Ka values typically on the order of 105-108 M^{-1} in toluene their 1:1 or 2:1 complexes typically result in either the complete isolation of the fullerenes or the clustering of only a handful of fullerene molecules in the crystalline lattice. This isolated arrangement of C_{60} molecules is not ideally suited to electronic applications where the ability to move electrons between them in a bulk material is important for the performance of devices such as OFETs. There are, however, some instances where multiple C_{60} molecules have been positioned within close contact of each other, resulting[333] in their incorporation into stable one-dimensional arrays. The most notable example of this kind of intermolecular arrangement was discovered by Luzzi et al.,[334] who observed several C_{60} molecules residing within the cavities of single-walled carbon nanotubes (SWCNTs) so as to form a supramolecular assembly that has been referred[334] to as a "nanopeapod", despite the fact that only 5% of the SWCNTs are occupied. Although the ability to incorporate C_{60} molecules into the cavities of SWCNTs has been raised[335] to 80-85% more recently, it seems that full occupancy will be difficult to achieve. In addition to the challenge of obtaining complete alignment of the host

SWCNTs throughout the bulk material, the role of C_{60} in these nano-peapods is to enhance the existing semiconducting properties[336] of the SWCNTs through a charge transfer mechanism[337] with the electron-deficient fullerene. Similarly, the nanostructure and electrical performance of fullerene-polymer blends that have been reported[338–340] previously are dictated more so by the side chains and semiconducting properties of the electron-rich component, respectively, than by the C_{60} molecules themselves.

A family of box-like cyclophanes,[10,341,342] the so-called **ExBox**$^{4+}$ series of tetracationic extended bipyridinium-based receptors possess the ability to bind polycyclic aromatic hydrocarbons (PAHs), ranging in size from two through seven fused benzenoid rings. The binding of PAHs inside the cavities of these cyclophanes is enthalpically driven, usually as a consequence of the π-electronrich PAHs entering into strong donor-acceptor interactions with the π-electron-deficient **ExBox**$^{4+}$ series. A new member of the **ExBox**$^{4+}$ family was synthesized (Figure 7.1) wherein each p-xylylene bridge has been expanded by one paraphenylene ring, increasing the width of the cavity relative to that (Figure 7.1a) of the original **ExBox**$^{4+}$. This structural modification results in the near doubling of the width of the cavity from 0.69 to 1.22 nm at the longest atom-to-atom distance. Since this novel tetracationic cyclophane is approximately twice the width of the original **ExBox**$^{4+}$, the descriptor **ExBox**$_2^{4+}$ is used. This section demonstrates that this π-electron-deficient host possesses a cavity of a size suitable for binding the electron-deficient fullerene, C_{60}, predominantly as a consequence of solvophobic processes in solution that result (Figure 7.2) in the self-assembly of the $C_{60}\subset$ **ExBox**$_2^{4+}$ 1:1 inclusion complexes into continuous one-dimensional arrays which span the length of the millimeter-sized crystals. The room-temperature dark electrical conductivity of these crystals under ambient conditions surpasses, by several orders of magnitude, that reported[343,344] for undoped, pure C_{60}-based materials where O_2 was not evacuated. The values obtained also match the electrical conductivity of crystals and films comprised of C_{60} which are normally prepared through stringent sublimation/vapor transport techniques,[345,346] followed by the exhaustive removal of O_2.

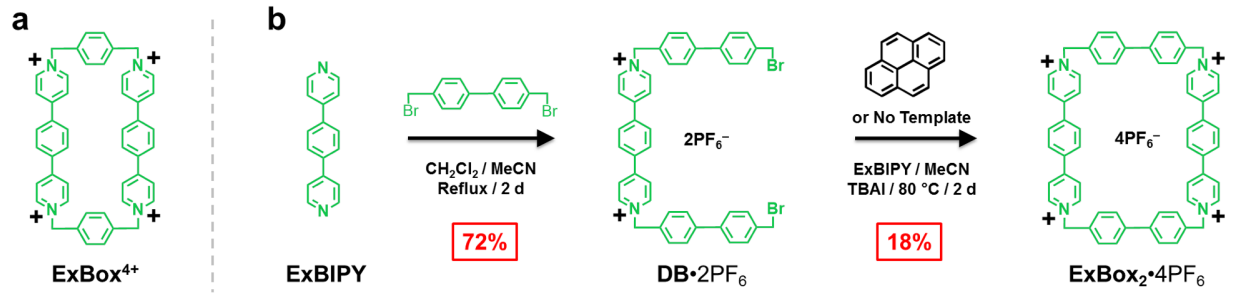

Figure 7.1: (a) Structural formula of $\mathbf{ExBox}^{4+}$. (b) Synthesis of $\mathbf{ExBox}_2 \cdot 4PF_6$ from its precursors, ExBIPY and $\mathbf{DB} \cdot 2PF_6$.

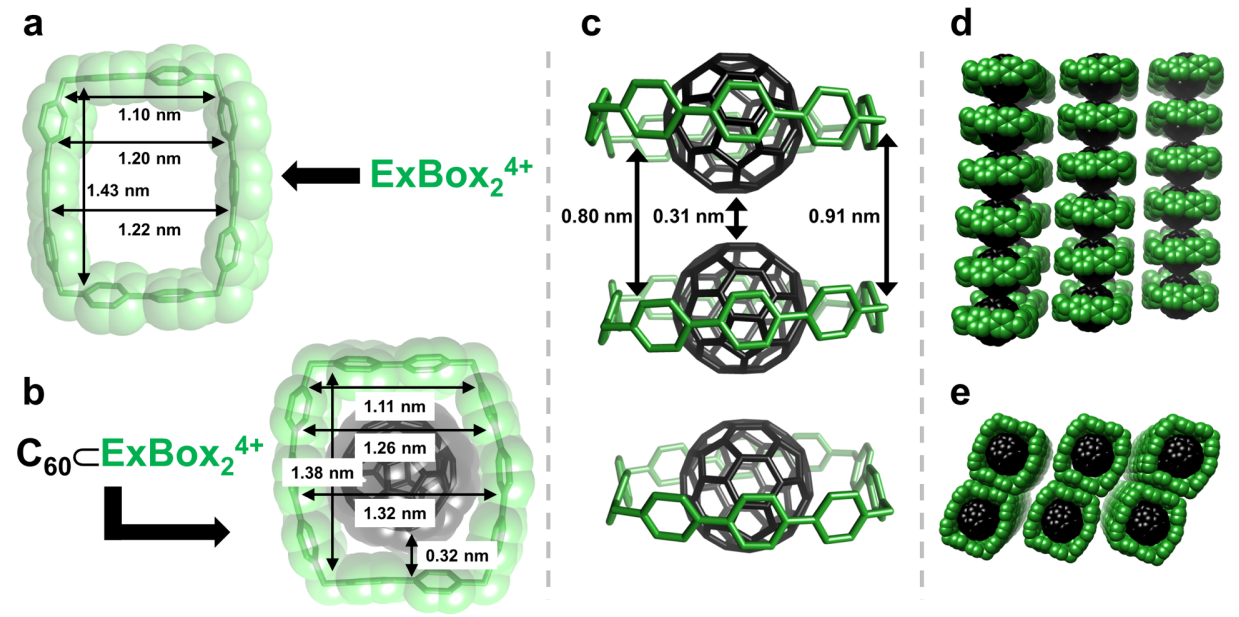

Figure 7.2: (Super)structures of (a) $\mathbf{ExBox}_2^{4+}$ and (b) $C_{60} \subset \mathbf{ExBox}_2^{4+}$ obtained from X-ray diffraction analyses performed on their respective single crystals. The close packing arrangement of each $C_{60} \subset \mathbf{ExBox}_2^{4+}$ results in (c) a fullerene-to-fullerene distance of 0.31 nm (atom-to-atom) between the aligned C_{60} molecules. The side-on view (d) and plan view (e) of the solid-state superstructure illustrate the close packing arrangement of each inclusion complex into segregated one-dimensional arrays that propagate the whole length of the crystal

7.3 RESULTS AND DISCUSSION

7.3.1 *Synthesis and Crystal Structure*

The synthesis (Figure 7.1b) of $\mathbf{ExBox}_2 \cdot 4PF_6$ follows a modified procedure[342] that makes use of tetrabutylammonium iodide (TBAI) as a catalyst during the reaction of ExBIPY with $\mathbf{DB} \cdot 2PF_6$. Using this procedure, we were able to obtain several hundred milligrams of $\mathbf{ExBox}_2 \cdot 4PF_6$ in 18% yield, allowing solution-phase and solid-state investigations to be carried out in the presence of C_{60}. The solid-state structure (Figure 7.2a) of $\mathbf{ExBox}_2 \cdot 4PF_6$ illustrates the size of the cavity of $\mathbf{ExBox}_2^{4+}$, where its atom-to-atom dimensions measure 1.43 nm in length and 1.22 nm at its widest point. The superstructure (Figure 7.3) of $\mathbf{ExBox}_2^{4+}$ illustrates how crystal packing forces dictate a herringbone packing arrangement when no guest is present, where each cyclophane is staggered relative to one another. In contrast, the solid-state superstructure of the 1:1 inclusion complex $C_{60} \subset \mathbf{ExBox}_2^{4+}$ (Figure 7.2b) highlights the dimensions, where, atom-to-atom, it measures 1.38 nm in length and 1.32 nm at its widest point. This change in geometry of the host in the 1:1 complex relative to that of the empty host suggests that $\mathbf{ExBox}_2^{4+}$ is willing to contort and twist its original conformation in order to shorten its length and increase its width such that it can embrace C_{60} in an approximately centrosymmetric fashion. Figure 7.2c portrays the intercomplex atom-to atom distances where the encircled C_{60} molecules are separated by 0.31 nm. This distance is indicative of van der Waals interactions between the fullerenes of adjacent inclusion complexes. The side-on view (Figure 7.2d) of the $C_{60} \subset \mathbf{ExBox}_2^{4+}$ solid-state superstructure illustrates the complete alignment of the inclusion complexes into discrete one-dimensional arrays. Moreover, the plan view (Figure 7.2e) of these discrete linear arrays shows how each C_{60} molecule in each self-assembled supramolecular wire[347–349] i.e., each stack of 1:1 inclusion complexes is segregated from the others as a consequence of intermolecular biphenylene π-π stacking and $ExBIPY^{2+}$ subunit slipped alignments between adjacent hosts. This arrangement contrasts with the typical fcc packing of pure C_{60} at room temperature

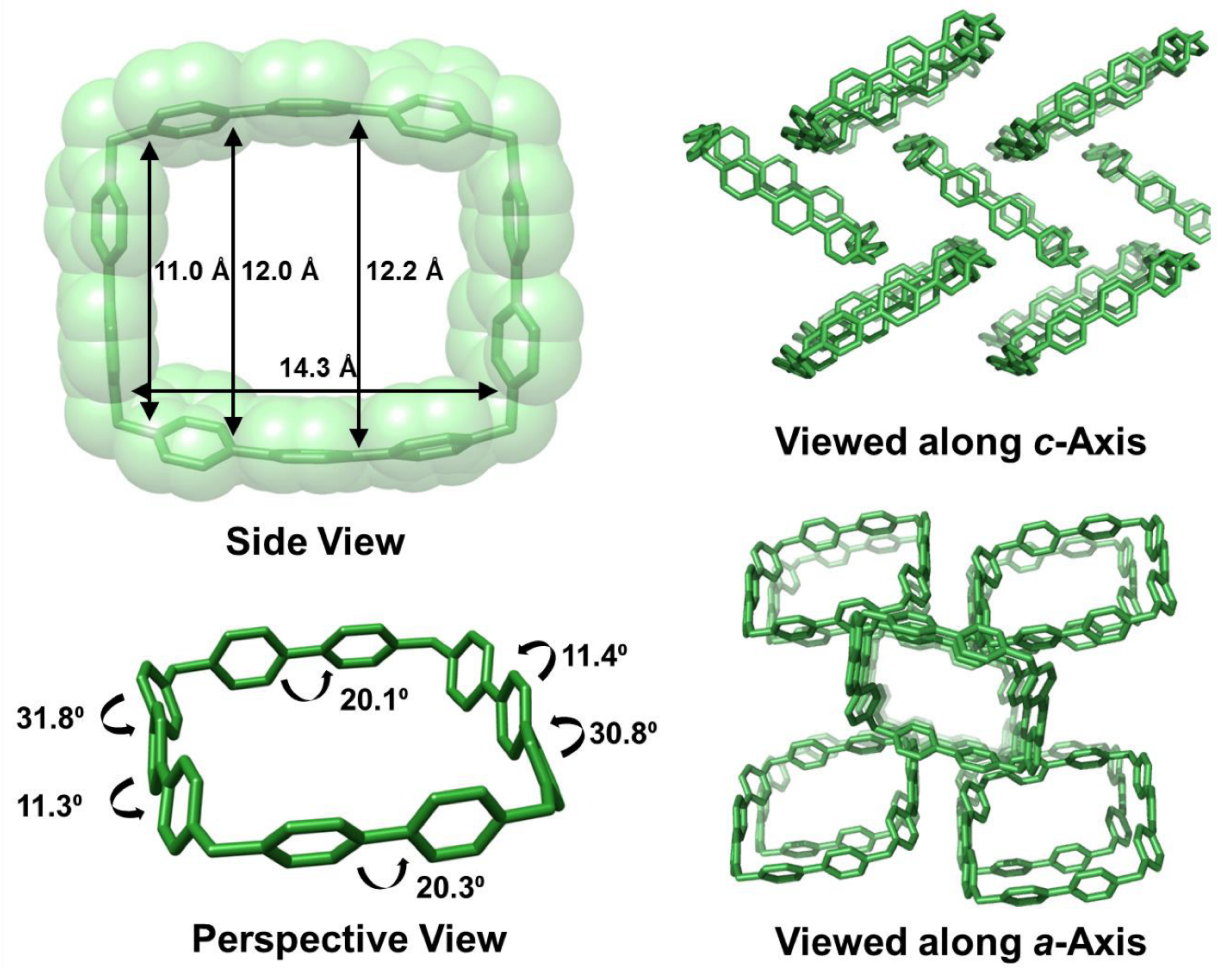

Figure 7.3: Different crystallographic projections of $\mathbf{ExBox}_2^{4+}$. Counterions and solvent molecules are omitted for the sake of clarity

and ultimately leads to van der Waals interactions between fullerenes propagated in one dimension throughout the crystal lattice.

7.3.2 *Isothermal Calorimetry*

In order to understand the nature of molecular recognition that occurs in solution, which ultimately results in the self-assembly of the $C_{60} \subset \mathbf{ExBox}_2^{4+}$ in the solid state, we carried out isothermal titration calorimetry (ITC). To elucidate the binding affinity between C_{60} and $\mathbf{ExBox}_2^{4+}$ in solution, ITC was carried out (Figure 7.4) in a 1:1 mixture of DMF/PhMe at 298 K to gain insight into the

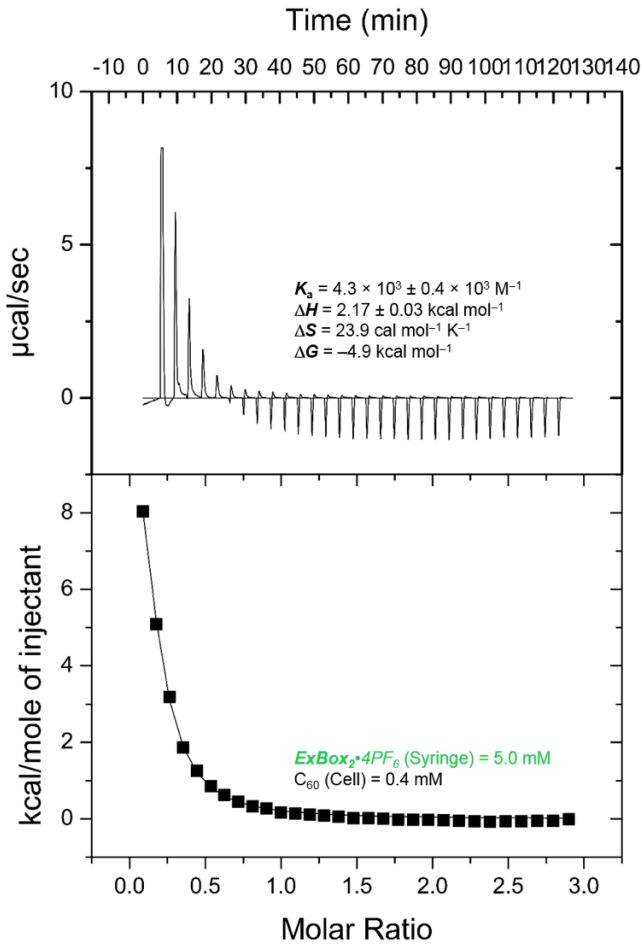

Figure 7.4: Representative ITC data for the formation of $C_{60} \subset$ **ExBox**$_2 \cdot PF_6$

binding thermodynamics in solution. The results from this ITC investigation indicate that the binding of C_{60} by $\mathbf{ExBox}_2^{4+}$ in solution is a favorable process that is predominantly driven by entropy, as evidenced by $\Delta H = 2.6 \pm 0.3 kcal mol^{-1}$ and $\Delta S = 23.9 \pm 0.5 cal mol^{-1} K^{-1}$, with an overall $\Delta G = -4.6 \pm 0.3 kcal mol^{-1}$. Importantly, the Ka value ($(2.5 \pm 1.3) \times 10^3 M^{-1}$) obtained from ITC is lower than that for traditional electron-rich C_{60} hosts is not surprising, given the unfavorable enthalpic interactions between the π-electron poor $\mathbf{ExBox}_2^{4+}$ and C_{60}.

7.3.3 *Spectroelectrochemistry*

To determine whether the energy gap between the HOMO and LUMO of C_{60} is affected once C_{60} is encircled by $\mathbf{ExBox}_2^{4+}$ in solution, cyclic voltammetry measurements were carried out (Figure 7.5) in DMF/PhMe containing 0.1 M $TBAPF_6$ (Ag/AgCl reference electrode) in order to estimate the approximate ionization potential and electron affinity energies. A general depiction of the complex formed between C_{60} and $\mathbf{ExBox}_2^{4+}$, in addition to the scenario when C_{60} is reduced to the radical anion through the addition of one electron, is illustrated in Figure 7.5a. The CV measurements reveal that the first and second redox waves of $\mathbf{ExBox}_2^{4+}$ (Figure 7.5b, green trace) are broad and overlap one another on account of the weakened electronic coupling between the individual pyridinium rings of the viologen subunits of the host. Furthermore, the first three one-electron redox processes of C_{60} are defined (Figure 7.4b, black trace) in the DMF/PhMe solvent mixture, as well as the redox processes (Figure 7.4b, red trace) for $C_{60} \subset \mathbf{ExBox}_2^{4+}$. The redox potentials for each component of the 1:1 complex undergo only minor shifts in comparison to those of the unbound C_{60} and $\mathbf{ExBox}_2^{4+}$ molecules. Since the first reduction wave of C_{60} does not overlap with the first reduction wave of $\mathbf{ExBox}_2^{4+}$, it is possible to carry out a SEC analysis (Figure 7.5c) of the $C_{60}^{\bullet-} \subset \mathbf{ExBox}_2^{4+}$ inclusion complex where the radical anion of C_{60} (namely, $C_{60}^{\bullet-}$) can be generated electrochemically by applying a potential of -0.49 V to a 0.42 mM DMF/PhMe solution of the complex for ≈30 min. The radical absorption bands of $C_{60}^{\bullet-}$ (Figure 4c, black trace) appear at 934 and 1078 nm and correspond to the allowed transition[350] of the unpaired electron from the singly occupied molecular orbital (SOMO) to the nearest unoccupied molecular orbital, t1u → t1g. In the presence of an equimolar amount of $\mathbf{ExBox}_2^{4+}$, however, the signature radical absorption bands for $C_{60}^{\bullet-}$ are nonexistent. The absence of these diagnostic radical absorption bands is consistent with previously reported[351] solvated ion-pairing interactions in systems containing $C_{60}^{\bullet-}$.

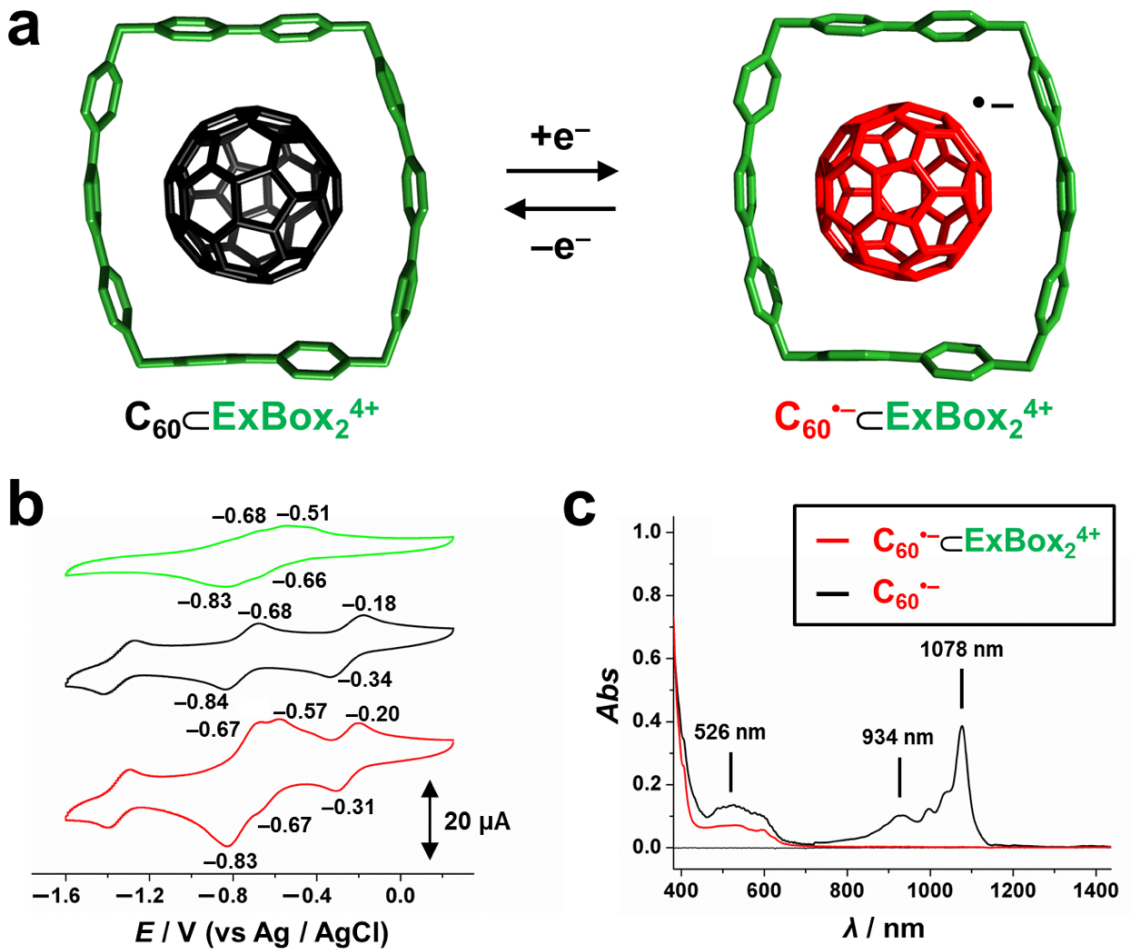

Figure 7.5: (a) Generation of the reduced inclusion complex $C_{60}^{\bullet-} \subset \mathbf{ExBox}_2^{4+}$ after the addition of one electron to C_{60}. (b) When cyclic voltammetry of $\mathbf{ExBox}_2^{4+}$ (green trace), C_{60} (black trace), and $C_{60} \subset \mathbf{ExBox}_2^{4+}$ (red trace) was carried out, a shift of only +30 mV was observed for the first reduction wave of the bound C_{60} in a DMF/ PhMe solvent system and 0.1 M $TBAPF_6$ electrolyte. (c) Spectroelectrochemistry performed in a 2 mm cell on the bound C_{60} (black trace) at an applied potential of −0.49 V produced the signature radical absorption peaks for $C_{60}^{\bullet-}$ at 934 and 1078 nm. In the presence of an equimolar amount of $\mathbf{ExBox}_2^{4+}$ (red trace), these radical absorption peaks were nonexistent, indicating strong ionpairing between the host and reduced guest.

7.3.4 *Bulk Conductivity*

In order to measure the bulk electrical conductivity of the $C_{60}\subset$ **ExBox**$_2^{4+}$ inclusion complexes, single crystals (Figure 7.6a) of the 1:1 complex were grown using a modified procedure (Section 7.4). These crystals were never placed under vacuum to remove residual O_2, and conductivity measurements were carried out under ambient conditions. Crystallographic indexing proved (Figure 7.6b) that the fullerene arrays were aligned with the long axis of the crystal. In order to construct a device (Figure 7.6c), single crystals of $C_{60}\subset$ **ExBox**$_2 \cdot 4PF_6$ were placed across gold electrodes spaced 100 μm apart on a Si/SiO_2 wafer. The ends of the crystal were painted with a conductive gold paste to secure a conducting pathway to the patterned electrodes. Dark electrical current was measured (Figure 7.6d, red trace) at room temperature between 0 and +1 V. Conductivity was extrapolated within the strict ohmic region (0 to +0.15 V) of the measured I-V curve, since the region beyond +0.15 V is more representative of a Shottky barrier. Multiple single crystals were analyzed using this method, and the average electrical conductivity was found to be $(5.83 \pm 0.15) \times 10^{-7} Scm^{-1}$. This value is nearly 2-3 orders of magnitude greater than the first reported electrical conductivity of pure C_{60} single crystals[343,344] and films[344] where O_2 was not removed. While no effort was made to remove O_2 from the $C_{60}\subset$ **ExBox**$_2 \cdot 4PF_6$ crystals, the room-temperature dark electrical conductivity is still comparable to that[345,346] ($10^{-6} - 10^{-8} Scm^{-1}$) measured in pure C_{60}-based materials where the strict removal of O_2 contamination was required. Unlike the stringent high-temperature vaporization techniques for the preparation of these purely C_{60}-based materials, the preparation of $C_{60}\subset$ **ExBox**$_2 \cdot 4PF_6$ crystals relies on facile, room-temperature crystallization from solution. In the absence of C_{60}, control measurements (Figure 7.6c, green trace) on of **ExBox**$_2 \cdot 4PF_6$ single crystals resulted in an average conductivity of $(1.20 \pm 0.17) \times 10^{-9} Scm^{-1}$. Based on these measurements, the necessity of C_{60} for higher electrical conductivities is evident, and the alignment of C_{60} molecules into discrete supramolecular one-dimensional arrays leads to improved electrical conductivity over **ExBox**$_2^{4+}$ and C_{60} systems without the rigorous exclusion of O_2.

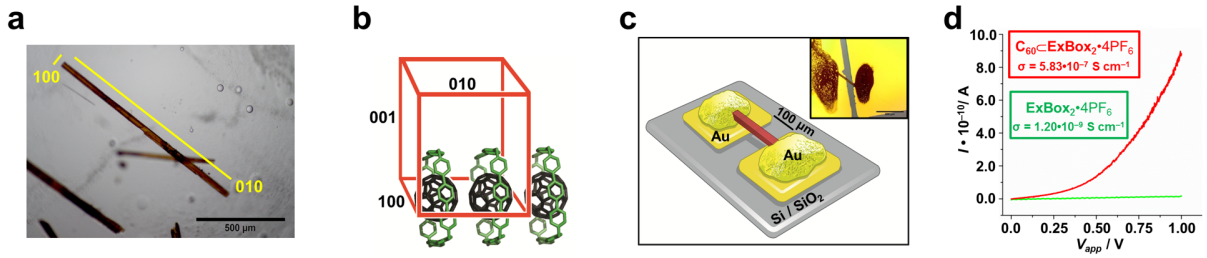

Figure 7.6: (a) Single crystals of $C_{60}\subset$ **ExBox**$_2 \cdot 4PF_6$ were grown by slow vapor diffusion of iPr_2O into a DMF/PhMe solution and were indexed to confirm (b) the orientation of the C_{60} molecules before the crystal was mounted (c) onto a Si/SiO_2 wafer patterned with gold electrodes, followed by the application of a gold paste to the ends of the crystal. The scale bar for the inset device picture is 500 μm. (d) Electrical conductivity measurements performed on single crystals of $C_{60}\subset$ **ExBox**$_2 \cdot 4PF_6$ and **ExBox**$_2 \cdot 4PF_6$ revealed a difference of nearly 2.5 orders of magnitude in conductivity when C_{60} is present.

7.4 CONCLUSION

The semiconducting properties of C_{60} and its derivatives make them attractive components for organic molecular electronic devices, such as in OFETs and OPV solar cells. Although materials comprised of pure, undoped C_{60} have shown promise in terms of their electrical conductivity, stringent high temperature mass transport/sublimation techniques are required to grow the single crystals and polycrystalline films. Moreover, the electrical performance of these purely C_{60}-based devices relies heavily on post-synthetic annealing techniques to remove interstitial O_2 as a consequence of their porous structure. The use of host-guest chemistry to bind C_{60} and disrupt its standard fcc packing arrangement has been achieved on a number of occasions over the past 20 years. Although there are many examples in the literature of one-dimensional alignment of functionalized C_{60} molecules, there are only a handful of examples where a host has been capable of directing the formation of unfunctionalized C_{60} into discrete, one-dimensional arrays that span the entire length of millimeter-sized crystals. The of $C_{60}\subset$ **ExBox**$_2 \cdot 4PF_6$ single crystals described in this investigation are grown under ambient conditions using a solution-processable protocol that excludes O_2 during the favorable self-assembly process, leading to a situation where the removal of residual O_2

does not affect the electrical conductivity of the material, measuring $(5.83 \pm 0.15) \times 10^{-7} Scm^{-1}$. The result of this form of crystal engineering is a conductivity value that is 2-3 orders of magnitude greater than that of the earliest reported materials comprised of undoped C_{60} and matches that of high-quality, nearly oxygen-free C_{60} single crystals prepared through stringent high-temperature mass transport/annealing techniques. Moreover, the tetracationic $\mathbf{ExBox}_2^{4+}$ is a suitable host for binding the reduced states of C_{60}, demonstrated specifically for $C_{60}^{\bullet -}$ in this work. Since the entropically driven complexation of C_{60} by $\mathbf{ExBox}_2^{4+}$ in a DMF/PhMe solution does not greatly affect the orbital energy gap of C_{60}, there is potential to implement its use in solution-processable protocols to fabricate organic-based electronic devices that would benefit from ordered assemblies of the semiconducting fullerene. The strategy reported here to create fullerene-based semiconducting supramolecular wires may potentially be applied toward (i) the fabrication of OFET devices consisting of ordered stacks of of $C_{60} \subset \mathbf{ExBox}_2 \cdot 4PF_6$, (ii) solid-state photoinduced polymerization of the ordered C_{60} molecules in the 1:1 inclusion complexes to generate polypseudorotaxanes, (iii) highly ordered conducting metallofullerene- based devices, and (iv) similar linear arrangements of segregated stacks with host molecules and other carbon allotropes,[352] such as C_{70} and C_{82}, as well as single-walled carbon nanotubes of appropriate diameter.

7.5 MATERIALS AND METHODS

General Materials/Intrumentation

All reagents were purchased from commercial suppliers and used without further purification unless stated otherwise. Solvents were deoxygenated by passing Ar through the solvent for 30 min. 4,4'-(1,4-Phenylene)bispyridine[10] (**ExBIPY**) and 4,4'-bis(bromomethyl)biphenyl[353] were synthesized based on previous literature procedures. Analytical high-performance liquid chromatography (HPLC) was performed on reverse-phase HPLC (RP-HPLC) instruments, using a C_{18}-column and a binary solvent system (MeCN and H_2O with 0.1% CF_3CO_2H). Column chromatography was

carried out on silica gel 60F (Merck 9385, 0.040-0.063 mm. Nuclear magnetic resonance (NMR) spectra were recorded on a Bruker Avance III 600 MHz, Bruker Avance III 500 MHz, and Agilent 500 MHz spectrometers, with working frequencies of 600, 500, and 500 MHz (^1H NMR), respectively, and at 150, 125, and 125 MHz (^{13}C NMR), respectively. Chemical shifts are reported in ppm relative to the signals corresponding to the residual non-deuterated solvents (CD_3CN: $\delta H = 1.94 ppm$ and $\delta C = 1.32$ and $118.26 ppm$; PhMe-d8: $\delta H = 2.09, 6.98, 7.00$, and $7.09 ppm$ and $\delta C = 20.40, 125.49, 128.33$, and $129.24 ppm$; DMF-d7: $\delta H = 2.75, 2.92$, and $8.03 ppm$ and $\delta C = 29.76, 34.89$, and $163.15 ppm$). High-resolution mass spectra (HRMS) were measured on an Agilent 6210 Time-of-Flight (TOF) LC-MS, using an ESI source, coupled with Agilent 1100 HPLC stack, using direct infusion (0.6 mL min^{-1}).

Synthesis of ***DB*** $\cdot 2PF_6$

4,4'-Bis(bromomethyl)-1,1'-biphenyl (1.36 g, 4.0 mmol) was added to a 1:1 mixture of CH_2Cl_2/MeCN (50 mL) in a round-bottomed three-necked flask and the resulting mixture was heated at 60°C while stirring until all of the solid material dissolved. Next, the temperature of the oil bath was raised to 90°C and a suspension of **ExBIPY** (92.8 mg, 0.40 mmol) in MeCN (25 mL) was added in aliquots slowly over the course of 2 h. After heating under reflux for 24 h, the reaction mixture was cooled to room temperature and the precipitate was collected by filtration and washed with CH_2Cl_2. The yellow solid was dissolved in cold (≤RT) MeOH (≈1 L) followed by the addition of NH_4PF_6 and cold (≤RT) H_2O, resulting in the precipitation of pure **DB** $\cdot 2PF_6$ (0.30 g, 72%) that was collected by filtration as a yellowish solid. ^{1}H NMR (500 MHz, CD_3CN, ppm): $\delta H = 8.84$ (H_α, d, J = 6.4 Hz, 4H), 8.34 (H_β, J = 6.3 Hz, 4H), 8.13 (H_γ, s, 4H), 7.80 (H_{Phen}, J = 7.8 Hz, 4H), 7.66 (H_{Phen}, J = 7.9 Hz, 4H), 7.57 (H_{Phen}, J = 7.9 Hz, 4H), 7.54 (H_{Phen}, J = 7.8 Hz, 4H), 5.70 (H_{CH2}, s, 4H). 4.65 (H_{CH2}, s, 4H). ^{13}C NMR (125 MHz, CD_3CN, ppm): δ_c 156.2, 145.6, 142.6, 140.5, 139.2, 138.1, 133.4, 130.7, 130.6, 130.3, 128.9, 128.4, 126.9, 64.5, 34.2.

Synthesis of ***Exbox***$_2 \cdot 4PF_6$

A mixture of **ExBIPY** (66.8 mg, 288 μmol), **DB** $\cdot$ 2PF_6 (300 mg, 288 μmol), and TBAI (21.0 mg, 58.0 μmol) in dry MeCN (96 mL) was stirred at 80 °C for 48 h. Concentrated HCl was added to halt the reaction and to precipitate the crude product from the MeCN solution. The precipitate was collected by filtration and washed (Me_2CO and CH_2Cl_2) in order to remove the residual tetrabutylammonium salt. The crude product was dissolved in H_2O, precipitated as its PF_6^- salt by adding solid NH_4PF_6, and collected by filtration. It was then subjected to column chromatography (SiO_2:MeCN and 0.05-0.25% NH_4PF_6 in MeCN), followed by reverse-phase HPLC using a binary solvent system (MeCN and H_2O with 0.1% CF_3CO_2H). After removal of MeCN, pure **Exbox**$_2 \cdot 4PF_6$ (72.8 mg, 18%) was obtained as a white solid after precipitation with NH_4PF_6. HRMS-ESI for **Exbox**$_2 \cdot 4PF_6$: calcd for $C_{60}H_{48}F_{24}N_4P_4$, m/z = 1259.2804 $[M-PF_6]^+$; found 1259.2735 $[M-PF_6]^+$. ^{1}H NMR (500 MHz, CD_3CN, ppm): δH = 8.82 (H_α, d, J = 7.0 Hz, 8H), 8.24 (H_β,d, J = 7.0 Hz, 8H), 8.01 (H_γ, s, 8H), 7.68 (H_{Phen}, d, J = 8.4 Hz, 8H), 7.55 (H_{Phen}, d, J = 8.4 Hz, 8H), 5.74 (H_{CH2}, s, 8H). ^{13}C NMR (125 MHz, CD_3CN, ppm): δ_c 155.8, 145.3, 141.5, 137.7, 134.9, 130.5, 130.2, 128.7, 126.8, 64.7.

X-ray Diffraction

Crystal Parameters of **ExBox**$_2 \cdot 4PF_6$

$[C_{60}H_{48}N_4 \cdot (PF_6)_4] \cdot (CH_3CN)_8$, colorless blocks ($0.35 \times 0.35 \times 0.05 mm$), monoclinic, $P2_1/n$; a = 16.2695(7), b = 15.9492(7), and c = 16.5922(7) ; $\alpha = 90.000, \beta = 110.464(3)$, and $\gamma = 90.000°$; V = 4033.7(3) ^{3}, Z = 2, T = 99.99 K, ρ_{calc} = 1.427 g cm^{-3}, μ = 1.806 mm^{-1}. Data were collected at 100 K on a Bruker Kappa APEX2 CCD diffractometer equipped with a Cu Kα microsource with Quazar optics. Of a total of 21 617 reflections that were collected, 6605 were unique. Final R_1 = 0.0790 and wR_2 = 0.2104. Distance restraints were imposed on the disordered PF_6^- anions and MeCN molecules. Rigid-bond restraints were also imposed on the displacement parameters as well

as restraints on similar amplitudes separated by less than 1.7 on the disordered molecules. Deposited as CCDC No. 1022763.

Crystal Parameters of $C_{60}\subset$ **ExBox**$_2 \cdot 4PF_6$

$C_{60}\subset C_{60}H_{48}N_4\cdot(PF_6)_4\cdot(DMF)_2\cdot(PhMe)_6$, red blocks ($0.45 \times 0.10 \times 0.06mm$), triclinic, $P\overline{1}$; a = 17.5692(4), b = 19.4448(5), and c = 20.6000(5) ; $\alpha = 83.1741(17)$, $\beta = 65.6972(15)$, and $\gamma = 82.9265(16)°$; V = 6347.0(3) 3, Z = 2, T = 99.94 K, ρcalc = 1.478 g cm^{-3}, μ = 1.396 mm^{-1}. Data were collected at 100 K on a Bruker Kappa APEX2 CCD diffractometer equipped with a Cu Kα microsource with MX optics. Of a total of 43 241 reflections that were collected, 20 638 were unique. Final R_1 = 0.1091 and wR_2 = 0.2692. The enhanced rigid-bond restraint was applied globally. Group anisotropic displacement parameters were refined for the disordered toluene solvents. Deposited as CCDC No. 1022765

Cyclic Voltammetry

CV experiments were carried out at room temperature in argon-purged solutions in 1:1 DMF/PhMe with a Gamry multipurpose instrument (Reference 600) interfaced to a personal computer. All CV experiments were performed using a glassy carbon working electrode (0.071 cm^2). The electrode surface was polished routinely with a 0.05 μm alumina-water slurry on a felt surface immediately before use. The counter electrode was a Pt coil, and the reference electrode was a Ag/AgCl electrode. The concentration of the supporting electrolyte, tetrabutylammonium hexafluorophosphate ($TBAPF_6$), was 0.10 M. The CV cell was dried in an oven immediately before use, and argon was flushed continually through the cell as it was cooled to room temperature to avoid condensation of water.

Optical Absorption Spectroscopy

UV-vis absorbance spectra were recorded using a UV-3600 Shimadzu spectrophotometer. The path length of the cuvette in all cases was 2 mm. For the spectroelectrochemical (SEC) measurements, a platinum mesh was used as the working electrode, a platinum coil functioned as the counter electrode, and the reference was a Ag/AgCl electrode. The solvent consisted of a 1:1 DMF/PhMe solution of 0.1 M $TBAPF_6$ electrolyte. The applied voltage was controlled by a Gamry Multipurpose instrument (Reference 600) interfaced to a PC while absorption scans were obtained.

Isothermal Calorimetry

All ITC measurements were performed in a 1:1 mixture of dry, degassed PhMe/DMF at 298 K. A guest solution of C_{60} (in PhMe/DMF) was used in a 1.8 mL cell. A solution of $\mathbf{ExBox}_2 \cdot 4PF_6$ (in PhMe/DMF), used as the host, was added by injecting 10 μL of titrant over 20 s (30×) with a 240 s interval between each injection. Experiments were repeated three times. Thermodynamic information was calculated using a one-site binding model utilizing data from which the heat of dilution of the guest was subtracted, with the average of three runs reported. A titration curve and thermodynamic data from a representative run are shown in Figure 7.5.

Although the molar ratio from the ITC curve (Figure 7.4) appears to assign 4 – 5 C_{60} molecules to each $\mathbf{ExBox}_2^{4+}$, the solid-state structure indicates only a 1:1 stoichiometry is possible. Similar inconsistencies in molar ratios have been observed[354] previously in ITC analyses of other systems where the binding event is an endothermic process driven by entropy.

Additionally, ITC titration experiments were performed in a single solvent system - namely, N-methylpyrrolidone (NMP), which is capable of solubilizing each component of the inclusion complex. The results of this experiment indicate that no binding was observed, but instead only the heat of dilution could be measured. Similarly, when an ITC binding titration was attempted employing the smaller analogue – namely, $\mathbf{ExBox}^{4+}$ - no binding is observed, a result which eliminates the possible proposal for side-on interactions as a mechanism for solution-phase binding.

Conductivity Measurements

Crystals of the 1:1 inclusion complex were obtained by dissolving $\mathbf{ExBox}_2 \cdot 4PF_6$ ($\approx 10mg$) in DMF (2 mL) in a 20 mL scintillation vial. A saturated C_{60} solution in PhMe was added to the point where the mixture appeared slightly opaque. After a single drop of DMF had been added, the solution became transparent once again, and the vial was placed in a jar containing iPr_2O ($\approx 20mL$). Slow vapor diffusion of iPr_2O into the resulting DMF/PhMe solution over a period of 3-4 d yielded red single crystals of $C_{60} \subset \mathbf{ExBox}_2 \cdot 4PF_6$. The presence of the 1:1 inclusion complex was confirmed by unit cell measurements using X-ray diffraction. The crystals were washed with a dilute solution of DMF in PhMe and stored in hexanes prior to conductivity measurements. Four-inch Silicon Quest International Si wafers with a 300 nm oxide surface coating were used as substrates on which electrodes were fabricated. The wafers were cut into 2×2 cm squares using a diamond cutter, scrubbed with soapy water, cleaned by ultrasonication in a 1:1:1 mixture of Me_2CO/MeOH/iPrOH, and then blown dry in a stream of N_2 gas. Electrodes (spaced at 100 μm) were patterned onto the surface of the wafer by thermally evaporating 6 of Cr and then 50 nm of Au through a defined shadow mask at a pressure of 10^{-6} mbar. Single crystals of $C_{60} \subset \mathbf{ExBox}_2 \cdot 4PF_6$ were picked up using a Pelco vacuum pick-up system and placed across the electrodes. The ends of crystals were painted with Pelco conductive gold paste to secure a conducting pathway to the patterned electrodes. Two-probe measurements were performed at a Signatone probe station, in conjunction with an Agilent 4155C semiconductor parameter analyzer. Current output was measured at room temperature for DC voltage sweeps from 0 to +1 V. All measurements were carried out in a US FED STD 209E Class 100 (ISO 5) clean room.

The conductivity of the $C_{60} \subset \mathbf{ExBox}_2 \cdot 4PF_6$ single crystal was calculated using the following equations:

$$I = G \cdot V \tag{1}$$

$$G = \sigma t w L \tag{2}$$

where G is electrical conductance, t is the cross-sectional thickness of the crystal, w is the width of the crystal, L is the length of crystal between the electrodes, and σ is the calculated electrical conductivity of $C_{60} \subset \mathbf{ExBox}_2 \cdot 4PF_6$. In this investigation, t was equal to 6.44×10^{-6} cm^2, while $L = 340.0\mu m$ and $w = 28.0\mu m$. The dimensions of the empty $\mathbf{ExBox}_2 \cdot 4PF_6$ crystals that were assessed for electrical conductance were $t = 6.57^{-4} cm^2$, $L = 428.0\mu m$, and $w = 292.0\mu m$

8 Summary and Future Outlook

8.1 summary

The work in this thesis presents the efficacy of intermolecular charge transfer complexes in developing novel electronic and self-assembling materials. The introduction of electron transfer interactions between an aromatic donor and acceptor molecules, in addition to π-π stacking intermolecular binding interactions, offer new avenues to elucidate electronic and supramolecular function from chemistry and molecular packing.

8.1.1 *Charge Transfer as a Motif for Room-Temperature Ferroelectricity*

The hallmark of the intermolecular CT complexes presented in this thesis lies in the discovery of room-temperature ferroelectricity and second harmonic activity across two axes in an intermolecular CT co-crystal (Chapter 2). The co-crystal was designed along the blueprint defined by Lock Arm Supramolecular Ordering, where flexible diethylene glycol arms were functionalized onto core electron donor or acceptor molecules to add hydrogen bonding interactions to the solvophobic, charge transfer and van der Waals noncovalent intermolecular forces driving co-crystallization. In Chapter 2, a co-crystal of 1-amino-5-naphtol and a pyromellitic diimide acceptor formed a two-dimensional sheet like structure, with two axes of charge transfer. Applying near orthogonal electric fields across the two axes of the co-crystal saw two distinct ferroelectric polarizations, attributed to the two directions of charge transfer. In addition, the centrosymmetric co-crystal displayed evidence of second harmonic activity, supporting the observed ferroelectric behavior and suggesting that crystallography alone may not be sufficient to resolve the presence of lack of an inversion center in these low-symmetry organic co-crystalline systems.

Chapter 3 then expanded upon this library of ferroelectric LASO co-crystals, and provided a systematic link between donor/acceptor chemistry and functional ferroelectric properties. Here, the

diethylene glycol arms were functionalized on the donor instead of the acceptor, and the chemistry of the aromatic donor systematically altered from a diamino- to dioxynapthalene. While co-crystals of these donor/acceptor molecules were all isostructural, their photophysical and electronic properties could not differ more. The diaminonaphthalene co-crystal displayed both second harmonic activity and ferroelectric polarization, traits that were lost in sequential core substitution of oxygens in the place of the amine functionality. This was attributed to the change in the degree of charge transfer, which was significantly higher for the diamino-functionalized than that for the dioxy-functionalized donors.

8.1.2 *Charge Transfer as a Motif for Semiconductivity*

Translating these supramolecular CT motifs to a solution-based form involved symmetrically functionalizing the dioxynaphthalene donor and pyromellitic diimide acceptor with tetraethylene glycol linkers (Chapter 3). In addition, the electron donor was functionalized with urea motifs, and the acceptor with sulfonamide motifs, since the thermodynamically favorable urea-sulfonamide heterodimer would promote intermolecular association between the donor and acceptor molecules. While association between the donor and acceptor molecules was observed in solution, casting the co-assembly into a film saw a phase separation of the donor and acceptor molecules. Despite this, a significant increase in the conductivity, and ambipolar field-effect mobility was observed for the co-assembled system, far greater than that of the donor or acceptor or even a layered donor/acceptor system. This difference was attributed to residual charge transfer interactions in the co-assembled films, likely due to dopant donor or acceptor molecules within the supramolecular acceptor and donor assemblies. In addition, the importance of the structure-driving hydrogen bonding motifs was elucidated, as co-assemblies of the donor and acceptor molecules without urea and sulfonamide functionality saw far lower thin film conductivities. It is believed that the supramolecular assembly offered by the combination of CT and hydrogen bonding interactions helps provide conducting pathways for the mobile charge carriers, therein boosting the measured linear conductivity.

The incorporation of CT interactions with entropically driven host-guest assembly is highlighted in Chapter 7, where a tetracationic 'box'-like cyclophane was able to bind pure, undoped C_{60}. Not only was host-guest chemistry used to bind C_{60} and disrupt its standard fcc packing arrangement, but it also directed the supramolecular assembly of linear, one-dimensional arrays of complexed C_{60}. These arrays grew, under ambient conditions with a simple solution-based protocol, into single crystals that spanned over a millimeter in length. The close packing and directional alignment of the complexed C_{60} molecules enabled the observation of linear conductivity values that were 2-3 orders of magnitude greater than that of undoped single crystals of C_{60}. In fact, the conductivities matched that of oxygen-free C_{60} crystals, prepared through stringent high temperature fabrication methods.

8.1.3 *Charge Transfer as a Motif for Peptide Self-Assembly*

Incorporating CT complexes to existing amphiphilic PA chemistry offers an additional noncovalent driving force that defines the thermodynamics and kinetics of assembly in amphiphilic molecules. Functionalizing tetrapeptide sequences with naphthalene diimide electron acceptor or dioxynaphthalene electron donor cores results (Chapter 5 in pH-sensitive self-assembly of the donor/acceptor amphiphiles. The acceptor molecules were shown to undergo chiral inversion, and the donor chiral induction, upon small changes in pH. This was attributed to the changing balance between hydrogen bonding and aromatic π-π stacking in driving supramolecular assembly. Co-assembling the two molecules, however, resulted in CT interactions and a supramolecular assembly driven solely by the association between the aromatic chromophores. Yet the most interesting aspect of this chapter is the observation of supramolecular exchange, mediated by charge transfer interactions, between pre-assembled nanostructures, where there is an intrinsic driving force for association. This is especially unique, as aromatic chromophores are nested in the shielded hydrophobic pocket of the supramolecular nanostructure, implying that exchange involved the dissolution,

followed by the clustered insertion of complementary donor/acceptor molecules to form a CT complex.

The work in Chapter 5 on the exchange dynamics of pre-assembled supramolecular systems warranted a study of the influence of amino acid hydrophobicity in tuning the balance between hydrogen bonding and charge transfer interactions in these supramolecular systems. As a start, Chapter 6 explored the self-assembly of PAs (all with a linear 16-carbon hydrophobic tail) with varying degrees of amino acid hydrophobicity. Coarse-grained molecular dynamics illustrated that increasing hydrophobicity increased the stability of supramolecular interactions, regulated through the number of PA-water contacts in the hydrophobic core of the nanostructures. Experimental evidence corroborated this observation, with imaging and pH titrations suggesting that hydrophobic amino acids drive a more stable assembly, characterized by decreases in lysine pKa and the formation of a dense network of nanostructures characterized by intrafiber lateral aggregation.

8.2 FUTURE OUTLOOK

8.2.1 *Expanding the Knowledge Base of LASO Ferroelectrics*

The basis set of room-temperature LASO ferroelectrics remains at 6 ferroelectric co-crystals. While the initial discovery and subsequent data on ferroelectricity in these co-crystals helps build the library of organic RT ferroelectric materials, little is still known about the mechanism of ferroelectricity in these systems. As a result, further study is warranted along a number of fronts.

Ferroelectricity in LASO Co-Crystals with Disubstituted-Pyromellitic Diimides

We have established, by a sequential study of LASO CT complexes (Chapter 3), that the chemical functionality on aromatic electron donors influences the second harmonic and therefore the ferroelectric properties of LASO co-crystals. Specifically, more electron donating functional groups, such as -NH_2 promote symmetry-breaking dimerization over less electron donating groups such

as -OH. This study can and should be extended to understanding the influence of chemical functionalization of the *acceptor* molecule. A crystallographic study exists[355] for the co-crystallization of naphthalene donors and 3,6-dihalopyromellitic diimide acceptor molecules, where in addition to charge transfer, hydrogen bonding and van der Waals interactions, halogen bonding helps define the supramolecular structure of these co-crystals. Adding electron-withdrawing functional groups to the core acceptor, in turn, should strengthen the CT interactions in a similar vein to that observed when adding electron donating groups to the donor. A systematic study of the influence of this chemical functionalization on the CT properties, second harmonic activity and ferroelectric polarization of CT co-crystals will add to the literature precedent and knowledge base on how to design an organic crystalline ferroelectric material, mediated by intermolecular CT interactions.

Origins of Ferroelectricity in LASO Co-Crystals

The source of ferroelectricity in these LASO CT complexes have as yet eluded experimentalists. The seemingly apparent contradiction is the observation of ferroelectricity and second harmonic activity in a crystallographically centrosymmetric co-crystal. It has been hypothesized that this disparity could be due to (i) symmetry breaking hydrogen atoms, which cannot be located crystallographically, (ii) space group averaging of multiple noncentrosymmetric grains in across the co-crystal, and (iii) asymmetries in π-electron cloud distributions, that arise from CT interactions, between the donor and acceptor molecules. Regardless, understanding the source of ferroelectricity in these systems can help spur further attempts and molecular and crystal design, as well as aid in the translation of these materials to commercial applications. Attempts[195] at density functional theory (DFT) simulations have cast a shadow on the original work on LASO ferroelectrics, despite plenty of issues with the simulations themselves. Notwithstanding the absurd argument that simulations in a carefully controlled computational environment can completely undermine and disprove experimental data, the simulations did not take into account the added complexities of hydrogen bonding. Since hydrogen bonding is a central part of structural morphology and supramolecular function in

LASO co-crystals, a thorough study of these systems, that incorporates hydrogen bonding functionality to define electronic function, is much needed to ensure the train of scientific development keeps moving forward.

Magnetic Ordering and Multiferroicity in LASO Co-Crystals

Within the ionic phase of CT complexes, the transfer of an electron from the donor to acceptor intrinsically results in an antiferromagnetic coupling between the molecules in the dimer pair.[356,357] This is largely due to the spin-Peierls phase transition from a neutral to a dimerized CT complex.[43] The magnetic coupling, in turn, helps amplify the ferroelectric response by increasing the electronic component (due to intermolecular dipoles that arise due to CT interactions) of the measured polarization (as opposed to the ionic component, which is due to the spatial asymmetry of the partially ionic molecules).[120] Since the LASO co-crystals are structurally centrosymmetric, ionic polarization components can be assumed to be minimal. As a result, electronic polarizations, heavily mediated by antiferromagnetic coupling, is the dominant source of polarization in the LASO co-crystals. As a result, studying the antiferromagnetic coupling in LASO co-crystals, and exploring the effect of applied *magnetic* fields on the *ferroelectric* polarization of these CT systems would open doors to exploring multiferroicity in these systems, which has thus far been a pipe dream for organic CT complexes.

8.2.2 *Charge Transfer-Mediated Molecular Exchange in Supramolecular Amphiphiles*

Mediating CT Interactions and Mixing Through Amphiphile Chemistry

Chapter 6 demonstrated the use of amino acid chemistry to mediate the strength of PA assemblies in aqueous media. Incorporating the donor and acceptor motifs to the studied amino acid sequences could introduce another handle to modulate the thermodynamics and kinetics of assembly in these CT amphiphile molecules. The balance and interplay between π-π stacking, CT interactions and hydrogen bonding could be tuned by changing the amino acid hydrophobicity, leading

to interesting morphology, and internal dynamics of the resulting nanostructure. In addition, the stability of the supramolecular assembly could influence how these assembled molecules mix when in the presence of their complementary acceptor or donor assemblies. This knowledge will, in turn, educate an understanding of the 'internal' driving forces that mediate assembly and mixing in these CT complexes.

Additional work could involve incorporating CT interactions to different regions of the PA, be it the β-sheet forming or the external hydrophilic region. Where the work thus far has focused on CT interactions in the hydrophobic core of the amphiphile, changing the location of the donor and acceptor moieties would significantly alter the assembly and intermolecular interactions within and between supramolecular architectures. Introducing CT interactions in the β-sheet assembling region could, for example, take the shape of a PA with perflurophenylalanine electron acceptors, and a second molecule with phenylalanine electron donors. Doing so would add a secondary interaction, namely electrostatic CT, in close proximity to existing π-π stacking and β-sheet driving hydrogen bonding interactions, and could potentially push the supramolecular system either out of or in to new equilibrium structures. The balance between hydrogen bonding and CT interactions can also be tuned by 'external' stimuli such as annealing and ageing, building a thermodynamic landscape for these supramolecular systems.

Lastly, incorporating CT complexation to the exterior of the peptide amphiphile, such as a viologen electron acceptor on one molecule, and a naphthalene electron donor on another molecule, would exploit the unique electronic properties of CT complexes. The location of the complex could make it more accessible for relevant catalytic[358,359] reactions under the appropriate conditions. Understanding the underlying kinetics of these reactions is necessary, specifically with how it relates to the thermodynamics and kinetics behind the formation of the CT complexes.

Elucidating Mechanisms for Intermolecular Exchange and Reorganization

What made the exchange study presented here unique was that intermolecular exchange occurred on time scales that were far shorter than that presented in previous experiments.[42] The working hypothesis is that the charge transfer, the driving force for intermolecular exchange, forces the pre-assembled molecules to associate despite the entropic and enthalpic penalty of dissociating one assembled nanostructure to mix with another. This also suggests an altered mechanism for association in these CT amphiphiles, different from the previous understanding of clustered molecular mixing. Conducting time-resolved photoluminescence, as well as electron paramagnetic resonance (EPR) experiments on these systems can help resolve the kinetics and energetics required for intermolecular exchange, as well as elucidate a mechanism for the mixing of donor and acceptor supramolecular amphiphiles in aqueous solvents.

REFERENCES

(1) Lehn, J.-M., *Supramolecular Chemistry: Concepts and Perspectives*; Wiley-VCH: Weinheim; New York, 1995.

(2) Lehn, J.-M. *Chem. Soc. Rev.* **2007**, *36*, 151–160.

(3) Lehn, J.-M. *Nobel lectures in chemistry, 1981-1990* **1992**, 444.

(4) Lehn, J.-M. *Proceedings of the National Academy of Sciences* **2002**, *99*, 4763–4768.

(5) Hoeben, F. J. M.; Jonkheijm, P.; Meijer, E. W.; Schenning, A. P. H. J. *Chemical Reviews* **2005**, *105*, 1491–1546.

(6) Brunsveld, L.; Folmer, B. J. B.; Meijer, E. W.; Sijbesma, R. P. *Chemical Reviews* **2001**, *101*, 4071–4098.

(7) Bruns, C. J.; Stoddart, J. F. *Accounts of Chemical Research* **2014**, *47*, 2186–2199.

(8) Bruns, C. J.; Stoddart, J. F. *Nature Nanotechnology* **2013**, *8*.

(9) Bruns, C. J.; Stoddart, J. F., *The Nature of the Mechanical Bond: From Molecules to Machines*; John Wiley & Sons: 2016.

(10) Barnes, J. C.; Juríček, M.; Strutt, N. L.; Frasconi, M.; Sampath, S.; Giesener, M. A.; McGrier, P. L.; Bruns, C. J.; Stern, C. L.; Sarjeant, A. A.; Stoddart, J. F. *Journal of the American Chemical Society* **2013**, *135*, 183–192.

(11) Dale, E. J.; Vermeulen, N. A.; Thomas, A. A.; Barnes, J. C.; Juríček, M.; Blackburn, A. K.; Strutt, N. L.; Sarjeant, A. A.; Stern, C. L.; Denmark, S. E.; Stoddart, J. F. *Journal of the American Chemical Society* **2014**, *136*, 10669–10682.

(12) Cui, H.; Webber, M. J.; Stupp, S. I. *Biopolymers* **2010**, *94*, 1–18.

(13) Shimizu, T.; Masuda, M.; Minamikawa, H. *Chemical Reviews* **2005**, *105*, 1401–1444.

(14) Atwood, J. L.; Lehn, J.-M., *Comprehensive Supramolecular Chemistry: Supramolecular reactivity and transport : bioinorganic systems*; Elsevier: 1996.

(15) Braun, E.; Eichen, Y.; Sivan, U.; Ben-Yoseph, G. *Nature* **1998**, *391*, 775.

(16) Schimmel, P. *Annual Review of Biochemistry* **1987**, *56*, 125–158.

(17) Lehn, J.-M. *Science* **1985**, *227*, 849–856.

(18) Kabsch, W.; Sander, C. *Biopolymers* **1983**, *22*, 2577–2637.

(19) Aida, T.; Meijer, E. W.; Stupp, S. I. *Science* **2012**, *335*, 813–817.

(20) Stupp, S. I.; Palmer, L. C. *Chemistry of Materials* **2014**, *26*, 507–518.

(21) Pashuck, E. T.; Stupp, S. I. *Journal of the American Chemical Society* **2010**, *132*, 8819–8821.

(22) Cui, H.; Muraoka, T.; Cheetham, A. G.; Stupp, S. I. *Nano Letters* **2009**, *9*, 945–951.

(23) Thompson, N. L.; Brian, A. A.; McConnell, H. M. *Biochimica et Biophysica Acta - Biomembranes* **1984**, *772*, 10–19.

(24) Jain, R. K.; Gupta, C. M.; Anand, N. *Tetrahedron Letters* **1981**, *22*, 2317–2320.

(25) Berndt, P.; Fields, G. B.; Tirrell, M. *Journal of the American Chemical Society* **1995**, *117*, 9515–9522.

(26) Israelachvili, J. N.; Mitchell, J. D.; W. Ninham, B. *Journal of the Chemical Society, Faraday Transactions 2* **1976**, *72*, 1525–1568.

(27) Hartgerink D., J.; Beniash, E.; Stupp, S. I. *Science* **2001**, *294*, 1684–1688.

(28) Stupp, S. I.; LeBonheur, V.; Walker, K.; Li, L. S.; Huggins, K. E.; Keser, M.; Amstutz, A. *Science* **1997**, *276*, 384–389.

(29) Hendricks, M. P.; Sato, K.; Palmer, L. C.; Stupp, S. I. *Accounts of Chemical Research* **2017**, *50*, 2440–2448.

(30) Chow, L. W.; Bitton, R.; Webber, M. J.; Carvajal, D.; Shull, K. R.; Sharma, A. K.; Stupp, S. I. *Biomaterials* **2011**, *32*, 1574–1582.

(31) Chow, L. W.; Wang, L.-j.; Kaufman, D. B.; Stupp, S. I. *Biomaterials* **2010**, *31*, 6154–6161.

(32) Lee, S. S.; Huang, B. J.; Kaltz, S. R.; Sur, S.; Newcomb, C. J.; Stock, S. R.; Shah, R. N.; Stupp, S. I. *Biomaterials* **2013**, *34*, 452–459.

(33) Shah, R. N.; Shah, N. A.; Del Rosario Lim, M. M.; Hsieh, C.; Nuber, G.; Stupp, S. I. *Proceedings of the National Academy of Sciences* **2010**, *107*, 3293–3298.

(34) Silva, G. A.; Czeisler, C.; Niece, K. L.; Beniash, E.; Harrington, D. A.; Kessler, J. A.; Stupp, S. I. *Science* **2004**, *303*, 1352–1355.

(35) Niece, K. L.; Hartgerink, J. D.; Donners, J. J. J. M.; Stupp, S. I. *Journal of the American Chemical Society* **2003**, *125*, 7146–7147.

(36) Tysseling-Mattiace, V. M.; Sahni, V.; Niece, K. L.; Birch, D.; Czeisler, C.; Fehlings, M. G.; Stupp, S. I.; Kessler, J. A. *Journal of Neuroscience* **2008**, *28*, 3814–3823.

(37) Preslar, A. T.; Parigi, G.; McClendon, M. T.; Sefick, S. S.; Moyer, T. J.; Haney, C. R.; Waters, E. A.; MacRenaris, K. W.; Luchinat, C.; Stupp, S. I.; Meade, T. J. *ACS Nano* **2014**, *8*, 7325–7332.

(38) Preslar, A. T.; Tantakitti, F.; Park, K.; Zhang, S.; Stupp, S. I.; Meade, T. J. *ACS Nano* **2016**, *10*, 7376–7384.

(39) Ortony, J. H.; Newcomb, C. J.; Matson, J. B.; Palmer, L. C.; Doan, P. E.; Hoffman, B. M.; Stupp, S. I. *Nature Materials* **2014**, *13*, 812–816.

(40) Moyer, T. J.; Cui, H.; Stupp, S. I. *The Journal of Physical Chemistry B* **2013**, *117*, 4604–4610.

(41) Cui, H.; Cheetham, A. G.; Pashuck, E. T.; Stupp, S. I. *Journal of the American Chemical Society* **2014**, *136*, 12461–12468.

(42) Da Silva, R. M. P.; van der Zwaag, D.; Albertazzi, L.; Lee, S. S.; Meijer, E. W.; Stupp, S. I. *Nature Communications* **2016**, *7*, 11561.

(43) Foster, R., *Organic Charge Transfer Complexes*, 2nd; Academic Press: London, 1970.

(44) Dewar, M. J.; Lepley, A. R. *Journal of American Chemical Society* **1961**, *83*, 4560–4563.

(45) Torrance, J. B. *Accounts of Chemical Research* **1979**, *12*, 79–85.

(46) Benesi, H. A.; Hildebrand, J. H. *Journal of the American Chemical Society* **1949**, *71*, 2703–2707.

(47) Mulliken, R. S. *Journal of the American Chemical Society* **1950**, *72*, 600–608.

(48) Mulliken, R. S. *Journal of American Chemical Society* **1950**, *72*, 4493–4503.

(49) Mulliken, R. S. *The Journal of Chemical Physics* **1955**, *23*, 397–398.

(50) Mulliken, R. S. *The Journal of Physical Chemistry* **1952**, *56*, 801–822.

(51) Foster, R. *The Journal of Physical Chemistry* **1980**, *84*, 2135–2141.

(52) Brédas, J.-L.; Beljonne, D.; Coropceanu, V.; Cornil, J. *Chemical Reviews* **2004**, *104*, 4971–5004.

(53) Li, Y.; Liu, T.; Liu, H.; Tian, M.-Z.; Li, Y. *Accounts of Chemical Research* **2014**, *47*, 1186–1198.

(54) Yuan, W. Z.; Gong, Y.; Chen, S.; Shen, X. Y.; Lam, J. W. Y.; Lu, P.; Lu, Y.; Wang, Z.; Hu, R.; Xie, N.; Kwok, H. S.; Zhang, Y.; Sun, J. Z.; Tang, B. Z. *Chemistry of Materials* **2012**, *24*, 1518–1528.

(55) Hamasaki, K.; Ikeda, H.; Nakamura, A.; Ueno, A.; Toda, F.; Suzuki, I.; Osa, T. *Journal of American Chemical Society* **1993**, *115*, 5035–5040.

(56) Peng, X.; Song, F.; Lu, E.; Wang, Y.; Zhou, W.; Fan, J.; Gao, Y. *Journal of the American Chemical Society* **2005**, *127*, 4170–4171.

(57) Zhang, Q. T.; Tour, J. M. *Journal of the American Chemical Society* **1998**, *120*, 5355–5362.

(58) Jenekhe, S. A.; Lu, L.; Alam, M. M. *Macromolecules* **2001**, *34*, 7315–7324.

(59) Chen, S.; Li, Y.; Liu, C.; Yang, W.; Li, Y. *European Journal of Organic Chemistry* **2011**, *2011*, 6445–6451.

(60) Chen, S.; Qin, Z.; Liu, T.; Wu, X.; Li, Y.; Liu, H.; Song, Y.; Li, Y. *Physical Chemistry Chemical Physics* **2013**, *15*, 12660.

(61) Jiang, D.; Xue, Z.; Li, Y.; Liu, H.; Yang, W. *Journal of Materials Chemistry C* **2013**, *1*, 5694.

(62) Sariciftci, N. S.; Smilowitz, L.; Heeger, A. J.; Wudl, F. *Science* **1992**, 1474–1476.

(63) Yamamoto, Y.; Fukushima, T.; Suna, Y.; Ishii, N.; Saeki, A.; Seki, S.; Tagawa, S.; Taniguchi, M.; Kawai, T.; Aida, T. *Science* **2006**, *314*, 1761–1765.

(64) Edvinsson, T.; Li, C.; Pschirer, N.; Schöneboom, J.; Eickemeyer, F.; Sens, R.; Boschloo, G.; Herrmann, A.; Müllen, K.; Hagfeldt, A. *The Journal of Physical Chemistry C* **2007**, *111*, 15137–15140.

(65) Bessho, T.; Zakeeruddin, S. M.; Yeh, C.-Y.; Diau, E. W.-G.; Grätzel, M. *Angewandte Chemie International Edition* **2010**, *49*, 6646–6649.

(66) Xu, J.; Wen, L.; Zhou, W.; Lv, J.; Guo, Y.; Zhu, M.; Liu, H.; Li, Y.; Jiang, L. *The Journal of Physical Chemistry C* **2009**, *113*, 5924–5932.

(67) Albert, I. D.; Marks, T. J.; Ratner, M. A. *Chemistry of Materials* **1998**, *10*, 753–762.

(68) Dereka, B.; Koch, M.; Vauthey, E. *Accounts of Chemical Research* **2017**, *50*, 426–434.

(69) Goetz, K. P.; Vermeulen, D.; Payne, M. E.; Kloc, C.; McNeil, L. E.; Jurchescu, O. D. *Journal of Materials Chemistry C* **2014**, *2*, 3065–3076.

(70) Soos, Z. G. *Annual Review of Physical Chemistry* **1974**, *25*, 121–153.

(71) Mulliken, R. S. *Journal of the American Chemical Society* **1952**, *74*, 811–824.

(72) Beckers, E. H. A.; Meskers, S. C. J.; Schenning, A. P. H. J.; Chen, Z.; Würthner, F.; Marsal, P.; Beljonne, D.; Cornil, J.; Janssen, R. A. J. *Journal of the American Chemical Society* **2006**, *128*, 649–657.

(73) Herbstein, F. H.; Snyman, J. A. *Philosophical Transactions of the Royal Society of London A* **1969**, *264*, 635–662.

(74) Fyfe, C. A. *Journal of the Chemical Society, Faraday Transactions 2* **1974**, *70*, 1633–1641.

(75) Kulkarni, C.; Periyasamy, G.; Balasubramanian, S.; George, S. J. *Physical Chemistry Chemical Physics* **2014**, *16*, 14661.

(76) Grabner, G.; Rechthaler, K.; Mayer, B.; Köhler, G.; Rotkiewicz, K. *The Journal of Physical Chemistry A* **2000**, *104*, 1365–1376.

(77) Cubberley, M. S.; Iverson, B. L. *Journal of the American Chemical Society* **2001**, *123*, 7560–7563.

(78) Tayi, A. S.; Kaeser, A.; Matsumoto, M.; Aida, T.; Stupp, S. I. *Nature Chemistry* **2015**, *7*, 281–294.

(79) Tayi, A. S. et al. *Nature* **2012**, *488*, 485–489.

(80) Horiuchi, S.; Okimoto, Y.; Kumai, R.; Tokura, Y. *Journal of the Physical Society of Japan* **2000**, *69*, 1302–1305.

(81) Tokura, Y.; Koshihara, S.; Iwasa, Y.; Okamoto, H.; Komatsu, T.; Koda, T.; Iwasawa, N.; Saito, G. *Physical Review Letters* **1989**, *63*, 2405.

(82) Horiuchi, S.; Kagawa, F.; Hatahara, K.; Kobayashi, K.; Kumai, R.; Murakami, Y.; Tokura, Y. *Nature Communications* **2012**, *3*, 1308.

(83) Horiuchi, S.; Tokura, Y. *Nature Materials* **2008**, *7*, 357–366.

(84) Saito, G.; Yoshida, Y. *Bulletin of the Chemical Society of Japan* **2007**, *80*, 1–137.

(85) Alves, H.; Molinari, A. S.; Xie, H.; Morpurgo, A. F. *Nature Materials* **2008**, *7*, 574–580.

(86) LeBlanc, O. H. *The Journal of Chemical Physics* **1965**, *42*, 4307–4308.

(87) Ferraris, J.; Cowan, D. O.; Walatka, V. t.; Perlstein, J. H. *Journal of the American Chemical Society* **1973**, *95*, 948–949.

(88) Warmack, R. J.; Callcott, T. A.; Watson, C. R. *Physical Review B* **1975**, *12*, 3336.

(89) Shchegolev, I. F. *Physica Status Solidi A* **1972**, *12*, 9–45.

(90) Torrance, J. B.; Silverman, B. D. *Physical Review B* **1977**, *15*, 788.

(91) Fritchie, C. J.; Arthur, P. *Acta Crystallographica* **1966**, *21*, 139–145.

(92) Fritchie, C. J. *Acta Crystallographica* **1966**, *20*, 892–898.

(93) Charvet, R.; Yamamoto, Y.; Sasaki, T.; Kim, J.; Kato, K.; Takata, M.; Saeki, A.; Seki, S.; Aida, T. *Journal of the American Chemical Society* **2012**, *134*, 2524–2527.

(94) Das, A.; Ghosh, S. *Chemical Communications* **2011**, *47*, 8922.

(95) Chakraborty, S.; Kar, H.; Sikder, A.; Ghosh, S. *Chemical Science* **2017**, *8*, 1040–1045.

(96) Torrance, J. B.; Vazquez, J. E.; Mayerle, J. J.; Lee, V. Y. *Physical Review Letters* **1981**, *46*, 253–257.

(97) Torrance, J. B.; Girlando, A.; Mayerle, J. J.; Crowley, J. I.; Lee, V. Y.; Batail, P.; LaPlaca, S. J. *Physical Review Letters* **1981**, *47*, 1747.

(98) Le Cointe, M.; Lemée-Cailleau, M. H.; Cailleau, H.; Toudic, B.; Toupet, L.; Heger, G.; Moussa, F.; Schweiss, P.; Kraft, K. H.; Karl, N. *Physical Review B* **1995**, *51*, 3374.

(99) Okimoto, Y.; Horiuchi, S.; Saitoh, E.; Kumai, R.; Tokura, Y. *Physical Review Letters* **2001**, *87*.

(100) Kagawa, F.; Horiuchi, S.; Matsui, H.; Kumai, R.; Onose, Y.; Hasegawa, T.; Tokura, Y. *Physical Review Letters* **2010**, *104*.

(101) Kumar, M.; Venkata Rao, K.; George, S. J. *Physical Chemistry Chemical Physics* **2014**, *16*, 1300–1313.

(102) Das, A.; Ghosh, S. *Angewandte Chemie International Edition* **2014**, *53*, 2038–2054.

(103) Blackburn, A. K. et al. *Journal of the American Chemical Society* **2014**, *136*, 17224–17235.

(104) Gidden, J.; Wyttenbach, T.; Jackson, A. T.; Scrivens, J. H.; Bowers, M. T. *Journal of the American Chemical Society* **2000**, *122*, 4692–4699.

(105) Fyfe, M. C.; Glink, P. T.; Menzer, S.; Stoddart, J. F.; White, A. J.; Williams, D. J. *Angewandte Chemie International Edition* **1997**, *36*, 2068–2070.

(106) Yaghi, O. M.; O'keeffe, M.; Ockwig, N. W.; Chae, H. K.; Eddaoudi, M.; Kim, J. *Nature* **2003**, *423*, 705–714.

(107) Eddaoudi, M.; Moler, D. B.; Li, H.; Chen, B.; Reineke, T. M.; O'Keeffe, M.; Yaghi, O. M. *Accounts of Chemical Research* **2001**, *34*, 319–330.

(108) Long, J. R.; Yaghi, O. M. *Chemical Society Reviews* **2009**, *38*, 1213.

(109) Zhang, J.; Tan, J.; Ma, Z.; Xu, W.; Zhao, G.; Geng, H.; Di, C.; Hu, W.; Shuai, Z.; Singh, K.; Zhu, D. *Journal of the American Chemical Society* **2013**, *135*, 558–561.

(110) Zhang, J.; Geng, H.; Virk, T. S.; Zhao, Y.; Tan, J.; Di, C.-a.; Xu, W.; Singh, K.; Hu, W.; Shuai, Z.; Liu, Y.; Zhu, D. *Advanced Materials* **2012**, *24*, 2603–2607.

(111) Claborn, K.; Chu, A.-S.; Jang, S.-H.; Su, F.; Kaminsky, W.; Kahr, B. *Crystal Growth & Design* **2005**, *5*, 2117–2123.

(112) Kahr, B.; Gurney, R. W. *Chemical Reviews* **2001**, *101*, 893–952.

(113) Marsh, R. E. *Acta Crystallographica, Section B* **1995**, *51*, 897–907.

(114) Flack, H. D. *Acta Crystallographica, Section A* **1983**, *39*, 876–881.

(115) Lines, M. E.; Glass, A. M., *Principles and Applications of Ferroelectrics and Related Materials*; Clarendon Press; Oxford University Press: Oxford; New York, 2001.

(116) Valasek, J. *Physical Review* **1921**, *17*, 475.

(117) Kawai, H. *Japan Journal of Applied Physics* **1969**, *8*.

(118) Kepler, R. G. *Annual Review of Physical Chemistry* **1978**, *29*, 497–518.

(119) Sato, O. *Nature Chemistry* **2016**, *8*, 644–656.

(120) Horiuchi, S.; Kobayashi, K.; Kumai, R.; Ishibashi, S. *Chemistry Letters* **2014**, *43*, 26–35.

(121) Fridkin, V.; Ducharme, S., *Ferroelectricity at the Nanoscale*; NanoScience and Technology, DOI: 10.1007/978-3-642-41007-9; Springer Berlin Heidelberg: Berlin, Heidelberg, 2014.

(122) Horiuchi, S.; Kumai, R.; Fujioka, J.; Tokura, Y. *Physica B* **2010**, *405*, S334–S337.

(123) Bolla, G.; Dong, H.; Zhen, Y.; Wang, Z.; Hu, W. *Science China Materials* **2016**, *59*, 523–530.

(124) Martin, L. W.; Rappe, A. M. *Nature Reviews Materials* **2016**, *2*, 16087.

(125) Devonshire, A. F. *Advances in Physics* **1954**, *3*, 85–130.

(126) Devonshire, A. F. *The London, Edinburgh, and Dublin Philosophical Magazine and Journal of Science* **1949**, *40*, 1040–1063.

(127) Devonshire, A. F. *The London, Edinburgh, and Dublin Philosophical Magazine and Journal of Science* **1951**, *42*, 1065–1079.

(128) Blinc, R.; Detoni, S.; Pintar, M. *Physical Review* **1961**, *124*, 1036–1038.

(129) Jaffe, B., *Piezoelectric Ceramics*; Elsevier: 2012.

(130) Scott, J. F. *Science* **2007**, *315*, 954–959.

(131) Scott, J. F.; Araujo, C. A. P. d. *Science* **1989**, *246*, 1400–1405.

(132) Scott, J. F. *Journal of Physics: Condensed Matter* **2008**, *20*, 021001.

(133) Kurtz, S. K. *Journal of Applied Physics* **1968**, *39*, 3798–3813.

(134) Bergman, J. G. *Applied Physics Letters* **1971**, *18*, 203–205.

(135) Campagnola, P. J.; Loew, L. M. *Nature Biotechnology* **2003**, *21*, 1356–1360.

(136) Fiebig, M.; Pavlov, V. V.; Pisarev, R. V. *Journal of the Optical Society of America B* **2005**, *22*, 96–118.

(137) Benedek, N. A.; Rondinelli, J. M.; Djani, H.; Ghosez, P.; Lightfoot, P. *Dalton Transactions* **2015**, *44*, 10543–10558.

(138) Schmidt, V. H. *Ferroelectrics* **1987**, *72*, 157–173.

(139) Bousquet, E.; Dawber, M.; Stucki, N.; Lichtensteiger, C.; Hermet, P.; Gariglio, S.; Triscone, J.-M.; Ghosez, P. *Nature* **2008**, *452*, 732.

(140) Mulder, A. T.; Benedek, N. A.; Rondinelli, J. M.; Fennie, C. J. *Advanced Functional Materials* **2013**, *23*, 4810–4820.

(141) Lee, J. H. et al. *Nature* **2010**, *466*, 954–958.

(142) Slater, J. C. *The Journal of Chemical Physics* **1941**, *9*, 16–33.

(143) Lovinger, A. J. *Science* **1983**, *220*, 1115–1121.

(144) Miyajima, D.; Araoka, F.; Takezoe, H.; Kim, J.; Kato, K.; Takata, M.; Aida, T. *Science* **2012**, *336*, 209–213.

(145) Akutagawa, T.; Koshinaka, H.; Sato, D.; Takeda, S.; Noro, S.-I.; Takahashi, H.; Kumai, R.; Tokura, Y.; Nakamura, T. *Nature Materials* **2009**, *8*, 342–347.

(146) Naber, R. C. G.; Asadi, K.; Blom, P. W. M.; de Leeuw, D. M.; de Boer, B. *Advanced Materials* **2010**, *22*, 933–945.

(147) Meyer, R. B. *Molecular Crystals and Liquid Crystals* **1977**, *40*, 33–48.

(148) Araoka, F.; Masuko, S.; Kogure, A.; Miyajima, D.; Aida, T.; Takezoe, H. *Advanced Materials* **2013**, *25*, 4014–4017.

(149) Katrusiak, A.; Szafrański, M. *Physical Review Letters* **1999**, *82*, 576–579.

(150) Horiuchi, S.; Ishii, F.; Kumai, R.; Okimoto, Y.; Tachibana, H.; Nagaosa, N.; Tokura, Y. *Nature Materials* **2005**, *4*, 163.

(151) Horiuchi, S.; Kumai, R.; Tokunaga, Y.; Tokura, Y. *Journal of the American Chemical Society* **2008**, *130*, 13382–13391.

(152) Horiuchi, S.; Tokunaga, Y.; Giovannetti, G.; Picozzi, S.; Itoh, H.; Shimano, R.; Kumai, R.; Tokura, Y. *Nature* **2010**, *463*, 789–792.

(153) Szafrański, M.; Katrusiak, A.; McIntyre, G. J. *Physical Review Letters* **2002**, *89*, 215507.

(154) Kobayashi, K.; Horiuchi, S.; Kumai, R.; Kagawa, F.; Murakami, Y.; Tokura, Y. *Physical Review Letters* **2012**, *108*.

(155) Mitani, T.; Kaneko, Y.; Tanuma, S.; Tokura, Y.; Koda, T.; Saito, G. *Physical Review B* **1987**, *35*, 427–429.

(156) Kishida, H.; Takamatsu, H.; Fujinuma, K.; Okamoto, H. *Physical Review B* **2009**, *80*, 205201.

(157) Kagawa, F.; Horiuchi, S.; Tokunaga, M.; Fujioka, J.; Tokura, Y. *Nature Physics* **2010**, *6*, 169–172.

(158) Kagawa, F.; Horiuchi, S.; Tokura, Y. *Crystals* **2017**, *7*, 106.

(159) Horiuchi, S.; Kobayashi, K.; Kumai, R.; Minami, N.; Kagawa, F.; Tokura, Y. *Nature Communications* **2015**, *6*, 7469.

(160) Rabe, K. M.; Ahn, C. H.; Triscone, J.-M., *Physics of Ferroelectrics: A Modern Perspective*; Springer: Berlin; New York, 2007.

(161) Choi, T.; Horibe, Y.; Yi, H. T.; Choi, Y. J.; Wu, W.; Cheong, S.-W. *Nature Materials* **2010**, *9*, 253–258.

(162) Balke, N. et al. *Nature Physics* **2011**, *8*, 81–88.

(163) Miller, R. C. *Physical Review* **1964**, *134*, A1313–A1319.

(164) Frey, M. H.; Payne, D. A. *Physical Review B* **1996**, *54*, 3158–3168.

(165) Fu, D.-W.; Cai, H.-L.; Liu, Y.; Ye, Q.; Zhang, W.; Zhang, Y.; Chen, X.-Y.; Giovannetti, G.; Capone, M.; Li, J.; Xiong, R.-G. *Science* **2013**, *339*, 425–428.

(166) Dawber, M.; Chandra, P.; Littlewood, P. B.; Scott, J. F. *Journal of Physics: Condensed Matter* **2003**, *15*, L393.

(167) Mehta, R. R. *Journal of Applied Physics* **1973**, *44*, 3379.

(168) Naumov, I. I.; Bellaiche, L.; Fu, H. *Nature* **2004**, *432*, 737–740.

(169) McQuaid, R.; McGilly, L.; Sharma, P.; Gruverman, A.; Gregg, J. *Nature Communications* **2011**, *2*, 404.

(170) Rodriguez, B. J.; Gao, X. S.; Liu, L. F.; Lee, W.; Naumov, I. I.; Bratkovsky, A. M.; Hesse, D.; Alexe, M. *Nano Letters* **2009**, *9*, 1127–1131.

(171) Gruverman, A.; Wu, D.; Fan, H.-J.; Vrejoiu, I.; Alexe, M.; Harrison, R. J.; Scott, J. F. *Journal of Physics: Condensed Matter* **2008**, *20*, 342201.

(172) Jia, C.-L.; Urban, K. W.; Alexe, M.; Hesse, D.; Vrejoiu, I. *Science* **2011**, *331*, 1420–1423.

(173) Lutkenhaus, J. L.; McEnnis, K.; Serghei, A.; Russell, T. P. *Macromolecules* **2010**, *43*, 3844–3850.

(174) Lovinger, A. J.; Davis, D. D.; Cais, R. E.; Kometani, J. M. *Macromolecules* **1986**, *19*, 1491–1494.

(175) Koga, K.; Ohigashi, H. *Journal of Applied Physics* **1986**, *59*, 2142–2150.

(176) Schein, B. J. B.; Lingafelter, E. C.; Stewart, J. M. *The Journal of Chemical Physics* **1967**, *47*, 5183–5189.

(177) Kagawa, F.; Minami, N.; Horiuchi, S.; Tokura, Y. *Nature Communications* **2016**, *7*, 10675.

(178) Westrip, S. P. *Journal of Applied Crystallography* **2010**, *43*, 920–925.

(179) Spek, A. L. *Acta Crystallographica, Section D* **2009**, *65*, 148–155.

(180) Ok, K. M.; Chi, E. O.; Halasyamani, P. S. *Chemical Society Reviews* **2006**, *35*, 710–717.

(181) Coda, A.; Pandarese, F. *Journal of Applied Crystallography* **1976**, *9*, 193–198.

(182) Nalla, V.; Medishetty, R.; Wang, Y.; Bai, Z.; Sun, H.; Wei, J.; Vittal, J. J. *IUCrJ* **2015**, *2*, 317–321.

(183) Patil, P. S.; Bhumannavar, V. M.; Bannur, M. S.; Kulkarni, H. N.; Bhagavannarayana, G. *Journal of Crystallization Process and Technology* **2013**, *03*, 108–117.

(184) Cai, H.-L.; Fu, D.-W.; Zhang, Y.; Zhang, W.; Xiong, R.-G. *Physical Review Letters* **2012**, *109*, 16901.

(185) Shi, P.-P.; Tang, Y.-Y.; Li, P.-F.; Liao, W.-Q.; Wang, Z.-X.; Ye, Q.; Xiong, R.-G. *Chemical Society Reviews* **2016**, *45*, 3811–3827.

(186) Jain, P.; Stroppa, A.; Nabok, D.; Marino, A.; Rubano, A.; Paparo, D.; Matsubara, M.; Nakotte, H.; Fiebig, M.; Picozzi, S., et al. *Quantum Materials* **2016**, *1*, 16012.

(187) Kurimura, S.; Uesu, Y. *Journal of Applied Physics* **1997**, *81*, 369–375.

(188) Bhar, G. *Japan Journal of Applied Physics* **1993**, *32*, 653–659.

(189) Lai, W.-H.; Haynes, A. S.; Frazer, L.; Chang, Y.-M.; Liu, T.-K.; Lin, J.-F.; Liang, I.-C.; Sheu, H.-S.; Ketterson, J. B.; Kanatzidis, M. G.; Hsu, K.-F. *Chemistry of Materials* **2015**, *27*, 1316–1326.

(190) Desiraju, G. R.; Curtin, D. Y.; Paul, I. C. *Molecular Crystals and Liquid Crystals* **1979**, *52*, 259–266.

(191) Sipe, J. E.; Moss, D. J.; van Driel, H. M. *Physical Review B* **1987**, *35*, 1129–1141.

(192) Dadap, J. I.; Shan, J.; Heinz, T. F. *Journal of the Optical Society of America B* **2004**, *21*, 1328–1347.

(193) Wensheng, G.; Guo, F.; Wei, C.; Liu, Q.; Zhou, G.; Wang, D.; Shao, Z. *Science in China Series B: Chemistry* **2002**, *45*, 267–274.

(194) Chen, S.; Zeng, X. C. *Journal of the American Chemical Society* **2014**, *136*, 6428–6436.

(195) D'Avino, G.; Verstraete, M. J. *Physical Review Letters* **2014**, *113*, 237602.

(196) Sheldrick, G. M. *Acta Crystallographica, Section A* **2008**, *64*, 112–122.

(197) Narayanan, A.; Cao, D.; Frazer, L.; Tayi, A. S.; Blackburn, A. K.; Sue, A. C.-H.; Ketterson, J. B.; Stoddart, J. F.; Stupp, S. I. *Journal of the American Chemical Society* **2017**, *139*, 9186–9191.

(198) Hansch, C.; Leo, A.; Taft, R. W. *Chemical Reviews* **1991**, *91*, 165–195.

(199) Sue, C.-H.; Basu, S.; Fahrenbach, A. C.; Shveyd, A. K.; Dey, S. K.; Botros, Y. Y.; Stoddart, J. F. *Chemical Science* **2010**, *1*, 119–125.

(200) Fujii, S.; Lehn, J.-M. *Angewandte Chemie International Edition* **2009**, *48*, 7635–7638.

(201) Lockett, J.; Short, W. F. *Journal of the Chemical Society (Resumed)* **1939**, *0*, 787–790.

(202) Schenning, A. P. H. J.; Meijer, E. W. *Chemical Communications* **2005**, 3245.

(203) Murphy, A. R.; Fréchet, J. M. J. *Chemical Reviews* **2007**, *107*, 1066–1096.

(204) Lezama, I. G.; Nakano, M.; Minder, N. A.; Chen, Z.; Di Girolamo, F. V.; Facchetti, A.; Morpurgo, A. F. *Nature Materials* **2012**, *11*, 788–794.

(205) Jain, A.; George, S. J. *Materials Today* **2015**, *18*, 206–214.

(206) Das, A.; Molla, M. R.; Banerjee, A.; Paul, A.; Ghosh, S. *Chemistry - A European Journal* **2011**, *17*, 6061–6066.

(207) Das, A.; Molla, M. R.; Maity, B.; Koley, D.; Ghosh, S. *Chemistry - A European Journal* **2012**, *18*, 9849–9859.

(208) Kato, S.-i.; Matsumoto, T.; Ideta, K.; Shimasaki, T.; Goto, K.; Shinmyozu, T. *The Journal of Organic Chemistry* **2006**, *71*, 4723–4733.

(209) Mukhopadhyay, P.; Iwashita, Y.; Shirakawa, M.; Kawano, S.-i.; Fujita, N.; Shinkai, S. *Angewandte Chemie International Edition* **2006**, *45*, 1592–1595.

(210) Zhu, W.; Zheng, R.; Fu, X.; Fu, H.; Shi, Q.; Zhen, Y.; Dong, H.; Hu, W. *Angewandte Chemie International Edition* **2015**, n/a–n/a.

(211) Kübel, J.; Schroot, R.; Wächtler, M.; Schubert, U. S.; Dietzek, B.; Jäger, M. *The Journal of Physical Chemistry C* **2015**, *119*, 4742–4751.

(212) Park, S. K. et al. *Advanced Materials* **2017**, *29*, 1701346.

(213) Jin, X.-H.; Chen, C.; Ren, C.-X.; Cai, L.-X.; Zhang, J. *Chem. Commun.* **2014**, *50*, 15878–15881.

(214) Calderon, R. M. K.; Valero, J.; Grimm, B.; de Mendoza, J.; Guldi, D. M. *Journal of the American Chemical Society* **2014**, *136*, 11436–11443.

(215) Kumar, B. V. V. S. P.; Rao, K. V.; Soumya, T.; George, S. J.; Eswaramoorthy, M. *Journal of the American Chemical Society* **2013**, *135*, 10902–10905.

(216) Shivanna, R.; Pramanik, D.; Kumar, H.; Rao, K. V.; George, S. J.; Maiti, P. K.; Narayan, K. S. *Soft Matter* **2013**, *9*, 10196.

(217) Jeon, Y. J.; Bharadwaj, P. K.; Choi, S.; Lee, J. W.; Kim, K. *Angewandte Chemie* **2002**, *114*, 4654–4656.

(218) Nalluri, S. K. M.; Berdugo, C.; Javid, N.; Frederix, P. W. J. M.; Ulijn, R. V. *Angewandte Chemie International Edition* **2014**, *53*, 5882–5887.

(219) Wang, C.; Wu, N.; Jacobs, D. L.; Xu, M.; Yang, X.; Zang, L. *Chemical Communications* **2017**, *53*, 1132–1135.

(220) Sagade, A. A.; Rao, K. V.; Mogera, U.; George, S. J.; Datta, A.; Kulkarni, G. U. *Advanced Materials* **2013**, *25*, 559–564.

(221) Rao, K. V.; George, S. J. *Chemistry - A European Journal* **2012**, *18*, 14286–14291.

(222) Jain, A.; Rao, K. V.; Mogera, U.; Sagade, A. A.; George, S. J. *Chemistry - A European Journal* **2011**, *17*, 12355–12361.

(223) Mondal, T.; Sakurai, T.; Yoneda, S.; Seki, S.; Ghosh, S. *Macromolecules* **2015**, *48*, 879–888.

(224) Tatewaki, Y.; Hatanaka, T.; Tsunashima, R.; Nakamura, T.; Kimura, M.; Shirai, H. *Chemistry - An Asian Journal* **2009**, *4*, 1474–1479.

(225) Nalluri, S. K. M.; Shivarova, N.; Kanibolotsky, A. L.; Zelzer, M.; Gupta, S.; Frederix, P. W. J. M.; Skabara, P. J.; Gleskova, H.; Ulijn, R. V. *Langmuir* **2014**, *30*, 12429–12437.

(226) Zhang, J.; Liu, G.; Zhou, Y.; Long, G.; Gu, P.; Zhang, Q. *ACS Applied Materials & Interfaces* **2017**, *9*, 1183–1188.

(227) Guan, Y.-S.; Qin, Y.; Sun, Y.; Chen, J.; Xu, W.; Zhu, D. *Chemical Communications* **2016**, *52*, 4648–4651.

(228) Martín, T.; Obst, U.; Rebek Jr., J. *Science* **1998**, *281*, 1842–1845.

(229) Johnson, D. W.; Hof, F.; Palmer, L. C.; Mart□n, T.; Obst, U.; Rebek Jr., J. *Chemical Communications* **2003**, 1638.

(230) Goldstein, R. F.; Stryer, L. *Biophysical Journal* **1986**, *50*, 583–599.

(231) Smulders, M. M. J.; Nieuwenhuizen, M. M. L.; deâ Greef, T. F. A.; vanâ derâ Schoot, P.; Schenning, A. P. H. J.; Meijer, E. W. *Chemistry - A European Journal* **2010**, *16*, 362–367.

(232) Korevaar, P. A.; de Greef, T. F. A.; Meijer, E. W. *Chemistry of Materials* **2014**, *26*, 576–586.

(233) Korevaar, P. A.; George, S. J.; Markvoort, A. J.; Smulders, M. M. J.; Hilbers, P. A. J.; Schenning, A. P. H. J.; De Greef, T. F. A.; Meijer, E. W. *Nature* **2012**, *481*, 492–496.

(234) Renny, J. S.; Tomasevich, L. L.; Tallmadge, E. H.; Collum, D. B. *Angewandte Chemie International Edition* **2013**, *52*, 11998–12013.

(235) Olson, E. J.; Bühlmann, P. *The Journal of Organic Chemistry* **2011**, *76*, 8406–8412.

(236) Longsworth, L. G. *The Journal of Physical Chemistry* **1960**, *64*, 1914–1917.

(237) Cohen, Y.; Avram, L.; Frish, L. *Angewandte Chemie International Edition* **2005**, *44*, 520–554.

(238) Ho Ko, Y.; Kim, E.; Hwang, I.; Kim, K. *Chemical Communications* **2007**, *0*, 1305–1315.

(239) Šmejkalová, D.; Piccolo, A. *Environmental Science & Technology* **2008**, *42*, 699–706.

(240) Coropceanu, V.; Cornil, J.; da Silva Filho, D. A.; Olivier, Y.; Silbey, R.; Brédas, J.-L. *Chemical Reviews* **2007**, *107*, 926–952.

(241) Méndez, H.; Heimel, G.; Opitz, A.; Sauer, K.; Barkowski, P.; Oehzelt, M.; Soeda, J.; Okamoto, T.; Takeya, J.; Arlin, J.-B.; Balandier, J.-Y.; Geerts, Y.; Koch, N.; Salzmann, I. *Angewandte Chemie International Edition* **2013**, *52*, 7751–7755.

(242) Girlando, A.; Marzola, F.; Pecile, C.; Torrance, J. B. *The Journal of Chemical Physics* **1983**, *79*, 1075–1085.

(243) Ranzieri, P.; Masino, M.; Girlando, A.; Lemée-Cailleau, M.-H. *Physical Review B* **2007**, *76*, DOI: 10.1103/PhysRevB.76.134115.

(244) Ferguson, E. E.; Matsen, F. A. *The Journal of Chemical Physics* **1958**, *29*, 105–107.

(245) Ferguson, E. E.; Matsen, F. A. *Journal of the American Chemical Society* **1960**, *82*, 3268–3271.

(246) Ferguson, E. E. *Journal de Chimie Physique* **1964**, *61*, 257–262.

(247) Friedrich, H. B.; Person, W. B. *The Journal of Chemical Physics* **1966**, *44*, 2161–2170.

(248) Wang, C.; Zhang, D.; Zhu, D. *Journal of the American Chemical Society* **2005**, *127*, 16372–16373.

(249) Kar, H.; Ghosh, S. *Chem. Commun.* **2014**, *50*, 1064–1066.

(250) Cui, Y.; Tan, M.; Zhu, A.; Guo, M. *J. Mater. Chem. B* **2015**, *3*, 2834–2841.

(251) Babu, P.; Sangeetha, N. M.; Vijaykumar, P.; Maitra, U.; Rissanen, K.; Raju, A. R. *Chemistry - A European Journal* **2003**, *9*, 1922–1932.

(252) Dimitrakopoulos, C. D.; Malenfort, P. R. L. *Advanced Materials* **2009**, *14*, 99–117.

(253) Stallinga, P.; Gomes, H. *Synthetic Metals* **2006**, *156*, 1305–1315.

(254) Stallinga, P.; Gomes, H. *Synthetic Metals* **2006**, *156*, 1316–1326.

(255) Kang, M. S.; Frisbie, C. D. *ChemPhysChem* **2013**, *14*, 1547–1552.

(256) Reinhardt, C. J.; Zhou, E. Y.; Jorgensen, M. D.; Partipilo, G.; Chan, J. *Journal of the American Chemical Society* **2018**, *140*, 1011–1018.

(257) Lahav, D. et al. *Journal of the American Chemical Society* **2017**, *139*, 14192–14197.

(258) Liu, X.; Ling, Q.; Zhao, L.; Qiu, G.; Wang, Y.; Song, L.; Zhang, Y.; Ruiz, J.; Astruc, D.; Gu, H. *Macromolecular Rapid Communications* **2017**, *38*, 1700448.

(259) Sayyadi, N.; Connally, R. E.; Try, A. *Chemical Communications* **2016**, *52*, 1154–1157.

(260) Park, Y.; Choong, V.; Gao, Y.; Hsieh, B. R.; Tang, C. W. *Applied Physics Letters* **1996**, *68*, 2699–2701.

(261) Stupp, S. I. *Nano Letters* **2010**, *10*, 4783–4786.

(262) Marchi-Artzner, V.; Gulik-Krzywicki, T.; Guedeau-Boudeville, M.-A.; Gosse, C.; Sanderson, J. M.; Dedieu, J.-C.; Lehn, J.-M. *ChemPhysChem* **2001**, *2*, 367–376.

(263) Cui, H.; Pashuck, E. T.; Velichko, Y. S.; Weigand, S. J.; Cheetham, A. G.; Newcomb, C. J.; Stupp, S. I. *Science* **2010**, *327*, 555–559.

(264) Fleming, S.; Ulijn, R. V. *Chem. Soc. Rev.* **2014**, *43*, 8150–8177.

(265) Fleming, S.; Debnath, S.; Frederix, P. W. J. M.; Tuttle, T.; Ulijn, R. V. *Chemical Communications* **2013**, *49*, 10587.

(266) Frederix, P. W. J. M.; Scott, G. G.; Abul-Haija, Y. M.; Kalafatovic, D.; Pappas, C. G.; Javid, N.; Hunt, N. T.; Ulijn, R. V.; Tuttle, T. *Nature Chemistry* **2015**, *7*, 30.

(267) Zhou, J.; Du, X.; Gao, Y.; Shi, J.; Xu, B. *Journal of the American Chemical Society* **2014**, *136*, 2970–2973.

(268) Chen, L.; Morris, K.; Laybourn, A.; Elias, D.; Hicks, M. R.; Rodger, A.; Serpell, L.; Adams, D. J. *Langmuir* **2010**, *26*, 5232–5242.

(269) Reches, M.; Gazit, E. *Nano Letters* **2004**, *4*, 581–585.

(270) Garifullin, R.; Guler, M. O. *Chemical Communications* **2015**, *51*, 12470–12473.

(271) Insuasty, A.; Atienza, C.; López, J. L.; Martín, N. *Chemical Communications* **2015**, *51*, 10506–10509.

(272) Nalluri, S. K. M.; Ulijn, R. V. *Chemical Science* **2013**, *4*, 3699.

(273) Ardoña, H. A. M.; Tovar, J. D. *Chem. Sci.* **2015**, *6*, 1474–1484.

(274) Xu, H.; Das, A. K.; Horie, M.; Shaik, M. S.; Smith, A. M.; Luo, Y.; Lu, X.; Collins, R.; Liem, S. Y.; Song, A.; Popelier, P. L. A.; Turner, M. L.; Xiao, P.; Kinloch, I. A.; Ulijn, R. V. *Nanoscale* **2010**, *2*, 960.

(275) Hunter, C. A.; Sanders, J. K. *Journal of the American Chemical Society* **1990**, *112*, 5525–5534.

(276) Al Kobaisi, M.; Bhosale, S. V.; Latham, K.; Raynor, A. M.; Bhosale, S. V. *Chemical Reviews* **2016**, *116*, 11685–11796.

(277) Thisayukta, J.; Nakayama, Y.; Kawauchi, S.; Takezoe, H.; Watanabe, J. *Journal of the American Chemical Society* **2000**, *122*, 7441–7448.

(278) Yang, Z.; Liang, G.; Ma, M.; Gao, Y.; Xu, B. *Journal of Materials Chemistry* **2007**, *17*, 850–854.

(279) Gawronski, J.; Brzostowska, M.; Kacprzak, K.; Holbon, H.; Skowronek, P. *Chirality* **2000**, *12*, 263–268.

(280) Gawroński, J.; Gawrońska, K.; Skowronek, P.; Holmén, A. *The Journal of Organic Chemistry* **1999**, *64*, 234–241.

(281) Yashima, E.; Ousaka, N.; Taura, D.; Shimomura, K.; Ikai, T.; Maeda, K. *Chemical Reviews* **2016**, *116*, 13752–13990.

(282) Guilbaud, J.-B.; Saiani, A. *Chemical Society Reviews* **2011**, *40*, 1200–1210.

(283) Kumar, M.; Brocorens, P.; Tonnelé, C.; Beljonne, D.; Surin, M.; George, S. J. *Nature Communications* **2014**, *5*, 5793.

(284) Tang, C.; Ulijn, R. V.; Saiani, A. *Langmuir* **2011**, *27*, 14438–14449.

(285) Tang, C.; Ulijn, R. V.; Saiani, A. *The European Physical Journal E* **2013**, *36*, DOI: 10.1140/epje/i2013-13111-3.

(286) Jonkman, H. T.; Kommandeur, J. *Chemical Physics Letters* **1972**, *15*, 496–499.

(287) Rudkevich, D. M.; Xu, H. *Chemical Communications* **2005**, 2651.

(288) Hampe, E. M.; Rudkevich, D. M. *Tetrahedron* **2003**, *59*, 9619–9625.

(289) Hampe, E. M.; Rudkevich, D. M. *Chemical Communications* **2002**, *0*, 1450–1451.

(290) Xu, H.; Rudkevich, D. M. *The Journal of Organic Chemistry* **2004**, *69*, 8609–8617.

(291) Ortony, J. H.; Qiao, B.; Newcomb, C. J.; Keller, T. J.; Palmer, L. C.; Deiss-Yehiely, E.; Olvera de la Cruz, M.; Han, S.; Stupp, S. I. *Journal of the American Chemical Society* **2017**, *139*, 8915–8921.

(292) Greenfield, M. A.; Hoffman, J. R.; Olvera de la Cruz, M.; Stupp, S. I. *Langmuir* **2010**, *26*, 3641–3647.

(293) Sur, S.; Newcomb, C. J.; Webber, M. J.; Stupp, S. I. *Biomaterials* **2013**, *34*, 4749–4757.

(294) Hanwell, M. D.; Curtis, D. E.; Lonie, D. C.; Vandermeersch, T.; Zurek, E.; Hutchison, G. R. *Journal of Cheminformatics* **2012**, *4*, 17.

(295) Marrink, S. J.; de Vries, A. H.; Mark, A. E. *The Journal of Physical Chemistry B* **2004**, *108*, 750–760.

(296) Marrink, S. J.; Risselada, H. J.; Yefimov, S.; Tieleman, D. P.; de Vries, A. H. *The Journal of Physical Chemistry B* **2007**, *111*, 7812–7824.

(297) Monticelli, L.; Kandasamy, S. K.; Periole, X.; Larson, R. G.; Tieleman, D. P.; Marrink, S.-J. *Journal of Chemical Theory and Computation* **2008**, *4*, 819–834.

(298) De Jong, D. H.; Singh, G.; Bennett, W. F. D.; Arnarez, C.; Wassenaar, T. A.; Schäfer, L. V.; Periole, X.; Tieleman, D. P.; Marrink, S. J. *Journal of Chemical Theory and Computation* **2013**, *9*, 687–697.

(299) Lee, O.-S.; Cho, V.; Schatz, G. C. *Nano Letters* **2012**, *12*, 4907–4913.

(300) Guo, C.; Luo, Y.; Zhou, R.; Wei, G. *ACS Nano* **2012**, *6*, 3907–3918.

(301) Mayans, E.; Ballano, G.; Casanovas, J.; Díaz, A.; Pérez-Madrigal, M. M.; Estrany, F.; Puiggalí, J.; Cativiela, C.; Alemán, C. *Chemistry – A European Journal* **2015**, *21*, 16895–16905.

(302) Humphrey, W.; Dalke, A.; Schulten, K. *Journal of Molecular Graphics* **1996**, *14*, 33–38.

(303) Abraham, M. J.; Murtola, T.; Schulz, R.; Páll, S.; Smith, J. C.; Hess, B.; Lindahl, E. *SoftwareX* **2015**, *1-2*, 19–25.

(304) De Jong, D. H.; Baoukina, S.; Ingólfsson, H. I.; Marrink, S. J. *Computer Physics Communications* **2016**, *199*, 1–7.

(305) Bussi, G.; Donadio, D.; Parrinello, M. *The Journal of Chemical Physics* **2007**, *126*, 014101.

(306) Berendsen, H. J. C.; Postma, J. P. M.; van Gunsteren, W. F.; DiNola, A.; Haak, J. R. *The Journal of Chemical Physics* **1984**, *81*, 3684–3690.

(307) Kroto, H. W.; Allaf, A. W.; Balm, S. P. *Chemical Reviews* **1991**, *91*, 1213–1235.

(308) Krätschmer, W.; Lamb, L. D.; Fostiropoulos, K.; Huffman, D. R. *Nature* **1990**, *347*, 354.

(309) Saito, S.; Oshiyama, A. *Physical Review Letters* **1991**, *66*, 2637–2640.

(310) Lof, R. W.; van Veenendaal, M. A.; Koopmans, B.; Jonkman, H. T.; Sawatzky, G. A. *Physical Review Letters* **1992**, *68*, 3924–3927.

(311) Haddon, R. C. et al. *Nature* **1991**, *350*, 320.

(312) Hebard, A. F.; Rosseinsky, M. J.; Haddon, R. C.; Murphy, D. W.; Glarum, S. H.; Palstra, T. T. M.; Ramirez, A. P.; Kortan, A. R. *Nature* **1991**, *350*, 600.

(313) David, W. I. F.; Ibberson, R. M.; Matthewman, J. C.; Prassides, K.; Dennis, T. J. S.; Hare, J. P.; Kroto, H. W.; Taylor, R.; Walton, D. R. M. *Nature* **1991**, *353*, 147.

(314) Diederich, F.; Gómez-López, M. *Chemical Society Reviews* **1999**, *28*, 263–277.

(315) Rao, A. M.; Zhou, P.; Wang, K.-A.; Hager, G. T.; Holden, J. M.; Wang, Y.; Lee, W.-T.; Bi, X.-X.; Eklund, P. C.; Cornett, D. S.; Duncan, M. A.; Amster, I. J. *Science* **1993**, *259*, 955–957.

(316) Roy, X.; Lee, C.-H.; Crowther, A. C.; Schenck, C. L.; Besara, T.; Lalancette, R. A.; Siegrist, T.; Stephens, P. W.; Brus, L. E.; Kim, P.; Steigerwald, M. L.; Nuckolls, C. *Science* **2013**, *341*, 157–160.

(317) Dunk, P. W.; Mulet-Gas, M.; Nakanishi, Y.; Kaiser, N. K.; Rodríguez-Fortea, A.; Shinohara, H.; Poblet, J. M.; Marshall, A. G.; Kroto, H. W. *Nature Communications* **2014**, *5*, 5844.

(318) Chikamatsu, M.; Nagamatsu, S.; Yoshida, Y.; Saito, K.; Yase, K.; Kikuchi, K. *Applied Physics Letters* **2005**, *87*, 203504.

(319) Chu, C.-C.; Raffy, G.; Ray, D.; Guerzo, A. D.; Kauffmann, B.; Wantz, G.; Hirsch, L.; Bassani, D. M. *Journal of the American Chemical Society* **2010**, *132*, 12717–12723.

(320) Schiros, T. et al. *Advanced Energy Materials* **2013**, *3*, 894–902.

(321) Menke, S. M.; Luhman, W. A.; Holmes, R. J. *Nature Materials* **2013**, *12*, 152.

(322) Atwood, J. L.; Koutsantonis, G. A.; Raston, C. L. *Nature* **1994**, *368*, 229.

(323) Effing, J.; Jonas, U.; Jullien, L.; Plesnivy, T.; Ringsdorf, H.; Diederich, F.; Thilgen, C.; Weinstein, D. *Angewandte Chemie International Edition* **1992**, *31*, 1599–1602.

(324) Pan, G.-B.; Cheng, X.-H.; Höger, S.; Freyland, W. *Journal of the American Chemical Society* **2006**, *128*, 4218–4219.

(325) Barbour, L. J.; Orr, G. W.; Atwood, J. L. *Chemical Communications* **1997**, *0*, 1439–1440.

(326) Andersson, T.; Nilsson, K.; Sundahl, M.; Westman, G.; Wennerström, O. *Journal of the Chemical Society, Chemical Communications* **1992**, *0*, 604–606.

(327) Priyadarsini, K. I.; Mohan, H.; Tyagi, A. K.; Mittal, J. P. *The Journal of Physical Chemistry* **1994**, *98*, 4756–4759.

(328) Tashiro, K.; Aida, T.; Zheng, J.-Y.; Kinbara, K.; Saigo, K.; Sakamoto, S.; Yamaguchi, K. *Journal of the American Chemical Society* **1999**, *121*, 9477–9478.

(329) Kieran, A. L.; Pascu, S. I.; Jarrosson, T.; Sanders, J. K. M. *Chemical Communications* **2005**, *0*, 1276–1278.

(330) Steed, J. W.; Junk, P. C.; Atwood, J. L.; Barnes, M. J.; Raston, C. L.; Burkhalter, R. S. *Journal of the American Chemical Society* **1994**, *116*, 10346–10347.

(331) Atwood, J. L.; Barnes, M. J.; Gardiner, M. G.; Raston, C. L. *Chemical Communications* **1996**, *0*, 1449–1450.

(332) Kawase, T.; Tanaka, K.; Fujiwara, N.; Darabi, H. R.; Oda, M. *Angewandte Chemie International Edition* **2003**, *42*, 1624–1628.

(333) Veen, E. M.; Feringa, B. L.; Postma, P. M.; Jonkman, H. T.; Spek, A. L. *Chemical Communications* **1999**, *0*, 1709–1710.

(334) Smith, B. W.; Monthioux, M.; Luzzi, D. E. *Nature* **1998**, *396*, 323.

(335) Kitaura, R.; Shinohara, H. *Chemistry – An Asian Journal* **2006**, *1*, 646–655.

(336) Vavro, J.; Llaguno, M. C.; Satishkumar, B. C.; Luzzi, D. E.; Fischer, J. E. *Applied Physics Letters* **2002**, *80*, 1450–1452.

(337) Pati, R.; Senapati, L.; Ajayan, P. M.; Nayak, S. K. *Journal of Applied Physics* **2003**, *95*, 694–697.

(338) Mayer, A. C.; Toney, M. F.; Scully, S. R.; Rivnay, J.; Brabec, C. J.; Scharber, M.; Koppe, M.; Heeney, M.; McCulloch, I.; McGehee, M. D. *Advanced Functional Materials* **2009**, *19*, 1173–1179.

(339) Miller, N. C.; Cho, E.; Gysel, R.; Risko, C.; Coropceanu, V.; Miller, C. E.; Sweetnam, S.; Sellinger, A.; Heeney, M.; McCulloch, I.; Brédas, J.-L.; Toney, M. F.; McGehee, M. D. *Advanced Energy Materials* **2012**, *2*, 1208–1217.

(340) Miller, N. C. et al. *Advanced Materials* **2012**, *24*, 6071–6079.

(341) Juríček, M.; Barnes, J. C.; Dale, E. J.; Liu, W.-G.; Strutt, N. L.; Bruns, C. J.; Vermeulen, N. A.; Ghooray, K. C.; Sarjeant, A. A.; Stern, C. L.; Botros, Y. Y.; Goddard, W. A.; Stoddart, J. F. *Journal of the American Chemical Society* **2013**, *135*, 12736–12746.

(342) Barnes, J. C.; Juríček, M.; Vermeulen, N. A.; Dale, E. J.; Stoddart, J. F. *The Journal of Organic Chemistry* **2013**, *78*, 11962–11969.

(343) Alers, G. B.; Golding, B.; Kortan, A. R.; Haddon, R. C.; Theil, F. A. *Science* **1992**, *257*, 511–514.

(344) Wen, C.; Li, J.; Kitazawa, K.; Aida, T.; Honma, I.; Komiyama, H.; Yamada, K. *Applied Physics Letters* **1992**, *61*, 2162–2163.

(345) Hamed, A.; Sun, Y. Y.; Tao, Y. K.; Meng, R. L.; Hor, P. H. *Physical Review B* **1993**, *47*, 10873–10880.

(346) Chiu, K.-C.; Su, Y.-C.; Chen, R.-S.; Lin, Y.-J.; Cheng, W.-R.; Tang, S.-J. *Japanese Journal of Applied Physics* **2002**, *41*, 6028.

(347) Frampton, M. J.; Anderson, H. L. *Angewandte Chemie International Edition* **2007**, *46*, 1028–1064.

(348) Zhang, W.; Jin, W.; Fukushima, T.; Saeki, A.; Seki, S.; Aida, T. *Science* **2011**, *334*, 340–343.

(349) Bassani, D. M. *Nature* **2011**, *480*, 326.

(350) Kato, T.; Kodama, T.; Shida, T.; Nakagawa, T.; Matsui, Y.; Suzuki, S.; Shiromaru, H.; Yamauchi, K.; Achiba, Y. *Chemical Physics Letters* **1991**, *180*, 446–450.

(351) Aoyagi, S. et al. *Nature Chemistry* **2010**, *2*, 678.

(352) Iwamoto, T.; Watanabe, Y.; Takaya, H.; Haino, T.; Yasuda, N.; Yamago, S. *Chemistry - A European Journal* **2013**, *19*, 14061–14068.

(353) Finkelstein, H. *Berichte der Deutschen Chemischen Gesellschaft* **1910**, *43*, 1528–1532.

(354) Kang, S. O.; Lynch, V. M.; Day, V. W.; Anslyn, E. V. *Organometallics* **2011**, *30*, 6233–6240.

(355) Cao, D.; Hong, M.; K. Blackburn, A.; Liu, Z.; M. Holcroft, J.; Fraser Stoddart, J. *Chemical Science* **2014**, *5*, 4242–4248.

(356) Giovannetti, G.; Kumar, S.; Stroppa, A.; van den Brink, J.; Picozzi, S. *Physical Review Letters* **2009**, *103*.

(357) Di Maiolo, F.; Sissa, C.; Painelli, A. *Scientific Reports* **2016**, *6*.

(358) Sun, S.; Gao, W.; Liu, F.; Fan, J.; Peng, X. *Journal of Materials Chemistry* **2010**, *20*, 5888–5892.

(359) Zou, D.; Andersson, S.; Zhang, R.; Sun, S.; Åkermark, B.; Sun, L. *The Journal of Organic Chemistry* **2008**, *73*, 3775–3783.

(360) D'Avino, G.; Souto, M.; Masino, M.; Fischer, J. K.; Ratera, I.; Fontrodona, X.; Giovannetti, G.; Verstraete, M. J.; Painell, A.; Lunkenheimer, P.; Veciana, J.; Girlando, A. *Nature* **2017**, *547*, E9–E15.

Appendix I: Charge Transfer - A Quantum Mechanical Depiction

A quantum-mechanical depiction of the resonance ground state of these complexes was postulated by Mulliken:[50,71]

$$\psi_N = a\psi_0(A, D) + b\psi_1(A^-D^+) \tag{1}$$

where ψ_N is the ground state wavefunction of the system, $\psi_0(A, D)$ the 'no-bond' wavefunction, and $\psi_1(A^-D^+)$ the dative "charge-transfer" wavefunction between A^- and D^+. Specifically, $\psi_0(A, D)$ corresponds to the complex where binding is entirely due to 'physical' interactions such as van der Waals and hydrogen bonding. The wavefunction $\psi_1(A^-D^+)$ corresponds to the complex where one electron has been completely transferred from the donor to the acceptor, essentially ionizing both donor and acceptor species. The ratios between the no-bond and dative state is modulated in Equation 1 by the constants a and b, where b^2/a^2 varies from 0 for no transfer, and ∞ for complete (ionic) transfer. For typical complexes $a > b$, indicative of partial ionization and charge transfer between the donor and acceptor moieties. It is important to note that while Equation 1 describes a 1:1 complex of donor to acceptor, it can be easily modified for a more general though m:n complex.

Quantum mechanics dictate that ψ_N, $\psi_0(A, D)$ and $\psi_0(A^-D^+)$ be normalized such that $\int \psi_N^2 d\tau = 1$, $\int \psi_0^2 d\tau = 1$ and $\int \psi_1^2 d\tau = 1$. As a result, the coefficients a and b are related by:

$$\begin{gathered} a^2 + 2abS_{01} + b^2 = 1 \\ \text{where } S_{01} = \int \psi_0 \psi_1 d\tau \end{gathered} \tag{2}$$

For weak interactions, the ground-state energy (W_N) is a function of the energy of the 'no-bond' state (W_0) and the energy of interaction (X_0) between the donor and acceptor molecules. W_0 in

turn is comprised of the energy of the separated donor and acceptor components (assuming no interaction) (W_∞) and the energy of no-bond interaction (G_0), such that:

$$\begin{aligned} W_N &= W_\infty + G_0 - X_0 \\ &= W_0 - X_0 \end{aligned} \tag{3}$$

W_N can be further expanded by second-order perturbation theory:

$$\begin{aligned} W_N &\equiv \int \psi_N H \psi_N d\tau \\ &\approx W_0 - \frac{(H_{01} - S_{01}W_0)^2}{(W_1 - W_0)} \end{aligned} \tag{4}$$

where the energy of the 'no-bond' state (W_0), energy of the dative A^-D^+ state (W_1) and the interaction energy of the between A, D and A^-D^+ (H_{01}) can described as follows:

$$\begin{aligned} W_0 &= \int \psi_0 H \psi_0 d\tau \\ W_1 &= \int \psi_1 H \psi_1 d\tau \\ H_{01} &= \int \psi_0 H \psi_1 d\tau \end{aligned}$$

As a result, a quantum mechanical formulation for the relationship between the coefficients a and b in Equation refap1eq1 can be described using the tools of second order perturbation theory:

$$\frac{b}{a} \approx \frac{(H_{01} - S_{01}W_0)}{(W_1 - W_0)} \tag{5}$$

A similar analysis can be done for the excited state of the system (ψ_E), wherein

$$\psi_E = a^* \psi_1(A^-D^+) + b^* \psi_0(A, D) \tag{6}$$

If the wavefunction ψ_E is normalized in the same manner as done for ψ_N, the excited state energy (W_E) can be written in terms of W_1 and the resonance energy of the excited state (X_1):

$$\begin{aligned} W_E &= W_1 + X_1 \\ &= W_1 + \frac{(H_{01} - S_{01}W_1)^2}{(W_1 - W_0)} \end{aligned} \tag{7}$$

Here, the coefficients of the excited state interaction wavefunctions a^* and b^* are:

$$\frac{b^*}{a^*} = -\frac{(H_{01} - S_{01}W_1)}{(W_1 - W_0)} \tag{8}$$

For there to be a non-zero interaction between ψ_0 and ψ_1, both the orbital overlap S_{01} and the interaction energy H_{01} need to be non-zero. Since H has the total symmetry of the complex, both ψ_0 and ψ_1 must be from the same group-theoretic species and have the same spin-type (assuming weak spin-orbital coupling). In addition, it can also be shown that, for a one-electron transfer from D to A:

$$\begin{aligned} S_{01} &= \sqrt{2}S_{AD}(1 + S_{AD}^2)^{1/2} \\ \text{where } S_{AD} &= \int \psi_A \psi_D d\tau \end{aligned} \tag{9}$$

This depicts the overlap between the HOMO of the donor and the LUMO of the acceptor, and is thus a simple quantum mechanical explanation for the electron transfer process in charge transfer complexes.

The presence of new ground and excited energy states upon the co-assembly of donor and acceptor moieties, namely W_N and W_E, implies an energy transition that can be described using photophysical terms. Specifically, the band gap between the ground and excited energy states can be written in terms of the ionization potential of the donor (I^D) and the electron affinity of the acceptor

(E^A):

$$\begin{aligned} E_{CT} &= h\nu_{CT} \\ &= W_E - W_N \end{aligned} \tag{10}$$

From Equation 3 and 7:

$$\begin{aligned} E_{CT} &= (W_1 + X_1) - (W_0 - X_0) \\ &\text{where } W_0 = W_\infty - G_0 \end{aligned} \tag{11}$$

W_∞ is th energy of the separated components, and G_0 is the energy due to 'no-bond' interactions. Upon interaction, the energy of the dative structure $\psi_1(A^-D^+)$ (W_1) relative to the separated components W_∞ is the work involved to remove an electron from the donor, known as the ionization potential or energy of the donor (I^D), followed by that to add an electron by the acceptor, known as the electron affinity of the acceptor (E^A), and finally the energy of coulombic attraction between A^- and D^+ (G_1):

$$W_1 = W_\infty + I^D - E^A - G_1 \tag{12}$$

From Equation 11,

$$W_1 - W_0 = I^D - (E^A + G_1 - G_0) \tag{13}$$

Now, Equation 11 can be expressed in terms of I^D and E^A:

$$E_{CT} = I^D - E^A + (G_0 - G_1) + (X_0 + X_1) \tag{14}$$

These energy relationships ascertain that the energy gap between the ground and excited state for the charge transfer complex is primarily a function of the ionization potential of the donor, the electron affinity of the acceptor, as well as the bonding potentials to bring the donor and acceptor moieties into close proximity (G_0, G_1) and the resonance stabilization energies (X_0, X_1).

Appendix II: First- and Second-Order Ferroelectric Phase Transitions

Deriving the first- and second-order phase transitions for ferroelectric materials requires knowledge of basic thermodynamics:

$$G = U - TS - Xx - ED \tag{15}$$

Where G is the Gibbs free energy of the system, U is the internal energy, T is temperature, S is the entropy of the system, X and x are the stresses and strains imparted on the system, and finally E and D are the electric field and electric displacement vectors. From equation 15, we can derive the following:

$$\left(\frac{\partial G}{\partial D}\right)_{x,T} = E \tag{16}$$

$$\left(\frac{\partial E}{\partial D}\right)_{x,T} = \kappa^{x,T} \tag{17}$$

$$\begin{aligned} \kappa^{x,T} &= \frac{1}{\chi} \\ &= \frac{1}{\varepsilon - 1} \end{aligned} \tag{18}$$

Equation 15 defines a linear relationship between G and its constituent components. Near a phase transition, the free energy as a function of electric field E and displacement D can be expanded into its nonlinear terms:

$$G = \frac{\alpha}{2}D^2 + \frac{\gamma}{4}D^4 + \frac{\delta}{6}D^6 \tag{19}$$

whereγ and δ are temperature independent coefficients.

From here, the two derivations begin.

SECOND-ORDER FERROELECTRICS

The biggest assumption made in deriving the second-order phase transition is that γ and δ are always positive. Using this assumption, a qualitative sketch of G as a function of D can be seen in figure 1.16a. At positive values of α, there exists only one free energy minima, at $D = 0$. This implies that when $\alpha > 0$, the only thermodynamic equilibrium exists at zero spontaneous polarization. In contrast, negative values of α results in two degenerate energy minima, indicative of two non-zero polarization states. To deduce the location of the polarization states, we have to set the electric field of the system to zero. The electric field can be expressed as a function of electric displacement using equationap2ep5

$$E = \left(\frac{\partial G}{\partial D}\right)_{x,T} = \alpha D + \gamma D^3 + \delta D^5 \tag{20}$$

Conventional Devonshire theory assumes that near the Curie phase transition temperature, the coeffiecient α linearly depends on temperature:

$$\alpha = \beta(T - T_c) = \kappa^{X,T}, \qquad T > T_c \tag{21}$$

where T_c is the Curie temperature at which phase transition from a ferroelectric to paraelectric material occurs.

Now at $E = 0$, $D = P_s$ such that (ignoring the highest order term for D):

$$0 = \beta(T - T_c)P_s + \gamma P_s^3 \tag{22}$$

$$P_s^2 = \frac{\beta(T - T_c)}{\gamma} \tag{23}$$

Equation 23 now quantitatively describes the state of two degenerate polarization states at $E = 0$ when $\alpha < 0$, which corresponds to the thermodynamic free energy minimum. From before, when $\alpha > 0$, or more specifically when $T > T_c$, the only global energy minimum occurs at $D = 0$. As a result, the polarization remains finite when $T < T_c$, zero when $T \geq T_c$. This relationship is schematically drawn on Figure 1.16b.

In addition $\kappa^{X,T}$ can be calculated for the condition that $T < T_c$:

$$\kappa^{X,T} = \left(\frac{\partial E}{\partial D}\right)_{x,T} = \beta(T - T_c) + 3\gamma P_s^2 \tag{24}$$

Knowing P_s from equation 23:

$$\kappa^{X,T} = 2\beta(T_c - T) \qquad T < T_c \tag{25}$$

This implies a $\kappa^{X,T}$ with a negative slope as function of T when $T < T_c$, a positive slope (following equation 21) when $T > T_c$, and a value of zero when $T = T_c$. In turn, the dielectric susceptibility (and dielectric constant) of the material increases until it reaches an anomalous spike (technically $\varepsilon = \infty$) at $T = T_c$, followed by a decay at $T > T_c$. The anomalous spike in ε is often how researchers distinguish and delineate a ferroelectric-paralectric phase transition in ferroelectric materials.

FIRST-ORDER FERROELECTRICS

The primary difference between first- and second-order phase transitions is the assumption behind the constant γ in equation 19. Where the second-order derivation required $\gamma > 0$, first-order transitions assumes $\gamma < 0$. As a result:

$$G = \frac{\alpha}{2}D^2 - \frac{\gamma}{4}D^4 + \frac{\delta}{6}D^6 \tag{26}$$

Once again substituting the Devonshire approximation for α,

$$G = \frac{\beta(T - T_c)}{2}D^2 - \frac{\gamma}{4}D^4 + \frac{\delta}{6}D^6 \tag{27}$$

It is evident from equation 27 that the relationship between G and D is far more complicated (Figure 1.17a) than that in the second-order transitions. At $T > T_c$, only one global free energy minimum exists ($D = 0$), and no net polarization can be maintained ($P_s = 0$) by the material. At $T < T_c$, two degenerate minima exist that define non-zero net polarizations. At $T = T_c$, however, three equivalent global free energy minima exist, all at G = o. To further elucidate this oddity, we must first define E:

$$E = \left(\frac{\partial G}{\partial D}\right)_{x,T} = \beta(T - T_c)D + \gamma D^3 + \delta D^5 \tag{28}$$

At $T = T_c$, $G = E = 0$. As a result:

$$G = \frac{\alpha}{2}P_s^2 - \frac{\gamma}{4}P_s^4 + \frac{\delta}{6}P_s^6 = 0 \tag{29}$$

$$E = \beta(T - T_c)P_s + \gamma P_s^3 + \delta P_s^5 = 0 \tag{30}$$

Subtracting equation 29 from equation 30:

$$\frac{5\delta}{6}P_s^4 - \frac{3\gamma}{4}P_s^2 + \frac{\beta(T - T_c)}{2} = 0 \tag{31}$$

This condition is satisfied when

$$T = T_c + \frac{3}{16}\frac{\gamma^2}{\beta\delta} \tag{32}$$

Substituting back into equationap2eq15 and solving for P_s:

$$P_s^2 = \frac{3\gamma}{4\delta} \qquad T = T_c \tag{33}$$

This states that at the transition temperature, the spontaneous polarization (P_s) does in fact have a finite value. Knowing that $P_s = 0$ when $T > T_c$, a qualitative picture of the spontaneous polarization as a function of temperature can be drawn (Figure 1.17b). Furthermore, the permittivity can be deduced from equation 28:

$$\kappa^{X,T} = \beta(T - T_c) - 3\gamma P_s^2 + 5\delta P_s^4 \tag{34}$$

From this, we can deduce the various forms of $\kappa^{X,T}$, above and below the transition temperature T_c:

$$\kappa^{X,T} = \beta(T - T_c) \qquad T > T_c \tag{35}$$

$$\kappa^{X,T} = \frac{3\gamma'}{4\delta} + 8\beta(T_c - T) \qquad T \to T_c^- \tag{36}$$

$$\kappa^{X,T} = \frac{3\gamma'}{16\delta} + \beta(T - T_c) \qquad T \to T_c^+ \tag{37}$$

This demonstrates (Figure 1.17c) that the dielectric susceptibility of the material (and therefore the dielectric constant) undergoes a discontinuous change at $T = T_c$, a hallmark of first-order ferroelectric transitions. Above and below T_c, however, the susceptibility is continuous with a positive, and negative slope respectively.

Appendix III: A Primer on Charge Transfer Ferroelectric Measurements

Measuring ferroelectricity in charge transfer co-crystals has been the subject of a lot of interest. Theoretical studies[194,195] have attempted to predict the remnant polarization and mechanism behind the ferroelectric behavior observed. Specifically, Chen et al.[194] attempted geometry optimization of the LASO co-crystals, while D'Avino et al.[195] chose to utilize density functional theory (DFT). While this section does not aim to critique each paper, both do not correctly predict the ferroelectric behavior in the LASO co-crystal system. Granted, this issue is compounded by our incomplete knowledge of the mechanism of ferroelectric polarization in these co-crystals. Traditional mechanisms of atomistic polarization,[78,115,160] where symmetry-breaking displacement of atoms within a crystal lattice induces polarization, is not applicable in this context as the organic molecules themselves are fixed in place. In addition, the centrosymmetric crystal refinement belies the possibility of a global lack of a crystallographic inversion center within the co-crystal, despite evidence of second harmonic activity and switchable polarization. Further studies are, of course, warranted to elucidate the mechanism behind the switchable polarization. These studies would not only delve into the details of each reported co-crystal, but also push to expand the library of possible ferroelectric LASO co-crystals.

This appendix provides intimate detail on how to reliably reproduce the crystallization and ferroelectric measurements, for LASO crystals and beyond. It is an effort to introduce transparency into a field that is mired with opaque practices,[360] spurred not by the quest for scientific discovery as much as an unyielding and unnecessary thirst for personal gain. The following is dedicated to those wishing to unravel the intricate and complex behavior behind these materials, in a manner devoid of questionable methods and unbiased results.

CRYSTALLIZATION

As mentioned in previous chapters, the co-crystallization of donor and acceptor molecules plays a key role in both the photophysical and electronic properties of the resulting material. Not only does co-crystallization define the dominant growth axis of the crystal, but it also defines the quality of electronic measurements obtained. As a result, care during the crystallization process is an essential first step in building this library of complex organic electronic materials.

To aid with this effort, below are some key tips and pointers that aid in preparation of these co-crystals. Note that these tips are meant to augment existing reported experimental protocols,[79,103,197] and should not be viewed as conflicting or substitutive. Most of these tips have been garnered through trial and error, and while they may not be the only method to obtain the specific results desired, they have worked in the past and have yielded multiple successful publications in the field.

Some of the details important to growing robust crystals are as follows:

1. The presence of water in the crystals is detrimental to crystal growth. It is responsible for crystal branching and splintering, as well as the growth of the fragile and thin crystals. In our system, water acts as an impurity, disrupting lattice formation and creating defects. These defects are detrimental and significantly degrade device performance.

   While it is difficult to remove all presence of water from the crystallization process, steps can be taken to minimize water in the crystallization process. These include:

   a) Washing all 16 × 150 mm or 18 × 150 mm test tubes with acetone, and drying the glassware in a glassware-drying oven for several days

   b) Using anhydrous solvents. While the strict use of anhydrous solvents is not vital, we often used anhydrous solvents from Aldrich Sure-Seal bottles

2. Since the crystals grow via liquid-liquid diffusion at the interface of two solvents, the following steps are vital to ensure a stable interface upon which crystallization can occur:

a) Passing the dichloromethane/diethyether co-assembly solutions through a 0.45 um filter into a dry test tube. This is done slowly to limit bubble formation, and down the side of the test tube to minimize splashing

b) The same is done for the counter-solvent (chlorobutane), with the exception of passing the solvent on the opposite wall of the test tube. This establishes the two visible solvent layers

c) Temperature fluctuations can inhibit crystal growth, as they induce convection currents that disrupt the interface between the two solvent layers. As a result, it is impactful to hold the crystallization tube by the top rather than the bottom, to limit the conduction of body heat to the solvents

3. Instant nucleation may occur, but experience dictates that higher quality crystals are obtained from tubes where there is at least a few minute delay prior to visible crystal growth. Crystal growth needs to occur for a few days, before they are long and robust enough for device preparation and handling

FERROELECTRIC SET UP

The set-up for ferroelectric devices and measurements is almost entirely custom-built, utilizing the best minds and abilities, and combining them with the best facilities available at Northwestern University. Doing so increased the transparency behind the ferroelectric measurements themselves, and allowed for more custom solutions to fit each measurement technique.

All measurements were done with the aid (Figure 8.1a) of a Phyiscal Property Measurement System (PPMS). This instrument not only offers flexibility and control of the temperature and atmosphere surrounding the crystal device, but also shielded the device measured from external electric fields. To further isolate the device from external electric noise, the PPMS was housed (Figure 8.1b) in a large Faraday cage. All measurements were performed under a constant flow of dry helium

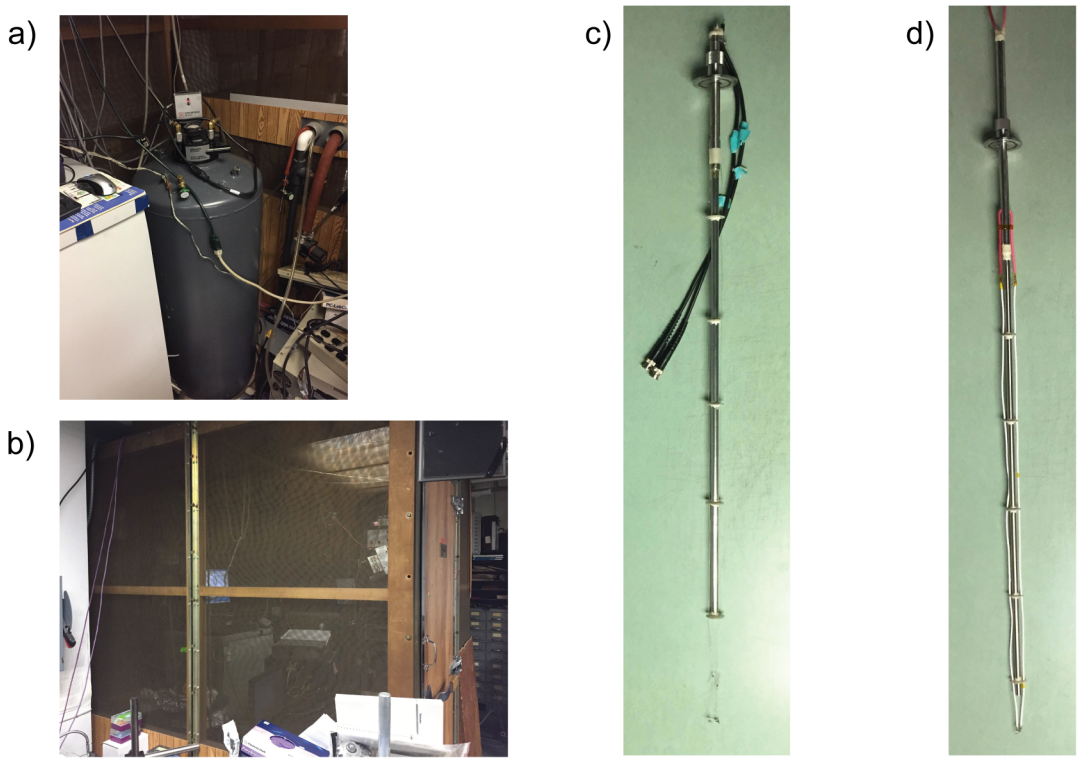

Figure 8.1: All ferroelectric measurements were performed with the aid of (a) a physical property measurement system (PPMS), housed inside a (b) Faraday cage. All crystals were mounted either on a (c) low-voltage or (d) high-voltage probe that enables application of voltages up to +300V or +2000V respectively.

atmosphere. This served two purposes: 1) to minimize the amount of water vapor and other gases susceptible to ionization at large electric fields, and 2) to conduct away any changes in temperature during the application of electric fields, minimizing internal crystal damage due to heating.

Custom Probes

The two probes (Figure 8.1c,d) used were custom-built based on the experimental conditions of the desired measurement. Both probes had the same frame that allowed for the positioning of the sample at the bottom the PPMS dewer: a stainless steel rod (l = 35 in, t = 0.01 in, O.D. = 0.375 in) attached to a quick-connect coupling adapter (KF to QF, Lesker), with fiberglass spacers for the

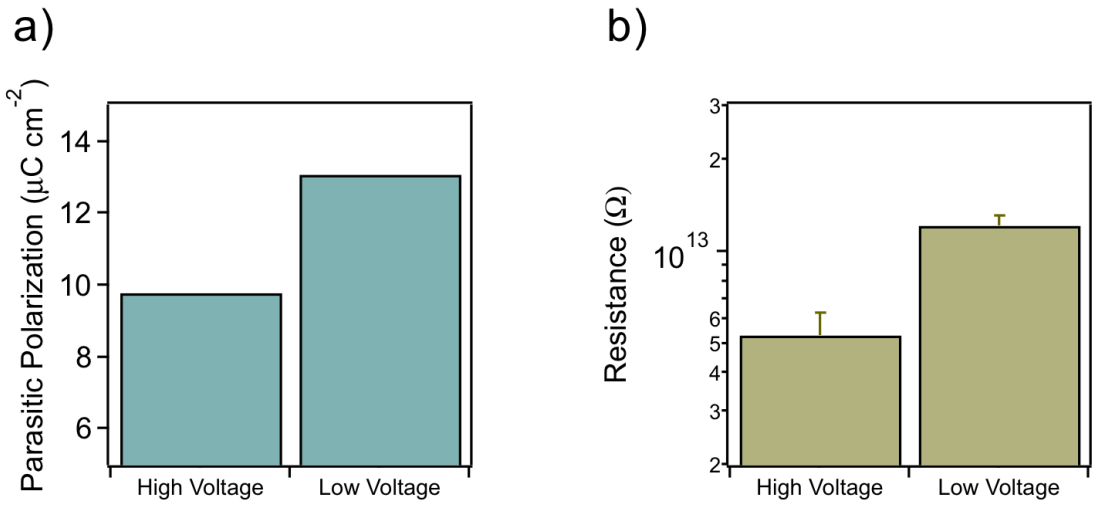

Figure 8.2: (a) Parasitic polarizations (capacitive) and (b) resistances of high-voltage and low-voltage custom ferroelectric probes

electrical wires to pass through. All connects and wires were glued and sealed together using Loctite Hysol 9462, which has displayed incredible temperature and electrical stability.

The high-voltage probe (Figure 8.1c) uses sheathed high voltage wire are the primary circuit component. The wire is rated up to 2000V, and does not display any signs of degradation through thousands of voltage-cycling experiments. The high voltage probe is typically used for high voltage room-temperature and cryogenic temperature polarization experiments, where the applied voltage often crosses the 1000V threshold.

The low-voltage probe (Figure 8.1d), on the other hand, uses a NiCu wire as its primary circuit component with a BNC connector. This probe is typically used for low-voltage, or dielectric constant measurements, as the wires and BNC connector are only rated up to 300V.

Both the probes have been engineered for high resistance, low capacitance applications. The probes themselves (Figure 8.2) have low capacitances (and parasitic polarizations), to minimize background signals that may occlude any ferroelectric polarization from the device measured, as well as high resistances to limit the current flow through the devices measured.

DEVICE PREPARATION

Preparing single crystals for ferroelectric measurements is an art as much as it is a science. Care needs to be taken to not only produce reliable and reproducible crystal devices, but also to impart minimal strains or damage onto the crystal itself before measuring. It is a low-throughput process that takes dozens of crystals and many months to become proficient at, but is a process that has worked for a number of years among a number of experimentalists. The following sections explores some of the nuances that take some of the art out of the science, and make the process of measurement more transparent and user-friendly.

Crystal Handling

One of the hallmarks of the LASO co-crystals is their temporal and air stability. These single crystals have known to be stable in air at atmospheric temperatures and pressures for years. Experience dictates that the best crystals to use for measurements are those that are devoid of splinters, have lengths on the order of 1mm, and widths/thicknesses on the order of 30-50 μm each. These crystals are typically the most robust for physical manipulation, and can withstand the high electric fields required to elicit a ferroelectric response. Care must be taken, however, in handling the crystals, since they are the very brittle and prone to shattering. Typically, careful manipulation using a sewing needle has been shown to work, as the needle tip provides the fine dexterity needed to separate, move or rotate crystals.

Making a Device

As mentioned in the previous section, all LASO co-crystals were manipulated and handled using a sewing needle. To measure ferroelectric polarization, electrodes have to be physically attached across the axis of measurement. This requires each individual crystal to be manipulated while temporarily fixed in place. A Ted Pella PELCO Vacuum Pick-up System, coupled with a 25 gauge tip, was used to pick up individual crystals for manipulation and device preparation. Care must be

taken in picking up these crystals, as the size and aspect ratio of these needle-like crystals can mean some crystals would be pulled inside the tip, clogging up the vacuum line and damaging the vacuum system. A successful crystal pick-up (Figure 8.3a) ensures that the edges of the crystal are well away from the tip of the vacuum tweezer, and that the crystal is aligned roughly parallel to the bench, allowing for easy electrode attachment. The next step in device preparation of attaching gold electrodes to the crystals involves using gold paste (Ted Pella PELCO Conductive Gold Paste) and 12.7 μm gold wire (Alfa Aesar Gold Wire, 0.0127 mM dia, 99.9%).

The use of the conductive gold paste is twofold: 1) to ensure a good electrical contact between the wire and the crystal and 2) to define the electrode dimensions for each device. Since typically the entire width and thickness of the crystal is covered when applying the gold paste, the cross-section of the material that is 'electrically active' is clearly defined. The diluent for the conductive gold paste, namely toluene, ethyl acetate and ethanol, were not shown to have any deleterious effects on the crystal itself. This is in contrast to other conductive pastes (such as graphite) that have either water-based or acetone-based diluents, both of which have been observed to degrade the crystal upon contact and exposure.

Applying gold onto the edges of the crystal involves using a sewing needle to pick up a droplet of the gold paste (Figure 8.3b), and lightly touching the crystal with the top of the convex meniscus. Given the volatile nature of the diluent solvent, the viscosity of the paste might have to be tuned so that the gold paste neither spreads all over the crystal (at extremely low viscosities) nor pulls the crystal off the vacuum tweezer (at high/near solid viscosities). This was done using a monopropylene gloycol methyl ether-based thinner (Ted Pella PELCO SEM-Gold/Silver Thinner/Extender).

Once gold paste has been applied to the both edges of the crystals (Figure 8.3c,d), gold wire is attached by first picking up the wire using self-closing tweezers and maneuvering it so that the tip of the wire is touching the gold paste. Care should be taken to ensure that the wire remains straight, as this makes manipulating the wires to mount the crystal onto the ferroelectric probe significantly easier. To adhere the gold wire onto the gold electrodes on the crystal, another small droplet of gold

paste placed in between the wire and crystal. As the solvent evaporates, the gold will adhere the wire onto the crystal, resulting in a completed electrode (Figure 8.3e). The same must be done on the other side of the crystal, to result in a finished (Figure 8.3f) crystal device.

Device Mounting

Mounting the crystal device onto the aforementioned ferroelectric probes involves a procedure similar to that used to prepare the crystal device itself. Here, instead of using gold paste as the conductive adhesive between the device and the ferroelectric probe, silver conductive paste (Ted Pella PELCO Colloidal Silver) is used. Here, the crystal device is maneuvered so that the gold wire rests on the end of the probe. Silver conductive paste (on a new sewing needle) is then used to adhere the wire onto the probe. To connect the second wire to the other side of the probe, some manipulation of the wire might be necessary. This can be done using tweezers, though care needs to be taken to make sure the wire does not break due to the stresses applied. A finished mounted device would have both wires adhered onto the ferroelectric probe, with little or no torque on the crystal itself.

FERROELECTRIC MEASUREMENTS

The following section outlines how best to perform ferroelectric hysteresis measurements on single crystals of LASO compounds. These methods have been optimized specifically for crystals with high coercive fields through trial and error, over hundreds of samples and a number of years. While these protocols may not apply for all ferroelectric measurements on all types of materials, they do work for measurements on single crystals.

Hysteresis Loops

All ferroelectric hysteresis loops measured are done using the high voltage probe, as described above. The reason behind this choice is that the coercive field in LASO compounds to induce ferro-

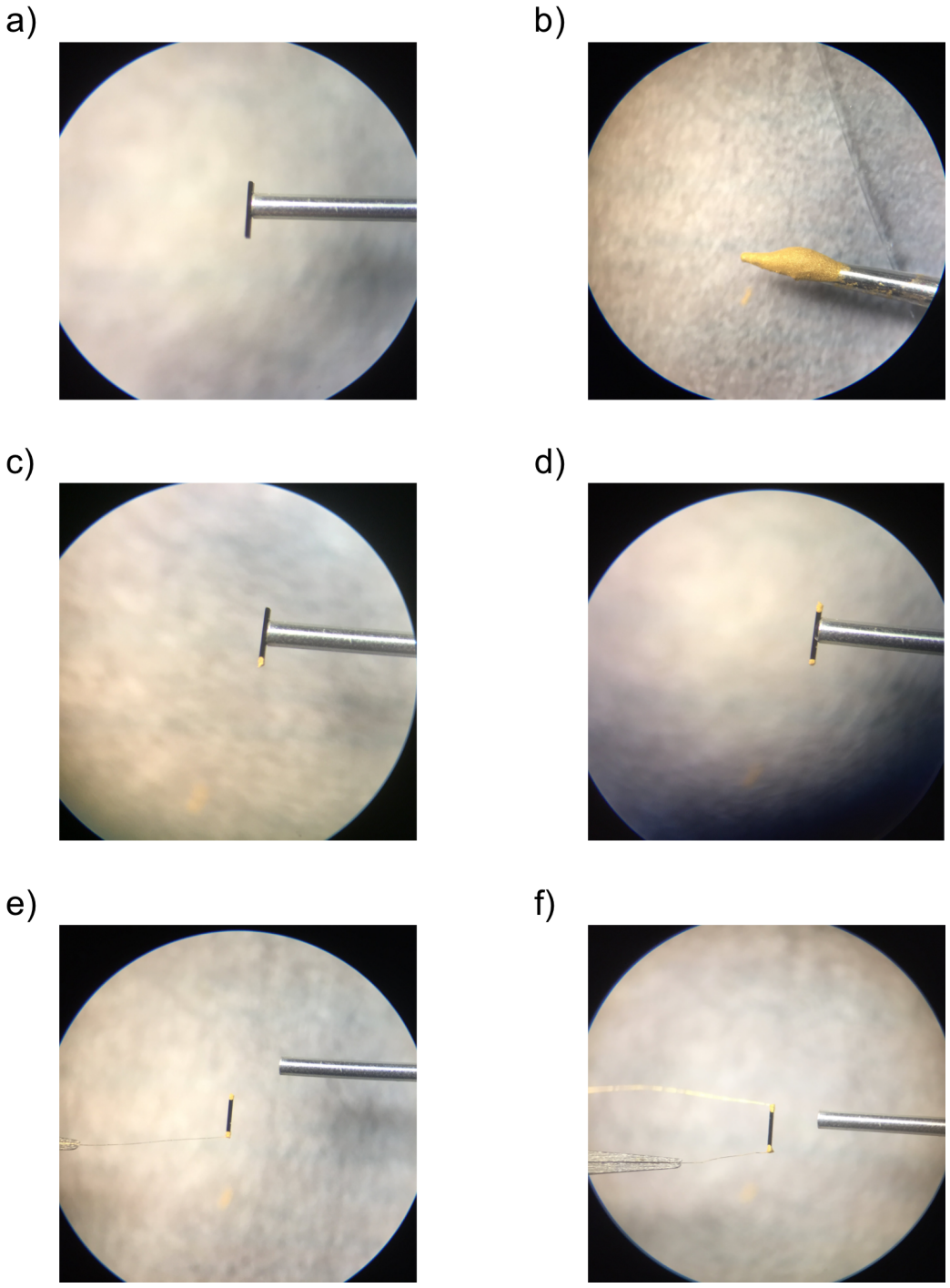

Figure 8.3: Step-by-step images involved in making a ferroelectric device from organic LASO co-crystals. (a) The co-crystals have to be picked up using vacuum tweezers. (b) Au paste, loaded on the edge of a needle, helps adhere the wires to the crystal. (c,d) Au is then applied to both sides of the crystal, after which (e,f) Au wires are adhered to result in a complete LASO ferroelectric device

electric switching is very high, requiring the application of hundreds of volts to induce switching. As a result, only the high voltage probe is used (in conjunction with the high voltage amplifier).

Due to spikes in inductive fields and eddy currents induced by sudden increases in high voltage measurements, all ferroelectric measurements were done by gradually scaling up the voltage until suitable ferroelectric hysteresis loops were obtained. These were typically done in increments of 100 V, with at least a gap of a few minutes in between subsequent increases to allow the system to equilibrate. In addition to incremental voltage scaling, each ferroelectric measurement was also repeated 10 times, to ensure reproducibility and absolve the possibility of erroneous hysteresis loops obtained due to space-charge or leaking current effects. Since all measurements were performed under careful temperature control and constant flow of helium, local heating of the crystals was considered negligible. That said, these LASO crystals do degrade at extremely high voltages (greater than 1000 V), so it is not uncommon for the crystal to degrade before achieving a saturated ferroelectric polarization loop.

The data output from the Sawyer-Tower-based ferroelectric tester includes capacitances from the wires and the probe itself, all of which has to be subtracted. Since the capacitances of the probes and wires are arranged in parallel, the net capacitance of the system is a linear sum of the capacitance of the probes, wires and crystal. This translates to the net polarizations, which is also a linear combination of the polarization of the probes, wires and crystal. As a result, manually subtracting a linear polarization-voltage relationship from the analyzed data reveals the polarization loop of the crystal itself. The underlying polarization of the probes and testing wires can be obtained by measuring the dielectric constant of the empty probe itself.

It is important to note that the quality of the crystal selected for ferroelectric hysteresis measurements greatly affects the polarization hysteresis loop obtained. Defects in the crystal (be they internal or external defects) can significantly influence whether the output polarization-voltage loop is indicative of a leaking dielectric, or an insulating ferroelectric material. Important control measurements such as the resistivity of the crystals elucidate information about the internal structure of

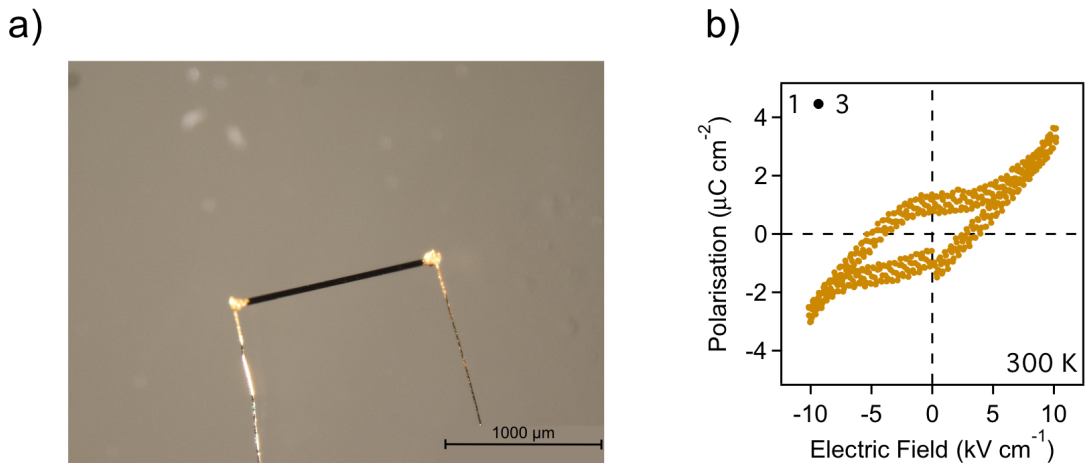

Figure 8.4: (a) Optical image and (b) room-temperature ferroelectric polarization of co-crystal **1•3**[79] from (Section 1.4.3.

the crystals, and to what extent leakage currents will play a role in the obtained polarization-voltage loops. In addition, optical images (Figure 8.4, 8.5) of the crystal can reveal information about crystal splintering. Since splinters concentrate charge on a local point, electric discharge can alter the polarization loops obtained, rendering a classic lossy dielectric loop[132] even though the underlying material itself is ferroelectric.

Dielectric Measurements

Measuring the dielectric response of the crystal as a function of temperature is a relatively simply endeavor, given the fine temperature control and large range obtainable using a Physical Property Measurement System (PPMS). The temperature range chosen (5K to 400K) is largely limited by the melting point of helium, the range of the PPMS, and the temperature at which the crystal degrades. High temperature dielectric measurements have not been possible for the LASO crystals described here for precisely these reasons. For each temperature, the dielectric constant is measured 5 times, with a gap of 3 seconds between each measurement, so as to reduce to signal-to-noise error associated with low-dielectric materials. It might be advantageous to attach multiple crystals in parallel to improve the signal-to-noise ratio, as the dielectric constant is an additive property in

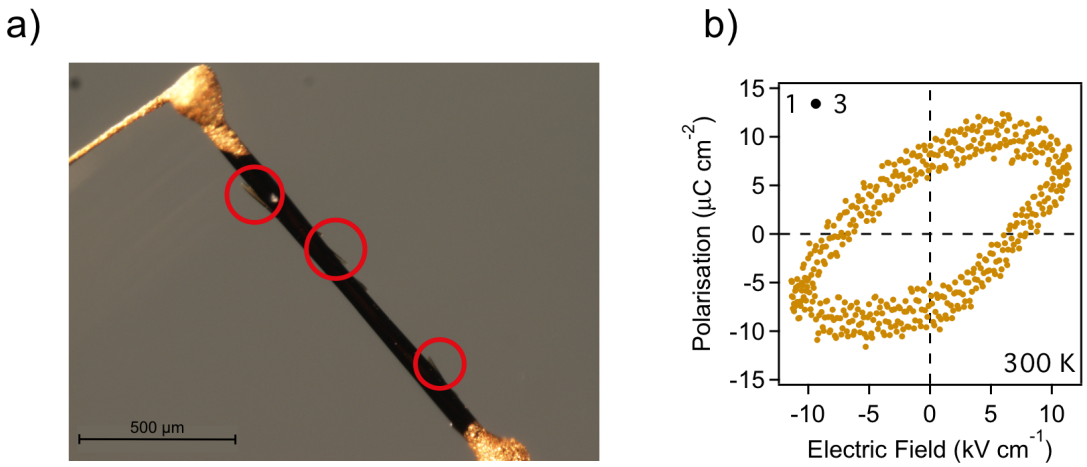

Figure 8.5: (a) Optical image and (b) room-temperature lossy dielectric[132] hysteresis of splintered co-crystal **1•3**[79] from (Section 1.4.3. The locations of the splintered edges are identified with red circles.

series circuits. Care must be taken, however, to ensure the wires or crystals do not touch each other, as this would cause a short circuit. In addition, as with the polarization hysteresis measurements, the dielectric behavior of the probe and wires need to be baseline subtracted to obtain that of the measured crystal itself.

Since the purpose of measuring the dielectric constant is to look for discontinuities indicative of a ferroelectric-paraelectric phase transition, spikes in the measured dielectric constant could inform a phase transition. Reproducing these spikes across multiple AC frequencies delineates the materials property (which should be independent of experimental condition) from any other anomalous causes. It is not uncommon for the measured dielectric constant to decrease with increasing AC frequency.

VITA

ASHWIN NARAYANAN

(607) 220-7823
ashwinn@u.northwestern.edu

2220 Campus Drive
Cook Hall, Room 3044
Evanston, IL 60208

EDUCATION

Northwestern University, McCormick School of Engineering, Evanston, IL (Anticipated) June 2018

Doctor of Philosophy;	Materials Science and Engineering,
Certificate;	Management for Scientists and Engineers
GPA:	3.76 out of 4
Thesis:	*Intermolecular Organic Charge Transfer Complexes for Electronic and Biological Applications*

Cornell University, College of Engineering, Ithaca, NY

Bachelor of Science;	Materials Science and Engineering; Cum Laude	May 2012
Thesis:	*Surface-Modified Iron Oxide Nanoparticle Hybrid Materials for Magnetic Shape Memory Applications*	

RESEARCH EXPERIENCE

Graduate Researcher, *Professor Samuel Stupp,* Northwestern University September 2012 – Present

- Developed a new class of organic ferroelectric materials that display spontaneous polarization and second harmonic activity along two independent axes
- Designed non-destructive experimental methods to probe electronic and structural properties of organic single crystals
- Investigated the assembly and ambipolar semiconducting properties of solution-processed host-guest crystals and charge transfer complexes for applications as thin-film transistors
- Synthesized amphiphilic molecules that couple aromatic organic chromophores with peptide moieties to yield dipolar supramolecular nanostructures
- Explored the kinetics and thermodynamics of molecular exchange between supramolecular amphiphiles using charge transfer fluorescent signalling
- Established a protocol to probe the mechanical properties of organic-inorganic hybrid perovskite films, as well as supramolecular photocatalytic nanostructures
- Assisted with grant writing and reporting towards securing funding upwards of $ 2M from the Department of Energy and National Science Foundation

Undergraduate Researcher, *Professor Lynden Archer,* Cornell University August 2010 – May 2012

- Optimized gram-scale synthetic and characterization methodology for 20 nm monodisperse iron oxide cubic nanoparticles
- Functionalized magnetic nanoparticles with 10 nm polymer corona to create core-shell magnetic organic-inorganic hybrid material soluble in aqueous solvents
- Probed magnetic properties of and began investigations into magnetic-induced shape memory effects

TEACHING EXPERIENCE

Teaching Assistant, *Northwestern University,* Phase Equilibria and Diffusion of Materials January 2017 – March 2017

- Conducted weekly recitation sections, encouraging group discussions to guide a glass of 25 undergraduate engineering students through coursework and assignments

Teaching Assistant, *Northwestern University,* Materials for Energy-Efficiency Technology September 2015 – December 2015

- Facilitated weekly office hours, where graduate and undergraduate students from the class of 40 were tutored on weekly class content, laboratories and problem sets
- Created and graded laboratories, problem sets and examinations that were representations of the class content, and forced students to think outside the box in applying concepts learned in class

Guest Lecturer, *Northwestern University,* Materials for Energy-Efficiency Technology September 2015 – December 2015

- Taught a 50 minute lecture to a class of 40 graduate and undergraduate students on the energy implications of magnetic and flash memory technology

Teaching Assistant, *Cornell University,* Materials Chemistry August 2011 – December 2011

- Guided over 50 undergraduate materials science students on course content, problem sets, laboratories and examinations through weekly office hours

STUDENT MENTEES

Emily C. Moy, Undergraduate Student — January 2016 – June 2018

Benjamin Swanson, MRSEC Research Experience for Undergraduates (REU) Summer Student — June 2014 – August 2014

ACADEMIC PUBLICATIONS

4. **Narayanan, A.**; Cao, D.; Frazer, L.; Tayi A. S.; Blackburn A. K.; Sue, A. C.-H.; Ketterson J. B.; Stoddart J. F.; Stupp S. I. "Ferroelectric Polarization and Second Harmonic Generation in Supramolecular Co-Crystals with Two Axes of Charge-Transfer", *Journal of the American Chemical Society* **2017**, 139, 9186-9191

3. Kazantsev, R.; Dannenhoffer, A.; Weingarten, A.; Phelan, B.; Harutyunyan, B.; Aytun, T.; **Narayanan, A.**; Fairfield, D.; Boekhoven, J.; Sai, H.; Senesi, A.; O'Dogherty, P.; Palmer, L.; Bedzyk, M.; Wasielewski, M.; Stupp, S. I. "Crystal-Phase Transitions and Photocatalysis in Supramolecular Scaffolds", *Journal of the Americal Chemical Society* **2017**, 139, 6120-6127

2. Barnes, J. C.; Dale, E. J.; Prokofjevs, A.; **Narayanan, A.**; Gibbs-Hall, I. C.; Juríček, M.; Stern, C. L.; Sarjeant, A. A.; Botros, Y. Y.; Stupp, S. I.; Stoddart, J. F. "Semiconducting Single Crystals Comprising Segregated Arrays of Complexes of C_{60}", *Journal of the American Chemical Society* **2015**, *137,* 2392–2399.

1. Blackburn, A. K.; Sue, A. C.-H.; Shveyd, A. K.; Cao, D.; Tayi, A.S.; **Narayanan, A.**; Rolczynski, B. S.; Szarko, J. M.; Bozdemir, O. A.; Wakabayashi, R.; Lehrman, J. A.; Kahr, B.; Chen, L. X.; Nassar, M. S.; Stupp, S. I.; Stoddart, J. F. "Lock-Arm Supramolecular Ordering: A Molecular Construction Set for Cocrystallizing Organic Charge Transfer Complexes", *Journal of the American Chemical Society* **2014**, *136*, 17224–17235.

(In preparation)

5. **Narayanan, A**.; Barreda, L.; Sai, H.; Passarelli, J. V.; Dannenhoffer, A. J.; Aytun, T.; Fairfield, D. J.; Moy, E. C.; Stupp, S. I. "Co-Assembly and Phase Separation in Semiconducting Hydrogen-Bonded Charge Transfer Complexes", *In Preparation.*

6. **Narayanan, A.**; Cao, D.; Sue, A.C.-H.; Manley, E.; Blackburn A. K.; Rolczynski, B.S.; Hong, M.; Holcroft, J. M.; Chen, L. X.; Stoddart, J.F.; Stupp, S. I. "Room-Temperature and Second Harmonic Activity in Co-Crystals of Pyomellitic Diimide with a Series of 1,5-Difunctionalized Naphthalenes", *In Preparation*

7. **Narayanan, A.**; Barreda. L.; Cao, D.; Sato, K.; Hendricks, M. P.; Moy, E. C.; Stupp, S. I. "Intermolecular Charge-Transfer and Molecular Exchange between Complementary Donor/Acceptor Peptide Amphiphiles", *In Preparation*

8. **Narayanan, A.**; Sasselli, I. R.; Sato, K.; Hendricks, M. P.; Moy, E. C.; Stupp, S. I. "Tuning Supramolecular Assembly by Amino Acid Hydrophobicity", *In Preparation*

9. Fairfield, D. J.; Sai, H.; **Narayanan, A.**; Passarelli, J. V.; Chen, M.; Palasz, J.; Qu, K.; Palmer, L. C.; Wasielewski, M, R.; Stupp, S. I. "Structure-Property Relationships and Chemical Stability in Polymer-Perovskite Hybrid Photovoltaic Active Layers", *In Preparation*

10. Dannenhoffer, A. J.; Sai, H.; Harutyunyan, B.; **Narayanan, A.**; Edelbrock, A, K.; Passarelli, J. V.; Bedzyk, M. J.; Stupp, S. I. "Enhanced Hydrogen Production from Supramolecular Nanoribbons", *In Preparation*

11. Dannenhoffer, A. J.; Sather, N. A.; **Narayanan, A.**; Zambrotta, R. T; Stupp, S. I. "Extrusion Printing of Supramolecular Optoelectronic Hydrogels", *In Preparation*

12. Sather, N.A.; Sai, H.; Sato, K.; Ji, W.; Sasselli, I. R.; Synatschke, C.; Dannenhoffer, A. J.; Wallace, S. G.; **Narayanan, A.**; Kohlmeyer, R. R.; Hardin, J. O.; Zambrotta, R.; Berrigan, J D.; Hersam, M. C.; Durstock, M. F.; Mirau, P.; Stupp, S. I.; "3D Printing of Supramolecular Liquid Crystalline Hydrogels with Nanoscale Alignment", *In Preparation*

PATENTS

Stupp, S.I.; Stoddart, J.F.; Shveyd A.K; Tayi, A.S; Sue, A.C-H.; **Narayanan, A.**; Modular Approach for co-crystallization of donors and acceptors into ordered networks. U.S. Patent 9449731, September 20, 2016

Stupp, S.I.; Stoddart, J.F.; Shveyd A.K; Tayi, A.S; Sue, A.C-H.; **Narayanan, A.**; Supramolecular networks with electron transfer in two dimensions. U.S. Patent 9443636, September 13, 2016

INVITED LECTURES AND POSTERS

Ferroelectricity in Organic Charge Transfer Co-Crystals, *John H. Hilliard Symposium*, Evanston IL — June 2017

Surface-Modified Iron Oxide Nanoparticle Synthesis, *Senior Thesis Presentation*, Ithaca NY — May 2012

AWARDS

2nd Place - John H. Hilliard Symposium: Best Presenter Awards, *Northwestern University*	June 2017
2nd Place - Senior Thesis Awards, *Cornell University*	May 2012
Tau Beta Pi Engineering Honours Society, *Cornell University*	August 2011
Kessler Fellow for Engineering Entrepreneurship, *Cornell University*	May 2011

RESEARCH SKILLS

Synthesis:	■ Solid-Phase Peptide Synthesis ■ Reverse-Phase HPLC ■ Organic Crystal Growth by Liquid-Liquid Diffusion ■ Iron Oxide Nanoparticle Synthesis
Imaging:	■ Atomic Force Microscopy (Tapping, PeakForce QNM, PeakForce Tunnelling Modes) ■ Transmission Electron Microscopy ■ Two-Photon Confocal Microscopy
Photophysical Characterization:	■ UV-Vis Absorption Spectroscopy ■ Fluorescence Spectroscopy ■ Circular Dichroism ■ Fourier Transfor Infrared Spectroscopy
Electromagnetic Characterization:	■ Dielectric Spectroscopy ■ Ferroelectric Polarization ■ Field-Effect Mobility Measurements ■ 2-Probe Thin-Film and Single Crystal Conductivity ■ Magnetic Polarization
X-ray Characterization:	■ Small Angle X-ray Scattering (static capillary) ■ Grazing Incidence X-ray Scattering
Device Fabrication:	■ Single Crystal 2-Probe Ferroelectric and Dielectric Devices ■ Thin-Film Transistors with Top and Bottom Electrode Contacts
Software:	■ MATLAB ■ Mathematica ■ JAVA ■ Visual Basic ■ Cinema 4D ■ Igor Pro ■ Adobe Creative Suite ■ Microsoft Office
Languages:	■ English (Fluent) ■ Tamil (Native) ■ French

LEADERSHIP EXPERIENCE

Recruiting Manager, *Professor Samuel Stupp,* Northwestern University — January 2014 – January 2018

- Communicated chemistry, medical and materials research projects to broad audience of prospective graduate students
- Planned annual open houses and quarterly posters sessions to recruit graduate students to Northwestern and to the lab
- Coordinated, and collated quarterly research updates from 40+ group members into representative posters and slides

Co-Founder, *FerraPower* — January 2016 – August 2016

- Developed a zero-carbon emission energy generation system powered by metal fuels
- Spearheaded market research and economic analyses to define value propositions and beachhead market
- Collaborated and communicated with relevant industry leaders to develop go-to-market strategy and competitive landscape
- Pitched at multiple national business plan competitions to secure traction and seed funding

Business Manager, *Northwestern Materials Science Student Association* — March 2013 – March 2014

- Maintained yearly budget and allotted funds towards professional and social development
- Wrote numerous grants to facilitate activities that promote student-faculty engagement within the Department of Materials Science.

Business Development & Marketing Intern, *Seeo, Inc.*, California — June 2011 – August 2011

- Constructed models to monetize the comparative advantage of Seeo's novel battery technology
- Oversaw project, in collaboration with UC Berkeley, to forecast renewable power generation in the United States.

VOLUNTEER EXPERIENCE

Dog Town Volunteer, *PAWS Chicago* — January 2016 – Present

- Advised and paired potential adopters with rescue dogs, looking to best fit the animal's needs with the adopter's lifestyle
- Collaborated and supported fellow volunteers and full-time staff members with daily dog feeding and training responsibilities
- Coached new volunteers on proper adopter-dog interactions, and how to match shelter animals with potential adopters
- Showed over 100 shelter dogs to potential adopters, personally overseeing over 30 successful adoptions
- Mentored and trained over 20 new volunteers about the PAWS mission and roles as volunteers